INVESTIGATION OF BRAIN TUMOUR METABOLISM USING NATURALLY OCCURRING CHEMICAL EXCHANGE SATURATION TRANSFER AGENTS WITH MAGNETIC RESONANCE IMAGING

Francisco Torrealdea

Thesis submitted for the degree of Doctor of Philosophy

Department of Brain Repair and Rehabilitation
UCL Institute of Neurology
21 October 2015, the Future

I, Francisco Torrealdea confirm that the work presented in this thesis is my own. Where information has been derived from other sources, I confirm that this has been indicated in the thesis.

To Cecilia and Javier.
For all your support, your perseverance and your unconditional love, thank you.

Abstract

This thesis presents a thorough study on the newly developed *glucoCEST* magnetic resonance imaging (MRI) technique and its application for the assessment of malignant brain tumours. The key asset in *glucoCEST* is that it allows the detection of small concentrations of glucose using standard MRI scanners and has the potential to become a novel imaging tool for the investigation of diseases in which glucose metabolism is affected, in particular cancer.

The physical principles and the rationale behind the *glucoCEST* technique are described in detail and factors influencing the measurements (both physiological and hardware related) are analysed using computer simulations and evaluated with *in vitro* experiments. Special attention is given to the analysis of the first four sugars along the glycolytic pathway i.e. glucose, glucose 6-phosphate, fructose 6-phosphate and fructose 1,6-biphosphate as contributors to the overall observed signal. The results of this analysis give grounds for the argument of the intracellular origin of the *glucoCEST* signal, which opens the possibility of characterising tumours based on their metabolism using MRI.

A preclinical *glucoCEST* study on mice bearing human xenograft glioblastoma is also presented in which cancers with diverse phenotype are scanned longitudinally throughout the different stages of tumour development. While not conclusive, the results suggest that the *glucoCEST* technique is able to identify the presence of cancer at an earlier stage than standard MRI methods.

Contents

List of Figures

List of abbreviations

^{18}F-FDG-PET	fluorodeoxyglucose positron emission tomography
13C	Carbon 13
2DG	2-Deoxy-D-glucose
31P	Phosphorus 31
3OMG	3-O-methyl-glucose
ALT	alanine transaminase
APT	amide proton transfer
ASL	arterial spin labelling
ATP	adenosine triphosphate
BBB	blood brain barrier
CEST	chemical exchange saturation transfer
CNR	contrast to noise ratio
CNS	central nervous system
CPMG	Car-Purcell-Meiboom-Gill
CSF	cerebrospinal fluid
DS	direct saturation
DWI	diffusion weighted imaging
ETL	echo train length
F16bP	fructose 1,6-biphosphate
F6P	fructose 6-phosphate
FLASH	fast low angle shot
fMRI	functional magnetic resonance imaging
FOV	field of view
FW3rdM	full width third maximum
FWHM	full width half maximum
G	glucose
G6P	glucose 6-phosphate
G_{PE}	phase encoding gradient
G_{RO}	frequency encoding gradient
G_{SS}	slice selection gradient

GBM	glioblastoma multiforme
GCE	glucoCEST enhancement
GE	gradient echo
GLUT	glucose transporter
HCl	hydrochloric acid
HK	hexokinase
IP	intraperitoneal
IV	intravenous
MRI	magnetic resonance imaging
MS	multiple sclerosis
MT	magnetization transfer
MTRasym	magnetisation transfer ratio asymmetry
NaOH	sodium hydroxide
NMR	nuclear magnetic resonance
NOE	nuclear Overhauser effect
PDw	proton density weighted
PET	positron emission tomography
PFK	phosphofructokinase
ppm	part per million
ppp	pentose phosphate pathway
RF	radio-frequency
ROI	region of interest
SAR	specific absorption rate
SE	spin echo
SGPT	serum glutamate-pyruvate transaminase
SNR	signal to noise ratio
STD	standard deviation
SWI	susceptibility weighted imaging
T1w	T1 weighted
T2w	T2 weighted
TE	echo time
TR	repetition time
ZAR	Z asymmetry ratio

Acknowledgements

For the knowledge they have shared and the support they have generously given over the course of my PhD, I am deeply grateful to the following people.

My primary supervisor Prof Xavier Golay for his constant support and enthusiasm through this long process. Dr David Thomas for being always so approachable and helpful and for sharing his deep knowledge of MRI. Dr Simon Walker-Samuel whose work sparked my curiosity and motivate further research.

I would also like to thank Prof Sebastian Brandner and his group; without their collaboration this project would not have been possible. Particularly I would like to thank Nick Henriquez, Anna Benedykcinska and Joanne Lau for their help with tumour grafting and teaching how to do brain extractions. Also, Jessica Broni and Angela Richard-Londt for kindly providing us with the immunohistochemistry analysis.

My sincere thanks to Dr Kai-Hsiang Chuang and Dr Fatima Ali Nasrallah who gave me the opportunity to visit their lab, learn from their experience and share delicious hot-pots in the streets of Singapore. Many thanks also to Dr Rouslan Sitnikov for sharing his MRI knowledge and especially for the deep philosophical basement discussions. I will never forget the telepathic cockroaches!

I would like to thank Dr Mohamed Tachrount for his constant help as well as the rest of the MRI group for creating the happy environment in which I was lucky to work. Thank you to all my friends, and especially my brother Xanti, for dragging me out to see the real world from time to time.

Lastly, I cannot express enough gratitude to Marilena, who has been by my side throughout this process, as a colleague, as a teacher, as an inspiration and always as best friend. With her happiness she made this long journey short.

Overview

Tumours are heterogeneous by nature. They display a huge diversity of physiological patterns, yet most of them share one common characteristic, increased glucose consumption. This phenomenon, known as the Warburg effect, has been exploited by [^{18}F]-fluorodeoxyglucose positron emission tomography (FDG-PET) as a discriminator of tumour malignancy and to assess anti-cancer treatment response for many years. Currently FDG-PET is considered the gold-standard tumour screening technique. Nevertheless it holds two important disadvantages, namely its elevated cost and the use of radioactive tracers. These drawbacks limit the extent of FDG-PET as a routine screening modality.

On the other hand, chemical exchange saturation transfer (CEST) is a fast emerging magnetic resonance imaging (MRI) technique that is pushing the boundaries of MRI sensitivity. The physical mechanism of exchange of magnetisation makes it possible to detect metabolites down to the millimolar concentration range. In addition, due to its sensitivity to several physiological parameters, CEST is particularly suited for *in vivo* applications. These features allow CEST to obtain information that was out of reach for MRI until recently, such as the detection of protein content, biomarker of tissue pH, or molecular imaging using endogenous CEST agents, to cite a few examples. The number of applications is quickly increasing and the full potential of CEST yet to be seen.

In a recent work by our group, a new way of detecting glucose uptake based on CEST MRI was presented, named glucoCEST.[1] A major advantage of the technique is that it uses natural glucose to produce image contrast and therefore no radioactive tracer is needed. This offers a potential alternative to FDG-PET for cases where the use of radiation is not advisable. In addition, compared to PET systems, MRI is more widely available and cost effective. Owing to these virtues, glucoCEST may offer a more economic, accessible and safer alternative to FDG-PET.

In the present work the glucoCEST technique, will be investigated as a marker of glucose metabolism. The focus of this work will be the study of tumour metabolism, and particularly the assessment of brain gliomas with glucoCEST. However, as a technique that could inform on glucose utilisation, glucoCEST can be potentially

useful in a number of metabolic disorders.

This work presents an extensive analysis of the glucoCEST technique, from the conceptual idea, to the optimisation of the technique and its evaluation as a potential biomarker of tumour growth and metabolism in various models of cancer.

In Chapter 1 the concept of CEST-MRI and the underlying mechanisms governing its contrast is introduced. The main features of *in vivo* CEST will be described and the current uses and development of the technique will be outlined.

Chapter 2 presents the rationale behind the use of glucoCEST in the context of cancer. The benefits, drawbacks and the recommended good practices are discussed, as well as presenting a review of the studies published to date.

In Chapter 3 the mathematical formulation of CEST is presented. Computer based simulations are used to provide an extensive analysis of the main variables modulating the CEST contrast. Additionally, the optimisation of parameter values for best glucoCEST results are derived.

Chapter 4 presents an experimental study in which the chemical exchange properties of different sugars along the the glycolytic pathway are thoroughly investigated.

In Chapter 5 the origin of the glucoCEST contrast and the possibility of intracellular signal contribution is discussed. To do so a System Dynamics model of blood delivery and glucose consumption in cancerous and healthy tissues is developed to simulate their respective glucoCEST response.

Chapter 6 presents an animal study on human xenograft glioma models in which the potential of glucoCEST as a diagnostic tool in brain cancer is assessed.

Lastly, Chapter 7 includes the ongoing and future projects regarding exogenous CEST as a continuation of the work done in this thesis.

1. Introduction to Chemical Exchange Saturation Transfer

Chemical exchange saturation transfer (CEST) is a promising MRI technique that can provide images with unique physiological information capable of improving the diagnostic potential of MRI examinations in the clinic.
While the contrast in most MRI methods is based on the concentration and relaxation properties of free water protons in tissues, CEST contrast relies critically on hydrogen atoms located at specific chemical structures (labile protons), other than water. More specifically, CEST contrast is generated as the consequence of the existing interaction between these labile protons and free water protons, which can be detected with a standard MRI readout as a reduction of the MR signal intensity.
Labile protons are first 'tagged' using a radio frequency (RF) pulse at their own specific resonant frequency. Consequently, the magnetic state of these 'tagged' spins is transferred to water through dipolar or chemical interactions which eventually results in a reduction of the observable MR signal. This is the principle behind *off-resonance saturation* based imaging methods, which includes CEST MRI.

1.1. Off-resonance saturation based imaging

Electrons orbiting atoms in different chemical structures produce variations in the local magnetic environment. As a consequence protons of specific chemical groups have their own characteristic Larmor frequency, each separated by a few parts per million (ppm) from the central resonant frequency. This phenomenon, called chemical shift, is the basis of NMR (nuclear magnetic resonance) spectroscopy, and it is fundamental in the context of 'off-resonance' imaging as it allows the delivery of energy to selected chemical structures by irradiation with frequency selective RF pulses. Due to the interactions between spins in the labelled structures and water (mediated predominantly by either dipolar coupling or chemical exchange), high energy spin states (irradiated with RF pulses) get transferred to water protons. Constant spin interactions over a sufficiently long excitation RF pulse result in a signif-

icant net energy transfer from labelled molecules to water. The overall result is the partial saturation (equal density of high and low energy states) of the water protons which reduces the available MR signal to produce an image. The intensity of the effect is largely dependent on the rate of the spin interaction and the concentration of labelled protons. The process of magnetisation transfer acts as an amplification mechanism, enabling the indirect measurement of metabolites at very low molecular concentrations. Studies have reported amplifications of more than 800 fold the standard MRI sensitivity.[1]

The advantages of the off-resonance saturation sequences include: the increased sensitivity that allows the detection of molecules at concentrations much lower than what is achievable with conventional MRI, the possibility of imaging macromolecule content with very short T2 relaxation times[2] or the possibility of mapping important physiological parameters such as pH.[3]

Depending on the nature of the molecular interactions, the off-resonance saturation techniques tend to be grouped into two main categories, Magnetisation Transfer (MT) imaging and CEST. The MT imaging method is associated with the dipolar interactions between protons in free water molecules and bound-water molecules, usually within the hydration layer of large macro-molecules. Several mechanisms are involved in MT, including intra-molecular dipolar cross-relaxation, cross-relaxation by nuclear Overhauser effect (NOE) between backbone protons and the exchangeable protons in the macromolecule side chain, and finally fast chemical proton exchange with water.[4]

Clinical applications of MT are extensive. Some examples include, contrast enhancement between myo-cardium and venous blood in MR angiography,[5] biomarker of demyelination in disorders of the central nervous system such as multiple sclerosis, Parkinson's and Huntington's disease,[6,7,8,9] or investigation of white matter lesions after traumatic brain injury.[10]

CEST, on the other hand, refers to the process by which magnetic information between spins is transferred via a chemical interaction, where hydrogen atoms in specific molecules physically swap position with protons in free water. The relatively fast exchange rate between the spins (CEST operates in the intermediate exchange rate, see section 1.3) makes the labile proton resonant frequency distribution considerably narrower (~100Hz) than that observed in MT (~100KHz) due to an *exchange narrowing* effect. Moreover, unlike MT which is predominantly observed in semi-solid macromolecular structures, CEST also occurs in small sized molecules such as dissolved sugars and amino-acids. The high mobility (low correlation time) of these molecules, confers them a relatively long T2 relaxation time, which again produces

a narrow absorption-bandwidth, in this case due to *motional narrowing*.

As in MT, the net effect in CEST is an observable reduction of longitudinal magnetisation which is caused by the progressive transfer of energy from irradiated protons to water protons. However, compared to MT, CEST provides sharper spectral bandwidths, allowing a selective saturation of the different molecules, as well as the possibility of labelling small molecules, usually undetectable by other MR imaging techniques.

The following sections present a description of the main features observed in CEST and the parameters that govern its behaviour, as well as a review of the different uses and applications.

1.2. The Z-Spectrum

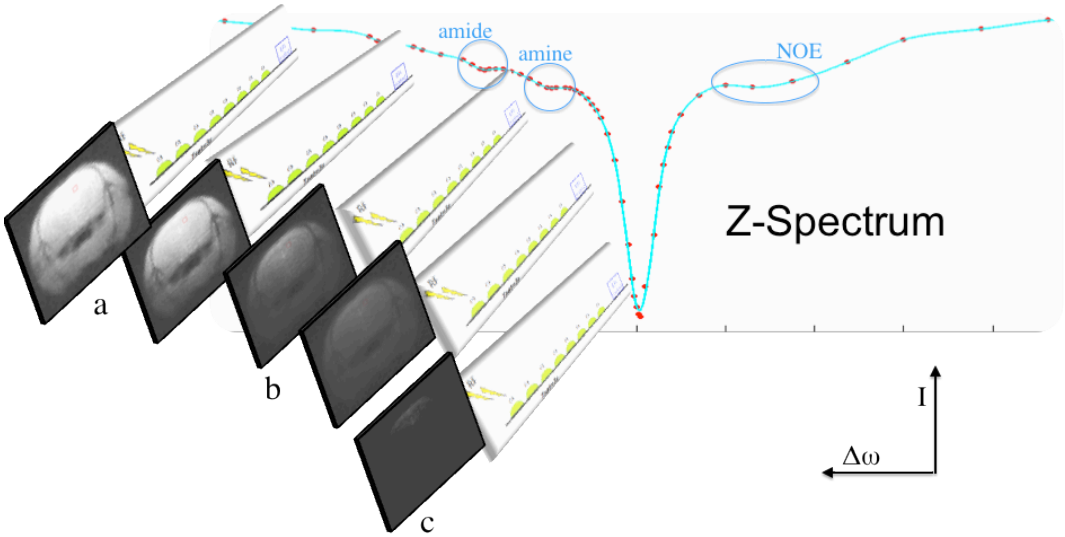

Figure 1.2.1.: *Z-spectrum of the mouse brain. Depending on the off-resonance saturation frequency images will display: a) no attenuation in case of no exchange. b) attenuation due to exchange from interacting protons. c) attenuation due to direct saturation close to water.*

The first phase of a CEST experiment involves the saturation of solute protons that will subsequently exchange magnetisation with water. To do so, most CEST experiments begin with the application of a long (on the order of seconds) off-resonance RF pulse (or train of pulses), followed by a standard readout, ideally with a proton density weighted acquisition. This procedure is repeated for a number of different frequency offsets, usually covering a range of frequencies centred at the water resonant frequency, which results in the acquisition of as many images as offset points.

Provided there is chemical exchange (or other type of magnetic transfer), the images obtained will display a certain degree of signal attenuation when the RF pulse is applied at the resonant frequency of the exchangeable molecules. The profile obtained by plotting the signal intensity as a function of the off-resonance frequency is called the Z-spectrum, and is the basic measure for the vast majority of CEST experiments. See illustration of the Z-Spectrum in figure 1.2.1.

1.3. Features of the Z-spectrum *in vivo*

As mentioned earlier, CEST is sensitive only in a narrow range chemical exchange rate. Let us imagine two spin populations at different magnetic environments resonating at their own specific frequency, separated by their chemical shift $\Delta\omega$. In the slow exchange limit, when the exchange rate is very small compared to the chemical shift ($k << \Delta\omega$), no exchange of hydrogen atoms take place (within the NMR time) which results in two defined NMR peaks and no CEST effect. On the other extreme, in the fast exchange limit ($k >> \Delta\omega$), rapid proton swaps between the two magnetic environments leads to a single averaged resonance frequency with only one distinct NMR peak, from which no metabolites can be separated. The optimum exchange rate for CEST lies between these two limits, in the so called 'intermediate' exchange regime ($k \sim \Delta\omega$), where chemical interaction between the two set of spins can affect each other, while still being able to distinguish them.

1.3.1. Chemical exchange mediated peaks

Among the organic chemical structures found in biology, hydrogen atoms within -OH and -NH chemical bonds tend to have the correct *intermediate* exchange rate able to produce CEST contrast.

Hydroxyl groups Present in all water molecules, hydroxyl (-OH) groups are the key component in the CEST process, allowing other labile protons to interact with hydrogen in water, which is ultimately how the CEST effect can be detected. Hydroxyls in molecules other than water also allow the CEST labelling of polysaccharides and sugars, like glycogen and glucose. These hydrogen nuclei resonate around 1 to 3 ppm from water and while they are usually not readily visible in a Z-spectrum *in vivo* (due to their low intensity and proximity to water), they are critically important in this work as they make the glucoCEST technique possible.

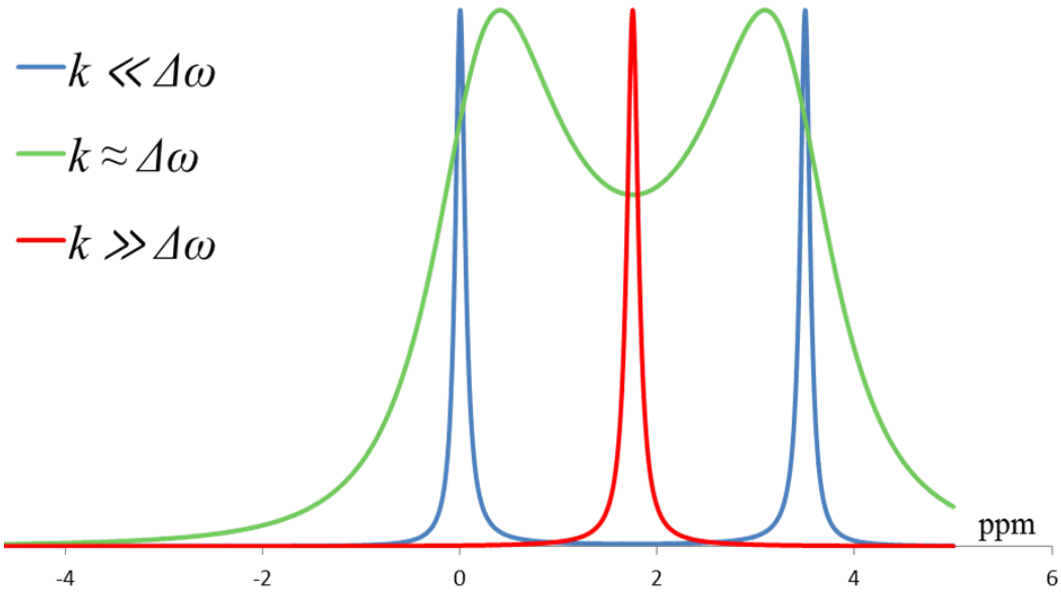

Figure 1.3.1.: *Simulations of two identical exchanging pools with 3.5 ppm chemical shift. Blue) A very slow exchange rate produces sharp NMR peaks but no CEST. Red) A very fast exchange rate leads to a single resonant frequency where the pools cannot be distinguished. Green) With an intermediate exchange rate, magnetisation is transferred from one pool to the other, producing the CEST effect.*

Amide, amine and imino groups Exchange sites containing -NH bonds include the imino, amine and amide groups. These are predominantly found in proteins structures and amino-acids, and have their resonant frequency between 2 and 3.5 ppm donwfield (higher frequency) from water. Among these groups, amides in the backbone of protein chains (forming the peptide bonds), have been particularly important in the CEST literature, as they are considered to be the source for the Amide Proton Transfer (APT) contrast, manifested as a peak in the Z-spectrum at $\sim$3.5 ppm offset. APT has been reported in a number of publications as a non-invasive method to image tissue pH, based on the fact that the chemical exchange rate of these amide protons is highly sensitive to *in vivo* pH variations.[11,12,13] On the other hand, side chain amides, as well as amine and imino groups tend to resonate around 2 ppm from water, with a more rapid exchange rate. Many important molecules in biology contain such chemical groups including amino-acids, several neuro-transmitters such as adrenaline, dopamine, acytylcholine and nucleosides in ADN (and RNA) like adenine, citosine or guanosine.

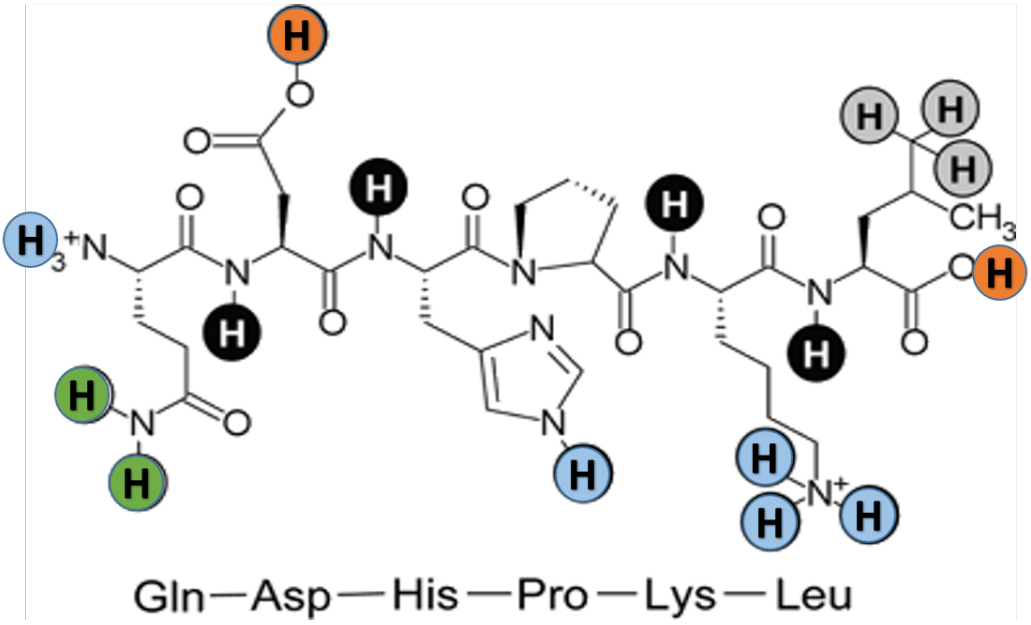

Figure 1.3.2.: *Types of hydrogens in proteins. The six-residue peptide Gln-Asp-His-Pro-Lys-Leu illustrates backbone amide hydrogens (in black), fast exchanging hydroxyl, amine and side-chain amide hydrogens (in orange, blue and green respectively) and nonexchangeable hydrogens bonded to carbon (in grey).*[14]

1.3.2. Non-pure CEST manifestations in the Z-spectrum

In addition to the already discussed CEST sensitive groups, protons in certain conditions can also modulate the Z-spectrum. These include protons associated with magnetisation transfer (MT) and Nuclear Overhauser Effects (NOE).

1.3.2.1. Magnetisation Transfer

As previously mentioned MT originates in large macromolecules and its effect is present in a wide spectral range ($\sim$100KHz) centred around water. While it is not driven by a chemical exchange (magnetisation transfer is mediated by dipolar coupling), it does however affect the interpretation of the CEST data, as it also reduces the available longitudinal magnetisation.

1.3.2.2. Nuclear Overhauser Effect

Closely related to MT, the NOE effect is thought to originate from protons in the aliphatic region, 3 to 5 ppm upfield (lower frequency) from water. Even though the underlying mechanisms are not fully understood, the effect is considered to be initially mediated by the cross relaxation via dipole-dipole interaction of the backbone

protons in medium sized molecules (small proteins). Once irradiated at their own resonant frequency, these backbone -CH and -COCH3 (Acetyl) hydrogen atoms can transfer magnetisation to exchangeable protons (-NH, -NH2, -OH) within the same molecule, which can then interact with water though chemical exchange. These effects, referred to as *exchange-relayed NOEs*, are believed to be a possible contributor to CEST signal centred around -3.5ppm.[15,16]

While intermolecular NOEs (between molecules) also exist, they are more significant between large macro-molecules and the hydration layer around them. With restricted molecular motion and short inter-atomic distances, protons are stronger coupled, leading to more efficient cross relaxation. As size of the molecules increase and structures become 'semisolid' the inter-molecular NOEs become important and contribute to generate the broad MT effect.

The practical difference of NOE with respect to MT, is that unlike MT, NOE manifests with narrow absorption line-width ($\sim$ 3 ppm) at the aliphatic region. Unfortunately, the fact that the offset frequency in NOE is opposite to the one in CEST, makes the analysis of the Z-spectrum and quantification of the exchangeable pool sizes more complicated. As such, until recently the majority of the CEST studies have regarded the NOE peak as 'contamination' of the CEST signal, and little attention has been paid to its significance. In recent publications however, researches acknowledge that the NOE effect might offer an additional source of contrast, possibly as valuable as CEST.[17,18,19]

The combined effect of these processes shapes the Z-spectrum. Finding ways to untangle the contribution of each spin population is a subject of intense research in the CEST community. Most of the proposed methods use symmetry arguments aimed at untangling DS and MT effects as their profile is effectively symmetrical around the water frequency. For non-symmetrical contributions to to the Z-spectrum, like the aliphatic NOEs, others methods exploit the characteristic times and power dependencies in each of the exchange process in order to quantify their effect. Some examples of these proposed methods are described in section 1.6.1.

1.4. Factors influencing the Z-spectrum

Besides the actual protons involved in the CEST mechanism, other external parameters exert a strong influence on the Z-spectrum. Some of these parameters can be adjusted and therefore optimised, while others need to be understood to evaluate their impact.

1.4.1. RF saturation power B1

A poorly saturated exchangeable proton pool will, in principle, produce a smaller CEST contrast. However, strong RF pulses produce undesired saturation of the water signal due to the off-resonance spill-over effect (DS). This results in the broadening of the water shape-line, which results in the reduction of the available MR signal, especially close to water. Therefore the sensitivity of the CEST technique to detect protons resonating close to the water frequency is hindered by the applied B1 irradiation power. Optimisation of the RF power for each application is critical in order to avoid excessive masking of the exchange processes occurring close to the water resonance frequency.

In another context, intense and prolonged saturation RF pulses can easily lead to SAR depositions above the regulated safe levels, which may constrain the detection sensitivity for fast exchangeable protons in the clinical setup. Additionally, the solid-state RF amplifiers in clinical MRI systems tend to have a low duty cycle limit, reducing even further the saturation efficiency in fast exchanging protons.

1.4.2. Field strength B0

The chemical shift between two hydrogen moieties is linearly proportional to the strength of the magnetic field B0. On the other hand, DS effect is dependent on the intensity of the applied saturation RF pulse B1, but not on the strength of B0. This implies that at high field the observed CEST peaks can be better resolved due to the larger separation and the lower attenuation from DS. Additionally, the strength of B0 field will alter the relation between the chemical shift and the protons exchange rate, leading to a better or worse regime for CEST ($k \sim \Delta\omega$). In this sense, CEST imaging of fast exchanging protons is more efficient at high fields.

1.4.3. Solute concentration

In order to observe the CEST effect, the concentration of the exchangeable protons needs to be sufficiently high. At the current stage of technology and for the naturally occurring endogenous CEST protons, the sensitivity threshold is in the milli-molar range for *in vivo* applications.

1.4.4. Relaxation times

Both longitudinal and transverse relaxation times are crucial parameters. In particular the water T1 relaxation time controls the extent of signal reduction from a

given CEST process, with longer T1 resulting in larger CEST signals. Direct saturation is strongly modulated by the transverse relaxation T2, which results in blurring of the CEST peaks around water at short T2. On the exchangeable molecule side, longer T2 values are associated with narrow absorption bandwidth which can produce sharper and deeper CEST peaks if the chemical exchange rate is in the slow to intermediate regime ($k \lesssim \Delta\omega$).

1.4.5. Exchange rate

As explained in the previous section CEST works best in the *intermediate* exchange regime. Deviations from the optimum chemical exchange reduces the effect of CEST.

	k_{sw}-range (s^{-1})	Functional group	Molecular unit
Proton exchange	10–30	NH (APT)	Multiple unknown amino acids
	20–1200	NH	L-Lysine
	500–10,000	NH_2	L-Arginine
	500–10,000	OH	Glucose
	2000–8000	Imino proton	Polyuridylic acid
Molecular exchange	2000–10,000	Bound water	Eu-DOTA-4AmCE
Compartmental exchange	10–250	Liposomal water	H_2O in 100 nm liposome

Figure 1.4.1.: *Exchange rate of the main CEST sensitive functional groups. Data obtained from van Zijl et al*[20]

For hydroxyl groups in sugars for instance, the exchange rate typically falls between 1000 to 10000 Hertz, and their chemical shift (from water) is around 1 to 3 ppm, which in a 9.4 Tesla scanner corresponds to 400 to 1200 Hertz. This suggests that the hydroxyl groups are generally in a regime faster than optimal for CEST and as such a decrease of the exchange rate would likely yield to the enhancement of the CEST contrast.

Proton exchange rate k is greatly influenced by the molecular structure in which they are located. Protons in complex structures like proteins generally have slow exchange rates due to the protection factor of the highly folded structures.[21,22] As such, the exchange rate of hydrogen atoms in the backbone of the molecules are

greatly reduced due to the restricted accessibility to the solvent compared to protons on the surface.

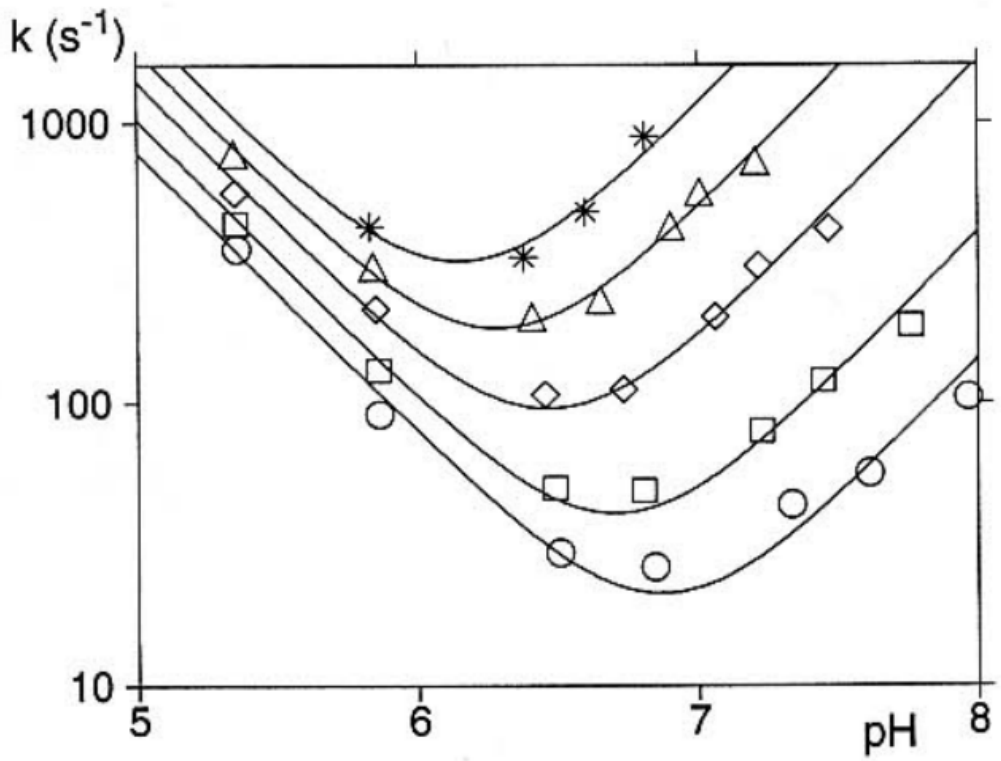

Figure 1.4.2.: *Exchange rate of side chain hydroxyl protons of acetyl-threonine-OCH3 versus pH in aqueous solution. The different curves represent measurements at 36°, 30°, 20°, 10°and 4°(from top to bottom respectively). Figure reproduced from Liepinsh et al.*[23]

Additionally, several environmental factors can alter the effective chemical exchange rate between protons, i.e temperature,[24,25,23] pH,[26,27,13] concentration of exchange catalysers such as phosphates, or viscosity of the solvent.[28] Hydrogen exchange rate depends upon the pH and other exchange catalyst by the general relationship:

$$K = k_a \times 10^{-pH} + k_b \times 10^{pH-pK_w} + k_0$$

where k_a and k_b are the acid- and base-catalysed rate constants respectively and k_0 represents the combined contributions from the possible exchange catalysts. pK_w is the water auto-dissociation constant, which is approximately 14 at 25° C. The relationships between exchange rate and pH of amide and amine groups found *in vivo* have been reported in the literature[12,27] as:

$$K_{amides} = 5.57 \times 10^{pH-6.4}$$

$$K_{amines} = 10^{pH-4.5}$$

The temperature dependency is implicit in the three catalyst constants k_a, k_b and k_0 which are governed by the by the Arrhenious equation displayed below:

$$k_x = Ae^{-E_a/RT}$$

where R is the universal gas constant ($8.314 \times 10 - 3kJ/mol/K$), Ea is the activation energy (in kJ/mol) and A is a reaction dependent constant which includes factors like the frequency of the molecular collisions and their orientation.

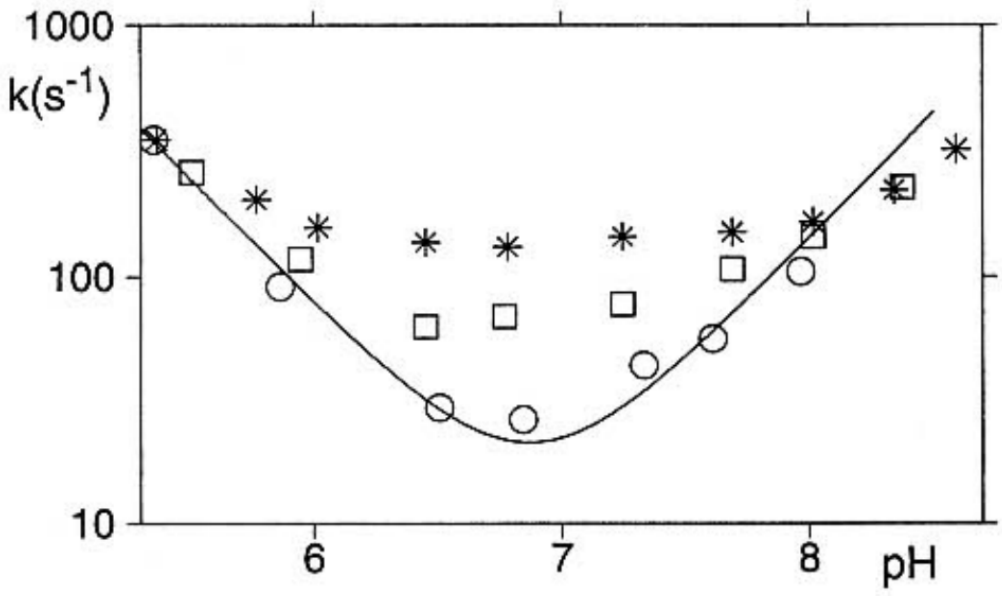

Figure 1.4.3.: *Exchange rates of the side chain hydroxyl proton of acetylotheonine-OCH3 at 4°C in the presence of sodium phosphate at a total concentration of 0, 5 and 10 mmolar (circles, square and squares respectively). Phosphate is one of the most effective exchange catalyst at neutral pH. Figure reproduced from Liepnsh et al.*[23]

The pH dependency of the chemical exchange rate of amide protons has allowed APT technique to become an effective non-invasive method to probe pH *in vivo*, where a unit of pH drop typically reduces the exchange rate by 90%, making APT contrast very sensitive to tissue local pH.[29,30]

1.4.6. Saturation length

The saturation time is another parameter usually cited in CEST literature and it refers to the duration of the saturation RF pulse. The most common approach in CEST is to use long saturation times allowing multiple exchange cycles to occur and ensure the spin system reaches a state of dynamic equilibrium between the magnetisation of the exchanging pools. This state is referred to as 'steady state saturation' and ensures maximal transfer of magnetisation. However, CEST is not a linear process and the largest reduction in the water signals occurs at the beginning of the saturation pulse. For this reason, a well design sequence with short saturation times (without reaching steady state) can produce better contrast efficiency. This approach is very convenient for the clinical setup as it can reduce acquisition time and SAR deposition. However, it also complicates the analysis and quantification of the CEST results as the complex dynamics of the exchange process are more difficult to interpret.

1.5. CEST data analysis

As a relatively new technique CEST lacks rigid standardised measures to quantity the magnitude of the chemical exchange process. While post-processing methods and new metrics are in constant development, currently the most common metric to analyse CEST data is probably the *magnetisation transfer ratio asymmetry* or MTR_{asym} which is defined by the equation:

$$MTR_{asym} = [M(-\Delta\omega) - M(+\Delta\omega]/\mathrm{M}_{ref}$$

where M_{ref} is the signal of water at the reference offset ($M_{ref} = M_0$ when an image with no saturation is used as reference) and $M(\Delta\omega)$ the water signal when the saturation RF pulse is applied at $\Delta\omega$ offset from the water resonant frequency.

The contrast in the CEST image is then obtained by evaluating the MTR_{asym} curve at a particular offset (or by integrating it for a range of frequencies). For instance, APT contrast is generated by evaluating the MTR_{asym} at 3.5 ppm on a pixel by pixel basis. Amine weighted contrast on the other hand would be produced as the integration of the MTR_{asym} around 2 ppm frequency offset from water.
The raw CEST data would generally require some pre-processing steps, which typically would involve sorting of the frequency offsets, correction of field inhomogeneities and normalisation of signal intensity.

1.5.1. Data sorting and interpolation

The acquired images are sorted according to the frequency offsets used in the saturation phase to form a Z-spectrum per pixel in the image. At this stage, the data would be usually interpolated (and sometimes smoothed) in order to generate a denser frequency resolution.

1.5.2. Field inhomogeneity corrections

Field inhomogeneities across the image slice produce variations of the water Larmor frequency. In order to achieve reliable MTR_{asym} curves, the water frequency has to be accurately determined and corrected for every pixel in the image. To do so, conventional field maps obtained by double echo phase images[31] can be acquired or alternatively the *water saturation shift referencing* (WASSR) method proposed by Kim et al[32] can also be used. This method uses pre-saturation pulses but applied at very weak power (B1=$\sim$ 0.1 μT) and short length in order to saturate only water. Thus the saturated water peak is used as the reference frequency for CEST which is an absolute measure of the frequency shift, as opposed to phase maps, which provide relative field shift from central frequency of water. However, both these methods required the acquisition of additional images, which lengthens the CEST protocol. These methods can be avoided by using the Z-Spectrum itself to correct for B0 inhomogeneity. This approach is particularly efficient at high fields provided that the Z-spectrum has enough frequency sampling and that the saturation power is low enough (usually B1 < 2 μ T) to give a sharp water peak.[25,33] Additionally, correction for B1 RF inhomogeneity is also possible but is not a common practice as it requires CEST data at different saturation powers which considerably extends the acquisition length.

1.5.3. Normalisation

The CEST data is then normalised to a reference value in order to define the CEST metric and be able compare different data. However, the frequency offset for normalisation is not fully standardised in the CEST field yet. The most commonly used approach comes from the MT imaging modality in which an image with no applied saturation is taken as the normalisation reference. In many studies this metric is used to analyse APT data, however, as will be discussed in Chapter 3, normalisation at other frequency offsets (closer to the water resonant frequency) can be more convenient in order to reduce effects derived from physiological noise.

1.6. Current uses and developments in CEST

Since its presentation by Wolff and Balaban[34] in 1990, CEST-MRI has gradually increased in popularity, particularly for *in vivo* applications. This interest relies on the fact that CEST can offer unique image contrast based on a signal that: a) is sensitive to a number of physiological parameters, b) is sensitive to low concentration of solutes and c) can be tuned to target specific sets of molecules. Due to its inherent flexibility, CEST based methods are currently being explored in a wide range of applications as an alternative source of useful information. Although the technique is still not standardized for the use in the clinic, clinical trials are being conducted in different areas of medicine. The following section will describe some of the reported work on CEST with potential application for the clinical practice.

Probably one of the most known applications of CEST is the work on pH evaluation. Using amide proton transfer (APT), a CEST imaging technique where the exchangeable sites are amide groups, researchers have reported imaging pH changes in ischemia animal models.[35,12] Using the same method, human studies on stroke patients have shown hypo-intense APT signal in areas affected by the insult.[36]

In the field of cancer research, APT-CEST has been reported to be able to distinguish between active malignant tumours and ischemic regions in the rat brain.[3] Moreover, in another study presented by Zhou and co-workers it was demonstrated that APT can discriminate between active glioma and necrotic tissue due to radiotherapy. While structural imaging is widely used in the diagnosis of brain tumours, it is considered to be inadequate for reliably distinguishing between treatment necrosis and tumour recurrence, because both lesion types display similar contrast. The gold standard for differentiating between tumour recurrence and treatment necrosis is currently biopsy, which is expensive and involves risks associated with surgery.[37] In this context APT-CEST stands out as a promising method for the evaluation of radiotherapy treatment response in oncology.[38]

Looking into CEST studies in which contrast is based on the hydroxyl protons, a CEST modality named gagCEST focuses on the saturation of the glycosaminoglycan chains in the knee to assess the condition of articular cartilage and has shown promise as an early marker of osteoarthritis.[39,40,41] The glycoCEST method, presented by van Zijl et al. in 2007,[42] is another variation of CEST in which hydroxyl groups in glycogen are saturated to create contrast. Researchers showed a reduction in glycoCEST signal following perfusion of glucagon in the liver, which corresponds with the expected breakdown of glycogen. This type of study could help in the screening of conditions like type 2 diabetes, insulin resistance or obesity.

The last example of the use -OH groups is glucoCEST, which was recently presented by Walker-Samuel[43] from our group. This method reports on the increased glucose uptake in cancer tissue, making it a potential alternative to ^{18}F-FDG-PET with the advantage of being less costly and free from exposure to radioactive tracers. This thesis is centred on the investigation of the glucoCEST technique in the context of cancer, and specifically on its application in brain tumours, as a potential bio-marker of tumour growth. In the following chapters the concept and the interpretation of glucoCEST contrast will be thoroughly discussed.

In a different context, the modality called paraCEST makes use of exogenous paramagnetic agents (based on lanthanide ions) to obtain functional and molecular images. Specifically designed, these agents can be used to probe temperature,[44] pH,[45] specific proteins[46] or enzymatic reactions.[47] Because chemical shifts associated with paramagnetic agents are large (~50 ppm) compared to those observed in diaCEST protons (~1-5 ppm) *in vivo*, undesired 'signal contamination' by endogenous protons stops being an issue. This is a major asset of the modality as it allows a more straight forward interpretation of the information present in paraCEST images.[48,49]

1.6.1. Developments in CEST pulse sequences

As a young MRI technique, the CEST field is very rapidly evolving. In this stage of fast progress new pulse sequences are continuously being developed to overcome the obstacles in specific research fields. Particularly, efforts are being made to come up with CEST protocols that can untangle the different effects observed in the Z-spectrum. In this sense, methods like LOVARS (Length and offset varied saturation) by Xiaolei et al.,[50] SAFARI (Saturation with Frequency Alternating RF Irradiation) by Scheidegger et al.,[51] or ZAPI (Z-spectroscopy using Alternating-Phase Irradiation) by Närväinen et al.[52] make use of multiple irradiation pulses and symmetry considerations to separate contributions of MT and direct saturation (DS) from CEST. While these methods provide a solution in certain applications, symmetry considerations fail in the presence of aliphatic NOEs, which manifest at around 3.5 ppm from water. In the brain, where NOEs are particularly strong, alternative methods are prone to provide more reliable results. For that matter, Zu et al.[53,54] have developed a technique named CERT (Chemical Exchange Rotation Transfer), that can distinguish CEST (APT) effects based on a dual measurement with different saturation schemes, which does not involve any asymmetry consideration. However, the method requires twice the amount of data per offset frequency, which

can lead to long protocols. A different approach that is gaining attention is FLEX (Frequency Labeled Exchange). Developed by Yadav et al.,[55] this method separates signal contributors by studying the frequency domain of the exchange process. Strictly speaking FLEX is not a CEST type of sequence, as it works by frequency labelling the spins instead of saturating them, however it is included in the CEST category, as it informs on the same exchange processes. Interestingly, FLEX has been shown to be quite effective in the fast exchange regime, a region in which most sequences start losing sensitivity.

New acquisition schemes and metrics can certainly be useful for different CEST applications. Most of the analysis in this thesis, however, is based on the standard 'saturation plus readout' sequence and the commonly used *MTR asymmetry* metric. This approach, although it might not be able to properly separate different contribution in the Z-spectrum, is simple, efficient and can be relatively quick, depending on the saturation length used. In the next chapter the specifics of the glucoCEST method will be discussed.

Chapter references

[1] K.M Ward, A.H Aletras, and R.S Balaban. “A New Class of Contrast Agents for MRI Based on Proton Chemical Exchange Dependent Saturation Transfer (CEST)”. In: *Journal of Magnetic Resonance* 143.1 (Mar. 2000). 00572, pp. 79–87. ISSN: 10907807. DOI: 10.1006/jmre.1999.1956 (cit. on p. 26).

[2] R. M. Henkelman, G. J. Stanisz, and S. J. Graham. “Magnetization transfer in MRI: a review”. In: *NMR in Biomedicine* 14.2 (Apr. 2001). 00457, pp. 57–64. ISSN: 0952-3480, 1099-1492. DOI: 10.1002/nbm.683 (cit. on p. 26).

[3] Jinyuan Zhou, Bachchu Lal, David A. Wilson, John Laterra, and Peter C.M. van Zijl. “Amide proton transfer (APT) contrast for imaging of brain tumors”. In: *Magnetic Resonance in Medicine* 50.6 (Dec. 2003). 00205, pp. 1120–1126. ISSN: 0740-3194, 1522-2594. DOI: 10.1002/mrm.10651 (cit. on pp. 26, 38).

[4] Peter C.M. van Zijl, Jinyuan Zhou, Noriko Mori, Jean-Francois Payen, David Wilson, and Susumu Mori. “Mechanism of magnetization transfer during on-resonance water saturation. A new approach to detect mobile proteins, peptides, and lipids”. In: *Magnetic Resonance in Medicine* 49.3 (Mar. 2003), pp. 440–449. ISSN: 0740-3194, 1522-2594. DOI: 10.1002/mrm.10398 (cit. on p. 26).

[5] Christian T. Stoeck, Peng Hu, Dana C. Peters, Kraig V. Kissinger, Beth Goddu, Lois Goepfert, Long Ngo, Warren J. Manning, Sebastian Kozerke, and Reza Nezafat. “Optimization of On-Resonant Magnetization Transfer Contrast in Coronary Vein MRI”. In: *Magnetic resonance in medicine : official journal of the Society of Magnetic Resonance in Medicine / Society of Magnetic Resonance in Medicine* 64.6 (Dec. 2010). 00002, pp. 1849–1854. ISSN: 0740-3194. DOI: 10.1002/mrm.22581. pmid: 20938974 (cit. on p. 26).

[6] Stéphane Lehéricy, Michael A. Sharman, Clarisse Longo Dos Santos, Raphaël Paquin, and Cecile Gallea. “Magnetic resonance imaging of the substantia nigra in Parkinson’s disease”. In: *Movement Disorders* 27.7 (June 1, 2012). 00037, pp. 822–830. ISSN: 1531-8257. DOI: 10.1002/mds.25015 (cit. on p. 26).

[7] Simon van den Bogaard, Eve Dumas, Jeroen van der Grond, Mark van Buchem, and Raymund Roos. “MRI biomarkers in Huntington’s disease”. In: *Frontiers in Bioscience (Elite Edition)* 4 (2012). 00012, pp. 1910–1925. ISSN: 1945-0508. pmid: 22202007 (cit. on p. 26).

[8] Nicola Tambasco, Pasquale Nigro, Michele Romoli, Simone Simoni, Lucilla Parnetti, and Paolo Calabresi. “Magnetization transfer MRI in dementia disorders, Huntington’s disease and parkinsonism”. In: *Journal of the Neurological Sciences* 353.1-2 (June 2015). 00000, pp. 1–8. ISSN: 0022510X. DOI: 10.1016/j.jns.2015.03.025 (cit. on p. 26).

[9] Basil H. Ridha, Daniel J. Tozer, Mark R. Symms, Katherine C. Stockton, Emma B. Lewis, Musib M. Siddique, David G. MacManus, Martin N. Rossor, Nick C. Fox, and Paul S. Tofts. "Quantitative Magnetization Transfer Imaging in Alzheimer Disease". In: *Radiology* 244.3 (Sept. 1, 2007). 00035, pp. 832–837. ISSN: 0033-8419. DOI: 10.1148/radiol.2443061128 (cit. on p. 26).

[10] J. C. McGowan, J. H. Yang, R. C. Plotkin, R. I. Grossman, E. M. Umile, K. M. Cecil, and L. J. Bagley. "Magnetization transfer imaging in the detection of injury associated with mild head trauma". In: *AJNR. American journal of neuroradiology* 21.5 (May 2000). 00079, pp. 875–880. ISSN: 0195-6108. pmid: 10815663 (cit. on p. 26).

[11] K. M. Ward and R. S. Balaban. "Determination of pH using water protons and chemical exchange dependent saturation transfer (CEST)". In: *Magnetic Resonance in Medicine* 44.5 (Nov. 2000), pp. 799–802. ISSN: 0740-3194. pmid: 11064415 (cit. on p. 29).

[12] Jinyuan Zhou, Jean-Francois Payen, David A. Wilson, Richard J. Traystman, and Peter C. M. van Zijl. "Using the amide proton signals of intracellular proteins and peptides to detect pH effects in MRI". In: *Nature Medicine* 9.8 (Aug. 2003). 00378, pp. 1085–1090. ISSN: 1078-8956. DOI: 10.1038/nm907. pmid: 12872167 (cit. on pp. 29, 34, 38).

[13] Marilena Rega. "Validation of APT as a measure of pH by 31P in a piglet model of HIE". In: *CEST Contrast: Methods & Applications*. ISMRM. 00000. Milan, 2014 (cit. on pp. 29, 34).

[14] Christopher R. Morgan and John R. Engen. "Investigating solution-phase protein structure and dynamics by hydrogen exchange mass spectrometry". In: *Current Protocols in Protein Science / Editorial Board, John E. Coligan ... [et Al.]* Chapter 17 (Nov. 2009). 00000, Unit 17.6.1–17. ISSN: 1934-3663. DOI: 10.1002/0471140864.ps1706s58. pmid: 19937720 (cit. on p. 30).

[15] Bertil Halle. "Cross-relaxation between macromolecular and solvent spins: The role of long-range dipole couplings". In: *The Journal of Chemical Physics* 119.23 (2003). 00073, p. 12372. ISSN: 00219606. DOI: 10.1063/1.1625632 (cit. on p. 31).

[16] Jiadi Xu, Nirbhay N. Yadav, Amnon Bar-Shir, Craig K. Jones, Kannie W. Y. Chan, Jiangyang Zhang, P. Walczak, Michael T. McMahon, and Peter C. M. van Zijl. "Variable delay multi-pulse train for fast chemical exchange saturation transfer and relayed-nuclear overhauser enhancement MRI: Variable Delay Multi-Pulse CEST". In: *Magnetic Resonance in Medicine* 71.5 (May 2014). 00000, pp. 1798–1812. ISSN: 07403194. DOI: 10.1002/mrm.24850 (cit. on p. 31).

[17] Jinyuan Zhou, Xiaohua Hong, Xuna Zhao, Jia-Hong Gao, and Jing Yuan. "APT-weighted and NOE-weighted image contrasts in glioma with different RF saturation powers based on magnetization transfer ratio asymmetry analyses: APT and NOE Imaging in Glioma". In: *Magnetic Resonance in Medicine* 70.2 (Aug. 2013), pp. 320–327. ISSN: 07403194. DOI: 10.1002/mrm.24784 (cit. on p. 31).

[18] Craig K Jones, Alan Huang, Jiadi Xu, Richard A E Edden, Michael Schär, Jun Hua, Nikita Oskolkov, Domenico Zacà, Jinyuan Zhou, Michael T McMahon, Jay J Pillai, and Peter C M van Zijl. "Nuclear Overhauser enhancement (NOE) imaging in the human brain at 7T." In: *NeuroImage* 77 (Aug. 2013). 00033 Cited by 0001, pp. 114–124. DOI: 10.1016/j.neuroimage.2013.03.047 (cit. on p. 31).

[19] Jianhua Lu, Jinyuan Zhou, Congbo Cai, Shuhui Cai, and Zhong Chen. “Observation of true and pseudo NOE signals using CEST-MRI and CEST-MRS sequences with and without lipid suppression”. In: *Magnetic Resonance in Medicine* 73.4 (Apr. 1, 2015). 00006, pp. 1615–1622. ISSN: 1522-2594. DOI: 10.1002/mrm.25277 (cit. on p. 31).

[20] Peter C M van Zijl and Nirbhay N Yadav. “Chemical exchange saturation transfer (CEST): what is in a name and what isn’t?” In: *Magnetic resonance in medicine* 65.4 (Apr. 2011). Cited by 0073, pp. 927–948. DOI: 10.1002/mrm.22761 (cit. on p. 33).

[21] Vincent J. Hilser and Ernesto Freire. “Structure-based Calculation of the Equilibrium Folding Pathway of Proteins. Correlation with Hydrogen Exchange Protection Factors”. In: *Journal of Molecular Biology* 262.5 (Oct. 11, 1996). 00231, pp. 756–772. ISSN: 0022-2836. DOI: 10.1006/jmbi.1996.0550 (cit. on p. 33).

[22] Walid A. Houry, J. Michael Sauder, Heinrich Roder, and Harold A. Scheraga. “Definition of amide protection factors for early kinetic intermediates in protein folding”. In: *Proceedings of the National Academy of Sciences of the United States of America* 95.8 (Apr. 14, 1998). 00023, pp. 4299–4302. ISSN: 0027-8424. pmid: 9539731 (cit. on p. 33).

[23] E. Liepinsh and G. Otting. “Proton exchange rates from amino acid side chains–implications for image contrast”. In: *Magnetic Resonance in Medicine: Official Journal of the Society of Magnetic Resonance in Medicine / Society of Magnetic Resonance in Medicine* 35.1 (Jan. 1996). 00182, pp. 30–42. ISSN: 0740-3194. pmid: 8771020 (cit. on pp. 34, 35).

[24] C. K. Woodward and B. D. Hilton. “Hydrogen isotope exchange kinetics of single protons in bovine pancreatic trypsin inhibitor”. In: *Biophysical Journal* 32.1 (Oct. 1980). 00115, pp. 561–575. ISSN: 0006-3495. DOI: 10.1016/S0006-3495(80)84990-3 (cit. on p. 34).

[25] Francisco Torrealdea, Marilena Rega, Mark F. Lythgoe, David L Thomas, Simon Walker-Samuel, and Xavier Golay. “CEST effects in hexoses and pentoses of the glycolytic pathway.” In: *ISMRM Annual Meeting Proceedings*. International Society for Magnetic Resonance in Medicine. 00000. Melbourne, 2012 (cit. on pp. 34, 37).

[26] Nevin McVicar, Alex X Li, Daniela F Gonçalves, Miranda Bellyou, Susan O Meakin, Marco AM Prado, and Robert Bartha. “Quantitative tissue pH measurement during cerebral ischemia using amine and amide concentration-independent detection AACID with MRI”. In: *Journal of Cerebral Blood Flow & Metabolism* 34.4 (Apr. 2014). 00008, pp. 690–698. ISSN: 0271-678X, 1559-7016. DOI: 10.1038/jcbfm.2014.12 (cit. on p. 34).

[27] Kimberly L. Desmond, Firas Moosvi, and Greg J. Stanisz. “Mapping of amide, amine, and aliphatic peaks in the CEST spectra of murine xenografts at 7 T: CEST Mapping in Murine Cancer Xenografts at 7T”. In: *Magnetic Resonance in Medicine* 71.5 (May 2014). 00000, pp. 1841–1853. ISSN: 07403194. DOI: 10.1002/mrm.24822 (cit. on p. 34).

[28] Fernando Hallwass, M. Engelsberg, A. M. Simas, and Wilson Barros. “Diffusion, reaction kinetics and exchange of sodium in aqueous solutions containing a crown ether”. In: *Chemical Physics Letters* 335.1–2 (Feb. 16, 2001). 00014, pp. 43–49. ISSN: 0009-2614. DOI: 10.1016/S0009-2614(01)00012-4 (cit. on p. 34).

[29] Phillip Zhe Sun, Enfeng Wang, and Jerry S. Cheung. "Imaging acute ischemic tissue acidosis with pH-sensitive endogenous amide proton transfer (APT) MRI—Correction of tissue relaxation and concomitant RF irradiation effects toward mapping quantitative cerebral tissue pH". In: *NeuroImage* 60.1 (Mar. 2012). 00028, pp. 1–6. ISSN: 10538119. DOI: 10.1016/j.neuroimage.2011.11.091 (cit. on p. 35).

[30] W. Zhou, S. Schwarting, S. Illanes, A. Liesz, M. Middelhoff, M. Zorn, M. Bendszus, S. Heiland, J. van Ryn, and R. Veltkamp. "Hemostatic Therapy in Experimental Intracerebral Hemorrhage Associated With the Direct Thrombin Inhibitor Dabigatran". In: *Stroke* 42.12 (Dec. 1, 2011), pp. 3594–3599. ISSN: 0039-2499, 1524-4628. DOI: 10.1161/STROKEAHA.111.624650 (cit. on p. 35).

[31] Phillip Zhe Sun, Christian T. Farrar, and A. Gregory Sorensen. "Correction for artifacts induced by B0 and B1 field inhomogeneities in pH-sensitive chemical exchange saturation transfer (CEST) imaging". In: *Magnetic Resonance in Medicine* 58.6 (Dec. 1, 2007). 00079, pp. 1207–1215. ISSN: 1522-2594. DOI: 10.1002/mrm.21398 (cit. on p. 37).

[32] Mina Kim, Joseph Gillen, Bennett A. Landman, Jinyuan Zhou, and Peter C. M. van Zijl. "Water saturation shift referencing (WASSR) for chemical exchange saturation transfer (CEST) experiments". In: *Magnetic Resonance in Medicine: Official Journal of the Society of Magnetic Resonance in Medicine / Society of Magnetic Resonance in Medicine* 61.6 (June 2009). 00138, pp. 1441–1450. ISSN: 1522-2594. DOI: 10.1002/mrm.21873. pmid: 19358232 (cit. on p. 37).

[33] Guanshu Liu, Xiaolei Song, Kannie W Y Chan, and Michael T McMahon. "Nuts and bolts of chemical exchange saturation transfer MRI". In: *NMR in biomedicine* (Jan. 10, 2013). Cited by 0003. ISSN: 1099-1492. DOI: 10.1002/nbm.2899 (cit. on p. 37).

[34] Steven D Wolff and Robert S Balaban. "NMR imaging of labile proton exchange". In: *Journal of Magnetic Resonance (1969)* 86.1 (Jan. 1, 1990). 00085, pp. 164–169. ISSN: 0022-2364. DOI: 10.1016/0022-2364(90)90220-4 (cit. on p. 38).

[35] Phillip Zhe Sun, Jinyuan Zhou, Weiyun Sun, Judy Huang, and Peter C M van Zijl. "Detection of the ischemic penumbra using pH-weighted MRI". In: *Journal of Cerebral Blood Flow* 27.6 (June 2007). 00131, pp. 1129–1136. ISSN: 0271-678X. DOI: 10.1038/sj.jcbfm.9600424 (cit. on p. 38).

[36] Xuna Zhao, Zhibo Wen, Fanheng Huang, Shilong Lu, Xianlong Wang, Shuguang Hu, Donglin Zu, and Jinyuan Zhou. "Saturation power dependence of amide proton transfer image contrasts in human brain tumors and strokes at 3 T". In: *Magnetic Resonance in Medicine* 66.4 (Oct. 2011). 00039, pp. 1033–1041. ISSN: 07403194. DOI: 10.1002/mrm.22891 (cit. on p. 38).

[37] N. Verma, M. C. Cowperthwaite, M. G. Burnett, and M. K. Markey. "Differentiating tumor recurrence from treatment necrosis: a review of neuro-oncologic imaging strategies". In: *Neuro-Oncology* 15.5 (May 1, 2013). 00019, pp. 515–534. ISSN: 1522-8517, 1523-5866. DOI: 10.1093/neuonc/nos307 (cit. on p. 38).

[38] Jinyuan Zhou, Erik Tryggestad, Zhibo Wen, Bachchu Lal, Tingting Zhou, Rachel Grossman, Silun Wang, Kun Yan, De-Xue Fu, Eric Ford, Betty Tyler, Jaishri Blakeley, John Laterra, and Peter C M van Zijl. "Differentiation between glioma and radiation necrosis using molecular magnetic resonance imaging of endogenous proteins and peptides". In: *Nature Medicine* 17.1 (Jan. 2011), pp. 130–134. ISSN: 1078-8956, 1546-170X. DOI: 10.1038/nm.2268 (cit. on p. 38).

[39] I. Krusche-Mandl, B. Schmitt, L. Zak, S. Apprich, S. Aldrian, V. Juras, K. M. Friedrich, S. Marlovits, M. Weber, and S. Trattnig. "Long-term results 8 years after autologous osteochondral transplantation: 7 T gagCEST and sodium magnetic resonance imaging with morphological and clinical correlation". In: *Osteoarthritis and Cartilage* 20.5 (May 2012). 00039, pp. 357–363. ISSN: 1063-4584. DOI: 10.1016/j.joca.2012.01.020 (cit. on p. 38).

[40] Anup Singh, Mohammad Haris, Kejia Cai, Victor B. Kassey, Feliks Kogan, Damodar Reddy, Hari Hariharan, and Ravinder Reddy. "Chemical exchange saturation transfer magnetic resonance imaging of human knee cartilage at 3 T and 7 T". In: *Magnetic Resonance in Medicine* 68.2 (Aug. 2012). 00050, pp. 588–594. ISSN: 07403194. DOI: 10.1002/mrm.23250 (cit. on p. 38).

[41] Wen Ling, Ravinder R. Regatte, Gil Navon, and Alexej Jerschow. "Assessment of glycosaminoglycan concentration in vivo by chemical exchange-dependent saturation transfer (gagCEST)". In: *Proceedings of the National Academy of Sciences of the United States of America* 105.7 (Feb. 19, 2008). 00250, pp. 2266–2270. ISSN: 1091-6490. DOI: 10.1073/pnas.0707666105. pmid: 18268341 (cit. on p. 38).

[42] P. C. M. van Zijl, C. K. Jones, J. Ren, C. R. Malloy, and A. D. Sherry. "MRI detection of glycogen in vivo by using chemical exchange saturation transfer imaging (glycoCEST)". In: *Proceedings of the National Academy of Sciences* 104.11 (Mar. 13, 2007). 00159, pp. 4359–4364. ISSN: 0027-8424, 1091-6490. DOI: 10.1073/pnas.0700281104 (cit. on p. 38).

[43] Simon Walker-Samuel, Rajiv Ramasawmy, Francisco Torrealdea, Marilena Rega, Vineeth Rajkumar, S. Peter Johnson, Simon Richardson, Miguel Gonçalves, Harold G. Parkes, Erik Arstad, David L. Thomas, R. Barbara Pedley, Mark F. Lythgoe, and Xavier Golay. "In vivo imaging of glucose uptake and metabolism in tumors". In: *Nature Medicine* 19.8 (Aug. 2013). 00044 Cited by 0001, pp. 1067–1072. ISSN: 1078-8956. DOI: 10.1038/nm.3252 (cit. on p. 39).

[44] Shanrong Zhang, Craig R. Malloy, and A. Dean Sherry. "MRI Thermometry Based on PARACEST Agents". In: *Journal of the American Chemical Society* 127.50 (Dec. 1, 2005), pp. 17572–17573. ISSN: 0002-7863. DOI: 10.1021/ja053799t (cit. on p. 39).

[45] Nevin McVicar, Alex X. Li, Mojmír Suchý, Robert H. E. Hudson, Ravi S. Menon, and Robert Bartha. "Simultaneous in vivo pH and temperature mapping using a PARACEST-MRI contrast agent: In Vivo pH and Temperature Mapping Using PARACEST-MRI". In: *Magnetic Resonance in Medicine* 70.4 (Oct. 2013), pp. 1016–1025. ISSN: 07403194. DOI: 10.1002/mrm.24539 (cit. on p. 39).

[46] M. Meser Ali, Mark Woods, Eul Hyun Suh, Zoltan Kovacs, Gyula Tircsó, Piyu Zhao, Vikram D. Kodibagkar, and A. Dean Sherry. "Albumin-binding PARACEST agents". In: *Journal of biological inorganic chemistry : JBIC : a publication of the Society of Biological Inorganic Chemistry* 12.6 (Aug. 2007). 00030, pp. 855–865. ISSN: 0949-8257. DOI: 10.1007/s00775-007-0240-z. pmid: 17534672 (cit. on p. 39).

[47] Byunghee Yoo and Marty D. Pagel. "A PARACEST MRI contrast agent to detect enzyme activity". In: *Journal of the American Chemical Society* 128.43 (Nov. 1, 2006). 00132, pp. 14032–14033. ISSN: 0002-7863. DOI: 10.1021/ja063874f. pmid: 17061878 (cit. on p. 39).

[48] Todd C. Soesbe, Yunkou Wu, and A. Dean Sherry. "Advantages of paramagnetic chemical exchange saturation transfer (CEST) complexes having slow to intermediate water exchange properties as responsive MRI agents: RESPONSIVE CHELATES FOR PARAMAGNETIC CEST IMAGING". In: *NMR in Biomedicine* 26.7 (July 2013). 00000, pp. 829–838. ISSN: 09523480. DOI: 10.1002/nbm.2874 (cit. on p. 39).

[49] Guanshu Liu, Yuguo Li, Vipul R Sheth, and Mark D Pagel. "Imaging in vivo extracellular pH with a single paramagnetic chemical exchange saturation transfer magnetic resonance imaging contrast agent." In: *Molecular imaging* 11.1 (Feb. 2012). 00042 Cited by 0000, pp. 47–57 (cit. on p. 39).

[50] Xiaolei Song, Assaf A Gilad, Suresh Joel, Guanshu Liu, Amnon Bar-Shir, Yajie Liang, Michael Gorelik, James J Pekar, Peter C M van Zijl, Jeff W M Bulte, and Michael T McMahon. "CEST phase mapping using a length and offset varied saturation (LOVARS) scheme." In: *Magnetic resonance in medicine : official journal of the Society of Magnetic Resonance in Medicine / Society of Magnetic Resonance in Medicine* 68.4 (Oct. 2012). Cited by 0009, pp. 1074–1086. DOI: 10.1002/mrm.23312 (cit. on p. 39).

[51] Rachel Scheidegger, Elena Vinogradov, and David C. Alsop. "Amide proton transfer imaging with improved robustness to magnetic field inhomogeneity and magnetization transfer asymmetry using saturation with frequency alternating RF irradiation". In: *Magnetic Resonance in Medicine* 66.5 (Nov. 2011). 00044, pp. 1275–1285. ISSN: 07403194. DOI: 10.1002/mrm.22912 (cit. on p. 39).

[52] Johanna Närväinen, Penny L. Hubbard, Risto A. Kauppinen, and Gareth A. Morris. "Z-spectroscopy with Alternating-Phase Irradiation". In: *Journal of Magnetic Resonance* 207.2 (Dec. 2010), pp. 242–250. ISSN: 10907807. DOI: 10.1016/j.jmr.2010.09.004 (cit. on p. 39).

[53] Zhongliang Zu, Vaibhav A. Janve, Junzhong Xu, Mark D. Does, John C. Gore, and Daniel F. Gochberg. "A new method for detecting exchanging amide protons using chemical exchange rotation transfer". In: *Magnetic Resonance in Medicine* 69.3 (Mar. 1, 2013), pp. 637–647. ISSN: 07403194. DOI: 10.1002/mrm.24284 (cit. on p. 39).

[54] Zhongliang Zu, Vaibhav A. Janve, Ke Li, Mark D. Does, John C. Gore, and Daniel F. Gochberg. "Multi-angle ratiometric approach to measure chemical exchange in amide proton transfer imaging". In: *Magnetic Resonance in Medicine* 68.3 (Sept. 2012). 00034, pp. 711–719. ISSN: 07403194. DOI: 10.1002/mrm.23276 (cit. on p. 39).

[55] Nirbhay N. Yadav, Craig K. Jones, Jiadi Xu, Amnon Bar-Shir, Assaf A. Gilad, Michael T. McMahon, and Peter C. M. van Zijl. “Detection of rapidly exchanging compounds using on-resonance frequency-labeled exchange (FLEX) transfer”. In: *Magnetic Resonance in Medicine* 68.4 (Oct. 2012), pp. 1048–1055. ISSN: 07403194. DOI: 10.1002/mrm.24420 (cit. on p. 40).

2. glucoCEST: imaging glucose in tumours

Glucose plays a central role in biology. Almost all organisms, from bacteria to humans, use it as an energy and biomass source to sustain their metabolic demands. In the human body, a single glucose molecule can provide up to 32 ATP molecules via complete aerobic respiration, but it can also be transformed into several carbon scaffolds for biosynthetic reactions.[1–3] Cancer cells avidly consume glucose in rates up to 20 times faster than their healthy counterparts. The elevated glucose uptake enables the cells to meet the energetic demands of fast cell proliferation and to produce many intermediate biosynthetic precursors involved in biomass duplication.[4,5]

Upregulated glycolysis is arguably the single most common feature in nearly all primary and metastatic cancers, a phenomenon known as the Warburg effect. Even in well oxygenated conditions, cancer cells metabolise glucose via the lactate production pathway, namely, aerobic glycolysis pathway.

The aberrant consumption of glucose by tumours has been widely exploited in the diagnosis of cancer with the use of fluorodeoxyglucose positron emission tomography (^{18}F-FDG-PET) in nuclear medicine. Similarly, in glucoCEST MRI tumours are studied by looking at the concentration of natural glucose in the tissue, which can be detected via the chemical exchange of protons in hydroxyl groups.

In this Chapter the principles and rational behind the glucoCEST technique are explained and a summary of the most recent developments in the field are presented. The initial work on glucoCEST by our group[6] is briefly described, highlighting the main findings in the study. These will serve as the starting point for the discussion of the following Chapters.

2.1. Metabolism of Cancer

2.1.1. Introduction

In contrast to normal cells, which grow and divide under a tightly controlled biological supervision, cancer cells have the ability to elude the body's regulatory processes and as a result they multiply in an uncontrolled manner. This ability to alter physiological pathways to their advantage is wired deep in the genetic code of the cancer cells. Overall, these genetic mutations give rise to a wide range of phenotypes, which makes both study and therapy of malignant neoplastic diseases difficult.

2.1.2. Hallmarks of Cancer

In the year 2000 cancer researchers Douglas Hanahan and Robert Weinberg published an article titled 'The Hallmarks of Cancer' in which they described a list of common traits characterising the transformation of normal cells to cancer (or malignant tumour) cells.[4]

Those hallmarks are: (1) self-sustained growth signals; (2) resistance to external inhibitory growth signals to stop expansion; (3) resistance to their own programmed cell death (apoptosis); (4) formation of new blood vessels around the tumour to supply nutrients (angiogenesis); (5) limitless replicative potential; and (6) local tissue invasion and spread to distant sites (metastasis).

'The Hallmarks of Cancer' have been largely accepted by the clinical and research community for the last decade, and have been used as guidelines to identify tumours, becoming an important reference in the field of cancer research. Nevertheless, the usefulness of those hallmarks has also been questioned. A notable comment in this regard was published by Yuri Lazebnik in 2010 in Nature Reviews.[7] In this article, by comparing the characteristics of benign tumours to malignant cancerous cells, the author argued that the true single hallmark of cancer is its metastatic ability.

Despite some critical voices, 'The Hallmarks of Cancer'remains the most cited article in Cell.
In 2011 a revision of the original paper was published. Incorporating the knowledge gained in the investigation of cancer over the past ten years, the authors compiled an updated list of hallmarks. Following the impact of the original paper, the updated manuscript has also become a key reference in the field, ranking the top cited article since its publication.[5]

In addition to the original list, four new features were included which the authors

classified under the following categories: '*enabling characteristics*' and '*emerging hallmarks*.' The two enabling characteristics of cancer are: DNA instability and Tumour-promoting inflammation. While these alone do not cause cancer, they assist cell mutation from normal to oncogenic. The two *emerging hallmarks* are: Evasion of the immune system and *Metabolic reprogramming*.

Metabolic reprogramming is understood as cancer cells' ability to alter the synthesis pathways to promote fast anabolic growth making extensive use of a range of metabolites including fatty acids, glutamine and, in particular, glucose.

Unsure of whether the last characteristics are prevalent in all cancers, the authors did not include them into the list of core hallmarks. Nonetheless, an increasing number of studies acknowledge the deregulated metabolism as a ubiquitous aspect of malignant tumours.[3,8,9]

In the following, the hallmark of *Metabolic reprogramming* of cancers will be addressed in more depth, as it is the main characteristic which ultimately allows glucoCEST contrast to be generated for its use in the diagnosis of cancer.

2.1.3. The Warburg effect

Towards the middle of the twentieth century Otto Warburg[10] observed that tumour cells favour the conversion of glucose into lactate as a means of energy production instead of recurring to the much more efficient mitochondrial oxidation process. This was odd as tumour cells need, in principle, more energy than the primitive cells. Warburg's opinion was that this respiratory defect, conversion of glucose into lactate together with the cancellation of the citric acid cycle in the mitochondria, was the most characteristic change of tumour cells. Ganapathy[11] contains a beautiful description of the main differences in transport and metabolism between normal and tumour cells. Although hypoxia in the tumoral tissue due to insufficient development of microvasculature is sometimes referred to as a possible contributing factor to mitochondrial malfunction, mitochondrial function is partially suppressed in most tumours cells even in abundance of oxygen.[11] Mitochondrial malfunction might be due to an alteration in the tumoral mitochondria's filamentation-defilamentation cycle which reduces its affinity to ADP below pyruvate kinase isoenzyme's affinity.[12] Thus, in the competition for ADP between mitochondria and glycolysis the latter is favoured.

Glycolytic transformation of glucose into lactate under normoxia conditions, a process sometimes referred to as 'aerobic glycolysis', is accompanied by the release of lactic acid to the extracellular compartment. Therefore 'aerobic glycolysis' in

tumours drives extracellular pH (pHe) acidic.[13] Some researchers believe that this acidic environment promotes invasion and enhances metastasis, which offers cancer a selective evolutionary advantage.[14,15]

Even though glycolysis yields only two ATP per molecule of glucose, tumours obtain energy by enhancing the glycolysis rate to at least 25-fold higher than in normal cells, more than compensating the glycolytic inefficiency. Obviously, this high rate of glycolysis can not be reached with normal enzymatic levels. To get such an extraordinary high rate of glucose conversion in 'aerobic glycolysis' cancer cells must coordinate glucose transport to the elevated glycolysis rate. Tumour cells must activate not only glucose transporters but also genes encoding necessary glycolytic enzymes to increase their expression to the required levels to enable the metabolism of an amount of glucose 25 times higher than normal. Hence the term *Metabolic reprogramming*.

Fast proliferation requires abundant energy as well as a constant supply of building blocks to enable the anabolism. As Otto Warburg himself noticed, respiration process in tumours is small compared to their glucose consumption, but not small relative to the respiration in normal tissues.[16]

During periods of rapid proliferation, many cell types ranging from microbes to lymphocytes resort to 'aerobic glycolysis', which suggests that it may play a crucial role in supporting cell growth.

Heiden et al.[2,3] argue that the main function of 'aerobic glycolysis' is to sustain high levels of glycolytic intermediates as the building blocks of the anabolic reactions in cells. Alternative to the plain energetic considerations, this argument provides an explanation for why increased glucose metabolism is chosen in proliferating cells throughout nature.

2.2. Targeting metabolism

For over three decades, diagnosis in oncology has exploited the elevated glucose uptake of tumours by using Positron Emission Tomography (PET) in combination with 2-Deoxyglucose labeled with ^{18}F radio-tracer. Based on the relative uptake of tissues, ^{18}F-FDG PET has enabled the distinction of areas of active tumour from non-tumour or necrotic regions. Furthermore, ^{18}F-FDG PET has been correlated with tumour grade in a wide range of cancers; with an intense PET signal associated to fast proliferating malignant cells.[17–20]

In the field of Nuclear Magnetic Resonance (NMR), spectroscopic techniques have successfully identified and characterized mostly primary brain tumors (gliomas)

based on their increased anaerobic pathway (glycolysis) of glucose, by measuring increases in lactate and choline concentrations together with a reduction of N-acetyl aspartate (NAA) in cancerous areas. Again, these NMR profiles correlate with gliomas grades, displaying high choline and lactate levels in the most common and aggressive Grade IV gliomas, also known as Glioblastoma Multiforme (GBM).[21,22]

In this context glucoCEST shows up as a novel potentially promising technique for the study of tumours by exploiting their aberrant metabolism.

It is worth pointing out that as a direct consequence of the elevated glycolysis, increased lactate is produced. This excess of lactate is secreted from the cell, which in turn, creates an acidic environment in the extracellular space (ECS). In this context cancer cells present an unusual situation in which extracellular pH becomes more acidic than the intracellular one. This anomaly, sometime referred to as ”reverse pH gradient”, could also play an important role in CEST based experiments, as the exchange rate is greatly influenced by the pH of the tissue. In this sense, image contrast could be enhanced based on the local pH variances around tumours.

Furthermore, because the pH control mechanisms are largely dysregulated in tumours, it is in principle possible to influence on the local pH of the cancerous tissue using biological buffers, like sodium bicarbonate (baking soda).[8,15] Dysregulation of pH is a process which occurs in early stages of cancers to promote cell invasion.[8] Combination of the exquisite pH sensitivity of CEST and the possibility of altering local pH in tumours can lead to a new CEST-MRI modality that could prove useful for early detection of cancer (see section 7.4).

2.3. glucoCEST: the concept

CEST is extremely sensitive to a number of chemical species and metabolites present in the body. All these species exchange magnetisation simultaneously resulting in a combined effect that produces a complex Z-spectrum. Moreover, in vivo transverse relaxation times are shorter than in aqueous solutions, which leads to broader absorption bandwidths of the solutes and to overlapping resonant frequencies. Accurate deconvolution of the Z-spectrum into its individual contributors is therefore very difficult and a major area of research in the CEST field. Owing to these limitations, exact quantification of glucose content in tissues is unrealistic at present.

The approach in glucoCEST however, is not to measure the intrinsic glucose content of tissues but rather the concentration increase following an external administration of glucose. For that purpose, two CEST images are acquired, one before and another after the dose of glucose. The final glucoCEST signal, namely, gluco-

CEST enhancement (GCE), arises from the difference of the two images (see figure 2.3.1). In this way, a substantial increase of glucose following administration leads to a strong glucoCEST signal, while no signal is observed in the absence of glucose uptake.

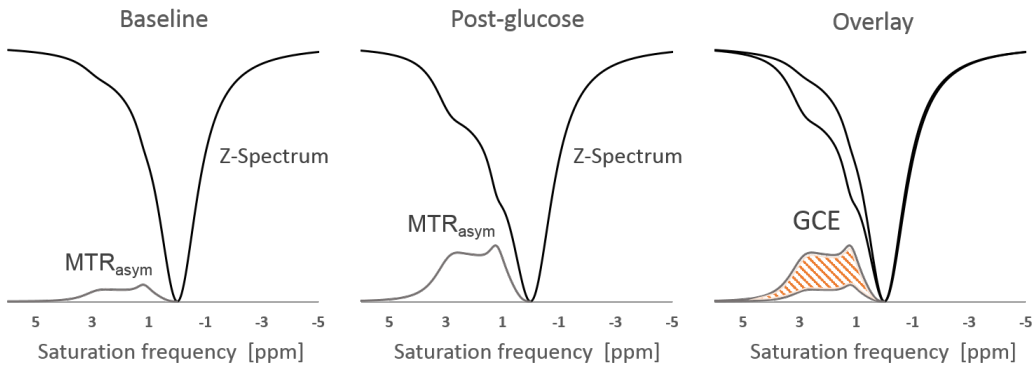

Figure 2.3.1.: *GlucoCEST concept diagram. Simulated Z-spectra of three hydroxyl group resonances alongside the magnetization transfer ratio asymmetry (MTRasym) before (left), and after (center) glucose administration. The signal from the hydroxyl groups resonating at 1.2, 2.1 and 2.9 ppm from water increases. The GCE is defined as the change in the area under the MTRasym curve from baseline (right).*

The approach taken in glucoCEST avoids many of the complications involved in the interpretation of CEST data. The first pre-glucose image serves as a reference from which changes can be measured, and therefore no deconvolution methods or sophisticated multi-pool fittings are required in order to identify the source of the signal. The method picks up regions of higher glucose concentration with relatively little manipulation of the data. In this way, glucoCEST may allow the use of natural sugar as a potential biomarker of metabolism. This makes it a very attractive and readily applicable technique for a number of metabolic related disorders.

2.3.1. Advantages

Like all the CEST based methods, glucoCEST offers an enhanced sensitivity to labile proton, glucose in this case, which allows *in vivo* and noninvasive imaging of glucose distribution in tissues.

In vivo Z-spectra display complex profiles deriving from various independent processes i.e spill-over, macromolecular MT, chemical exchange from amide, amines and hydroxyl groups, aliphatic NOE, and distortions from B1 inhomogeneities. A

major challenge in endogenous CEST is the lack of specificity to separate and weight the individual contribution of each process that shape the Z-spectrum. While under certain conditions, clever methods of data analysis can yield consistent values for the *in vivo* concentration of labile protons, reliable quantification is still very problematic, particularly for those proton species resonating in a frequency range close to water (~1ppm), as is the case of hydroxyls. Glucose administrated exogenously alters the basal in vivo CEST profile, which allows easier determination of its specific contribution to the CEST signal by a subtraction of the baseline image acquired prior to glucose administration.

2.3.2. Drawbacks

Currently the main limitation of glucoCEST is arguably its low SNR. As in fMRI, the CEST contrast is generated from the difference of two quasi-identical CEST images. Considering that these CEST images have a low signal to begin with (especially at high saturation powers where effects of direct saturation are dominant), the final glucoCEST image is prone to elevated noise. Hence, glucoCEST images tend to compromise spatial resolution in favour of higher SNR.

Another hurdle associated with glucoCEST imaging arises from the potential changes in the physiology during acquisition. As a biologically active compound, administration of glucose can change the physiological conditions of the inspected tissues. Altered blood flow, pH, oxygen and CO2 levels can lead to significant variations in the observed CEST profile. If not controlled, these changes can lead to misreadings of the influence of glucose in the Z-spectrum and consequently to the misinterpretation of the glucoCEST data.

Finally limitation on the applicable B1 power for saturation also diminishes the efficiency of glucoCEST in clinical applications. Intense and prolonged saturation RF pulses can easily lead to SAR depositions above the regulated safe levels. This can constrain the detection sensitivity for fast exchangeable protons in humans. Safety considerations aside, even within the allowed SAR limits, modern clinical MRI systems have very strictly controlled B1 power levels and the use of solid-state RF amplifiers inherently limits their duty cycle. These limitations do not always correspond to technical reasons but to rather arbitrary decisions. Provided all safety checks are passed, the scientific community should encourage the correction of arbitrary constraints in order to obtain better CEST performing MRI scanners.

2.4. glucoCEST: literature review

Over the last five years the number of studies involving CEST-MRI has largely expanded due to its attractiveness for in-vivo imaging of important physiological traits.

GlucoCEST differs from endogenous CEST modalities in that it relies on the detection of an exogenously administered CEST agent (or on its physiological effects). As such the analysis of glucoCEST data becomes more straight forward, as the endogenous CEST image serves as the control upon which new contrast is generated.

In the following, a brief review of the works published around the concept of glucoCEST and the detection of glucose through chemical exchange is presented.

2.4.1. The Origins: glycoCEST

In 2007 van Zijl et al.[23] published a seminal work demonstrating the feasibility of in-vivo imaging of glycogen content in the mouse liver based on CEST-MRI. The method, named glycoCEST, opened an opportunity to study glycogen metabolism of any disorders with MRI.

By applying a second long RF pulse (3 μT) 1 ppm downfield from water (higher frequency) proton in hydroxyl groups of glycogen saturate, producing a dip in the Z-spectra as they exchange with the hydroxyls in water. While the principles in glycoCEST are similar to other CEST methods, the publication set a precedent in the CEST community as for the first time it was possible to image fast exchanging -OH groups using a non-invasive technique.

The glycogen levels in the mouse liver were tracked in time by comparing CEST images irradiated at opposite sides of the water spectrum ($MTR_{asym}(\delta)$ = MTR(δ) - MTR($-\delta$), with δ=1 ppm), acquired with a [Saturation + Spin-Echo] sequence design in a 4.7 Tesla field scanner. The progressive breakdown of glycogen was sustained by constant infusion of glucagon and validated in parallel experiments by 13C MRS, the gold standard technique for non-invasive determination of glycogen concentration in vivo. The CEST measurements showed a gradual reduction of the MTR_{asym} for a period of 2 hours from the moment of the infusion, after which the MTR_{asym} stabilised, which marked the glycogen depletion point. The time for depletion of glycogen matched with the data found in 13C MRS.

The results were somewhat unexpected as the proton exchange rate between glycogen and water hydroxyls was supposed to be too fast compared to the small chemical shift (1 ppm) between the two species. While generally proton in -OH groups exchange too rapidly for optimum CEST contrast ($\kappa > \delta$), hydroxyls in glycogen

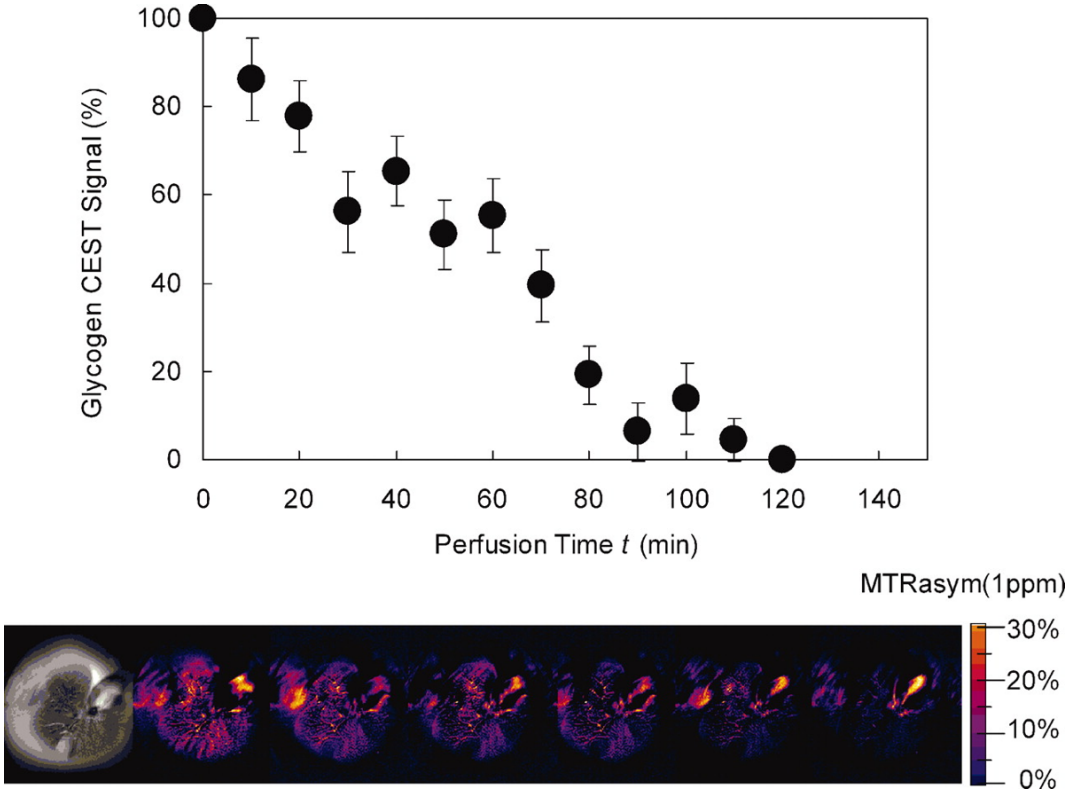

Figure 2.4.1.: *GlycoCEST imaging of a perfused fed-mouse liver at 4.7 T and 37° C. The first image (grey scale) marks the beginning of perfusion (t = 0) with glucose-free media containing 500 pg/ml glucagon. The liver tissue is darkened because of the CEST effect from pre-saturation at 1.0 ppm for 1 s at 3.0 μ T. Upon further perfusion with glucagon, the liver signal increased, corresponding to a decrease in CEST effect. The colorised glycoCEST images as a function of time during perfusion show the relative CEST intensity [MTR_{asym} (1 ppm)] of liver tissue as a function of perfusion time. The colour scale shows that there are regions of liver where the initial asymmetry difference between $\pm$1 ppm is as high as 55% (orange pixels) and as low as 5% (blue pixels). With time, as glycogen disappears, the CEST images become more uniformly dark blue, corresponding to minimal glycogen. The corresponding glycogen depletion for a homogeneous region of interest is quantified in the graph (n = 4). Figure reproduced from van Zijl et al.*[23]

macromolecules are relatively slow ($\kappa < 1000Hz$) given their restricted mobility and accessibility within the molecular structure.

Alternatively to MRI, a newly developed glycogen specific PET radioactive tracer has been recently used to image aberrant glycogen metabolism in cancerous mice.[24] While the sensitivity of the PET based modality exceeds the contrast achievable with CEST-MRI, glycogen concentration in the liver (and its variation due to physiology) is high enough for glycoCEST to detect it. Owing to the wide accessibility of MRI scanners and the safety of the imaging modality glycoCEST remains as an attractive, purely non-invasive method of imaging liver glycogen in vivo.

Since this first study, researchers in different labs have studied ways of exploiting the chemical exchange process to image biomolecules in the fast end of the intermediate exchange regime. A notable example of this is the study of glucose and its analogue sugars as CEST agents, fuelled by significant clinical interest due to their central role in a number of conditions where metabolism is disrupted.

2.4.2. Cancer studies

Particularly for the field of cancer research, glucoCEST has the qualities to become an ideal method to investigate the abnormally elevated glycolytic flux (Warburg effect) of proliferating tumours. Similar to the concept exploited in ^{18}F-FDG-PET, glucoCEST aims to differentiate healthy tissue from tumours based on their glucose concentration, which may also inform on the metabolism and aggressiveness of the tumour under study. Unlike ^{18}F-FDG-PET, glucoCEST is free of the burdens associated with the use of radio-tracers, i.e high production costs, limited accessibility and the safety implications of radioactive exposure.

Currently three independent studies have been published on the use of natural glucose as a CEST agent for the study of cancer in vivo: the work by Chan et al.[25] from Johns Hopkins University, the work by Walker-Samuel et at.[6] from our group at University College London, and the study by Rivlin et al.[26] from Tel Aviv University.

The Johns Hopkins University group looked at the glucoCEST signal in two different human breast xenograft models (MDA-MB-231 and the less aggressive MCF-7 cell-lines), and compared the data with ^{18}F-FDG-PET and Gd-DTPA contrast enhanced MRI scans, performed in the same mice cohort. Results of both tumour types displayed elevated signal for glucoCEST and PET with just partial Gd-enhancement. Furthermore, among the three techniques explored only glucoCEST showed significant separation between cancer cell-lines, suggesting the possibility of the characterisation of tumours based on their glucoCEST profile.

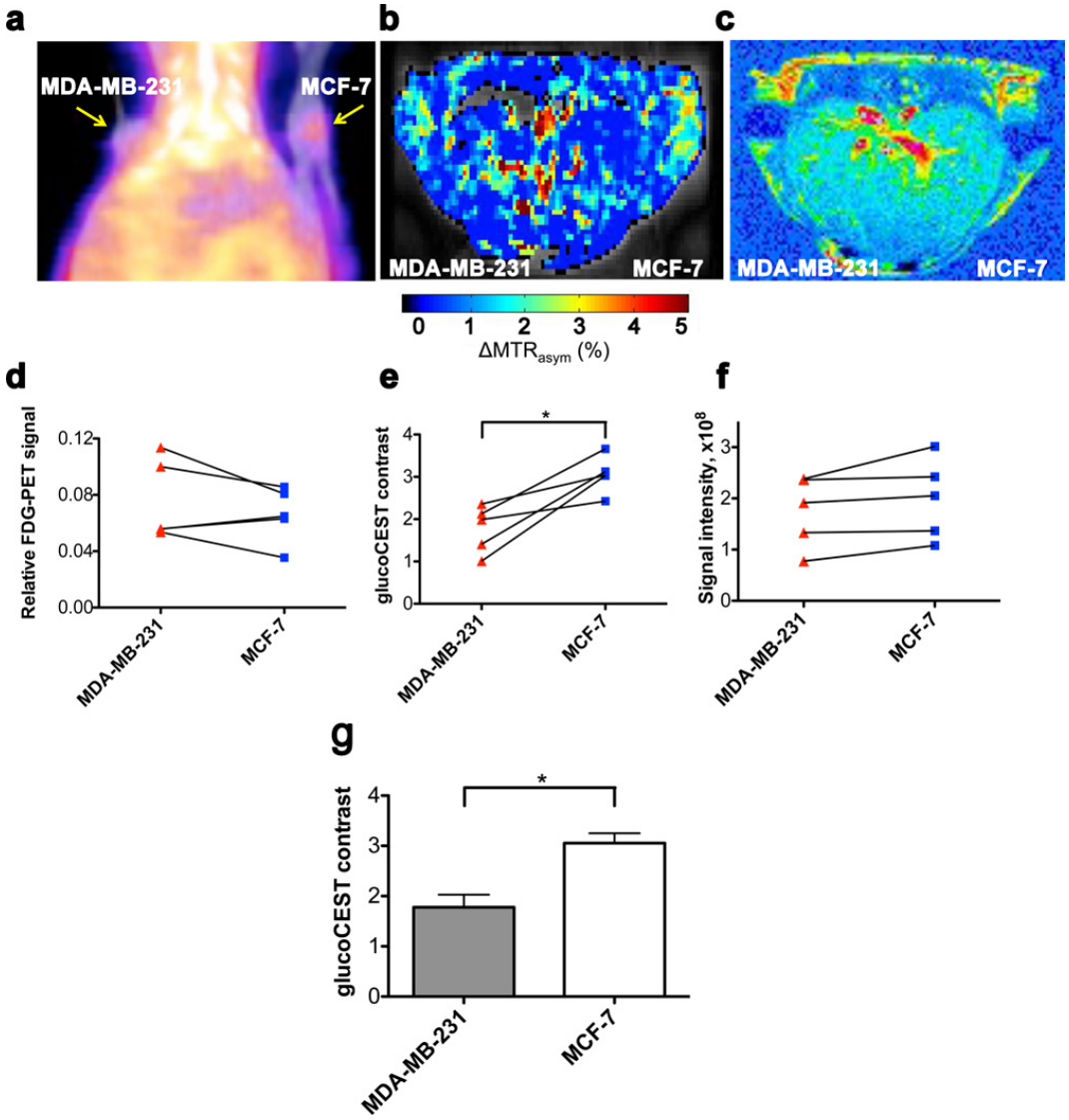

Figure 2.4.2.: *(a) ^{18}F-FDG-PET/CT coronal view obtained one hour after intravenous (i.v.) injection of ^{18}F-FDG showing accumulation in both tumors. (b) GlucoCEST Δ MTR_{asym} map (Infusion – Pre-infusion). (c) T_1-weighted difference image (Injection – pre-injection) showing Gd-enhanced regions, mainly in the edges of tumours. (d–f) Comparison of signal intensities (n = 5) for the three modalities using ROIs comprising the two tumours. Even though some trends appear visible for PET and contrast-enhanced MRI, significant differences ($p<0.05$; paired student's t-test) between the tumours could be detected only in glucoCEST. (g) Bar graph showing average glucoCEST contrast for MDA-MB-231 and MCF-7 tumors. Figure reproduced from Chan et al.*[25]

Interestingly, the glucoCEST signal was found to be consistently lower in the more aggressive phenotype tumours. These results, together with the idea that once inside the cell glucose rapidly converts into lactate, and the fact that acidic extracellular pH in tumours is likely to provide a more favourable exchange rate for the detection of hydroxyl groups in glucose, led researchers to conclude that glucoCEST does not directly inform on the metabolism but mainly on the interstitial glucose levels.

Nonetheless, the debate of the precise source of the glucoCEST signal was far from settled.

In the study presented by our group,[6] glucoCEST technique was compared to ^{18}F-FDG autoradiography in two mouse models of colorectal tumour (cell lines SW1222 and LS174T) with distinct metabolic characteristics. Animals were scanned with glucoCEST pre- and post-administration of glucose (1g/kg intra-peritoneal [IP] bolus to provide a more sustained glucose delivery than intra-vascular [IV] bolus) and 24 hours later ^{18}F-FDG autoradiography experiments were performed on the same animal cohort. The study also included parallel Gd-enchancement MRI, carbon 13 spectroscopic analysis (using uniformly-labelled 13C glucose) aimed to track the metabolic path of glucose in the tumours, as well as perfusion and hypoxia fluorescence microscopy images (using Hoechst 33342 and pimonidazole staining, respectively).

In agreement with the study by Chan et al, results showed that glucoCEST is sensitive to tumour glucose uptake and can distinguish tumour types with differing metabolism and pathophysiologies.

13C MRS showed ratios of glucose 6-phosphate (G6P) to the glucose concentration were found to be close to 40% in both tumours (42% and 38% in SW1222 and LS174T, respectively). In addition, glucose was observed to be metabolised into lactate and a number of amino-acids, such as glutamine, glutamate, taurine and alanine. In vitro assessment of the CEST properties of the glycolytic intermediates and amino-acids found in the tumours suggests that intracellular stages of glycolysis can be detected by glucoCEST, with G6P giving an approximately equal CEST contrast as glucose.

Provided that the metabolic activity of cancer cells increases in response to a sudden rise in glucose availability, it is expected that the glycolytic intermediates and amino-acids from fast catabolism of glucose will contribute to the observed glucoCEST signal.

The lack of correlation between either FDG or glucoCEST signal and perfusion (measured with Hoechst 33342 staining and Gd-DTPA) indicates that the measured

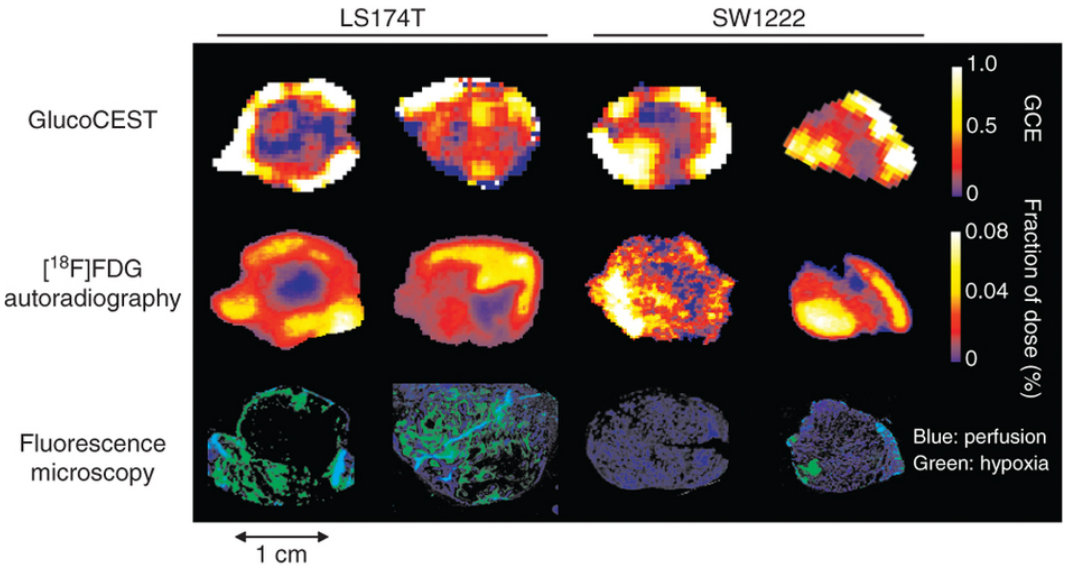

Figure 2.4.3.: *The fluorescence microscopy images show perfused (blue) and hypoxic (green) regions corresponding to Hoechst 33342 and pimonidazole staining, respectively. All CEST data in this figure were acquired using the GE-CEST sequence. Figure reproduced from Walker-Samuel et al.*[6]

glucoCEST contrast is not limited to the vascular delivery of glucose. In fact, based on the observed correlation between FDG and glucoCEST signal and the elevated presence of glucose intermediates found inside the cells, the researchers argued that a significant contribution to the glucoCEST contrast can be attributed to the intracellular compartment.

In the third work published on glucoCEST in cancer, the team from Tel Aviv University used glucose analogue molecules 2-deoxyglucose (2DG) and 2-fluorodeoxyglucose (FDG, non-radioactive stable isotope 19F) to study the glucoCEST response of a poorly differentiated mammary adenocarcinoma mouse model (cell line DA3-D1-DMBA-3). Both glucose analogues are taken into the cells by the GLUT transporters and phosphorylated by hexokinase, after which the catabolic process cannot continue. The molecules accumulate inside the cells until they are slowly cleared through dephosphorylation of 2-deoxyglucose-6-phosphate (2DG6P), or though isomerisation to 2-deoxyglucose-1-phosphate (2DG1) to form glycogen.[27,28]

Unlike natural glucose which quickly metabolises, the glucoCEST signal from the analogue molecules build up in the tumours over 2 hours after the IP administration of FDG/2DG. This results in an increased and long lasting CEST contrast. However, toxic effects of FDG and 2DG limit their use in clinical studies, where tolerated dose has been shown to be around 60 mg/kg/day IV (or 250 mg/kg orally), an order of

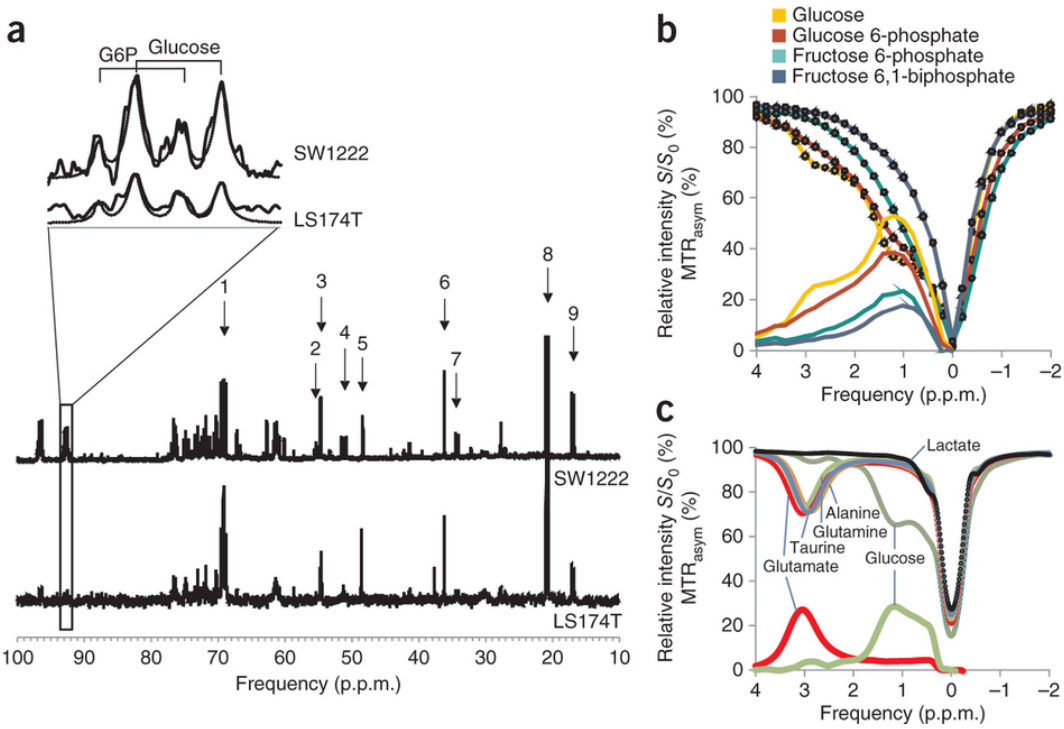

Figure 2.4.4.: *(a) Example 1H-decoupled 13C NMR spectra from SW1222 and LS174T tumours that were administered [U-13C]glucose following the protocol used in the glucoCEST experiments. The peak assignments are as follows: 1, lactate C2; 2, glutamate C2; 3, glutamine C2; 4, alanine C2; 5, taurine C1; 6, taurine C2; 7, glutamate C4; 8, lactate C3; and 9, alanine C3. An expansion of the C1α multiplet is shown that corresponds to doublets from glucose and glucose-6-phosphate (chemically shifted by 0.13 ppm from the glucose doublet). Fitted Lorentzian peaks are overlaid. (b) z and MTR_{asym} spectra from glucose, glucose 6-phosphate, fructose 6-phosphate and fructose 6,1-biphosphate. In vitro, glucose and glucose-6-phosphate show similar CEST effects, whereas fructose-6-phosphate and fructose 6,1-biphosphate display a smaller effect. Units on the vertical axis are signal intensity, S, normalised to a reference measurement, S0, at 200 p.p.m. from the peak of the water resonance. (c) z and MTR_{asym} spectra from glucose, lactate, glutamine, glutamate, alanine and taurine. Glucose shows a strong CEST effect from hydroxyl proton exchange, whereas the amino acids show a CEST effect through amide proton exchange. Lactate shows a minimal effect. Figure reproduced from Walker-Samuel et al.*[6]

magnitude below the dosage tested in the study.[26]

In a recent publication[29] the team in Tel Aviv have reported the use of the non-toxic glucose analogue 3-O-methyl-D-glucose (3OMG) as an alternative glucoCEST agent. Once inside the cell 3OMG does not undergo phosphorylation by hexokinase and can readily return to the blood stream (through the GLUT transporters) which consequently is fully excreted by the kidneys.
Tested on the same cancer model as in the previous study, the researchers observed an intense glucoCEST signal which slowly faded, retaining 70% of the maximum contrast 1 hour after the IP injection.
While further tolerance tests are needed to assess safety dosage of the compound in humans, initial data suggest that 3OMG can be potentially useful for the detection of tumours and monitoring of treatment in the clinic.

2.4.3. Brain studies

Focusing on the field of neuroimaging, where traditionally MRI excels, two published works on glucoCEST exploring the metabolism of the healthy brain can be found.

In the first one Nasrallah et al.[30] presents a thorough study of the evolution of the glucoCEST signal in the rat brain under different conditions.
The study shows a significantly elevated glucoCEST signal following the administration of both 2DG and natural D-glucose. Similarly to the results in other studies, signal from 2DG was shown to be nearly twice as intense and longer lasting than from natural D-glucose. Even with a sustained high blood D-glucose (via IV infusion), signal did not reach levels observed with 2DG, which points to the accumulation of 2DG6P inside the cell (rather than to the extracellular glucose concentration) as an important contributor to the glucoCEST contrast. This observation agrees with the similar changes observed in 2DG6P levels measured by in vivo 31P NMR, suggesting that glucoCEST reflects the rate of glucose assimilation.

Importantly, a dramatic attenuation of signal was observed when high levels of anaesthesia (2% isoflurane) were used, further supporting a link between glucoCEST contrast and the metabolic state of the brain.

Moreover, contribution from the intravascular compartment was ruled out by two independent experiments. First, no change in glucoCEST signal was measured with increased cerebral blood flow (CBF) under hypercapmic conditions (achieved with 1.8% CO2 in the gas mixture, which doubled basal CBF). Second, administration of

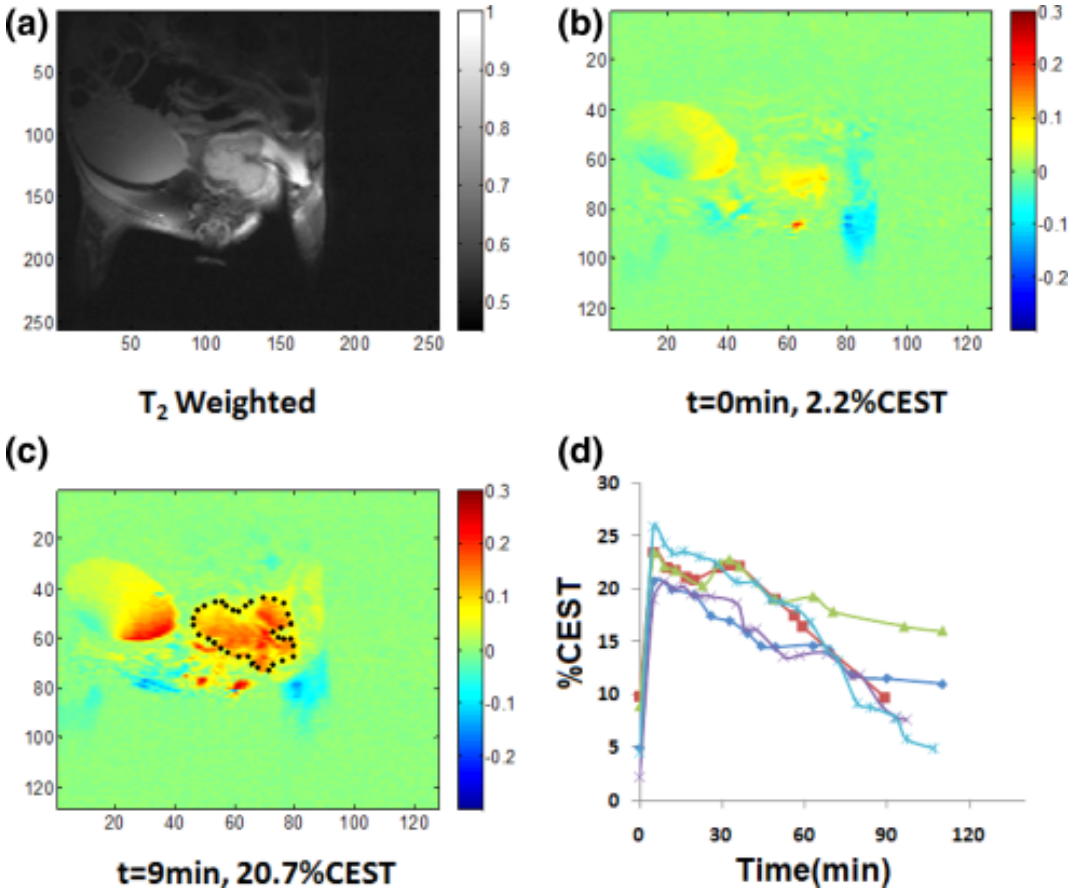

Figure 2.4.5.: *CEST MRI kinetic measurements in the tumour at different times following injection of 3OMG, 1.5 g/kg ($B1 = 2.5\mu T, B0 = 7T$). a: A T_2-weighted image before the administration of the agent. b: A CEST image before the administration of the agent. c: A CEST image 9 min after the injection. The marked ROI was used for the CEST calculation. d: The time series of the %CEST for the five mice tested. Figure reproduced from Rivlin et al.*[29]

L-glucose*, which does not leave the vascular compartment in the brain, produced no glucoCEST signal.

These results let the research team conclude that glucoCEST provides a widely available MRI method to image uptake and metabolism of glucose/2DG in the brain.

2.4.4. Alternative Techniques for glucose detection

The second MRI study exploring glucose uptake in the brain was published by Tao Jin et al.[32] in 2014 which strictly speaking is not a work based on CEST but on CESL, i.e. Chemical Exchange Spin-Lock. Recently Spin-Lock sequences have been proposed as alternative and more sensitive approach for the detection of fast exchanging protons, like the hydroxyls in glucose. The technique relies on the measurement of $T_{1\rho}$ (the spin-lattice relaxation time in the rotating frame) which as in CEST, ultimately depends on the concentration of exchangeable pool.

Using an on-resonance spin-lock technique (spin-lock at the water Larmor's frequency) Jin et al. measured a linear glucoCESL response to the glucose dose in the rat brain. Similar to what was reported in the study by Nasrallah et al.[30] the signal measured following administration of 2DG was more intense (~2.2 times) and prolonged in time than with natural glucose, which is consistent with the different metabolic characteristics previously discussed.

Compared to glucoCEST technique, advantages of on-resonance glucoCESL include: a) enhanced detection sensitivity for fast exchange regimes ($\kappa/\delta > 1$), which has been numerically demonstrated using two-pool model Bloch McConnell equations,[32] b) high temporal resolution, as the duration of the spin-locking irradiation is shorter (on the order of $T_{1\rho}$ as opposed to T_1 in CEST), and c) inherent robustness for B0 inhomogeneities with no asymmetry analysis required.

Importantly, the sensitivity enhancement of glucoCESL is expected to be higher at low B0 field as the ratio between the exchange rate and the chemical shift (κ/δ) is increased due to the smaller chemical shift. This makes on-resonance spin-lock particularly interesting for clinical systems.

$T_{1\rho}$ is modulated by all the simultaneously occurring chemical exchange processes, and therefore the signal measured with on-resonance spin-lock lacks specificity to any particular type of labile proton. While *in vivo* studies have shown $T_{1\rho}$ to be fairly insensitive to vascular oxygenation,[33] changes in vascular volume and

*L-glucose is the enantiomer (L-isomer) of the naturally occurring D-glucose. In vitro, it displays the same CEST signature as D-glucose. In vivo however, the Levo chirality prevents it from binding to the GLUT transporter (nor it servers as substrate for glycolytic enzymes) and therefore its permeability across the BBB is limited.[31]

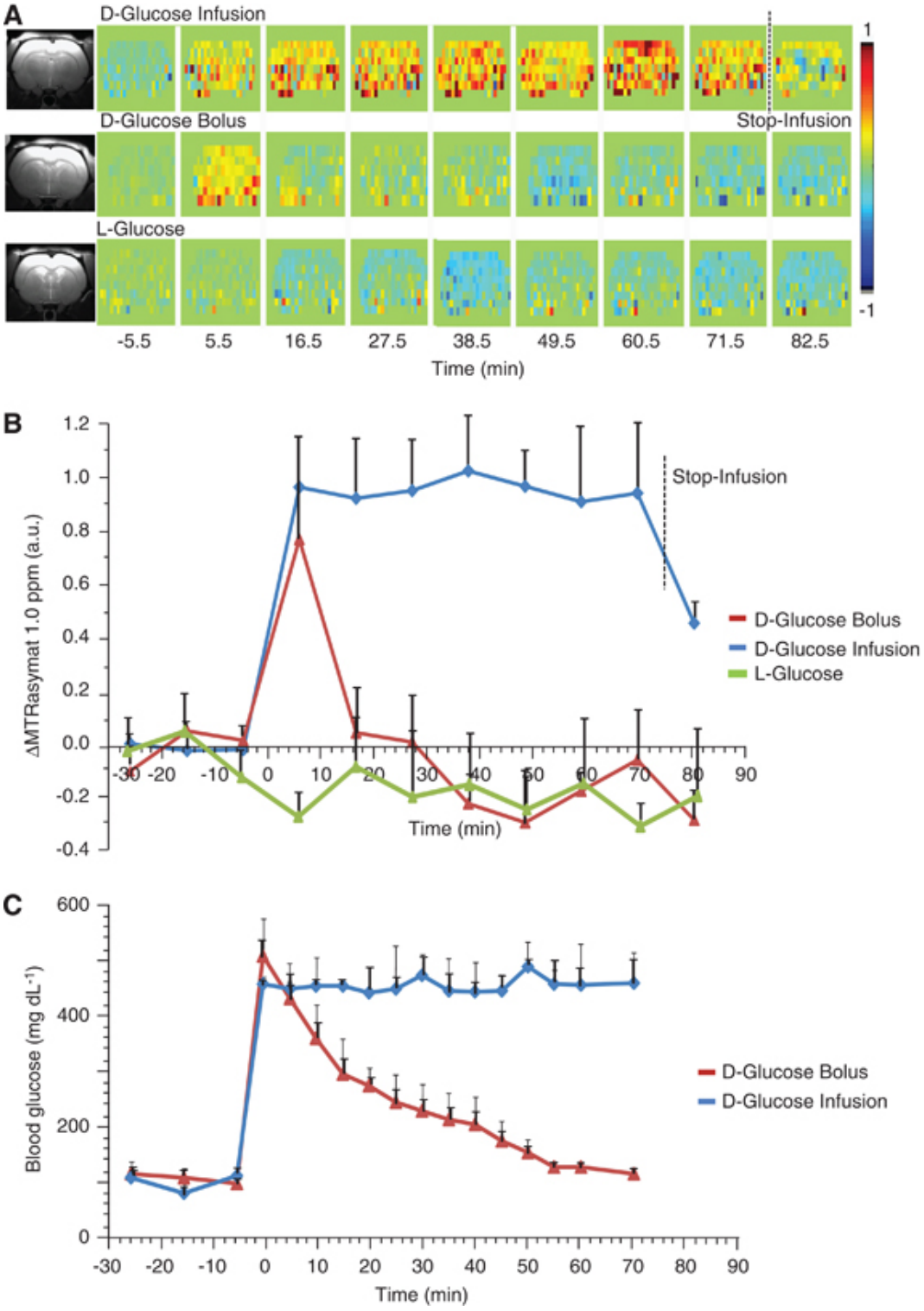

Figure 2.4.6.: *A) Time series of glucoCEST images of rat brain under constant infusion of D-glucose (top), after bolus injection of 1 g/kg D-glucose (middle), and after bolus injection of 1 g/kg L-glucose (bottom). The image intensity represents relative glucoCEST signal change from the baseline. (B) Time courses of glucoCEST signal under the above three injection conditions in (A). The signal represents the difference of MTR_{asym} integral around 1.0 p.p.m. from the baseline signal. (C) Arterial blood glucose with constant infusion (blue) and bolus injection (red) of D-glucose. Figure reproduced from Nasrallah et al.*[30]

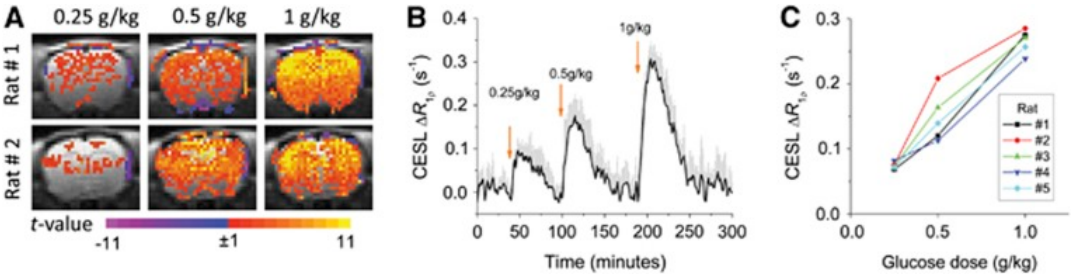

Figure 2.4.7.: *Rat-brain glucoCESL studies at 9.4T showing near-linear contrast for intravenously administered D-glucose (Glc) doses of 0.25, 0.5, and 1.0g/kg, and robust detection for doses 0.25g/kg (in vivo paradigm 1). (A) The t-maps for each dose for two of the animals show highest t-values in the cortex where surface coil sensitivity is higher. Colour scale: t-value. (B) Average of time courses for all animals (n=5, mean±s.e.m.) clearly shows the increase in brain Δ $R1\rho$ with Glc dose. Arrows indicate time of injection. (C) The nearly linear dependence of peak brain Δ $R1\rho$ on Glc dose appears for each individual animal. CESL, chemical exchange-sensitive spin lock. Figure reproduced from Jin et al.*[32]

CBF are known to cause variations in $T_{1\rho}$.[34,35] Therefore, in glucoCESL measurements of the contribution of glucose (and its derivatives) has to be carefully weighted against possible changes in tissue vasculature.

Although no journal publications have been documented exploring the possibilities of glucoCEST for the study of brain tumors, studies from the research groups at Johns Hopkins University and University College London have already been presented in various scientific conferences.

These ongoing studies aim to provide insight into relevant metabolic aspects of brain tumours as well as exploring the possibility of using natural glucose for the detection, characterisation of tumour aggressiveness and even for the monitoring of therapy based on their glucoCEST response.

As seen in this review CEST and CESL have been shown to be promising MRI techniques to investigate glucose uptake and metabolism in vivo, yet a more conventional method has recently been proposed as a measure of glucose concentration. Acknowledging the effect that chemical exchange processes have in the relaxation times of water, Yadav et al.[36] from Johns Hopkins University reported the *in vivo* detection of changes in glucose concentration by measuring the spin-spin relaxation constant T_2.

Using standard T_2-weighted images, researchers demonstrated the generation of contrast in mouse kidneys arising at the time of a glucose infusion (a bolus of 0.15 mL of 0.5 M glucose solution). The contrast in the kidneys lasted just over a minute, after which it returned to initial levels, within 2 minutes after the infusion.

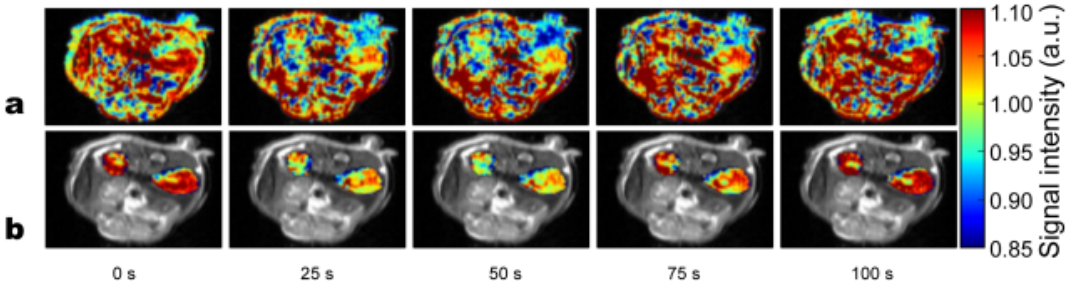

Figure 2.4.8.: *Transverse relaxation data from a dynamic in vivo glucose infusion experiment on a mouse. T_2 weighted images of mouse kidneys from the time of a glucose bolus infusion are displayed (time indicated below each image). a: Effects in all regions displayed. b: Only kidney signal displayed in colour on grayscale image to highlight effects. After infusion, the signal in the kidneys drops by approximately 10% and then recovers over the course of 50-100 s. Figure reproduced from Yadav et al.*[36]

Two of the greatest advantages of this technique is its simplicity (T2 relaxometry sequences are readily available on all the standard MRI systems) and the high temporal resolution, which allows for statistical averaging of the signal in order to boost the effective sensitivity.

However, $T_{1\rho}$ and T_2 based methods become less sensitive in tissues with high intrinsic R_{20} (exchange independent spin-spin relaxation constant). In practice, this might become a sensitivity limiting factor as very accurate measurements of the respective relaxation times are required. See Section 4.6 for a more thorough discussion on the subject.

2.5. glucoCEST: good practices

2.5.1. Drift of the main magnetic field B0

Correction for potential shifts of the water resonant frequency (B0 drifts) over the course of the experiments are essential for reliable asymmetry analysis and meaningful subtractions of the initial baseline image. Therefore special attention has to be given to making sure every CEST image acquired during the experiment can be adequately corrected. This can be done using different methods:

In a preclinical set-up, high field strengths produce sharp Z-spectra. Moreover, less stringent time constraints in animal studies allows for a denser packing of the off-resonant frequencies in the Z-spectrum. In this situation, correction of B0 inhomogeneities can be successfully achieved by simply interpolating the experimental

Z-spectra (typically with a non-parametric algorithm, such as smoothing spline or cubic interpolating spline) and repositioning the water frequency to the position of the minimum intensity (where water is fully saturated). By doing so in a pixel basis a map of the B0 shift is obtained which tells how much each pixel needs to be shifted (in the frequency dimension) before proceeding with the asymmetry analysis.

Alternatively, one can obtain B0 maps parallel to the CEST acquisitions (using the WASRR[37] method or by a standard double TE technique) from which to correct for B0 irregularities in the image slab.

This last approach is predominant in clinical systems where due to lower field and shorter scan times, the Z-Spectra tend to be less defined around the water peak.

If the chosen method for B0 correction is to acquire an independent B0 map, multiple instances of it should be run in order to track the evolution of B0 in time.

2.5.2. Timing of symmetrical offsets

It is important to avoid time delays between off-set frequencies downfield and upfield from water. During the relatively long acquisition time of a full Z-spectrum dataset, perceptible changes in the tissue glucose concentrations and drifts in field homogeneity may occur. A good practise to minimise the impact of these variations in the asymmetry analysis is to sample the offset frequencies in an alternating pattern, swapping from downfield to upfield frequencies centred at the water resonance. In this way symmetrical offset data-points are acquired with the minimum time gap between them.

2.5.3. Selection of the appropriate B1 and integration range

Choosing the appropriate saturation parameters that maximise the CEST signal is not a trivial matter. Generally, fast exchanging hydrogens (as in glucose) are expected to produce higher CEST contrast when saturated with elevated RF power, whereas slower exchanging molecules (like amide groups) need less power. However, the signal to noise ratio is also affected at high B1 levels. Intense spillover effect widens the Lorentzian absorption profile reducing the observable signal and resulting in lower SNR close to water (see section 3.11 in Chapter 3).

Moreover, strong spillover effects shift the MTR asymmetry profile away from water (see 3.12.1). Hence, the optimum range of offset frequencies that contain the CEST information also depends on the applied saturation power. Precise op-

timisation of the saturation power will depend on the characteristics of the tissue inspected.

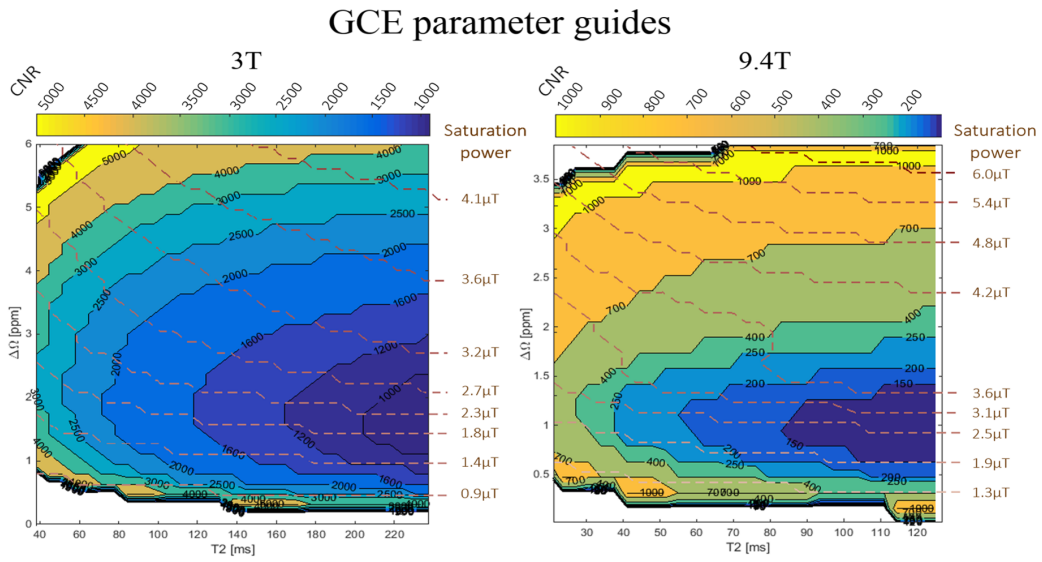

Figure 2.5.1.: *Optimum combination of parameters (ΔΩ, B1) for a range of T2 values, which results in the maximum sensitivity of glucoCEST at 3T (left) and 9.4T (right). For a given set of coordinates, the colour-map represents the required CNR (measured as the MTRasym/SEM) in order to differentiate an increase of 10 mMolar glucose concentration with 95% confidence interval.*

Here a guide for the selection of parameters (ΔΩ,B1) that maximise the sensitivity of glucoCEST in tumours is presented. The results are based on a theoretical glucoCEST experiment (simulated with the code introduced in Chapter 3), in which glucose concentration was increased from 5 mMolar baseline to 15 mMolar. The model parameters were previously fitted to *in vivo* and phantom data (see figures 3.6.1 and 3.7.1 in Chapter 3).

Normally distributed raw noise was introduced in the simulations from which the mean glucoCEST signal (GCE) and its standard error (SE) were estimated for a range of parameter values relevant to tumour physiology. Based on the combination of parameter values which maximise GCE/SE, maps of the highest glucoCEST sensitivity were defined for 3T and 9.4T field strengths. From these maps the required contrast to noise ratio (CNR) for differentiation (CI=95%) of 10 mMolar glucose increase was calculated.

Transverse relaxation of water, B1 saturation power and integration range were found to alter particularly the measured GCE signal and therefore variations of these 3 variables were explored. Tissue pH has also a substantial impact on the GCE out-

come (by changing the exchange rate) however pH was kept constant in the simulations (at pH=7.1). This is probably an acceptable assumption provided a relatively stable intracellular values across tumours[38] and the fact that the intracellular space accounts for ∼80% of the voxel volume.[39]

These maps should be taken as indicative values from where to start optimising a protocol. For example, if we were to try a glucoCEST sequence on a tumour with T2 of 160 ms at 3 Tesla, and we were using an equivalent B1 saturation power of 2.7μT, then the map tells us that we should be looking around the 2.5 ppm range in order to obtain best CEST sensitivity. It also estimates that we would need around 1500 CNR units to detect an increase of 10 mMolar glucose in the tissue (with 95% CI). These estimations match well with the experimental data performed on phantoms. Figure 2.5.2 shows maximum MTR asymmetry around 2.4 ppm for at B1 power of $2.3\mu T$. (Sample T2=95±7ms and pH=7.1±0.1).

These values can help in designing the imaging protocol (i.e. voxel size, number of averages) in order to meet the estimated requirements.

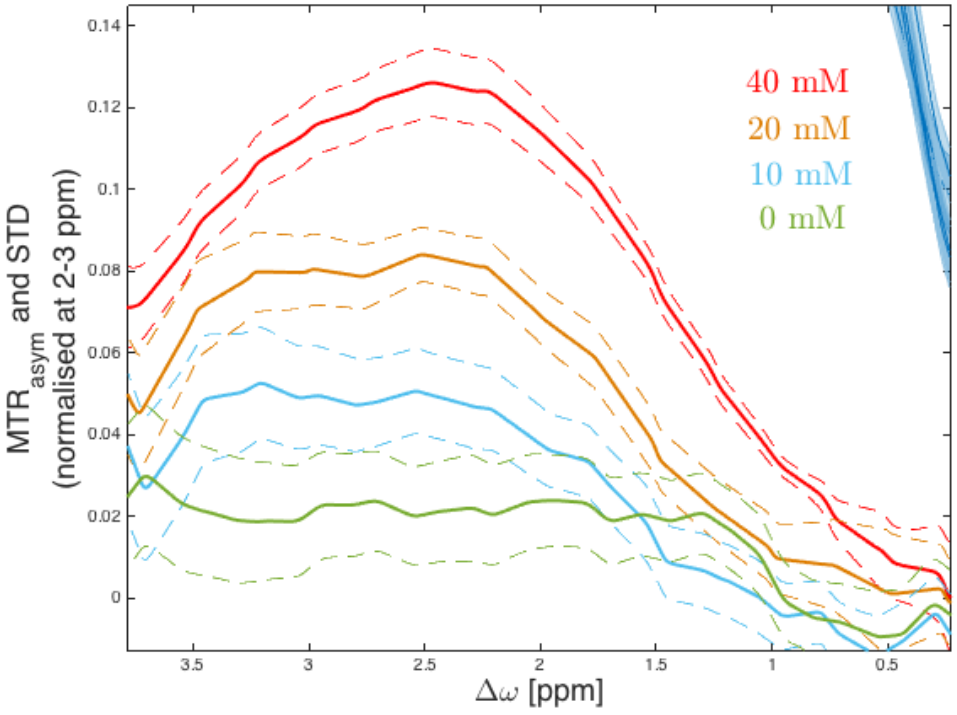

Figure 2.5.2.: *Phantom experiment (0, 10, 20 and 40 mM glucose solutions in 3%Agar and 0.07mM Gd providing tissue like T1 and T2 at pH 7.1) showing maximum MTR asymmetry at* $\Delta\omega \approx 2.4ppm$ *with* $B1 = 2.3\mu T$ *in 3T Philips Achieva system. The results match the simulated data shown in figure 2.5.1*

.

2.6. glucoCEST: open questions

The work presented by our team[6] is tangible proof of the use of glucoCEST for the study of cancer *in vivo*. The study showed both glucoCEST and ^{18}F-FDG autoradiography imaging methods to offer equivalent information.

Figure 2.6.1.: *Comparison of glucoCEST with ^{18}F-FDG*

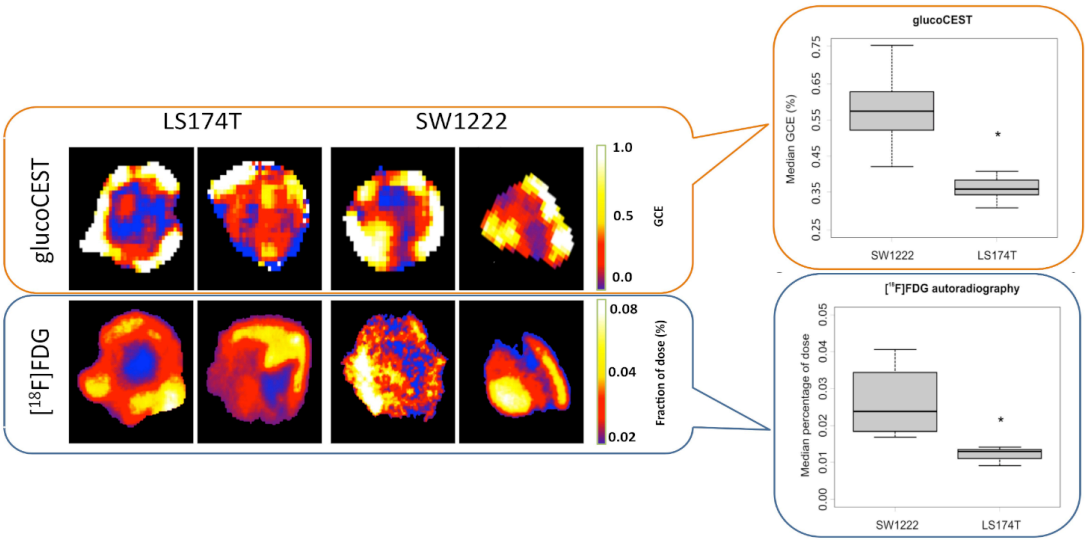

Left: glucoCEST and ^{18}F-FDG autoradiography provide equivalent information on areas of tumour activity for both type of tumours. Right: The more aggressive phenotype of the SW1222 model is distinguishable using either of the methods ($p<0.05$).

Aside from the physical principles of both imaging modalities, there is an important difference between the glucoCEST and PET methods which lies in the marker-molecule used. While ^{18}F-FDG (used in PET) is an analogue of glucose that cannot be metabolised, glucoCEST uses naturally occurring sugar that is free to go through all the steps of the metabolic chain. Hence glucose absorbed by the cells does not necessarily build up, as is the case for ^{18}F-FDG. This fundamental metabolic difference raises the question of whether the glucoCEST signal originates from sugars inside or outside the cells. Part of this work focused on the investigation of possible sources for the observed glucoCEST signal.

To date, there is no consensus among researchers on whether the glucoCEST signal originates from glucose only, or if other sugars along glycolytic pathway contribute to it as well. If glucoCEST was only sensitive to glucose, it is reasonable to think it would predominately reflect on the blood perfusion in the tissues. On the other hand, an intracellular origin of glucoCEST could open an exciting possibility to study the kinetics of cancer metabolism with MRI.

To shed some light on this topic, phantom experiments were performed aiming

to examine the CEST signal response of the first four molecules in the glycolytic pathway, at conditions similar to the expected ones *in vivo*. The content of this work is presented in Chapter 4.

Chapter references

[1] R. Douglas Fields and Geoffrey Burnstock. “Purinergic signalling in neuron–glia interactions”. In: *Nature reviews. Neuroscience* 7.6 (June 2006), pp. 423–436. ISSN: 1471-003X. DOI: 10.1038/nrn1928. pmid: 16715052 (cit. on p. 49).

[2] Matthew G. Vander Heiden, Lewis C. Cantley, and Craig B. Thompson. “Understanding the Warburg Effect: The Metabolic Requirements of Cell Proliferation”. In: *Science* 324.5930 (May 22, 2009). 03299, pp. 1029–1033. ISSN: 0036-8075, 1095-9203. DOI: 10.1126/science.1160809. pmid: 19460998 (cit. on pp. 49, 52).

[3] Sophia Y. Lunt and Matthew G. Vander Heiden. “Aerobic Glycolysis: Meeting the Metabolic Requirements of Cell Proliferation”. In: *Annual Review of Cell and Developmental Biology* 27.1 (Nov. 10, 2011). 00378, pp. 441–464. ISSN: 1081-0706, 1530-8995. DOI: 10.1146/annurev-cellbio-092910-154237 (cit. on pp. 49, 51, 52).

[4] D. Hanahan and R. A. Weinberg. “The hallmarks of cancer”. In: *Cell* 100.1 (Jan. 7, 2000), pp. 57–70. ISSN: 0092-8674. pmid: 10647931 (cit. on pp. 49, 50).

[5] Douglas Hanahan and Robert A. Weinberg. “Hallmarks of cancer: the next generation”. In: *Cell* 144.5 (Mar. 4, 2011). 12022, pp. 646–674. ISSN: 1097-4172. DOI: 10.1016/j.cell.2011.02.013. pmid: 21376230 (cit. on pp. 49, 50).

[6] Simon Walker-Samuel, Rajiv Ramasawmy, Francisco Torrealdea, Marilena Rega, Vineeth Rajkumar, S. Peter Johnson, Simon Richardson, Miguel Gonçalves, Harold G. Parkes, Erik Arstad, David L. Thomas, R. Barbara Pedley, Mark F. Lythgoe, and Xavier Golay. “In vivo imaging of glucose uptake and metabolism in tumors”. In: *Nature Medicine* 19.8 (Aug. 2013). 00044 Cited by 0001, pp. 1067–1072. ISSN: 1078-8956. DOI: 10.1038/nm.3252 (cit. on pp. 49, 58, 60–62, 73).

[7] Yuri Lazebnik. “What are the hallmarks of cancer?” In: *Nature Reviews Cancer* 10.4 (Apr. 2010), pp. 232–233. ISSN: 1474-175X. DOI: 10.1038/nrc2827 (cit. on p. 50).

[8] R. J. Gillies, I. Robey, and R. A. Gatenby. “Causes and Consequences of Increased Glucose Metabolism of Cancers”. In: *Journal of Nuclear Medicine* 49 (Suppl_2 June 1, 2008). 00328, 24S–42S. ISSN: 0161-5505. DOI: 10.2967/jnumed.107.047258 (cit. on pp. 51, 53).

[9] Robert A. Gatenby and Robert J. Gillies. “Why do cancers have high aerobic glycolysis?” In: *Nature Reviews Cancer* 4.11 (Nov. 2004), pp. 891–899. ISSN: 1474-175X, 1474-1768. DOI: 10.1038/nrc1478 (cit. on p. 51).

[10] Otto Warburg. “On the Origin of Cancer Cells”. In: *Science* 123.3191 (Feb. 24, 1956). 05638, pp. 309–314. ISSN: 0036-8075, 1095-9203. DOI: 10.1126/science.123.3191.309. pmid: 13298683 (cit. on p. 51).

[11] Vadivel Ganapathy, Muthusamy Thangaraju, and Puttur D. Prasad. "Nutrient transporters in cancer: Relevance to Warburg hypothesis and beyond". In: *Pharmacology & Therapeutics* 121.1 (Jan. 2009). 00313, pp. 29–40. ISSN: 01637258. DOI: 10.1016/j.pharmthera.2008.09.005 (cit. on p. 51).

[12] Mario Gosalvez. "Mitochondrial filamentation: a therapeutic target for neurodegeneration and aging". In: *American Journal of Alzheimer's Disease and Other Dementias* 28.5 (Aug. 2013). 00004, pp. 423–426. ISSN: 1938-2731. DOI: 10.1177/1533317513494451. pmid: 23925265 (cit. on p. 51).

[13] D. M. Prescott, H. C. Charles, J. M. Poulson, R. L. Page, D. E. Thrall, Z. Vujaskovic, and M. W. Dewhirst. "The relationship between intracellular and extracellular pH in spontaneous canine tumors". In: *Clinical Cancer Research: An Official Journal of the American Association for Cancer Research* 6.6 (June 2000), pp. 2501–2505. ISSN: 1078-0432. pmid: 10873105 (cit. on p. 52).

[14] Ian F. Robey and Lance A. Nesbit. "Investigating Mechanisms of Alkalinization for Reducing Primary Breast Tumor Invasion". In: *BioMed Research International* 2013 (2013), pp. 1–10. ISSN: 2314-6133, 2314-6141. DOI: 10.1155/2013/485196 (cit. on p. 52).

[15] I. F. Robey, B. K. Baggett, N. D. Kirkpatrick, D. J. Roe, J. Dosescu, B. F. Sloane, A. I. Hashim, D. L. Morse, N. Raghunand, R. A. Gatenby, and R. J. Gillies. "Bicarbonate Increases Tumor pH and Inhibits Spontaneous Metastases". In: *Cancer Research* 69.6 (Mar. 15, 2009), pp. 2260–2268. ISSN: 0008-5472, 1538-7445. DOI: 10.1158/0008-5472.CAN-07-5575 (cit. on pp. 52, 53).

[16] O. H. Warburg. "New Methods of Cell Physiology. Applied to cancer, photosynthesis, and mechanism of x-ray action." In: *Science* 137.3523 (June 7, 1962), pp. 30–31. ISSN: 0036-8075, 1095-9203. DOI: 10.1126/science.137.3523.30 (cit. on p. 52).

[17] Tien-Jen Lin, Chi-Chang Huang, I.-Jen Wang, Jia-Wei Lin, Kuo-Sheng Hung, Ling Fan, Hsin-Hsin Tsao, Ning-Sun Yang, and Kun-Ju Lin. "Validation of an animal FDG PET imaging system for study of glioblastoma xenografted mouse and rat models". In: *Ann Nucl Med Sci* 23 (2010). 00002, pp. 77–83 (cit. on p. 52).

[18] Takashi Nihashi, Issa J. Dahabreh, and Teruhiko Terasawa. "PET in the Clinical Management of Glioma: Evidence Map". In: *American Journal of Roentgenology* 200.6 (June 2013), W654–W660. ISSN: 0361-803X, 1546-3141. DOI: 10.2214/AJR.12.9168 (cit. on p. 52).

[19] Christopher C. Riedl, Elina Slobod, Maxine Jochelson, Monica Morrow, Debra A. Goldman, Mithat Gonen, Wolfgang A. Weber, and Gary A. Ulaner. "Retrospective analysis of 18F-FDG PET/CT for staging asymptomatic breast cancer patients younger than 40 years". In: *Journal of Nuclear Medicine: Official Publication, Society of Nuclear Medicine* 55.10 (Oct. 2014). 00004, pp. 1578–1583. ISSN: 1535-5667. DOI: 10.2967/jnumed.114.143297. pmid: 25214641 (cit. on p. 52).

[20] B. Gulyas and C. Halldin. "New PET radiopharmaceuticals beyond FDG for brain tumor imaging". In: *The quarterly journal of nuclear medicine and molecular imaging: official publication of the Italian Association of Nuclear Medicine (AIMN) [and] the International Association of Radiopharmacology (IAR), [and] Section of the Society of Radiopharmaceu-*

tical Chemistry and Biology 56.2 (Apr. 2012). 00049, pp. 173–190. ISSN: 1824-4785. pmid: 22617239 (cit. on p. 52).

[21] P. L. Pedersen. "Tumor mitochondria and the bioenergetics of cancer cells". In: *Progress in Experimental Tumor Research* 22 (1978). 00724, pp. 190–274. ISSN: 0079-6263. pmid: 149996 (cit. on p. 53).

[22] Alfonso Di Costanzo, Tommaso Scarabino, Francesca Trojsi, Teresa Popolizio, Domenico Catapano, Giuseppe M. Giannatempo, Simona Bonavita, Maurizio Portaluri, Michela Tosetti, Vincenzo A. d'Angelo, Ugo Salvolini, and Gioacchino Tedeschi. "Proton MR spectroscopy of cerebral gliomas at 3 T: spatial heterogeneity, and tumour grade and extent". In: *European Radiology* 18.8 (Aug. 2008), pp. 1727–1735. ISSN: 0938-7994. DOI: 10.1007/s00330-008-0938-5. pmid: 18389246 (cit. on p. 53).

[23] P. C. M. van Zijl, C. K. Jones, J. Ren, C. R. Malloy, and A. D. Sherry. "MRI detection of glycogen in vivo by using chemical exchange saturation transfer imaging (glycoCEST)". In: *Proceedings of the National Academy of Sciences* 104.11 (Mar. 13, 2007). 00159, pp. 4359–4364. ISSN: 0027-8424, 1091-6490. DOI: 10.1073/pnas.0700281104 (cit. on pp. 56, 57).

[24] Timothy H. Witney, Laurence Carroll, Israt S. Alam, Anil Chandrashekran, Quang-Dé Nguyen, Roberta Sala, Robert Harris, Ralph J. DeBerardinis, Roshan Agarwal, and Eric O. Aboagye. "A Novel Radiotracer to Image Glycogen Metabolism in Tumors by Positron Emission Tomography". In: *Cancer Research* 74.5 (Jan. 3, 2014). 00008, pp. 1319–1328. ISSN: 0008-5472, 1538-7445. DOI: 10.1158/0008-5472.CAN-13-2768. pmid: 24590807 (cit. on p. 58).

[25] Kannie W. Y. Chan, Michael T. McMahon, Yoshinori Kato, Guanshu Liu, Jeff W. M. Bulte, Zaver M. Bhujwalla, Dmitri Artemov, and Peter C. M. van Zijl. "Natural D-glucose as a biodegradable MRI contrast agent for detecting cancer". In: *Magnetic Resonance in Medicine* 68.6 (2012). Cited by 0012, pp. 1764–1773. ISSN: 1522-2594. DOI: 10.1002/mrm.24520 (cit. on pp. 58, 59).

[26] Michal Rivlin, Judith Horev, Ilan Tsarfaty, and Gil Navon. "Molecular imaging of tumors and metastases using chemical exchange saturation transfer (CEST) MRI". In: *Scientific Reports* 3 (Oct. 25, 2013). DOI: 10.1038/srep03045 (cit. on pp. 58, 63).

[27] George C. Newman, Frank E. Hospod, Behzad Maghsoudlou, and Clifford S. Patlak. "Simplified Brain Slice Glucose Utilization". In: *Journal of Cerebral Blood Flow & Metabolism* 16.5 (Sept. 1996). 00006, pp. 864–880. ISSN: 0271-678X. DOI: 10.1097/00004647-199609000-00011 (cit. on p. 61).

[28] George C. Newman, Frank E. Hospod, and Clifford S. Patlak. "Kinetic Model of 2-Deoxyglucose Metabolism Using Brain Slices". In: *Journal of Cerebral Blood Flow & Metabolism* 10.4 (July 1990), pp. 510–526. ISSN: 0271-678X. DOI: 10.1038/jcbfm.1990.93 (cit. on p. 61).

[29] Michal Rivlin, Ilan Tsarfaty, and Gil Navon. "Functional molecular imaging of tumors by chemical exchange saturation transfer MRI of 3-O-Methyl-D-glucose". In: *Magnetic Resonance in Medicine* 72.5 (Nov. 1, 2014), pp. 1375–1380. ISSN: 1522-2594. DOI: 10.1002/mrm.25467 (cit. on pp. 63, 64).

[30] Fatima A. Nasrallah, Guilhem Pagès, Philip W. Kuchel, Xavier Golay, and Kai-Hsiang Chuang. "Imaging brain deoxyglucose uptake and metabolism by glucoCEST MRI". In: *Journal of Cerebral Blood Flow & Metabolism* 33.8 (Aug. 2013). 00015 Cited by 0000, pp. 1270–1278. ISSN: 0271-678X. DOI: 10.1038/jcbfm.2013.79 (cit. on pp. 63, 65, 66).

[31] Alessandro Silvani, Valentina Asti, Chiara Berteotti, Tijana Bojic, Tullia Cianci, Vera Ferrari, Carlo Franzini, Pierluigi Lenzi, and Giovanna Zoccoli. "Sleep-related brain activation does not increase the permeability of the blood–brain barrier to glucose". In: *Journal of Cerebral Blood Flow & Metabolism* 25.8 (Mar. 9, 2005), pp. 990–997. ISSN: 0271-678X. DOI: 10.1038/sj.jcbfm.9600100 (cit. on p. 65).

[32] Tao Jin, Hunter Mehrens, Kristy S. Hendrich, and Seong-Gi Kim. "Mapping brain glucose uptake with chemical exchange-sensitive spin-lock magnetic resonance imaging". In: *Journal of Cerebral Blood Flow and Metabolism: Official Journal of the International Society of Cerebral Blood Flow and Metabolism* 34.8 (Aug. 2014), pp. 1402–1410. ISSN: 1559-7016. DOI: 10.1038/jcbfm.2014.97. pmid: 24865996 (cit. on pp. 65, 67).

[33] Vincent A. Magnotta, Hye-Young Heo, Brian J. Dlouhy, Nader S. Dahdaleh, Robin L. Follmer, Daniel R. Thedens, Michael J. Welsh, and John A. Wemmie. "Detecting activity-evoked pH changes in human brain". In: *Proceedings of the National Academy of Sciences* 109.21 (May 22, 2012). 00043, pp. 8270–8273. ISSN: 0027-8424, 1091-6490. DOI: 10.1073/pnas.1205902109. pmid: 22566645 (cit. on p. 65).

[34] Tao Jin, Ping Wang, Xiaopeng Zong, and Seong-Gi Kim. "MR imaging of the amide-proton transfer effect and the pH-insensitive nuclear overhauser effect at 9.4 T". In: *Magnetic Resonance in Medicine* 69.3 (Mar. 1, 2013). 00042, pp. 760–770. ISSN: 07403194. DOI: 10.1002/mrm.24315 (cit. on p. 67).

[35] Justin Hulvershorn, Arijitt Borthakur, Luke Bloy, Eugene E. Gualtieri, Ravinder Reddy, John S. Leigh, and Mark A. Elliott. "T1ρ Contrast in Functional Magnetic Resonance Imaging". In: *Magnetic resonance in medicine : official journal of the Society of Magnetic Resonance in Medicine / Society of Magnetic Resonance in Medicine* 54.5 (Nov. 2005). 00018, pp. 1155–1162. ISSN: 0740-3194. DOI: 10.1002/mrm.20698. pmid: 16217783 (cit. on p. 67).

[36] Nirbhay N. Yadav, Jiadi Xu, Amnon Bar-Shir, Qin Qin, Kannie W.Y. Chan, Ksenija Grgac, Wenbo Li, Michael T. McMahon, and Peter C.M. van Zijl. "Natural D-glucose as a biodegradable MRI relaxation agent: Glucose as an MRI Relaxation Agent". In: *Magnetic Resonance in Medicine* 72.3 (Sept. 2014), pp. 823–828. ISSN: 07403194. DOI: 10.1002/mrm.25329 (cit. on pp. 67, 68).

[37] Mina Kim, Joseph Gillen, Bennett A. Landman, Jinyuan Zhou, and Peter C. M. van Zijl. "Water saturation shift referencing (WASSR) for chemical exchange saturation transfer (CEST) experiments". In: *Magnetic Resonance in Medicine: Official Journal of the Society of Magnetic Resonance in Medicine / Society of Magnetic Resonance in Medicine* 61.6 (June 2009). 00138, pp. 1441–1450. ISSN: 1522-2594. DOI: 10.1002/mrm.21873. pmid: 19358232 (cit. on p. 69).

[38] Karim Snoussi, Jeff W.M. Bulte, Maurice Gueron, and Peter C.M. van Zijl. “Sensitive CEST agents based on nucleic acid imino proton exchange: Detection of poly(rU) and of a dendrimer-poly(rU) model for nucleic acid delivery and pharmacology”. In: *Magnetic Resonance in Medicine* 49.6 (June 2003), pp. 998–1005. ISSN: 0740-3194, 1522-2594. DOI: 10.1002/mrm.10463 (cit. on p. 71).

[39] E. Panagiotaki, S. Walker-Samuel, B. Siow, S. P. Johnson, V. Rajkumar, R. B. Pedley, M. F. Lythgoe, and D. C. Alexander. “Noninvasive Quantification of Solid Tumor Microstructure Using VERDICT MRI”. In: *Cancer Research* 74.7 (Apr. 1, 2014). 00008, pp. 1902–1912. ISSN: 0008-5472, 1538-7445. DOI: 10.1158/0008-5472.CAN-13-2511 (cit. on p. 71).

3. Computer model based optimisation of CEST-MRI

3.1. Abstract

In this chapter the mathematical description of the CEST mechanism is laid out which allows the construction of complex chemical exchange models. Using these models the outcomes of different hypothetical CEST experiments will be explored in search of the optimum combination of parameters to enhance the CEST contrast.

Computer simulations can provide an intuitive understanding of the CEST signal expected under certain situations by providing compelling visual feedback of relevant parameters evolving under complex dynamical processes in a way that is easy to familiarise with. As well as their instructive value, these mathematical models also provide an excellent tool for the optimisation of experimental parameters and the design of CEST sequences for different applications. In this context, the final design of a CEST protocol is the result of an iterative feedback between the experimental tests and the computer modelled based optimisations. Pulse sequence parameters such as the needed RF power or the optimum saturation time can be approximated using simulations. Moreover, effects due to tissue specific characteristics like the pH, macro-molecule content or different relaxation times can also be incorporated in the models and reasonable estimates about the outcome obtained for a number of experimental situations.

All the simulations shown in this chapter are based on multi-pool exchange models constructed with the concepts described below. As part of the work in this thesis the completed models used are provided in Matlab code form, which can be found in the appendices E and F.

3.2. Mathematical description of CEST:

Consider a frame of reference rotating at frequency ω_{RF} around the z axis. Assuming a static magnetic field B_0 acting along the z direction and a constant RF pulse applied in the x direction of the rotating frame, the Bloch equations of a set of spins can be written as:

$$\begin{aligned}
\frac{dM_x(t)}{dt} &= \Delta\omega M_y(t) - R_2 M_x(t) \\
\frac{dM_y(t)}{dt} &= -\Delta\omega M_x(t) - R_2 M_y + \omega_1 M_z(t) \\
\frac{dM_z(t)}{dt} &= -\omega_1 M_y(t) - R_1 (M_z(t) - M_0)
\end{aligned} \tag{3.2.1}$$

Where $\omega_1 = \gamma B_1$ represents the rotation speed of **M**(t) around the y axis due to the RF irradiation, $\Delta\omega = \omega_{RF} - \omega_0$ is the offset frequency of the RF pulse with respect to the Larmor frequency ω_0 and $R1 = 1/T1$ and $R2 = 1/T2$ denote the inverse of the longitudinal and transverse relaxation rates, respectively. Please refer to Appendix A for the derivation of the Bloch equations.

In matrix form these equations can be rewritten as:

$$\frac{d\mathbf{M}}{dt} = \mathbf{A} \cdot \mathbf{M} + \mathbf{B} \tag{3.2.2}$$

With $\mathbf{M} = [M_x(t), M_y(t), M_z(t)]^T$; $\mathbf{B} = (0,\ 0,\ R_1 M_0)^T$ where ^{T} denotes the transposed matrix, and

$$\mathbf{A} = \begin{pmatrix} -R_2 & \Delta\omega & 0 \\ -\Delta\omega & -R_2 & \omega_1 \\ 0 & -\omega_1 & -R_1 \end{pmatrix} \tag{3.2.3}$$

Another pool of spins, resonating at a slightly different frequency $\omega_0^c = S\gamma B_0$ due to a chemical shift S, would be described in a similar way as:

$$\frac{d\mathbf{M^c}}{dt} = \mathbf{A^c} \cdot \mathbf{M^c} \tag{3.2.4}$$

In this case, the matrix components $M_x^c(t)$, $M_y^c(t)$, $M_z^c(t)$, R_2^c, R_1^c, M_0^c and $\Delta\omega^c = \omega_{RF} - \omega_0^c$ refer to the properties of the second pool c.

In order to model the chemical exchange process, another relationship is imposed between the two pools.

$$Exchange \begin{cases} \frac{d\mathbf{M}^a}{dt} = k_c\mathbf{M}^c - k_a\mathbf{M}^a \\ \frac{d\mathbf{M}^c}{dt} = k_a\mathbf{M}^a - k_c\mathbf{M}^c \end{cases} \tag{3.2.5}$$

These relationships describe the influence of the exchange process on the magnetisation vector of each pool. Here k_c represents the exchange rate from pool c to pool a, and k_a the rate from pool a to pool c. As substrate concentrations do not change in time, these exchange rates are restricted to the mass balance between the two pools, which imposes that $k_a M_0^a = k_c M_0^c$.

Therefore, the full dynamics of each pool including the exchange process can be expressed as:

$$\frac{d\mathbf{M}^a}{dt} = \mathbf{A}^a \cdot \mathbf{M}^a + \mathbf{B}^a + k_c\mathbf{M}^c - k_a\mathbf{M}^a$$

$$\frac{d\mathbf{M}^c}{dt} = \mathbf{A}^c \cdot \mathbf{M}^c + \mathbf{B}^c + k_a\mathbf{M}^a - k_c\mathbf{M}^c \tag{3.2.6}$$

This system of differential equations, which are essentially two independent Bloch equations coupled by the exchange mechanism, is termed the Bloch-McConnell equation, and represents the most widely used mathematical description of exchange processes in the NMR field, including CEST.[1,2,3,4,5]

Figure 3.2.1.: *Exchange diagram*

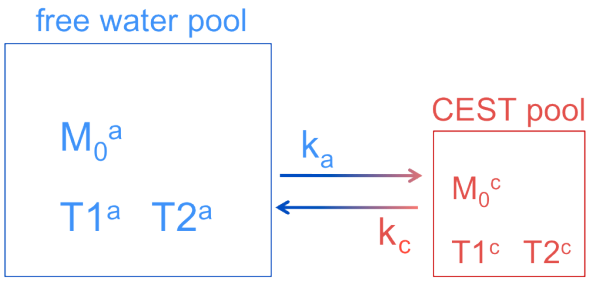

For the purpose of solving this system, it is useful to synthesize the expression to its matrix form, which can be written with the same structure as before:

$$\frac{d\mathbf{M}}{dt} = \mathbf{A} \cdot \mathbf{M} + \mathbf{B} \tag{3.2.7}$$

where now, **M**, **A** and **B** include the Cartesian components of both pools:

$$\mathbf{M} = [M_x^a(t), M_x^c(t), M_y^a(t), M_y^c(t), M_z^a(t), M_z^c(t)]^T$$

$$\mathbf{B} = (0,\, 0,\, 0,\, 0,\, R_1^a M_0^a,\, R_1^c M_0^c)^T$$

$$\mathbf{A} = \begin{pmatrix} -(R_2^a + k_a) & k_c & \Delta\omega^a & 0 & 0 & 0 \\ k_a & -(R_2^c + k_c) & 0 & \Delta\omega^c & 0 & 0 \\ -\Delta\omega^a & 0 & -(R_2^a + k_a) & k_c & \omega_1 & 0 \\ 0 & -\Delta\omega^c & k_a & -(R_2^c + k_b) & 0 & \omega_1 \\ 0 & 0 & -\omega_1 & 0 & -(R_2^a + k_a) & k_c \\ 0 & 0 & 0 & -\omega_1 & k_a & -(R_2^c + k_c) \end{pmatrix}$$

In this matrix form, it is easy to include additional pools just by adding the extra components into the matrix, following the same structure. Typically, one could include a number pools to account for MT, NOE, amide, amine and even multiple -OH sites.

Subsequently, the matrix equation can be solved either numerically or quasi analytically by using a matrix expansion series approach.[6,7]

3.3. Finding the net magnetisation: Time evolution vs steady state solution.

Once the system of exchangeable sites (concentration and resonant frequencies of each pool) and their interactions (exchange rates) are defined, the Bloch-McConnell equations can be numerically integrated to obtain the value of the variable of interest, usually the net water magnetisation along the *z* axis (M_z^a), at any given time. Calculation of the full evolution of the variables in time is a powerful tool which allows visualisations and understanding of the system's behaviour under different experimental conditions. Results from these simulations can provide educated guesses for the optimisation process of specific parameters such as the required RF power, the saturation length or the recommended readout schemes.

Integration over time of the exchange system is however a demanding number crunching task which can be very time consuming, especially for multiple pool systems.

Often the approach is to analyse the steady state solution which arises from the premise that a saturation RF pulse is applied for enough time so that the net mag-

netisation reaches a steady state equilibrium value from which it will not evolve until conditions are changed (i.e. the saturation RF pulse stops). In *steady state* the set of differential equations describing the model (the Bloch-McConnell equations) become a system of ordinary equations, which is much easier to solve. This allows fast inspection of the exchange process outcome over a range of parameters values. While solving the steady state problem is a very convenient method, it does not inform on the status of the magnetisation during the first instances of the RF saturation pulse, and hence it is not valid to study short saturation time schemes, nor is it useful for the analysis of different saturation schemes other than a continuous pulse.

Both solving the entire time evolution of the Bloch-McConnell system or taking the steady state approach to solve multi-pool system problems can be very helpful for a number of applications. On the other hand, it is sometimes useful to simplify the exchange system to the minimum working expression in order reduce number of parameters involved and be able to estimate the most important parameters in the process of maximising CEST contrast. In this context, for many situations a two pool model can be sufficient to provide insight of the system's general behaviour while keeping the number of unknown parameters to the minimum. The advantage of using simplified models is that under certain parameter conditions, it is possible to find an analytical solution to the system, that can help elucidate the relationships between the CEST contrast and the experimental parameters to optimise. In Chapter 4 for example the reductionist approach is used to provide a simple analytical description to describe the observed transverse relaxation time T2 as a function of the concentration of glucose in a sample.

In the following sections the mathematical models of chemical exchange are used extensively to evaluate and predict the expected CEST contrast in a variety of experimental situations.

3.4. Pulsed versus Continuous saturation.

Hardware limitations in the RF amplifiers prevent the use of long saturation pulses. This limitation is usually overcome by adopting a pulsed saturation approach in which several shorter pulses are applied instead of a single long RF pulse. Pulsed saturation schemes allow levels of saturation comparable to the ones achieved with continuous RF irradiation. However, peak power is higher in the pulsed saturation scheme, as the total energy delivered is spread over periods of no irradiation. This can become a limitation in the design of CEST pulse sequences, especially when planning for low duty cycle saturation schemes with relatively high equivalent B1

power,* as the peak power can quickly escalate.

Another consequence of applying pulsed saturation is related to the generated pulse bandwidth. Short pulses will produce wide spectral bandwidths which may be too broad to target the specific resonant frequencies of the CEST agents. Therefore a balance has to be found between the pulse length and bandwidth that will assure efficient labile proton saturation. In addition to the bandwidth from the main pulse, unwanted side-bands or secondary saturation bands can be formed due to the periodicity of the saturation train of pulses. Unexpected saturation peaks (equally spaced in frequencies) may be symptomatic of saturation side-bands. It is useful to analyse the Fourier transform of the entire saturation train in order to check for potential side-bands interfering with the inspected frequency range.

The following examples shows the simulated time evolution of the magnetisation along the z axis, M_z, during saturation applied at the resonant frequency of the CEST pool for both pulsed and continuous saturation schemes. The pulse and system parameters used for the simulation are detail in the figure 3.4.1 caption. The graph also shows the steady state value calculated for M_z^a and M_z^c. As can be observed the longitudinal magnetisation evolves towards the value of the steady state solution. In this particular case the time to reach 95% of the steady state is around 5 seconds (after which the saturation is stopped and the magnetisation returns to equilibrium).

The optimum CEST contrast will not necessarily occur at saturation times of that length. As discussed later in section 3.16, optimum contrast can be obtained at a fraction of the saturation time.

*Equivalent B1, $B1_{eq}$, is referred to the field intensity of the hard RF pulse that would deliver the same amount of power as any given RF pulse, regardless of its shape:

$$P \propto \frac{\int_0^{\Delta t} B_1^2(t)\,dt}{\Delta t} = B_{1eq}^2$$

For example, the paradigm of pulsed saturation schemes, consisting of a train of Gaussian pulses would have an equivalent B1 described by:

$$B1_{eq} = \frac{\theta}{2\gamma}\left(\sqrt{2\pi}\sigma_g erf\left(n\sigma/\sqrt{2}\right)\left(t_{gauss}+t_{delay}\right)\right)^{-1/2}$$

where θ is the flip angle of the Gaussian pulse, with σ_g its standard deviation, (t_{gauss} the duration and (t_{delay} the delay between each Gaussian pulse. The gyromagnetic ratio of the nucleus is represented by γ, and $erf\left(n\sigma/\sqrt{2}\right)$ accounts for the number of standard deviations contained in actual pulse, as in practice the Gaussian shape produced by the RF coil is truncated in the edges.

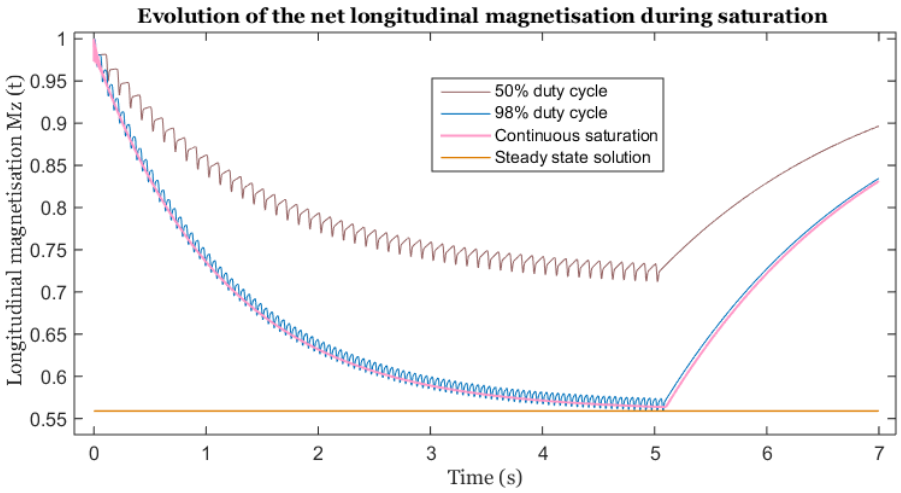

Figure 3.4.1.: *Time evolution of M_z^a and M_z^c under pulsed and continuous saturation. Data simulation with a two pool model with the following parameters: Relaxation times of the water pool $T_1^a = 2s$, $T_2^a = 40ms$. Relaxation times of the CEST pool $T_1^c = 1s$, $T_2^c = 10ms$. CEST offset frequency relative to water $(ppm^c = 1.2 : ppm)$. Shown in pink continuous B1 saturation power $2\mu T$. Shown in blue train of Gaussian pulses with and equivalent B1 power of $2\mu T$ and 98 percent duty cycle. Each of Gaussian pulses has a duration of $50ms$ and a standard deviation of $8.56ms$, mimicking the pulse specifications used in the Agilent 9.4T scanner. Using the same pulse but with a longer delay between them, the brown line shows the results of a lower power (and 50% duty cycle) saturation. The pink line corresponds to the solution for the continuous saturation scheme. The value corresponding to steady state solution is shown in orange.*

3.5. Mz recovery time.

Each offset frequency in the Z-spectrum needs to be equally weighted, and therefore after the readout the net magnetisation is usually let to recover fully before applying the next saturation RF pulse at a different frequency offset. This is very time inefficient as it adds extra waiting time to an already long preparation phase (saturation) for every offset point in the Z-spectrum. Although the extra waiting time for the recovery of the net magnetisation can be invested in acquiring a different slice of interest using a multi-slice readout approach, it is not always required or even applicable depending on the scan protocol.

Using computer simulations it is useful to observe that the recovery time can be avoided if sufficient saturation time is allowed. Application of a long RF irradiation pulse while net magnetisation is still recovering (right after the readout) has no impact on its final steady state, and therefore identical CEST contrast is achieved regardless of the initial condition $M_z^a(t=0)$. This knowledge can be used to considerably shorten scan times, reducing the duration for full Z-spectrum acquisition to half of the time in some cases.

3.6. Simulation of glucose CEST profile

Simulation of multiple CEST pools. Exchange rates of different pools can be estimated by fitting the experimental data to the mathematical model. In the following case, figure 3.6.1, the three exchange sites of glucose were simulated and compared with experimental data, which provided an estimation of the exchange rate of each -OH pool.

Values found comparing the simulated data to the phantom data represent a good starting point for the parameters in glucose, which is useful when running simulations *in vivo* conditions. Although it is expected that the exchange rates of each of the hydroxyls in glucose will vary (mostly depending on pH, phosphate concentration and the higher temperature *in vivo*), their resonant frequencies and even the approximate values of the exchange rates provide valuable information.

Assessment of saturation status. In the work published by Walker-Samuel[8] described in section 2.4.2, the two pool mathematical model was used to establish enough saturation was provided by the used pulse sequence (see figure 3.6.2).

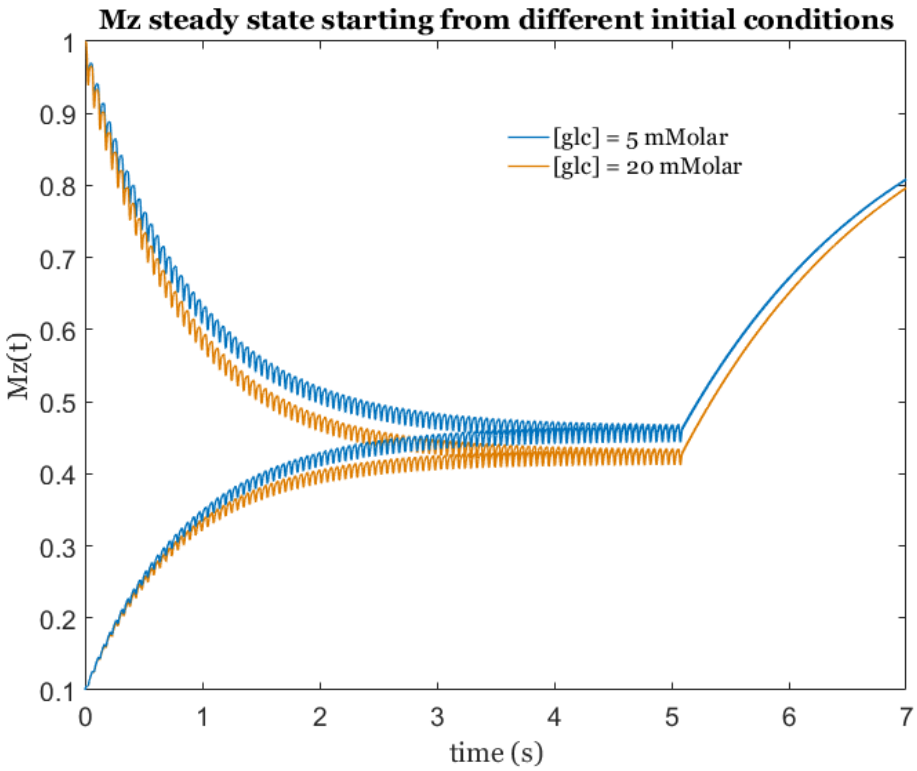

Figure 3.5.1.: *Time evolution of the net water magnetisation M_z^a starting from different initial conditions. Both at 5 and 20 mMolar glucose concentration the M_z^a reaches the same steady state value after the application of the irradiation pulse, independently of the initial condition $M_z^a(t=0)$. For all four cases, a simple 2-pool model (water-glucose) was simulated with a hard 1.3 μT B1 RF pulse applied on resonance with glucose at 1.2 ppm from water.*

Figure 3.6.1.: *CEST effect of glucose*

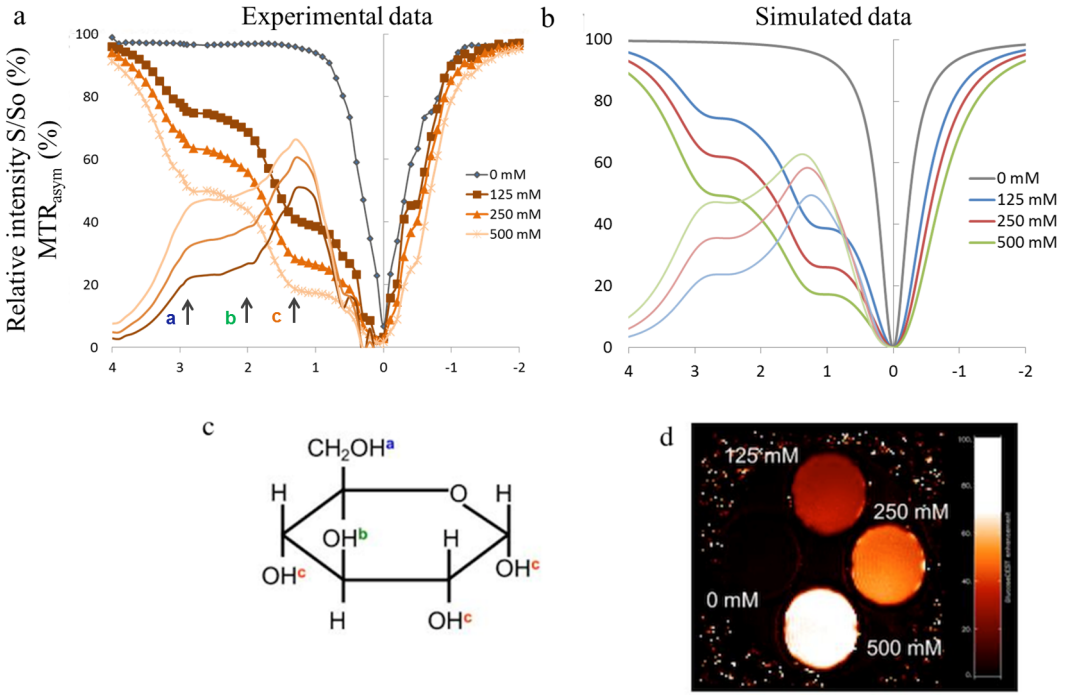

a) Z-spectra and MTR_{asym} of in vitro measurements with glucose solutions at 0, 125, 250 and 500 mMolar concentrations. b) Simulations of the Z-spectrum of glucose at the same concentrations as in vitro. Simulation parameters: $B1 = 1.2\,\mu T$, $T1_{water} = 2\,s$, $T1_{glucose} = 0.17\,s$, $T2_{water} = 500\,ms$, $T2_{glucose} = 10\,ms$, $\Delta\omega_a = 2.9\,ppm$, $k_{aw} = 1275\,Hz$, $\Delta\omega_b = 2.0 ppm$, $k_{bw} = 1700\,Hz$, $\Delta\omega_c = 1.3 ppm$, $k_{cw} = 935\,Hz$. c) Schematic diagram of a glucose molecule showing the location of hydroxyl groups susceptible for CEST. d) Image of the scanned phantoms showing the glucoCEST effect (pH = 7.2, 37°C). The image was produced by integration of MTRasym spectra between 0.75 and 4 ppm for each pixel. An enhanced CEST effect is observed for increasing glucose concentrations, both in in vitro and simulated data.

Figure 3.6.2.: *Simulation of approximation to steady state*

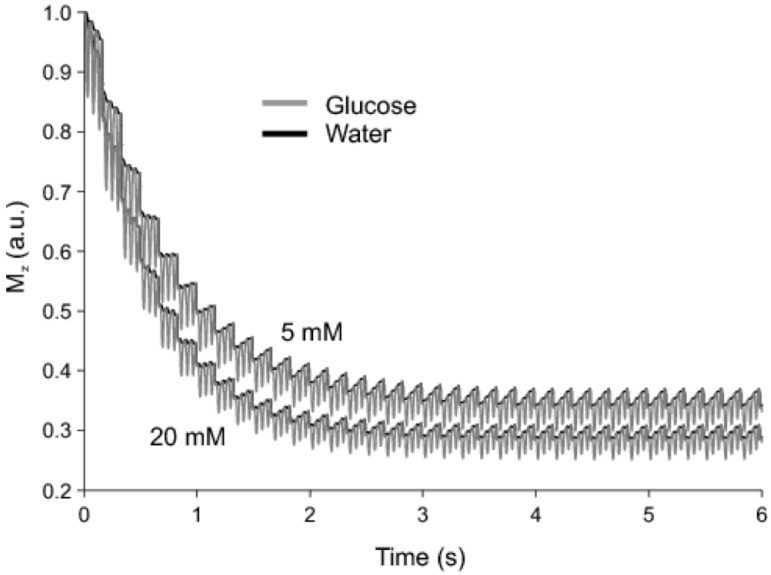

Simulations of the longitudinal magnetisation of glucose and water pools during a gradient echo CEST acquisition, for both 5 and 20 mM glucose solutions. Sets of 3 Gaussian off-resonance saturation pulses are simulated prior to a 20° readout pulse, for every k-space line. These simulations show that, for glucose concentrations of 5 and 20 mM, a steady state condition is reached within 3 seconds, which corresponds to 19 k-space acquisitions. For the 128 phase encoding steps used in the GE-CEST sequence, this suggests that only the outer 13% of k-space is acquired before the steady condition is met. Figure published in Nature Medicine Journal[8]

3.7. Simulating *in vivo* conditions

Unlike in phantoms where the Z-spectrum is formed by the interaction of water and the CEST agents of interest alone, *in vivo* spectra are shaped by a multitude of different parameters and exchanging pools.

In this section the impact of some of these parameters on the Z-spectrum will be analysed. The data produced are based on multi-pool exchange models for which the model parameters have been chosen to mimic as accurately as possible the experimental data obtained from *in vivo* CEST acquisitions.

Model variables: The model used for the CEST simulation of *in vivo* conditions is composed of eight sets of Bloch equations corresponding to the different type of protons in chemical exchange. The labile proton groups, each associated with a set of Bloch equations, are linked by a pseudo first order exchange mechanism to the set of Bloch equations associated with the water pool. The eight pools contained in the model represent: the macromolecular pool (MT pool), the amides and amine molecules, the aliphatic molecules responsible for the Nuclear Overhauser Effect (NOE), three pools for the hydroxyl groups in glucose and finally the water pool.

Each of these pool has five associated parameters that can be adjusted. These are: the concentration or pool size, T_1 and T_2 relaxation times, the exchange rate and resonant frequency with respect to the water pool.

The exchange rates of amides and amines are modelled by the environment pH (which needs to be entered in the model) by the relationships presented in Chapter 1, section 1.4.5. The system also needs to be provided with the specific B1 RF pulse profile over the integration time (or just intensity for the case of the steady state model). Optionally one can include additional pools and relationships between them. The model included in Appendix E contains an extra ninth exchangeable pool which can be used to fit more complicated profiles such a double NOE pool or other external agents that may need to be considered.

The model also allows for the possibility of connecting pools to each other in order to simulate processes of magnetisation exchange between them, such as the likely transfer of magnetic label from protein amides to amines and vice versa, for example.

By adjusting the parameters in the model it is possible to obtain a reliable Z-spectrum that fits well with the *in vivo* experimental data. Figure 3.7.1 shows the averaged Z-spectrum of mouse brain at two different powers. Once the parameters are fitted in the first power, the model can accurately fit the experimental data of the

second power, and provide an estimate of the *in vivo* CEST parameters.

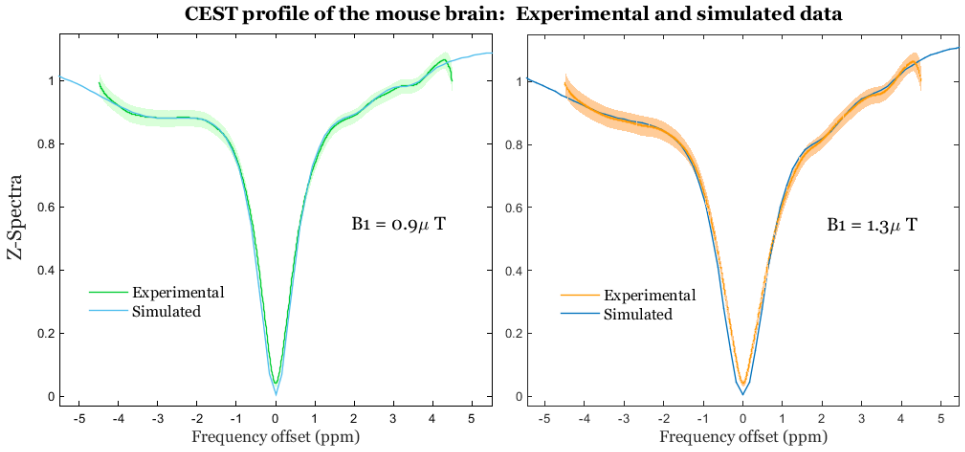

Figure 3.7.1.: *Z-spectra of the mouse brain acquired with $B1_{eq} = 0.9\mu T$ on the left and $B1_{eq} = 1.3\mu T$ on the right. Shaded lines correspond to the standard deviation of the Z profile across the brain. The blue lines that extend over $\pm 4.5ppm$ are simulated data. The parameter values used in the simulation which mimic the experimental result in vivo are listed below. Labile proton pool sizes in mmolar: $M_0^a = 55$ for water, $M_0^b = 5$ for the macromolecular (MT) pool, $M_0^c = 0.9$ and $M_0^d = 12 \times 10^-3$ for amine and amide groups. Glucose levels set at 5 mMolar with $M_0^e = 27 \times 10^-3$, $M_0^g = 9 \times 10^-4$ and $M_0^h = 1.8 \times 10^-4$ for each hydroxyl group in glucose. $M_0^f = 3.2 \times 10^-2$ for the aliphatic proton pool. Transfer rates (Hz): Value of pH was set at 7.2 and the pH dependent exchange rate relations defined as, $AminesEx = 0.5.10^{(pH-4.5)}$, $AmidesEx = 5.57.10^{(pH-6.4)}$. For the rest of the pools the exchange rates are: Re=1870; Rg=3400; Rh=2500; Exb=50; Exf=5. T1 relaxation times (s): T1a=1.85; T1b=1; T1c=1.1; T1d=1.1; T1f=1; T1e=1.2; T1g=1.2; T1h=1.2; T2 relaxation times (s): T2a=0.04; T2b=0.00001; T2c=0.0006; T2d=0.0018; T2f=0.00042; T2e=0.017; T2g=0.017; T2h=0.01. Resonant frequencies (ppm): ppmb=0; ppmc=+2.1; ppmd=3.5; ppmf=-3.15; ppme=1.1 ppmg=2; ppmh=2.9;*

3.8. Normalisation

The MTR (and MTRasym) measure was originally defined as the variation between irradiated and non-irradiated signal ($+\delta\omega$ and $-\delta\omega$ for MTRasym) divided by the non-irradiated signal.[5,9] The non-irradiated signal, M_0, is a logical reference for normalisation as it produces values of Z-spectra bound from 0 to 1 in the entire fre-

quency range. However, due to physiological noise* during *in vivo* acquisitions, normalisation at M_0 is not recommended. As physiological noise scales linearly with the signal intensity, variations in M_0 values can be large compared to the Z-spectrum intensity close to water. This has a serious impact on the stability of the signal and it is particularly harmful for exogenous CEST experiment, such as gluco-CEST, in which information is obtained from small differences in the CEST images acquired over the time-course of a generally lengthy experiment. Signal intensity jumps between different acquisitions can completely ruin an exogenous CEST experiment.

Use of a normalisation reference closer to the off-resonance frequencies of interest (where the signal strength is lower) can reduce the noise variability of physiological nature, which is crucial for CEST experiments where data has to be acquired several times. For that reason the *in vivo* data in this study has been normalised to the average signal level in the range between ± 4.3 and ± 4.5 ppm from the water resonant frequency.

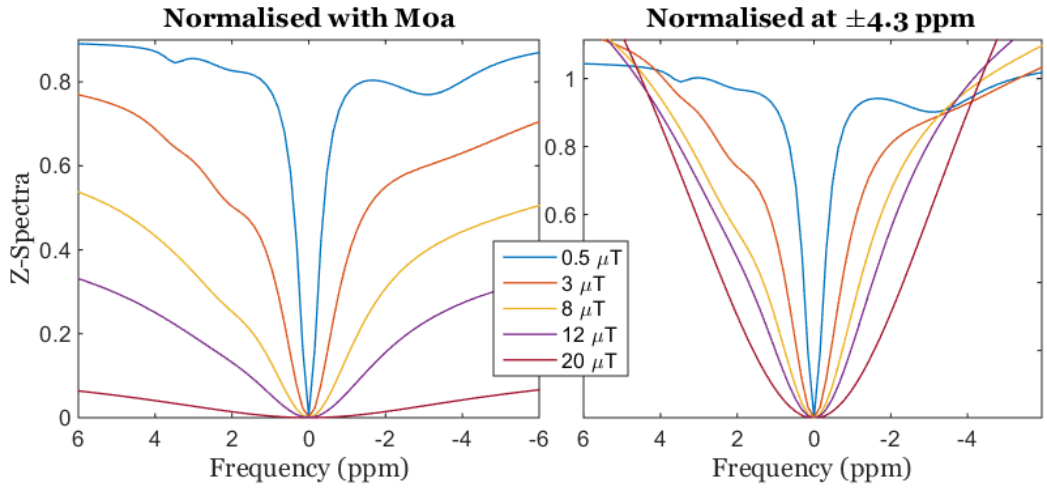

Figure 3.8.1.: *Normalisation approach. Two sets of Z-spectra at varying saturation powers are shown. On the left, normalisation is defined as the averaged signal intensity with no saturation,* $M_{ref} = \sum M_0^i \times e^{TE/T_2^i}$. *On the right the reference is taken as the mean value of the Z-spectrum between* $\pm$ *4.3 and* $\pm$ *4.5 ppm.*

*The image noise in MRI can be described as: $\sigma = \sqrt{\sigma_0^2 + \sigma_p^2}$ with $\sigma_p = \lambda S$ where σ_0 describes the electronics and other system noise that includes drift and imperfections in RF, gradient, and shims. σ_0 is considered the *raw* noise and has been shown to be proportional to B0, but independent of the signal strength. The term σ_p describes the physiological noise, which arises from fluctuations in the basal cerebral metabolism, blood flow, and blood volume and also from cardiac and respiratory functions that cause oscillations in the vascular system, motion from subtle brain pulsatility, and magnetic field modulations. In contrast to the raw noise, the physiological noise is signal-dependent. See[10] for more information on physiological noise.

Similar to the approach taken in this work, the research group lead by R. Reddy in Pennsylvania, have used the negative offset frequency as the reference for normalisation.[11–13]

$$CEST_{asym}(\Delta\omega) = \frac{M_{sat}(-\Delta\omega) - M_{sat}(+\Delta\omega)}{M_{sat}(-\Delta\omega)} \tag{3.8.1}$$

As a generalisation of the close reference normalisation approach, an alternative measure of the Z-spectrum asymmetry could be proposed as the ratio between the asymmetric and the symmetric components of the Z profile, ie:

$$ZAR = \frac{asymmetric part}{symetric part} = \frac{M_{sat}(-\Delta\omega) - M_{sat}(+\Delta\omega)}{M_{sat}(-\Delta\omega) + M_{sat}(+\Delta\omega)} \tag{3.8.2}$$

The Z asymmetry ratio, ZAR, is by definition a normalised measure, and as such not susceptible to variation due to the selection of a different normalisation reference (a common issue in the reported CEST values across different labs). ZAR provides similar information as $CEST_{asym}$, however it weights both sides of the Z-Spectrum equally and in the author's opinion it is conceptually more elegant.

3.9. Effect of pH *in vivo*

As mentioned before in Chapter 1, pH plays an important role in CEST, particularly for endogenous measurements where the peak intensities from amide and amine groups depend on the specific tissue pH. The simulation in figure 3.9.1 shows the extent and directionality of the change in the amide and amine peaks in relation to the pH. The exchange rate dependence of both amide and amine pools have been simulated according to the experimental pH relationship reported in the literature[14,15] and detailed in section 1.4.5.

The amide peak displays a clear monotonic relationship with pH, showing a pronounced peak at the normal pH values of 7.2 found in the brain tissue, to a complete disappearance of the peak at acidic pH values of around 6.6. The amine peak at 2 ppm has a less defined pattern, displaying similar intensities at different pH values. It is worth noting however, that in the depression formed between 0 and 2 ppm, signal appears to be modulated strongly by the pH, showing the same response as the one observed in the amide peak.

The intense effect of pH on the CEST outcome is the motivation behind all APT based pH weighted imaging methods.[16–20] While the models alone have so far failed to provide a reliable quantitative measure of pH, different approaches have been

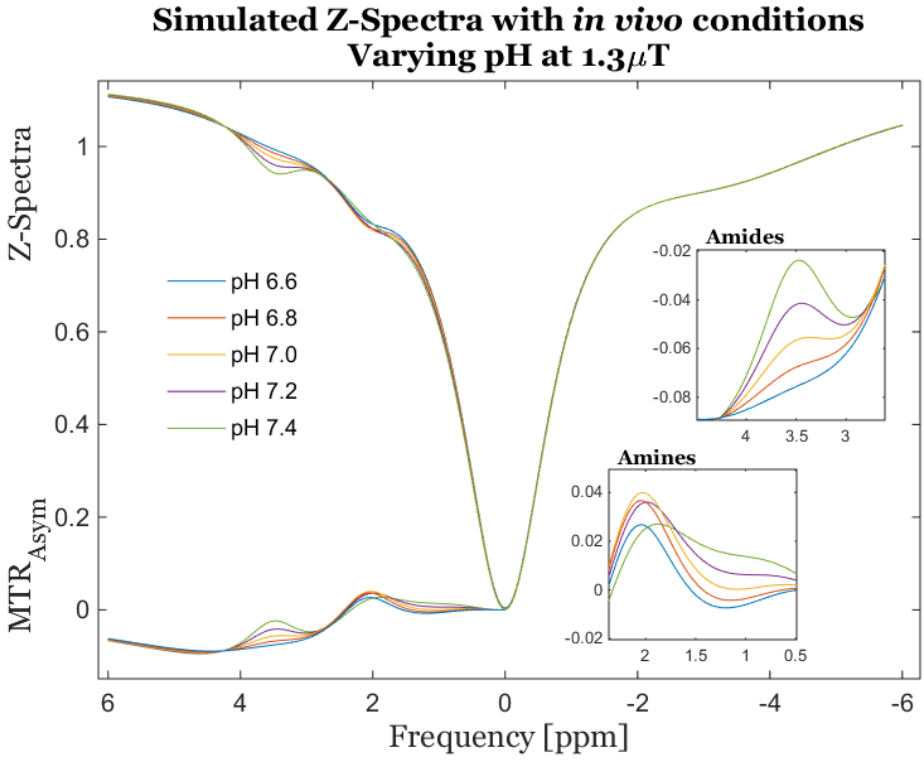

Figure 3.9.1.: *Effect of pH on amide and amine groups. The monotonic relation of amide peaks with pH is the principle of pH weighted imaging with CEST MRI.*

suggested to overcome this limitation. One possibility is the so called "radiometric approach" in which the pH can be deduced from the relationship of both amine and amide peaks. However, the method requires prior knowledge of the concentration of both pools[21] or alternatively the use of exogenous pH sensitive agents.[22,23] Alternatively semi-quatitative pH maps can be obtained from CEST images, prior calibration of the pH using 31P NMR spectroscopy. Using this method the team in our lab has recently been able to image the local pH change caused by hypoxia-ischaemia in the piglet brain.[24]

3.10. Effect of the Macromolecular pool

It has been shown both experimentally and theoretically that for many biological tissues, a Lorentzian function (which naturally arises from the Bloch equations) does not adequately describe the RF absorption line-shape of the protons in the hydrated layer of macromolecules. Dipole interactions in a rigid system have been accurately described with Gaussian line-shapes as opposed to the Lorentzian shapes suitable for the description of liquid samples.[4,25,26] In the intermediate exchange regime such as in biological tissues, the super-Lorentzian function, which includes the integration over all the dipolar orientations in the macromolecule, is found to be most appropriate.[27,28] The super-Lorentzian absorption line-shape can be written as:

$$\square_b(2\pi\Delta) = \int_0^{\frac{\pi}{2}} d\theta \sin\theta \sqrt{\frac{2}{\pi}} \frac{T_2^b}{|3\cos^2\theta - 1|} e^{-2\left(\frac{2\pi\Delta T_2^b}{|3\cos^2\theta-1|}\right)^2}$$

where Δ is the RF resonant frequency relative to water and θ the dipole orientation angle relative to the main magnetic field $\mathbf{B}_0$.

In the current simulations the semi-solid water pool is modelled with the above super Lorentzian absorption line-shape, and pool size of 11% bound to free water fraction, in agreement with values available in the literature.[25,29]

In ppm range close to the water resonant frequency, the exchange between the MT pool and water has a moderate effect on the Z-spectrum profile, which scales with saturation power. As shown in figure 3.10.1 the MT shifts the signal up slightly (this is due to the lower normalisation value) but without significantly affecting the sensitivity to detect CEST peaks. The effect of MT gets reduced to zero as the saturation offset gets closer to the water frequency. However, it should be said that in reality, the MT pool has a larger impact on the CEST outcome than shown by the simulations in Figure 3.10.1.

The dipolar exchange between the bound water (MT) and free water pool signifi-

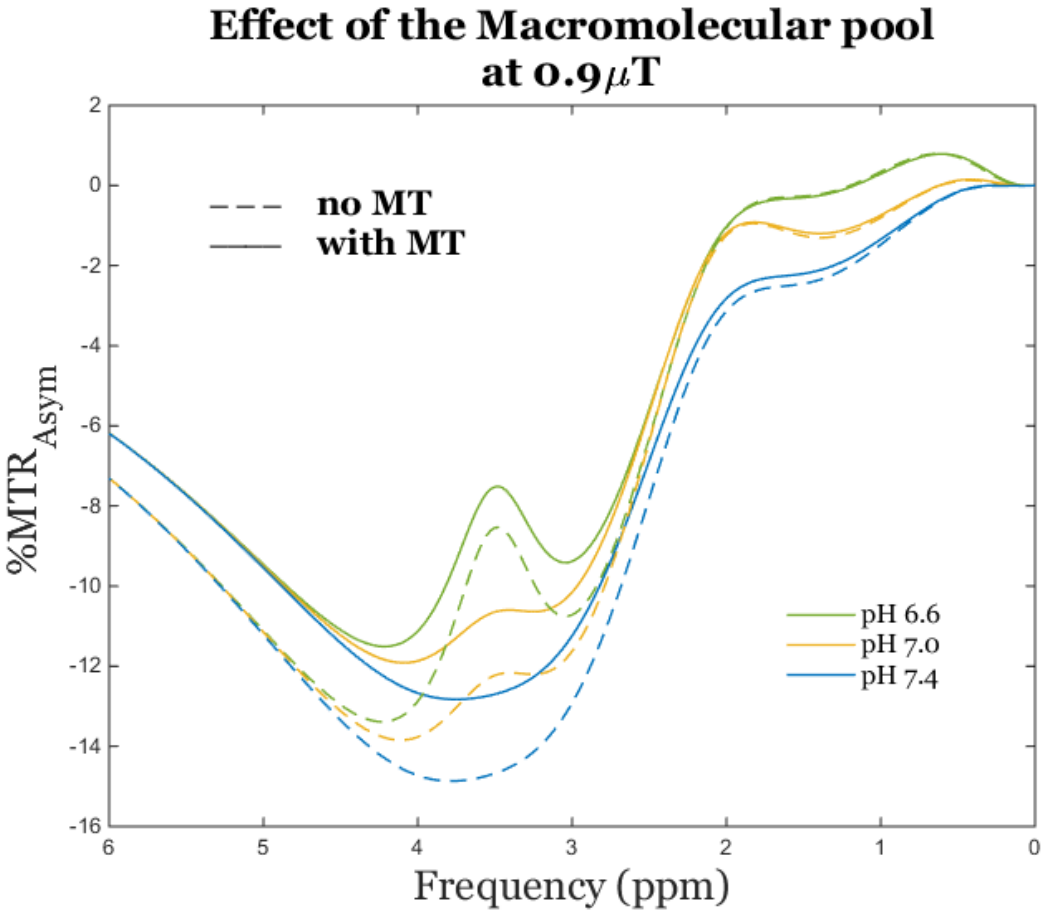

Figure 3.10.1.: *Effect of the macromolecular pool on the sensitivity of CEST. At the narrow frequency range relevant for endogenous CEST and usual power levels, the direct effect of MT exchange is not critically detrimental for the detection sensitivity of CEST. However the shortening of the spin-spin relaxation time T2 of water in the presence of macromolecules (not shown here) has a strong broadening effect in the Z-spectra, and thus the capacity to resolve CEST peaks is severely affected.*

cantly reduces the transverse relaxation time of the free water, which in turn widens the Z-spectrum and flattens the CEST peaks out, with the consequent loss in sensitivity. The model can be easily adapted to couple the water relaxation time to the MT concentration, with a proportionality relation, i.e. $T_{2a} = f(M_{0b})$. For the current simulation however, the T_{2a} time was deliberately fixed at the experimentally measured value. The purpose of it was to assess only the pure exchange effect, as it is studied in MT and qMT experiments, without accounting for the shortening in the water the relaxation time attributed to the macromolecular pool.

At far offset frequencies and at high power saturation schemes particularly, the effect of the macromolecular pool is much more evident, as shown in figure 3.10.2.

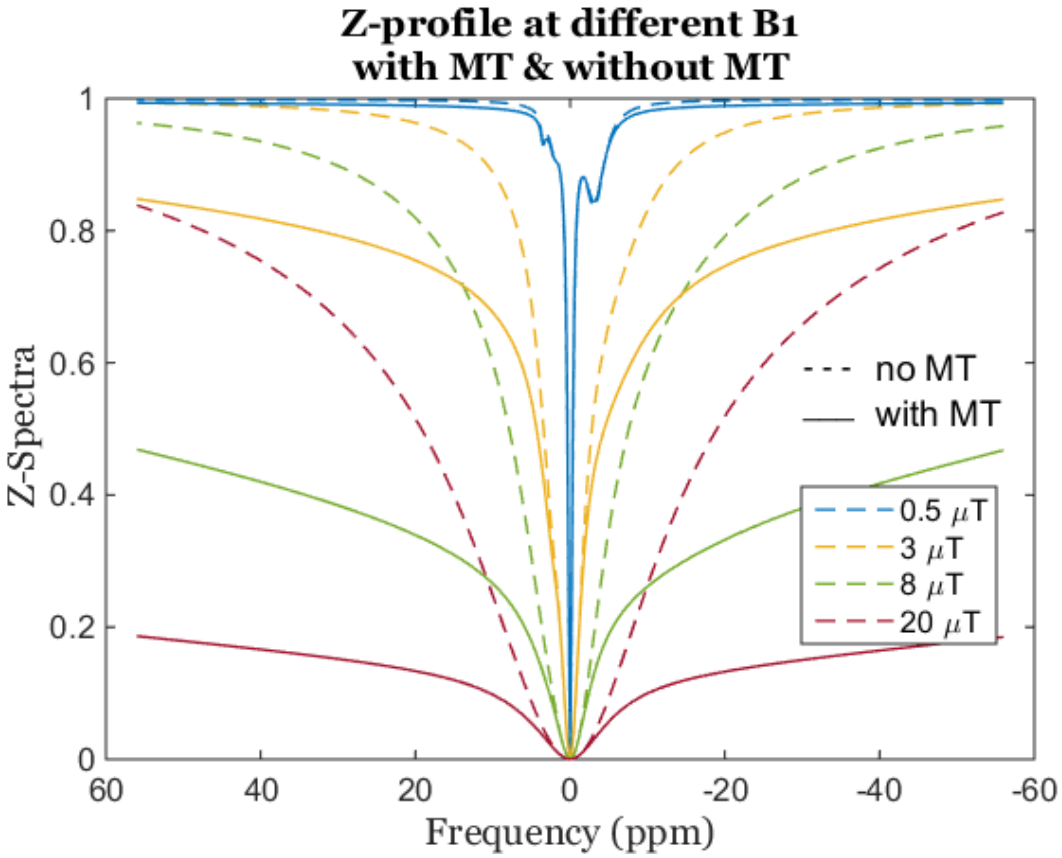

Figure 3.10.2.: *Comparison of the Z-spectrum shape with and without the macromolecular pool contribution. At elevated B1 powers and offsets above 3 to 5 ppm, the MT pool drags the signal intensity down up to 75% compared to the same power in absence of MT.*

3.11. Saturation power and noise

As a rule of thumb, fast exchanging hydrogens will produce better CEST contrast when saturated with high B1 powers. Defining the precise optimum saturation power however is still a controversial subject.

It is generally accepted that an estimate for the optimum B1 power for a given CEST agent can be deduced from the saturation efficiency equation, first introduced by Snoussi et al in 2003:[5,9,30]

$$MTR \propto k\alpha$$

where the saturation efficiency constant α is defined as

$$\alpha \approx \frac{(\gamma B_1)^2}{(\gamma B_1)^2 + k^2}$$

For an exchange rate on the order of 1000Hz, as in the case of hydroxyl groups in glucose, the equation predicts an optimum saturation power of above $10\,\mu T$. See figure 3.11.1.

While the equation may provide a good estimate for labile protons resonating away from the water frequency such as paraCEST agents, it fails to predict the optimum power of many endogenous CEST molecules.

For endogenous CEST agents resonating at frequencies close to water, the largest source of signal loss comes from the spillover or direct saturation effect. Yet the saturation efficiency equation does not take into account the consequence of spillover.

First, higher extent of spillover produces a proportionally smaller contrast, as the MTR does not scale linearly with signal.[31,32] Secondly, CEST labile protons with small offsets $\delta\omega$ are susceptible to secondary saturation effects. Excessive RF power applied at the $-\delta\omega$ frequency (needed for asymmetry analysis) will not only saturate the water but also the CEST agent itself, situated at $2\delta\omega$ away from the RF frequency. This partial saturation of the CEST pool from both sides of the water spectrum, further reduces the achievable CEST contrast, as the MTR asymmetry is reduced.

Lastly, the signal to noise ratio (SNR) is affected at high B1 powers. Spillover effects reduce the available water signal and hides the CEST label. The characteristic Lorentzian absorption profile (super-Lorentzian in semi-solid like organic tissues), limits the strength of the observable signal which inherently worsens the raw SNR of the measurement.

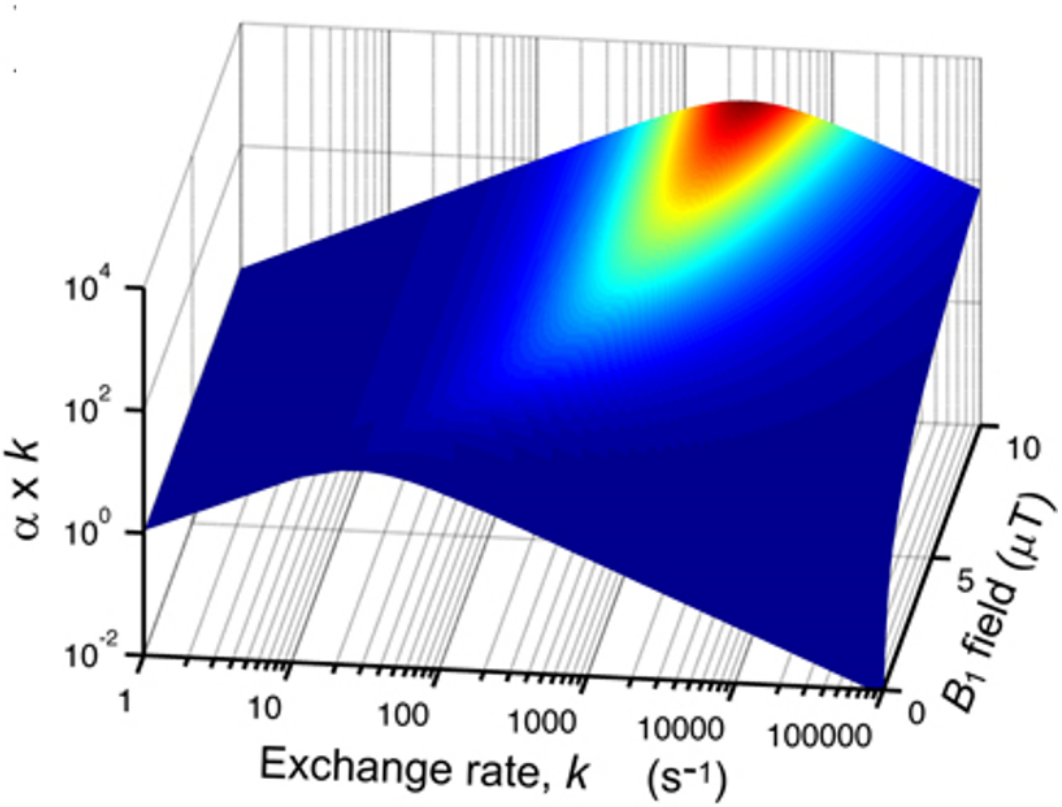

Figure 3.11.1.: *Saturation efficiency profile.[9] Dependence of the product of saturation transfer efficiency and exchange rate (k) on B1 and k. The graph shows an increased CEST efficiency at power levels up to 10 μT for labile proton with exchange rate k of ~1000 Hz. However, the effect of direct saturation is not taken into account.*

The multi-pool exchange model developed here allows the introduction of random noise* in the system to evaluate the effects of noise propagation on the quality of CEST measures. Simulation with different noise levels were run to asses the optimum B1 power and also inform on the ppm integration range † that would maximise the CEST contrast.

Figure 3.11.2 illustrates the deterioration of the signal due to noise as a consequence of increasing B1 power. Raw noise, which is independent of signal strength, becomes proportionally larger when intense direct saturation reduces the available signal. Note that all the Z-spectra are normalised to the same values, however the noise scales up with high powers. To see the actual reduction of available signal by the spillover effect refer to Figure 3.10.2.

These results reflect the importance of finely tuning the B1 power in a trade-off between SNR and saturation efficiency.

These simulations also reveal the need of pre-processing techniques aimed to reduce the noise before evaluating the CEST data. Spatial smoothing techniques, frequency filtering or other kind of data manipulation method that increase the effective SNR are crucial in order to confidently detect the subtle CEST changes encountered *in vivo*.

*It is known that the raw noise in MRI follows a Rician distribution, which for values of SNR larger than two approximates to a Gaussian distribution.[33] The model can simulate the presence of noise in the system. Raw (or thermal) noise σ_0 is simulated by adding a normally distributed random noise to the Z-spectrum before normalisation. Physiological noise in the data is simulated by giving every offset point in the spectrum a probability of being noisy and a normally distributed noise variance proportional to the Z-spectrum amplitude. $Znoisy = \sigma_0 + \sigma_p |Z_{pure}|$ The noise level is defined as the ratio between the variance and the mean signal intensity at the reference offset point. Please refer the Matlab code in Appendix F for the full derivation of the noise parameters.

†The MTR asymmetry is usually defined as a point-wise function in this form:

$$\mathrm{MTR_{asym}}(\delta\omega) = \frac{\mathrm{M}(-\delta\omega) - \mathrm{M}(\delta\omega)}{M_{reference}}$$

The expression requires the input of only two images, acquired with saturation at $+\delta\omega$ and $-\delta\omega$ (plus a reference image if the far away normalisation approach is to be used). This is convenient in terms of reducing scan time and has been commonly used in the clinic as Amide Proton Transfer (APT) imaging technique. $APT = MTR_{asym}(3.5ppm)$. The acquisition of multiple points in the Z-spectrum on the other hand allows for integration over a range of frequencies, aimed to achieve higher confidence in the measurement by sampling more than a single experimental point. Moreover, data from a rage of frequencies can be post-processed to minimise the harmful effects of B0 inhomogeneities across the image.

$$\mathrm{MTR_{asym}}(\Delta\delta\omega) = \int_{\delta\omega_1}^{\delta\omega_2} \frac{\mathrm{M}(-\delta\omega) - \mathrm{M}(\delta\omega)}{M_{reference}} d\delta\omega$$

Ideally the frequency range should be centred around the highest Z-asymmetry produced by the CEST agent of interest.

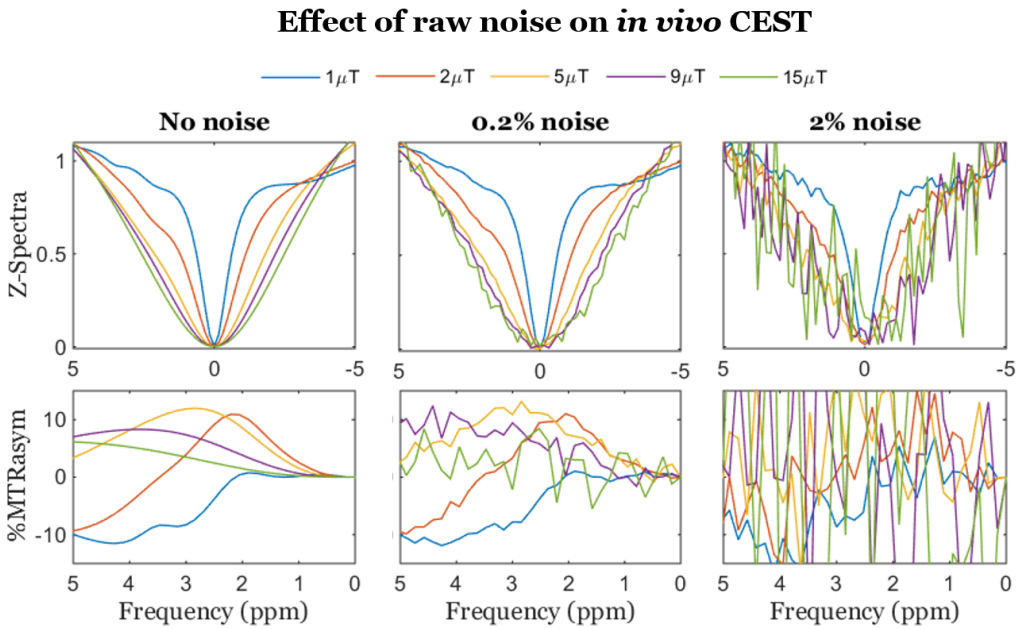

Figure 3.11.2.: *Propagation of noise with different saturation power. Normalised Z-spectra (top) and MTR asymmetry (bottom) at different levels of raw noise in the data (columns). Reduction of available signal due to direct saturation makes the noise increasingly more evident at high B1 powers.*

3.12. Measuring glucose increase *in vivo* conditions

In the following section a theoretical glucoCEST experiment is modelled, in which glucose concentration is increased from a baseline of 5 mMolar to 15 and 25 mMolar respectively. Model parameters are set to the values found by fitting the *in vivo* data with pH values set at 7.2 in agreement with the reported pH in normal brain tissue.[34–36]

The results of these simulations give a good estimation of the expected increase in CEST signal in an *in vivo* glucoCEST experiment at 9.4T.

Figure 3.12.1 shows simulations run with equivalent B1 powers of 1, 3 and 10 μT from left to right respectively. The Z-Spectra, the MTR asymmetry, and the increment in MTR asymmetry for the different glucose concentrations are displayed from top to bottom.

It is important to realise that the intensity of final glucoCEST image will be determined by the area under the ΔMTR_{asym} curves (bottom figures), on a pixel by pixel basis.

The area under the ΔMTR_{asym} curve, which will also be referred to as the glucoCEST enhancement signal (GCE), is clearly dependent on the saturation power used, and generally for fast exchanging hydroxyls groups, amplitudes of a few μTesla produce the largest contrast.

Interestingly, the GCE will also depend on the integration range in which the area is calculated. For example, in the range of frequencies from 0 to 1 ppm, the GCE is larger at $1\mu T$ than at $10\mu T$.

The flexibility in the selection of the integration range allows optimisation of the CEST data analysis according to the B1 power used in the acquisition, which usually falls shorter than the ideal one, especially in a clinical set up, where due to SAR limitations, B1 power is restricted to around 2 μ Tesla.

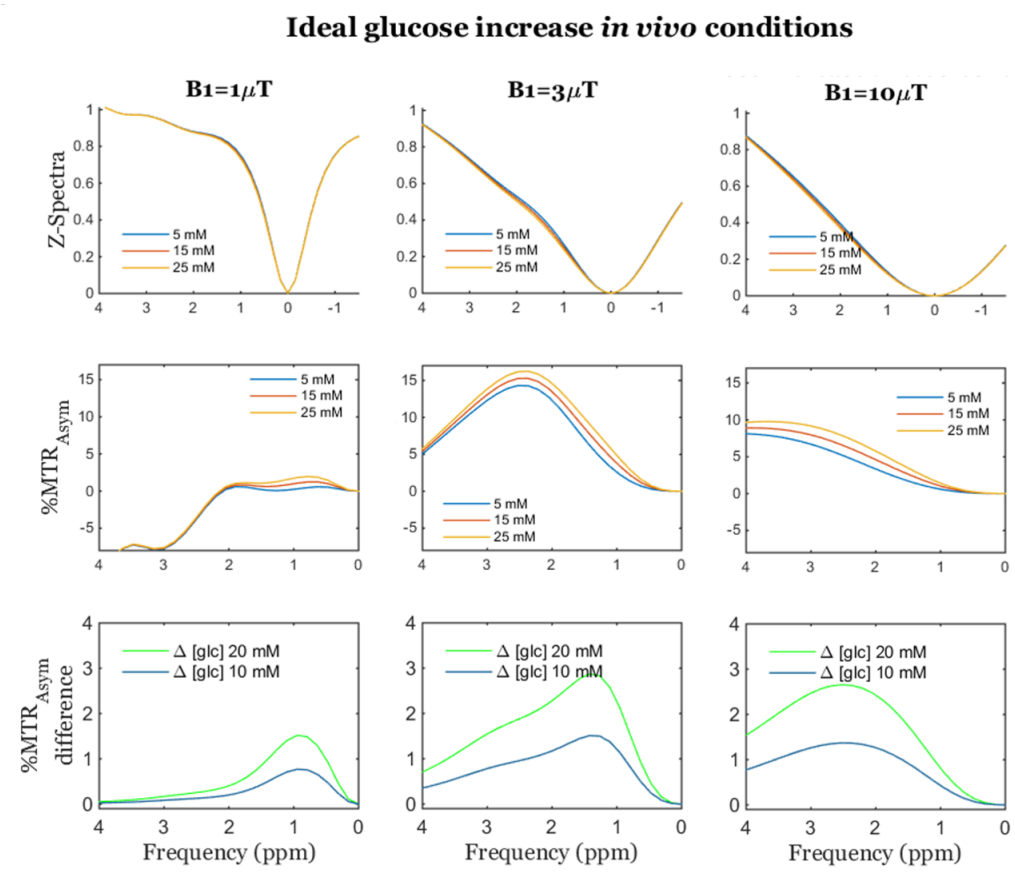

Figure 3.12.1.: *Detection of glucose increase in ideal in vivo conditions. Simulation of glucoCEST experiment for 5, 15 and 25 mMolar glucose concentration at different B1 irradiation powers, 1, 3 and 10 μT, in columns respectively. Z-spectra, %MTR asymmetry and change in the %MTR asymmetry due to glucose, in rows respectively. In ideal conditions high saturation powers (above 3 μT) offers an intense overall increase in the MTR asymmetry.*

3.13. GCE in noisy data

The sensitivity of CEST is very much limited to the noise level in the data, as previously discussed. After re-running the same simulations as in previous section with an added raw noise level of 0.5 percent (SNR=200), the picture changes drastically. The ΔMTR_{asym} is no longer a smooth curve and the signal enhancement is masked by the noise. In this context, measurement of the GCE becomes progressively less accurate as the intensity of the B1 increases. At very large powers the ΔMTR_{asym} becomes too noisy to confidently observe any change due to the rise in glucose concentration. Figure 3.13.1 visually demonstrates the damaging consequences of applying an excessive B1 power.

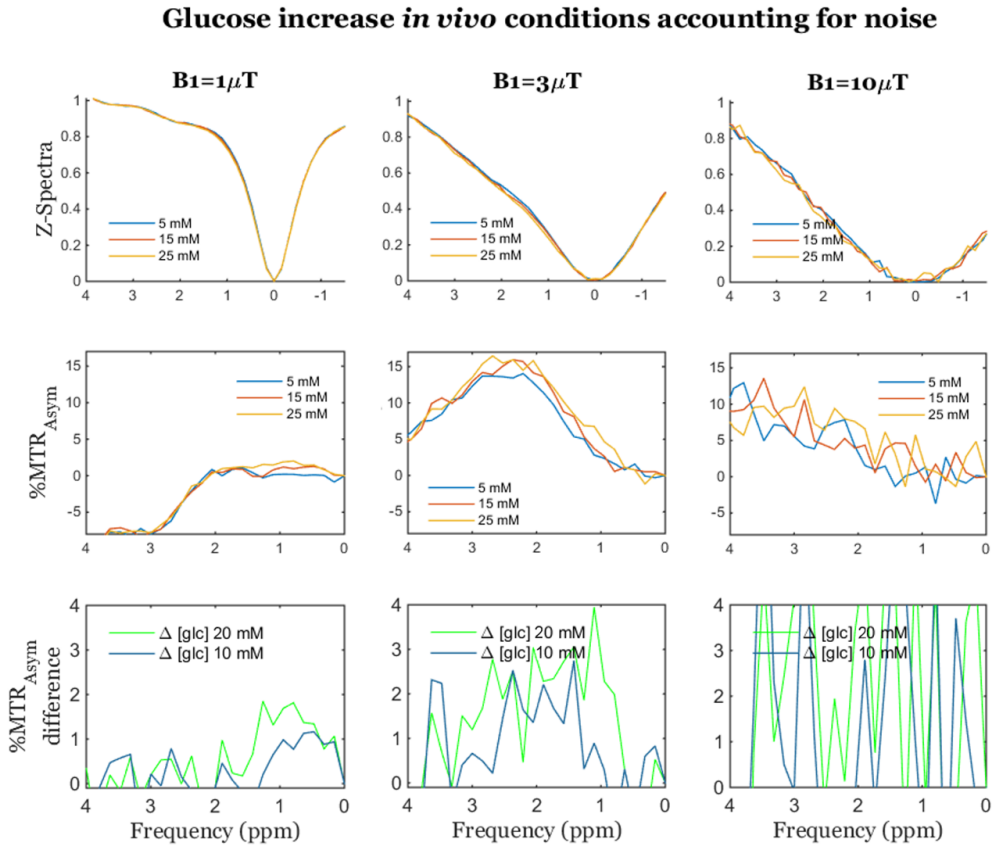

Figure 3.13.1.: *Detection of glucose increase in in vivo conditions with noise. Contrary to the results in Figure 3.12.1 elevated B1 powers deteriorate the glucoCEST signal due to the magnification of noise at high saturation fields.*

The average noise level per voxel in the *in vivo* experiments included in this study ranged between one and two percent (SNR between 50 and 100), before preprocessing of the data. Therefore in the light of the results in these simulations, for

most of the *in vivo* cases strong smoothing of the data was required at the expense of some loss in spatial resolution, to achieve SNR ratios above 250 units.

In the next section the relationship between the reliability of the GCE, B1 power and the chosen integration range will be further analysed.

3.14. Quality of the GCE data at different offset frequencies and saturation powers

Following the discussion above, a more in depth analysis of the interaction between power and observed signal is presented here. Using the *in vivo* parameters in the multi-pool simulator, the mean GCE signal and the standard error of the mean (SEM) are estimated for a range of saturation powers, varying noise levels and different frequency ranges. Figure 3.14.1 contains the results of the simulations at four different integration ranges: In figure 3.14.1a GCE is integrated in a very narrow range from 1 to 1.1 ppm. In figure 3.14.1b GCE is integrated from 1 to 2 ppm. In figure 3.14.1c from 0.1 to 2 ppm and in 3.14.1d from 0.1 to 4 ppm. The blue line in the centre of each figure represents the value of the GCE in an ideal noise-free situation. Shaded colours represent the spread of the standard error for different values of SNR.

The first point to emphasise is again the impact of noise in the GCE, and CEST the general. The adverse effect is exacerbated at higher powers which results in a rapid increase of the SEM along the 'saturation power' axis.

The error in the GCE measurement can be reduced by including more experimental points in the calculation. Comparison between figure 3.14.1a and 3.14.1b illustrates the advantage of calculating the GCE over a range of experimental offsets rather than sampling a single point in order to increase confidence about the measurement (see section 3.11). The narrow sampling range in figure 3.14.1a (equivalent of 1 experimental point in a typical scan) yields large SEM. On the other hand integration over 1 to 2 ppm in figure 3.14.1b provides a significantly lower uncertainty in the measurement.

It is clear from graphs 3.14.1b to 3.14.1d that the integration range can be optimised to the saturation power used in order to achieve better contrast. For the case of irradiation power of around 2 μT the frequency offsets which provide the highest signal lie around the 1 ppm range. To help minimise the standard error in the measurement and yet obtain high contrast from glucose, a range of frequency offsets close to one ppm should be considered for the calculation of the GCE signal.

The predicted noise-free signal (blue line) rapidly increases within the first few

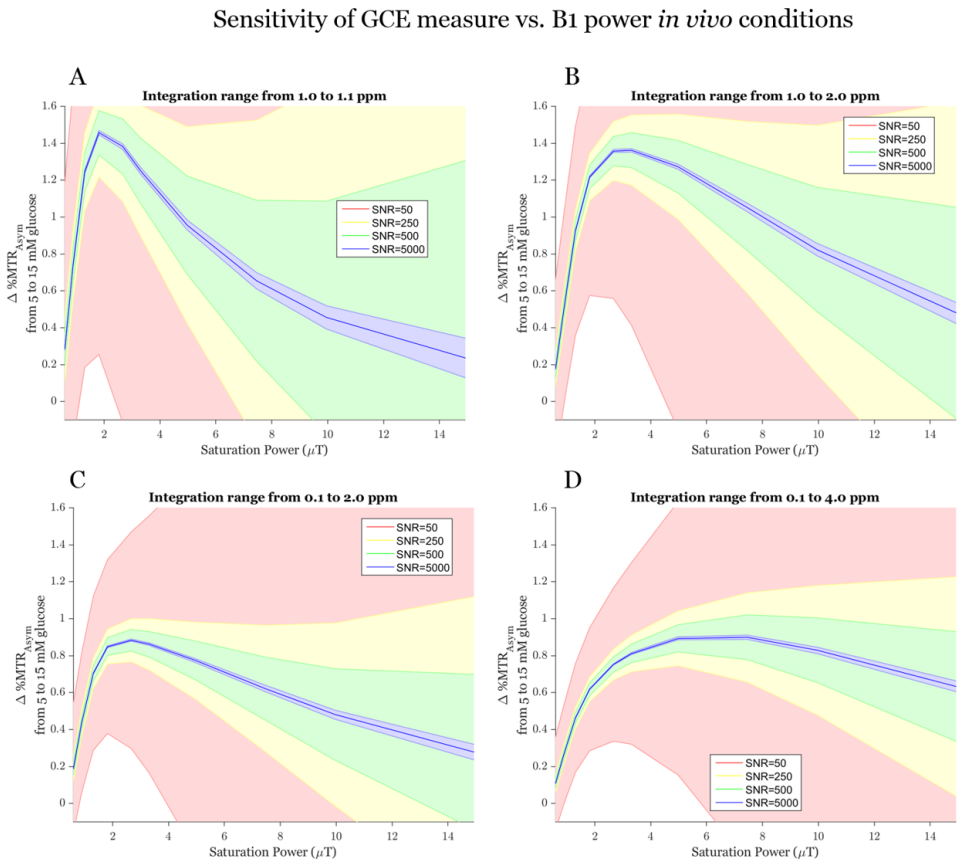

Figure 3.14.1.: *Predicted in vivo GCE signal at different B1 power and integration range. The blue line represents the value of the GCE in an ideal noise free situation. Shaded colors represent spread of the standard error of the mean. Integration range used is specified in each figures title. Given a particular B1 power and noise level, an optimised integration range can be chosen that increases the sensitivity of CEST.*

μT, after which it stabilises or reduces its amplitude. The SEM on the other hand increases fast with power. Based on these results it is fair to conclude that, saturation powers above 4 μT are unlikely to provide any advantage for the detection of glucose *in vivo*.

This conclusion is contrary to a common belief in the CEST field, that fast exchanging hydroxyls groups in glucose require far more intense saturation power for optimum contrast (see saturation efficiency in figure 3.11.1). This point is certainly debatable as large variations in the exchange rate of glucose could change the outcome of these simulations. For example at an average exchange rate of around 5000 Hz (twice as fast as in previous case) the optimum B1 power seems to shift towards higher intensities (see figure 3.14.2). However, the ability to select an optimum integration range can help mitigate the lack of powerful irradiation. Here, a sampling range from 1 to 2 ppm yields contrast close to the one achieved with larger B1 fields.

Sensitivity of GCE measure vs. B1 power.
Faster glc exchange rate (k_a=3740 , k_b=6800, k_c=5000 Hz)

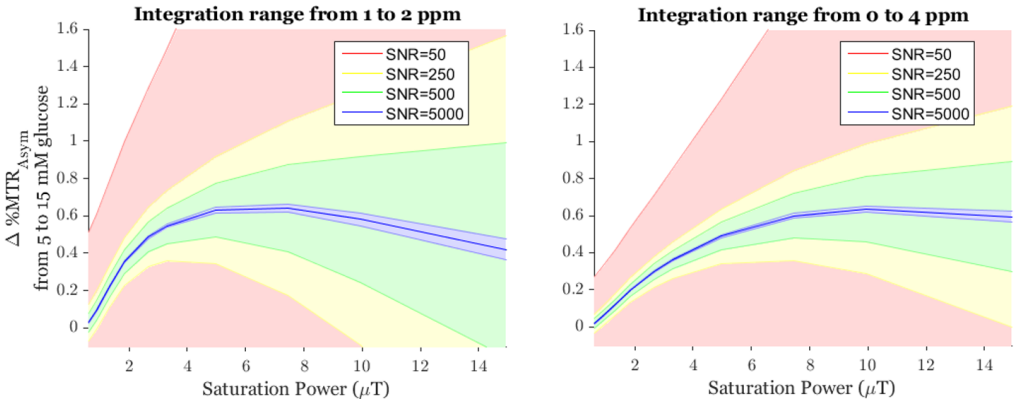

Figure 3.14.2.: *GCE with faster glucose exchange rate. Integration range from 1 to 2 ppm, figure on the left, shows the GCE signal to increase quicker at lower values of B1 compared to signal integrated from 0 to 4 ppm, on the right.*

3.15. Translation to the clinic

As a last point in the discussion of this chapter, it interesting from the point of view of the translation to the clinic, to assess the results of the same hypothetical glucoCEST experiment at 3 Tesla magnetic field. To do so certain parameters in the model had to be modified. Besides the B0 which was changed from 9.4T to 3T, relaxation times of each pool had to be adjusted to match experimental values at 3T, while chemical

exchange rate and relative resonant frequencies were assumed to be independent of the B0 field strength and therefore left untouched. Two different tissue types, grey and white matter, are considered in the simulations of which values of T1, T2 and M0b (size of the MT pool) were taken from Stanisz et al..[37] With these new parameter values the simulation results summarised in figure 3.15.1 show a significantly higher GCE signal in the grey matter compared to the white matter for the same glucose increase. Concerningly, for a 10 mMolar increase in glucose concentration, the expected magnitude of the GCE signal at 3T (and 2 μT power) falls below the 0.3% mark. These limited levels of signal, require values of SNR in the CEST data of at least 250 units in order to be reliably detected. The analysis stresses the need of high quality data for reliable glucoCEST results at 3T. Multiple CEST acquisitions with moderate spatial resolution would probably be needed, as well as intense preprocessing of the data to reduce noise and achieve sufficient SNR levels.

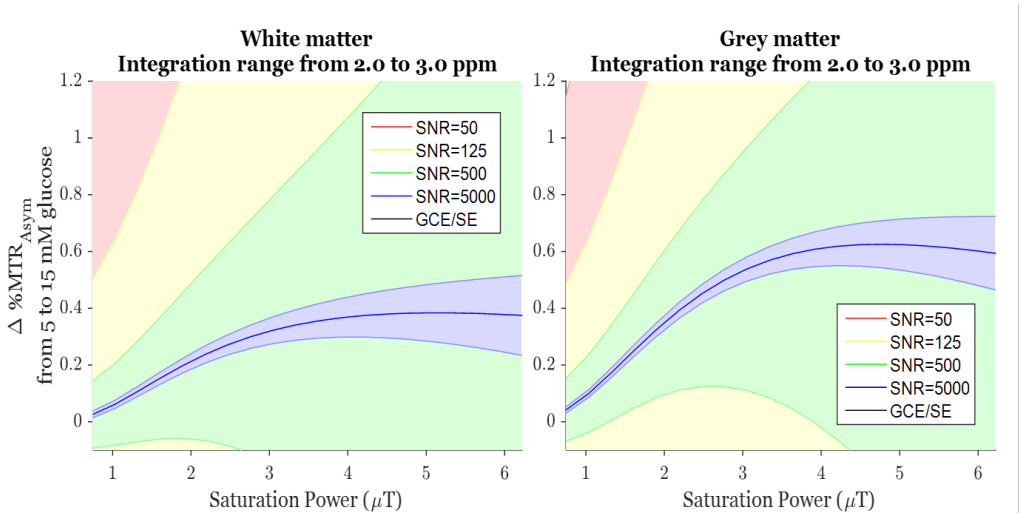

Figure 3.15.1.: *Sensitivity of GCE at 3T. Figure on the left shows the predicted signal for grey matter and on the right for white matter. Values of relaxation time and macromolecular pool content of each tissues were taken from the literature.*[37]

3.16. Saturation length

So far in the discussion of the hypothetical glucoCEST experiment the steady state solution of the system has been analysed, which assumed that a long RF irradiation was applied for the acquisition of the CEST data.

In this section the same hypothetical experiment will be studied, but now the focus

will be set on the evolution of the MTR_{asym} over the time of saturation, instead of the steady state solution.

The simulation parameters are set to the same values as previously except for the saturation irradiation scheme which in this case is defined as a train of 80 Gaussian pulses. Each Gaussian pulse is 50 ms long and it is followed by a 1 ms delay before the application of the next pulse. The overall equivalent B1 power accounting for the pulses and delays is set at 2 μT.

Figure 3.16.1 shows the time evolution of the MTR_{asym} (with its contour plot on the right), of the simulation with 5 and 20 mMolar glucose concentration and the difference of the two ΔMTR_{asym}.

As can be deduced from the plots in figure 3.16.1, the time evolution of the MTR_{asym} is governed by the rate of chemical exchange (κ) of each type of labile proton. For example, the fast exchanging amine group at 2 ppm rapidly stabilises (in less than 2 seconds) while the effect of the slow aliphatic pool, which makes the MTR asymmetry negative, is still building up 4 seconds after beginning of saturation (see maximum and minimum levels in contour plots). From that moment onwards saturation pulse is deliberately stopped and consequently the MTR asymmetry evolves towards zero (the thermal equilibrium state) with T1 relaxation time constant.

Taking a close look at the shape of the MTR_{asym} in figure 3.16.2, the emergence of a wavy pattern can be observed. This oscillating profile is a consequence of the pulsed irradiation, as was also seen in the example of figure 3.4.1. This can easily be verified by acknowledging that the number of oscillations match the periodicity of the saturation pulses train; one oscillation every 51 ms, in this case. While one could consider the existence of this wavy pattern as a problem for the stability of the CEST measurement, in practice it is not a concerning issue as the sampling of the data (the readout) is always done after an integer number of saturation loops, e.g. after 80 iterations of 'Gaussian pulse plus delay' blocks, but never after 80.5 iterations.

Only in the case of a more complicated saturation scheme, in which one would like to sample the data at a different phase of the saturation loop, the oscillations would have to be carefully taken into account in order get reliable CEST measurements.

Bringing attention back to the ΔMTR_{asym} in figure 3.16.1, it is noticeable that the surface reaches its maximum height within the first second of saturation irradiation, after which it approximates to a lower steady state value.

The different shapes of ΔMTR_{asym} curve at the first 6 seconds in the simulation are shown in figure 3.16.3.

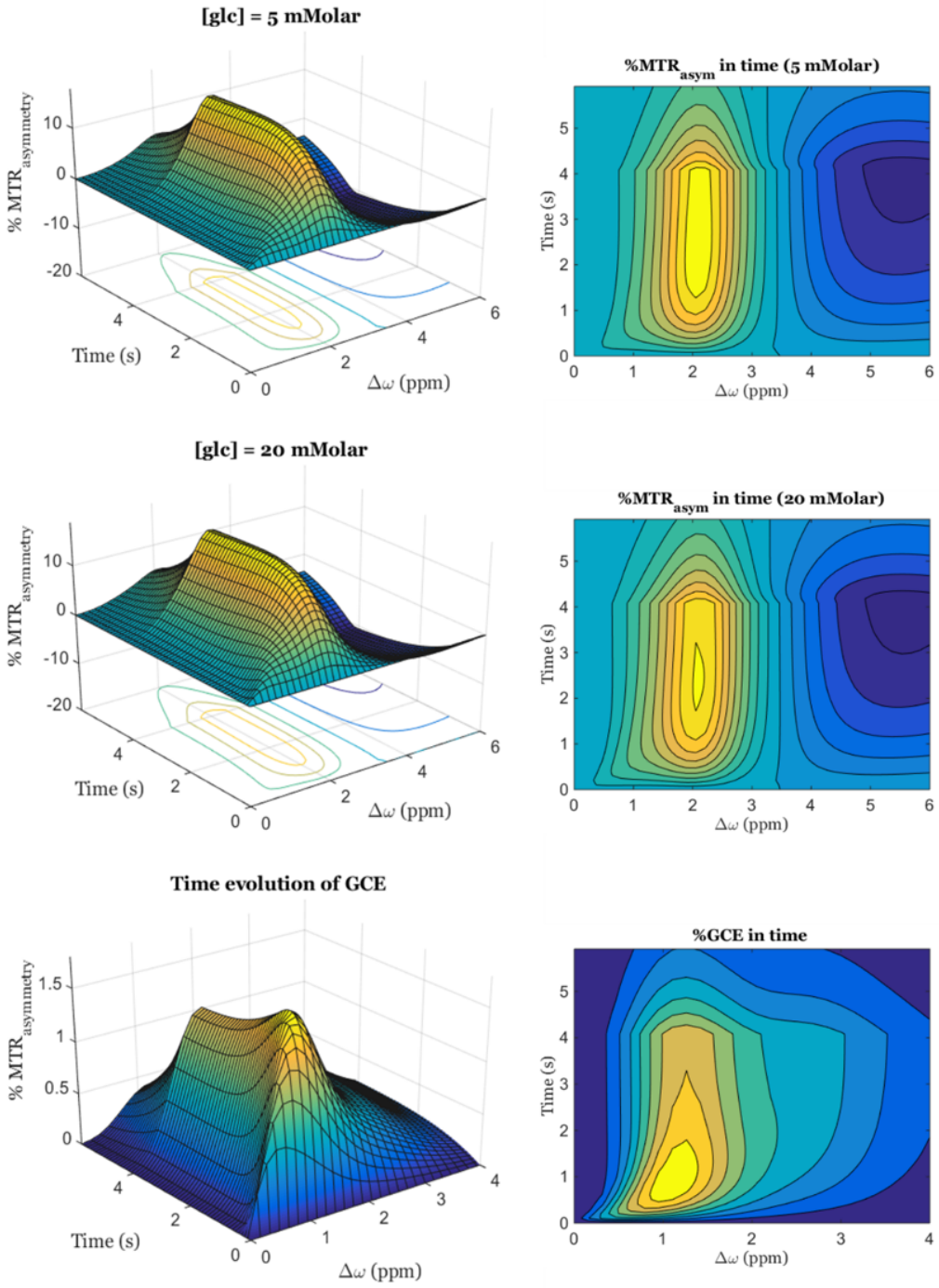

Figure 3.16.1.: *Time evolution of the MTR_{asym} and GCE in vivo conditions. The figure shows the MTR asymmetry in time for the case of 20 mMolar glucose content, 5 mMolar and the difference between the two, which gives rise to the GCE signal. Figure on the right shows the contour plots in each case. Notice how the GCE signal peaks in less than a second around the 1.2 ppm range. After about 3.5 seconds of saturation, the system approaches steady state where barely no changes are observed. After 4 seconds, the saturation pulse is stopped and the magnetisations evolves towards the thermal equilibrium value.*

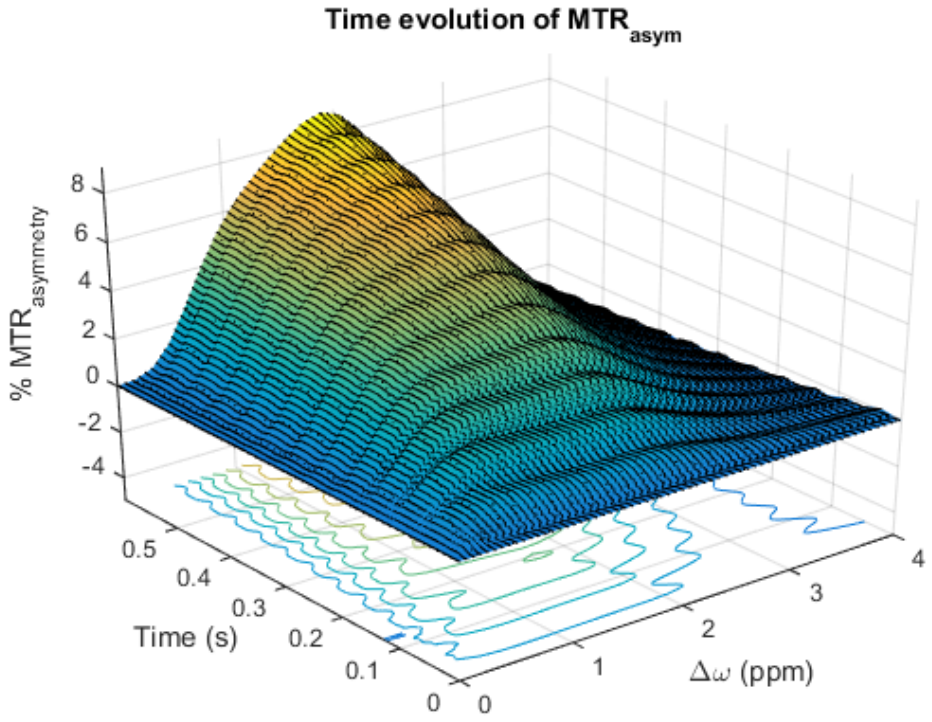

Figure 3.16.2.: *Oscillations due to pulsed saturation. The amplitude of the MTR asymmetry oscillates with the same periodicity as the Gaussian pulses, according to the variations in the instantaneous supply of power. In practice these oscillations are not observable as the data acquisition occurs always in the same phase, after an integer number of Gaussian pulses.*

Saturation length of as short as 1 second yields a higher glucoCEST contrast provided that the integration of the ΔMTR_{asym} signal is performed around 1.2 ppm. It is clear from the graphs that achieving steady state (with ~4 second saturation) does not necessarily provide the largest CEST signal. The significance of this result is that shorter saturation times can be used without compromising the quality of the signal. This has the advantage of shorter scan times (although time savings would be moderate as sufficient time between readouts has to be allowed for the recovery of the magnetisation), and more importantly the advantage of lower SAR values.

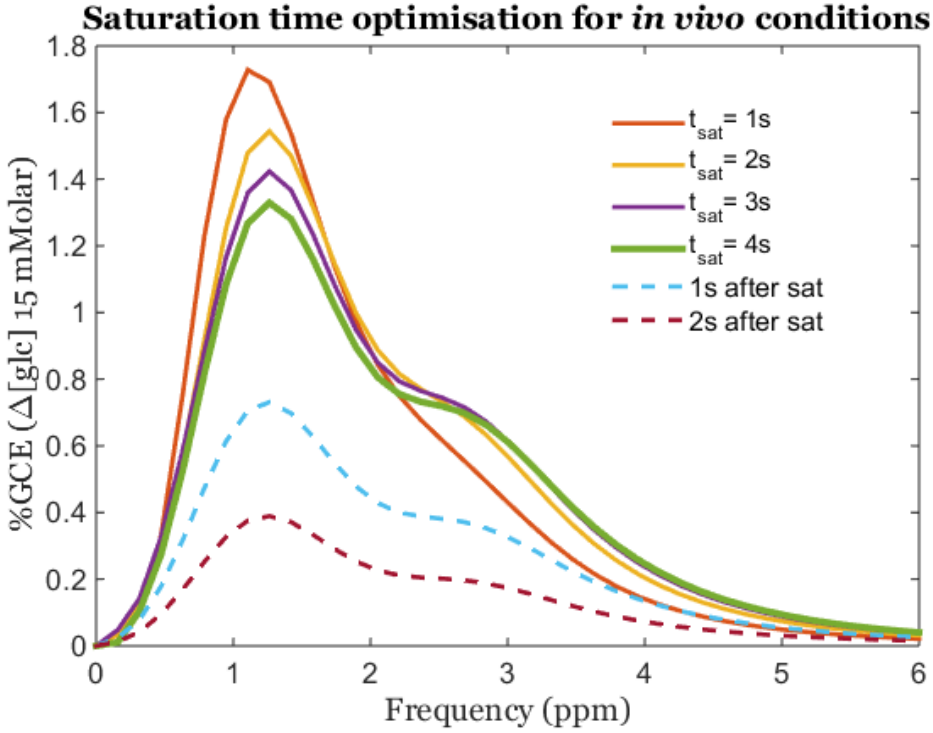

Figure 3.16.3.: *GCE profile at different saturation length. GCE build up quickly for fast exchanging hydroxyl groups, providing maximum signal at short saturation times. Long saturation stabilises the signal in the steady state with lower maximum asymmetry. After saturation is stopped GCE relaxes towards zero with T1.*

At 3 Tesla the reduction of the signal close to water due to direct saturation is more severe than at 9.4 Tesla (because the chemical shift is proportional to B0 while the absorption lineshape remains constant). Furthermore, commonly clinical MRI scanner manufacturers limit the maximum duty cycle for long RF pulses to 50%. This produces peaks of high saturation power which aggravate the effect of direct saturation for a given equivalent B1. As a consequence the GCE at 3T reaches its maximum amplitude around 2 ppm, in contrast to the 1 ppm range observed at 9.4T. Figure 3.16.4 shows the peak of the GCE signal to move away from the water

frequency as the slow MT effect builds up. The maximum intensity is achieved around the 2 ppm range for B1 power of 2 μT.

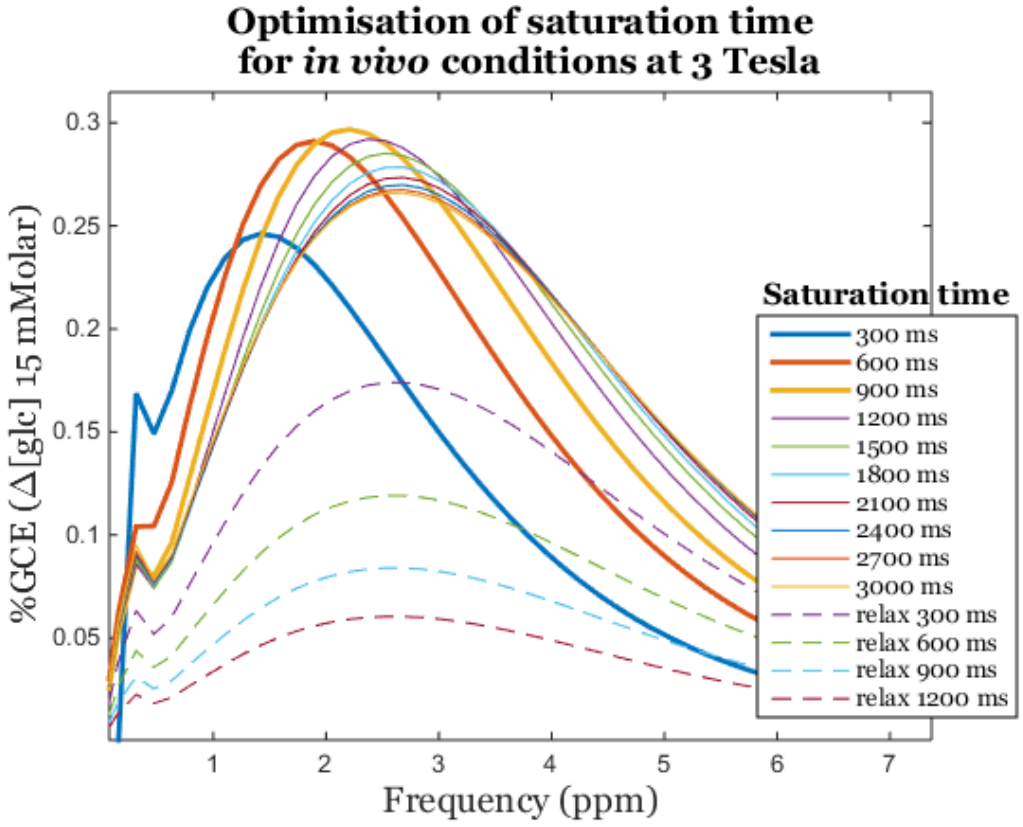

Figure 3.16.4.: *Saturation time optimisation at 3T. The GCE signal peaks at around 2 ppm and saturation length below 1 second. At steady steady state signal stabilises close to 3 ppm but with lower intensity than at shorter saturation times.*

3.17. Conclusion

The exchange principle behind CEST can be easily expressed in a mathematical form. Ranging from the most simple two-pool system to more complex multi-pool interactions, the dynamics of CEST can be accurately described using computer simulations.

This allows the inspection of each parameter's effect on the final CEST signal and helps form an intuitive understanding of the expected experimental result, before testing it in a real setting.

With this information, the process of optimising a CEST sequence for a particular application becomes more guided and efficient rather than a blind trial and error process.

In this chapter the behaviour of the CEST contrast under several conditions has been analysed. The CEST profile of glucose in different concentrations has been accurately modelled as well as the general Z-spectra of a mouse brain *in vivo*, which included the contributions of amides, amines, and aliphatic protons, as well as MT. The impact of different macromolecular pool content and pH levels on the MTR asymmetry have been assessed.

For cases where physiological noise is present, the benefits of taking a normalisation reference close to water has been explained. Along the same lines an alternative measure of CEST asymmetry has been proposed which is inherently normalised by its definition. As for the raw noise, the relationship between the saturation power, reliability of CEST contrast and the level of noise in data has been shown. The analysis indicated that for investigating glucose, B1 power levels of around 3 to 4 μT yields good CEST contrast in most situations and that an increase of power above that level is likely to increase uncertainty in the measurement due to loss in SNR.

The expected signal in an *in vivo* glucoCEST experiment is generally small. This is particularly true at low B0 fields and poses a big challenge for glucoCEST in the clinic where current standard strength is 3 Tesla and only a few centres in the world have access to 7 Tesla human scanners. Efforts to increase SNR are therefore necessary. Repeated acquisitions aimed to average noise out and sacrifices in spatial resolution may be required in order to confidently measure the glucoCEST signal.

On the other hand, optimisation of the scanned offset frequencies and the saturation length can yield increases in the GCE signal. The simulations show that at B0 field of 9.4 Tesla integration range around the 1.2 ppm offset provides the maximum glucoCEST contrast while at 3 Tesla and saturation with 50% duty cycle the optimum integration range appears to be around the 2 ppm range from water. At both fields short saturation times (below 1 second) offer superior signal than at steady state, which also helps reduce the acquisition time as well as the SAR of the glucoCEST protocol.

Chapter references

[1] F. Bloch. “Nuclear Induction”. In: *Physical Review* 70.7-8 (Oct. 1, 1946). 05782, pp. 460–474. DOI: 10.1103/PhysRev.70.460 (cit. on p. 83).

[2] Harden M. McConnell. “Reaction Rates by Nuclear Magnetic Resonance”. In: *The Journal of Chemical Physics* 28.3 (Mar. 1, 1958). 01286, pp. 430–431. ISSN: 0021-9606, 1089-7690. DOI: 10.1063/1.1744152 (cit. on p. 83).

[3] Daniel Abergel and Arthur G. Palmer. “Approximate solutions of the Bloch-McConnell equations for two-site chemical exchange”. In: *Chemphyschem: A European Journal of Chemical Physics and Physical Chemistry* 5.6 (June 21, 2004). 00012, pp. 787–793. ISSN: 1439-4235. DOI: 10.1002/cphc.200301051. pmid: 15253305 (cit. on p. 83).

[4] Clare Morrison and R. Mark Henkelman. “A Model for Magnetization Transfer in Tissues”. In: *Magnetic Resonance in Medicine* 33.4 (Apr. 1995). 00166, pp. 475–482. ISSN: 07403194, 15222594. DOI: 10.1002/mrm.1910330404 (cit. on pp. 83, 97).

[5] Guanshu Liu, Xiaolei Song, Kannie W Y Chan, and Michael T McMahon. “Nuts and bolts of chemical exchange saturation transfer MRI”. In: *NMR in biomedicine* (Jan. 10, 2013). Cited by 0003. ISSN: 1099-1492. DOI: 10.1002/nbm.2899 (cit. on pp. 83, 93, 100).

[6] Kenya Murase and Nobuyoshi Tanki. “Numerical solutions to the time-dependent Bloch equations revisited.” In: *Magnetic resonance imaging* 29.1 (Jan. 2011). Cited by 0009, pp. 126–131. DOI: 10.1016/j.mri.2010.07.003 (cit. on p. 84).

[7] Kenya Murase. “Generalized equation for describing the magnetization in spoiled gradient-echo imaging”. In: *Magnetic Resonance Imaging* 29.5 (June 2011). 00002, pp. 723–730. ISSN: 0730725X. DOI: 10.1016/j.mri.2011.02.005 (cit. on p. 84).

[8] Simon Walker-Samuel, Rajiv Ramasawmy, Francisco Torrealdea, Marilena Rega, Vineeth Rajkumar, S. Peter Johnson, Simon Richardson, Miguel Gonçalves, Harold G. Parkes, Erik Arstad, David L. Thomas, R. Barbara Pedley, Mark F. Lythgoe, and Xavier Golay. “In vivo imaging of glucose uptake and metabolism in tumors”. In: *Nature Medicine* 19.8 (Aug. 2013). 00044 Cited by 0001, pp. 1067–1072. ISSN: 1078-8956. DOI: 10.1038/nm.3252 (cit. on pp. 88, 91).

[9] Peter C M van Zijl and Nirbhay N Yadav. “Chemical exchange saturation transfer (CEST): what is in a name and what isn’t?” In: *Magnetic resonance in medicine* 65.4 (Apr. 2011). Cited by 0073, pp. 927–948. DOI: 10.1002/mrm.22761 (cit. on pp. 93, 100, 101).

[10] Gunnan Kruger. “Physiological Noise in Oxygenation-Sensitive Magnetic Resonance Imaging”. In: *Magnetic Resonance in Medicine* 46 (2001), pp. 631–637 (cit. on p. 94).

[11] Kejia Cai, He N Xu, Anup Singh, Mohammad Haris, Ravinder Reddy, and Lin Z Li. "Characterizing prostate tumor mouse xenografts with CEST and MT-MRI and redox scanning". In: *Advances in experimental medicine and biology* 765 (2013). 00005 Cited by 0002, pp. 39–45. ISSN: 0065-2598. DOI: 10.1007/978-1-4614-4989-8_6 (cit. on p. 95).

[12] Feliks Kogan, Hari Hariharan, and Ravinder Reddy. "Chemical Exchange Saturation Transfer (CEST) Imaging: Description of Technique and Potential Clinical Applications". In: *Current Radiology Reports* 1.2 (June 2013), pp. 102–114. ISSN: 2167-4825. DOI: 10.1007/s40134-013-0010-3 (cit. on p. 95).

[13] Kejia Cai, Mohammad Haris, Anup Singh, Feliks Kogan, Joel H Greenberg, Hari Hariharan, John A Detre, and Ravinder Reddy. "Magnetic resonance imaging of glutamate". In: *Nature Medicine* 18.2 (Jan. 22, 2012), pp. 302–306. ISSN: 1078-8956, 1546-170X. DOI: 10.1038/nm.2615 (cit. on p. 95).

[14] Kannie W. Y. Chan, Michael T. McMahon, Yoshinori Kato, Guanshu Liu, Jeff W. M. Bulte, Zaver M. Bhujwalla, Dmitri Artemov, and Peter C. M. van Zijl. "Natural D-glucose as a biodegradable MRI contrast agent for detecting cancer". In: *Magnetic Resonance in Medicine* 68.6 (2012). Cited by 0012, pp. 1764–1773. ISSN: 1522-2594. DOI: 10.1002/mrm.24520 (cit. on p. 95).

[15] Kimberly L Desmond and Greg J Stanisz. "Understanding quantitative pulsed CEST in the presence of MT". In: *Magnetic resonance in medicine: official journal of the Society of Magnetic Resonance in Medicine / Society of Magnetic Resonance in Medicine* 67.4 (Apr. 2012). Cited by 0015, pp. 979–990. ISSN: 1522-2594. DOI: 10.1002/mrm.23074 (cit. on p. 95).

[16] Jinyuan Zhou, Bachchu Lal, David A. Wilson, John Laterra, and Peter C.M. van Zijl. "Amide proton transfer (APT) contrast for imaging of brain tumors". In: *Magnetic Resonance in Medicine* 50.6 (Dec. 2003). 00205, pp. 1120–1126. ISSN: 0740-3194, 1522-2594. DOI: 10.1002/mrm.10651 (cit. on p. 95).

[17] Phillip Zhe Sun, Jinyuan Zhou, Judy Huang, and Peter van Zijl. "Simplified quantitative description of amide proton transfer (APT) imaging during acute ischemia". In: *Magnetic Resonance in Medicine* 57.2 (Feb. 2007). 00074, pp. 405–410. ISSN: 07403194, 15222594. DOI: 10.1002/mrm.21151 (cit. on p. 95).

[18] Phillip Zhe Sun, Jerry S Cheung, Enfeng Wang, Thomas Benner, and A Gregory Sorensen. "Fast multislice pH-weighted chemical exchange saturation transfer (CEST) MRI with Unevenly segmented RF irradiation." In: *Magnetic Resonance in Medicine* 65.2 (Feb. 2011). Cited by 0019, pp. 588–594. DOI: 10.1002/mrm.22628 (cit. on p. 95).

[19] Phillip Zhe Sun, Enfeng Wang, and Jerry S. Cheung. "Imaging acute ischemic tissue acidosis with pH-sensitive endogenous amide proton transfer (APT) MRI—Correction of tissue relaxation and concomitant RF irradiation effects toward mapping quantitative cerebral tissue pH". In: *NeuroImage* 60.1 (Mar. 2012). 00028, pp. 1–6. ISSN: 10538119. DOI: 10.1016/j.neuroimage.2011.11.091 (cit. on p. 95).

[20] K.M Ward, A.H Aletras, and R.S Balaban. "A New Class of Contrast Agents for MRI Based on Proton Chemical Exchange Dependent Saturation Transfer (CEST)". In: *Journal of Magnetic Resonance* 143.1 (Mar. 2000). 00572, pp. 79–87. ISSN: 10907807. DOI: 10.1006/jmre.1999.1956 (cit. on p. 95).

[21] Phillip Zhe Sun, Thomas Benner, Ashok Kumar, and A. Gregory Sorensen. “Investigation of optimizing and translating pH-sensitive pulsed-chemical exchange saturation transfer (CEST) imaging to a 3T clinical scanner”. In: *Magnetic Resonance in Medicine* 60.4 (Oct. 2008). 00071, pp. 834–841. ISSN: 07403194, 15222594. DOI: 10.1002/mrm.21714 (cit. on p. 97).

[22] Dario Livio Longo, Enza Di Gregorio, Riccardo Abategiovanni, Alberto Ceccon, Michael Assfalg, Henriette Molinari, and Silvio Aime. “Chemical exchange saturation transfer (CEST): an efficient tool for detecting molecular information on proteins’ behaviour”. In: *The Analyst* 139.11 (2014), p. 2687. ISSN: 0003-2654, 1364-5528. DOI: 10.1039/c4an00346b (cit. on p. 97).

[23] Dario Livio Longo, Walter Dastrù, Giuseppe Digilio, Jochen Keupp, Sander Langereis, Stefania Lanzardo, Simone Prestigio, Oliver Steinbach, Enzo Terreno, Fulvio Uggeri, and Silvio Aime. “Iopamidol as a responsive MRI-chemical exchange saturation transfer contrast agent for pH mapping of kidneys: In vivo studies in mice at 7 T”. In: *Magnetic Resonance in Medicine* 65.1 (Jan. 1, 2011). 00056, pp. 202–211. ISSN: 1522-2594. DOI: 10.1002/mrm.22608 (cit. on p. 97).

[24] Marilena Rega. “Validation of APT as a measure of pH by 31P in a piglet model of HIE”. In: *CEST Contrast: Methods & Applications*. ISMRM. 00000. Milan, 2014 (cit. on p. 97).

[25] A. Ramani, C. Dalton, D. H. Miller, P. S. Tofts, and G. J. Barker. “Precise estimate of fundamental in-vivo MT parameters in human brain in clinically feasible times”. In: *Magnetic Resonance Imaging* 20.10 (Dec. 2002). 00125, pp. 721–731. ISSN: 0730-725X. DOI: 10.1016/S0730-725X(02)00598-2 (cit. on p. 97).

[26] C. Morrison, G. Stanisz, and R. M. Henkelman. “Modeling Magnetization Transfer for Biological-like Systems Using a Semi-solid Pool with a Super-Lorentzian Lineshape and Dipolar Reservoir”. In: *Journal of Magnetic Resonance, Series B* 108.2 (Aug. 1995), pp. 103–113. ISSN: 1064-1866. DOI: 10.1006/jmrb.1995.1111 (cit. on p. 97).

[27] Christopher D. J. Sinclair, Rebecca S. Samson, David L. Thomas, Nikolaus Weiskopf, Antoine Lutti, John S. Thornton, and Xavier Golay. “Quantitative magnetization transfer in in vivo healthy human skeletal muscle at 3 T”. In: *Magnetic Resonance in Medicine* 64.6 (Dec. 2010), pp. 1739–1748. ISSN: 07403194. DOI: 10.1002/mrm.22562 (cit. on p. 97).

[28] R. Mark Henkelman, Xuemei Huang, Qing-San Xiang, G. J. Stanisz, Scott D. Swanson, and Michael J. Bronskill. “Quantitative interpretation of magnetization transfer”. In: *Magnetic Resonance in Medicine* 29.6 (June 1, 1993). 00406, pp. 759–766. ISSN: 1522-2594. DOI: 10.1002/mrm.1910290607 (cit. on p. 97).

[29] Richard D. Dortch, Jay Moore, Ke Li, Marcin Jankiewicz, Daniel F. Gochberg, Jane A. Hirtle, John C. Gore, and Seth A. Smith. “Quantitative magnetization transfer imaging of human brain at 7 T”. In: *NeuroImage* 64 (Jan. 1, 2013). 00000, pp. 640–649. ISSN: 1053-8119. DOI: 10.1016/j.neuroimage.2012.08.047 (cit. on p. 97).

[30] Karim Snoussi, Jeff W.M. Bulte, Maurice Gueron, and Peter C.M. van Zijl. “Sensitive CEST agents based on nucleic acid imino proton exchange: Detection of poly(rU) and of a dendrimer-poly(rU) model for nucleic acid delivery and pharmacology”. In: *Magnetic Resonance in Medicine* 49.6 (June 2003), pp. 998–1005. ISSN: 0740-3194, 1522-2594. DOI: 10.1002/mrm.10463 (cit. on p. 100).

[31] Moritz Zaiss, Junzhong Xu, Steffen Goerke, Imad S. Khan, Robert J. Singer, John C. Gore, Daniel F. Gochberg, and Peter Bachert. “Inverse Z-spectrum analysis for spillover, MT, and T1 corrected steady-state pulsed CEST-MRI - application to pH-weighted MRI of acute stroke.” In: *NMR in Biomedicine* 27.3 (Mar. 2014), pp. 240–252. ISSN: 09523480. DOI: 10.1002/nbm.3054 (cit. on p. 100).

[32] Moritz Zaiss, Benjamin Schmitt, and Peter Bachert. “Quantitative separation of CEST effect from magnetization transfer and spillover effects by Lorentzian-line-fit analysis of z-spectra”. In: *Journal of Magnetic Resonance* 211.2 (Aug. 2011). 00046, pp. 149–155. ISSN: 10907807. DOI: 10.1016/j.jmr.2011.05.001 (cit. on p. 100).

[33] Hakon Gudbjartsson and Samuel Patz. “The Rician Distribution of Noisy MRI Data”. In: *Magnetic resonance in medicine : official journal of the Society of Magnetic Resonance in Medicine / Society of Magnetic Resonance in Medicine* 34.6 (Dec. 1995), pp. 910–914. ISSN: 0740-3194. pmid: 8598820 (cit. on p. 102).

[34] Mehdi Damaghi, Jonathan W. Wojtkowiak, and Robert J. Gillies. “pH sensing and regulation in cancer”. In: *Frontiers in Physiology* 4 (2013). 00016. ISSN: 1664-042X. DOI: 10.3389/fphys.2013.00370 (cit. on p. 103).

[35] Nevin McVicar, Alex X Li, Daniela F Gonçalves, Miranda Bellyou, Susan O Meakin, Marco AM Prado, and Robert Bartha. “Quantitative tissue pH measurement during cerebral ischemia using amine and amide concentration-independent detection AACID with MRI”. In: *Journal of Cerebral Blood Flow & Metabolism* 34.4 (Apr. 2014). 00008, pp. 690–698. ISSN: 0271-678X, 1559-7016. DOI: 10.1038/jcbfm.2014.12 (cit. on p. 103).

[36] D. A. Rottenberg, J. Z. Ginos, K. J. Kearfott, L. Junck, and D. D. Bigner. “In vivo measurement of regional brain tissue pH using positron emission tomography”. In: *Annals of Neurology* 15 (S1 Jan. 1, 1984), pp. 98–102. ISSN: 1531-8249. DOI: 10.1002/ana.410150718 (cit. on p. 103).

[37] Greg J. Stanisz, Ewa E. Odrobina, Joseph Pun, Michael Escaravage, Simon J. Graham, Michael J. Bronskill, and R. Mark Henkelman. “T1, T2 relaxation and magnetization transfer in tissue at 3T”. In: *Magnetic Resonance in Medicine* 54.3 (Sept. 2005), pp. 507–512. ISSN: 0740-3194, 1522-2594. DOI: 10.1002/mrm.20605 (cit. on p. 109).

4. Chemical exchange properties of glycolytic sugars

4.1. Abstract

In this chapter the CEST properties of the first four sugars along the glycolytic pathway (glucose, glucose 6-phosphate (G6P), fructose 6-phosphate (F6P) and fructose 1,6-biphosphate (F16bP)) are explored under different conditions. Glucose and the first three glycolytic intermediate molecules will be tested as potential CEST agents which may be exploited as markers of increased metabolic activity in cancer and other conditions in which the metabolism is disturbed. With the obtained results the possibility of intracellular origin of glucoCEST signal is discussed.

As the second part of the study, the influence of glucose on the observed relaxation rate R2 is investigated. The method has been recently proposed by Yadav *et al.*[1] as an alternative method to glucoCEST for the detection of small concentration of glucose with MRI. Results of the T_2 relaxivity due to glucose are compared to the contrast obtained from CEST.

4.2. Introduction

GlucoCEST has been shown to be sensitive to distinguish elevated glucose uptake in tumours.[2] However, to this date, it is not clear whether the glucoCEST signal comes from glucose molecules only, or if other sugars from the break down process of glucose contribute to the signal as well.

Initial reports in the literature revealed a sceptical opinion about the possibility of intracellular signal detection. However, more recent reports consider the source of glucoCEST signal as being intracellular.[2–5]

If shown to be the case, the detection of intracellular glucoCEST signal could open an exciting possibility to study the kinetics of cellular glucose uptake and utilisation with MRI. This kind of dynamic analysis can be useful for the characterisation of

several conditions associated with dis-regulated glucose metabolism including diabetes, neurological disorders such as epilepsy and cancer.

4.2.1. Bioenergetic pathways background

4.2.1.1. Cellular Respiration

Cellular catabolic reactions convert biochemical energy from nutrients into adenosine triphosphate (ATP), the energy 'currency' of living organisms. The chemical energy stored* in ATP is used to drive energy hungry processes including cell signalling, biosynthesis, locomotion or transportation of molecules across cell membranes.[6,7] The process of converting organic matter into small energy packages able to generate work is generally called cellular respiration.

Across nearly all living organisms, glucose is the primary fuel molecule used to harvest energy through cellular respiration. Overall, the metabolism of glucose inside the cell consists of the oxidation of glucose to CO_2 and H_2O. In the process, through a complex path of enzymatic chemical reactions, more than 30 molecules of high energy ATP are synthesized from adenosine diphosphate (ADP) and inorganic phosphate Pi.[8] Overall the process of harvesting energy from glucose can be divided into three stages namely, glycolysis, citric acid cycle and the electron transport chain.

For conciseness and relevance to this work, the process of glycolysis will be explained in the following and only a brief mention of the citric acid cycle and the electron transport chain will be made for completeness. To obtain more information about the metabolism of carbohydrates specificity please see reference Lodish et al.[9] in the bibliography.

4.2.1.2. Glycolysis

Glucose is transferred into the cytosol of the cell by the GLUT† transporters where the process of glycolysis takes place. In the glycolytic process, also known as the Embden-Meyerhof pathway, glucose is split into two molecules of pyruvate with a resulting net production of two molecules of ATP per molecule of glucose.

The chain of glycolytic reactions is constituted by the following 10 steps:

*The weakly bonded phosphate groups in ATP molecules are easy to brake which allows stronger bonds to form, effectively transferring energy from one molecule to another.

†GLUT or glucose transporters are a group of membrane proteins that facilitate the transport of glucose across plasma membranes. Each GLUT isoform plays a precise role in the metabolism of glucose, which is determined by its specificity to substrates, the transport kinetics, and their regulation under different physiological conditions.[10,11]

1.

$$\mathbf{G} \rightarrow \mathbf{G6P}\ \ (-\mathbf{ATP})$$

Phosphorylation of glucose (G) into glucose-6-phosphate (G6P). The hydrogen on the alcohol on carbon 6 of glucose is replaced by a phosphate group from the ATP by hexokinase enzyme.

2.

$$\mathbf{G6P} \rightarrow \mathbf{F6P}$$

Phosphoglucose isomerase changes the glucose structure to fructose by swapping the C=O and alcohol groups on carbons 1&2 to form fructose-6-phosphate (F6P).

3.

$$\mathbf{F6P} \rightarrow \mathbf{F16biP}\ \ (-\mathbf{ATP})$$

Phosphofructokinase replaces the hydrogen on the alcohol group of C1 with another phosphate group to produce fructose-1,6-bisphosphate (F16biP).

4.

$$\mathbf{F16biP} \rightarrow \mathbf{GLAP} + \mathbf{DHAP}$$

Aldolase splits F16biP into two 3 carbon molecules, glyceraldehyde 3-phosphate (GLAP) and dihydroxyacetone phosphate (DHAP).

5.

$$\mathbf{DHAP} \rightarrow \mathbf{GLAP}$$

Triose phosphate isomerase converts DHAP into GLAP by changing the structural configuration. From this step onwards there are two molecules per one of glucose.

6.

$$2x\ \ \{\mathbf{GLAP} \rightarrow \mathbf{13biPG}\ \ (-\mathbf{P_i})\ (+\mathbf{NADH})\}$$

Glyceraldehyde 3-phosphate dehydrogenase replaces hydrogen on C1 with oxygen and a phosphate group to produces 1,3-bisphosphoglycerate (13biPG) and a reduced nicotinamide adenine dinucleotide molecule (NADH).

7.

$$2x\ \ \{\mathbf{13biPG} \rightarrow \mathbf{3PG}\ \ (+\mathbf{ATP})\}$$

Phosphoglycerate kinase removes the phosphate group from C1 from 13biPG to give 3-phosphoglycerate (3PG) and adenosine triphosphate (ATP).

8.
$$2x\ \{\mathbf{3PG} \rightarrow \mathbf{2PG}\}$$

Phosphoglycerate mutase swaps C2 & C3 to create 2-phosphoglycerate (2PG).

9.
$$2x\ \{\mathbf{2PG} \rightarrow \mathbf{2PEP}\ (+\mathbf{H_2O})\}$$

Enolase removes the alcohol on C3 forming a C=C between C2 & C3 and produces phosphoenolpyruvate (PEP) and water.

10.
$$2x\ \{\mathbf{2PEP} \rightarrow \mathbf{Pyruvate}\ (+\mathbf{ATP})\}$$

Pyruvate kinase removes the phosphate group from C2 in 2PG to yield in pyruvate and another ATP molecule.

Glycolysis alone brings just about 5% of all the biochemical energy in glucose. However, it is a very rapid reaction and most importantly it does not rely on oxygen.

During step 6 of the intermediates glycolytic reactions the coenzyme nicotinamide adenine dinucleotide NAD+ is reduced to NADH. This coenzyme is essential for glycolysis and the reaction cannot continue in its absence, which is why a constant replenishment of NAD+ in the cytosol is required. In normal oxygen conditions (normoxia) the regeneration occurs via the mitochondrial oxidation of NADH in the electron transport chain.

In the absence of oxygen, the cell resorts to an emergency procedure. In this situation, glycolysis does not end in pyruvate but in lactate instead mediated by one last reaction.

$$2x\ \{\mathbf{Pyruvate} + \mathbf{NADH} + \mathbf{H}^+ \rightarrow \mathbf{Lactate} + \mathbf{NAD}^+\}$$

The NADH is re-oxidized by reducing pyruvate to produce lactate. The production of lactate from glucose is known as anaerobic glycolysis and is a rapid process that allows glycolysis to proceed at a fast rate*

*In cancer cells the anaerobic glycolysis pathway is active even in the presence of oxygen, a phenomenon known in the cancer research field as the '*Warburg effect*' or somewhat confusingly as '*aerobic glycolysis*', to emphasise the fact that the fermentative (lactic acid) process occurs despite the abundance of oxygen. The over-expression of the '*aerobic glycolysis*' in tumour cells is considered a Hallmark of Cancer which is further analysed in Chapter 5.

The net production of ATP by glycolysis (in the absence of oxygen) is two molecules of ATP per molecule of glucose. But as a fast reaction it can provide energy and the necessary glycolytic intermediates at an elevated rate. Despite an inefficient ratio of ATP generation per glucose consumed, glycolysis can produce ATP molecules at a rate 100 times faster than the aerobic respiration.[12] This is part of the reason why during short periods of intense exercise, when oxygen supply cannot cope with the demand, muscle cells switch to anaerobic glycolysis.

It is important to be reminded that the cellular membrane is not permeable to the sugars produced in the glycolytic chain, and unlike glucose which is abundant outside the cell, the glycolytic intermediates are only present inside the cell.

4.2.1.3. Citric acid cycle and electron transport chain

A protein transport system takes the pyruvate from the cytoplasm into the mitochondria. In the mitochondria the pyruvate formed during glycolysis gets converted to acetyl CoA. Enzymatic reactions known as the citric acid cycle, Kreb's Cycle or Tricarboxylic Acid Cycle, breakdown the acetyl CoA into CO2 and H2O with the release of energy in the form of ATP, NADH and FADH2.

In the electron transport chain the electron carriers in the inner mitochondrial membrane are organized in such a way that each transport steps reduces the free energy of the biochemical system. The released energy in these reactions is used to generate ATP from ADP and P_i. Overall, thirty molecules of ATP are synthesized per one molecule of glucose. In the process NADH formed in glycolysis gets re-oxidized to NAD+ which keeps the glycolytic metabolic cycle going in the cytoplasm.

4.3. Aim of the study

4.3.1. Parameter optimisation

A number of parameters influence the CEST signal. As such part of this study aims to explore which of these parameter and under which conditions the CEST contrast could be maximised. The dependence of CEST data on sugar levels, concentration of phosphates, pH values, temperature and B1 saturation power will be explored in each of the glycolytic intermediate molecules.

To shed some light on whether intracellular sugars could contribute to the observed CEST signal, a phantom experiment was planned, aiming to investigate the

CEST signal response of the first four molecules in the glycolytic pathway, at conditions similar to the expected ones in vivo.

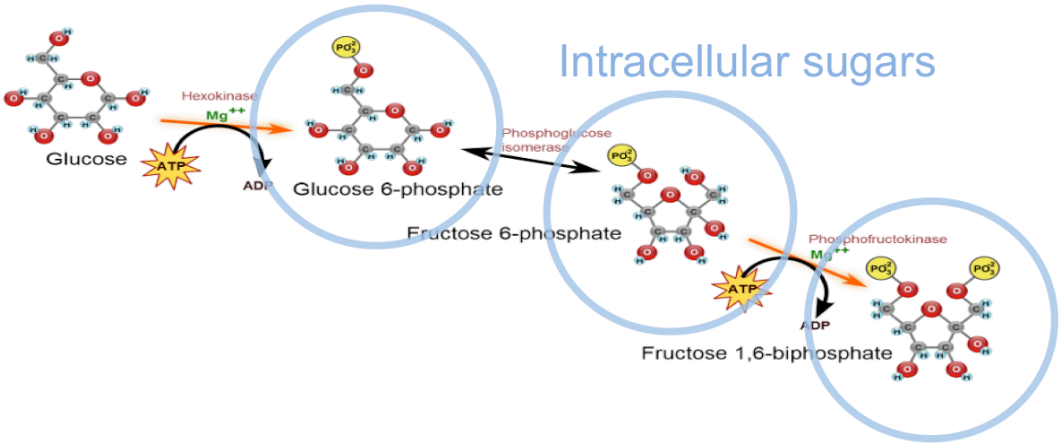

Figure 4.3.1.: *The monosaccharides involved in the first 3 steps of the glycolytic pathway. Among them only glucose is present outside the cells.*

4.3.2. Spatial reproducibility check

When dealing with small signals any variations in the setup can yield to significant changes in the experiment outcome. One possible variation is the performance of the transmitter coil to produce an homogenous irradiation field inside the coil. Spatial variations of the B1 field could result in important signal drifts. To address this concern a study was planned to measure the robustness of the CEST measurement by scanning sugar samples at two positions inside the RF coil. Simply enough the second setting was obtained by rotating the sample 90°clockwise from the original position (see Figure 4.5.13).

4.3.3. Relaxation time

Chemical exchange processes in a solution are known to alter the observed relaxation time of the solvent. In a second part of the study, the effect of glucose on the relaxation properties of water is analysed. Comparison between CEST data, T_1 and T_2 maps are performed in order to check possible relationships between the two contrast mechanisms and obtain more information on potential confounding factors affecting CEST imaging technique.

4.3.4. Correlation of T_2 with Z-spectrum width

Lastly, the relationship between the T_2 relaxation time of the sample and the width of the Z-spectrum will be explored as an alternative method to estimate T_2 relaxation times.

4.4. Experimental procedure

4.4.1. Sample preparation

Two groups of phantoms were prepared. The first set comprised 64 liquid phantoms, combining concentration of sugars and pH in a range of physiological values. A second set of 16 solid phantoms was prepared with relaxation times matching the ones *in vivo*. Specifics for each set are described below.

4.4.2. Liquid samples

Glucose, glucose 6-phosphate (G6P), fructose 6-phosphate (F6P) and fructose 1,6-biphosphate (F16biP) were chosen as they contain the largest number of exchangeable -OH groups, 5, 4, 4 and 3, respectively. Solution of these compounds were prepared in 1% PBS at the chosen concentrations of 5, 10, 20 and 40 mMolar. An initial highly concentrated sample was also prepared to be able to distinguish the resonance frequencies of the labile molecules from the marked peaks produced at high levels of CEST agent. Values for pH were calibrated at 6.8, 7.0, 7.2 and 7.4 using hydrochloric acid (HCl) and sodium hydroxide (NaOH). All phantoms were prepared and scanned within the same day to avoid potential pH drifts and consumption of glucose by bacteria. The samples were scanned at 23°, 29°, 33°and 37°Celsius, allowing a 30 minute gap between scans to guarantee constant temperature.

4.4.3. Solid samples

Solutions of glucose and glucose 6-phosphate were prepared with 3% agar and 0.07 mMolar gadolinium in 0.2X PBS solution, in order to achieve the consistency and relaxation times similar to the observed ones in the brain; T_1 of 1800 ms and T_2 of 40 ms (at 9.4 Tesla).

Solutions were prepared in gadolinium doped water to the specific concentrations and pH. The same amount of agar was added to all samples prior heating them in a microwave at low power setting. Calibration of pH was checked before and after

the cooking process to ensure stability of the pH. The different sugar concentrations were prepared ranging from 5 to 20 mMolar in steps of 5 mMolar. The pH was titrated at 4 different values; 7.3, 7.0, 6.7 and 6.4 using HCl and NaOH.

4.4.4. Temperature control

Temperature in the scanner was monitored by a thermocouple temperature probe and controlled by the flow of warm air though the scanner bore (Small Animal Instrument). For large sized phantoms, even when the mean temperature of the samples is stable, circulation of water due to convection is unavoidable. These water movements produce inhomogeneities which cannot be fixed by a standard B0 correction as the magnetic field variation is dynamic in time. As a consequence the saturation profile is less homogeneous and the quality of the CEST data gets affected. An effective way to reduce the harm is to make the phantoms smaller (particularly along the direction of the temperature gradient) and if possible to make more viscous phantoms that would resist the fast movements of mass. In practice the eroding effect of the convection phenomenon is not too concerning. The analysis of these type of phantoms usually requires information on the averaged CEST value for a particular sample, which leaves spatial information from a pixel by pixel analysis in a second place. Furthermore, for *in vivo* studies convection effects are minimal as the biological tissues are mostly semi-solids, have no large volumes of liquid around (CSF could be an exception, but no structural information is expected) and do not experience significant temperature gradients.

4.4.5. MRI Sequence

The phantoms were scanned in a horizontal 9.4T MR scanner (Agilent Technologies) with a volume receive/transmit RF coil with a 33 millimetre internal diameter (Rapid Biomedical). Prior the scan all phantoms were shimmed to a linewidth below 20 Hz (an average of 17 ± 3 Hz).

4.4.5.1. CEST

The sequence used to acquire the CEST data was a modified Turbo-FLASH (64x64, FOV=19x19x4mm, TR=3.5s, TE=1.52ms) for the readout part, with the inclusion of a 4.5 second duration pre-saturation train of pulses. Each pulse consisted of 50 millisecond Gaussian (standard deviation of 8.55 ms) RF shape followed by 5 ms delay to reduce the stress on the amplifier by lowering the duty cycle (91%). The Z-

spectrum was sampled at 59 equally distributed offsets over a 10 ppm range centred at the water frequency.

During the readout the data matrix was filled starting from the centre of the K-space and expanding towards the edges (inverse centric), in order to maximize the contrast in the low frequencies, at the expense of a higher definition in the images. This was done assuming the contrast in the CEST images changes smoothly, as would be the case inside each phantom.
A set of radiation powers were used, equivalent of a constant B1 RF pulse of 0.9, 1.28, 1.6, 1.92, 2.56 and 3.2 μT.

4.4.6. CEST analysis

Calculation of the CEST signal was done by fitting a Lorentzian curve to the Z-spectra in a pixel by pixel basis. To avoid any asymmetry errors when fitting the Lorentzian, data on the negative side of the spectrum (from -1 ppm to 0 ppm) were fitted. Subsequently, any B0 shifts found in the images were corrected by setting the frequency of water to minimum point of the Lorentzian fitted curve. Finally the CEST values were calculated by integrating the difference between the experimental Z-spectra and the fitted Lorentzian between 0 and 4 ppm.

It has to be noted that in the absence of aliphatic peaks, MTR asymmetry analysis produced the same outcomes as the Lorentzian fitting approach. Therefore, when referring to the CEST signal the term MTRasym will be used indistinctively.

Results and discussion

Part I:

4.5. CEST properties of sugars

4.5.1. CEST contrast in all the sugars

The first clear result is that all four molecules generate significant CEST signal. This is an important outcome because it confirms a necessary condition for the hypothesis of intracellular origin of CEST, that is, sugars formed inside the cell can generate CEST signal. For the case of G6P in particular, the averaged magnitude of the observed CEST is consistently within the same range as in glucose. There

are even certain conditions, discussed below, in which G6P appears to exceed the CEST contrast capacity of glucose.

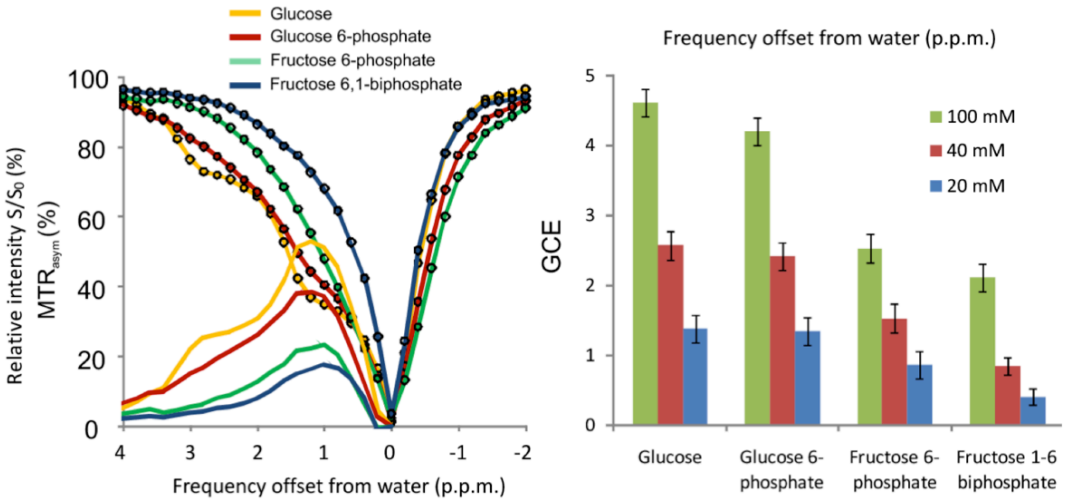

Figure 4.5.1.: *Reprinted from Walker-Samuel et al.[2] Left: Z- and MTRasym spectra from glucose, glucose 6-phosphate, fructose 6-phosphate and fructose 1,6-biphosphate, at 100 mM concentration and 37°C. Right: Averaged signal (integration of the MTR_{asym}) from the same sugars at different concentrations. The two pentoses, fructose 6-phosphate and fructose 1,6-biphosphate, give considerably less CEST signal.*

It is also worth noting at the signal discrepancies between the hexoses and the pentoses. At the same conditions, both hexoses (glucose and G6P) produce significantly higher signal than the pentoses (F6P and F16bP). The average signal ratios relative to glucose are 0.93 ± 0.11, 0.61 ± 0.09 and 0.54 ± 0.13 for G6F, F6P and F16bP respectively.

As a first guess one would expect the CEST signal to be proportional to the number of exchangeable sites in the molecule. The total number of hydroxyl groups in each of these monosaccharides is 5, 4, 4 and 3 for G, G6P, F6P and F16biP respectively. It is clear that this relationship does not match with the signal intensity observed experimentally.

4.5.1.1. CEST contributing protons in monosaccharides.

It is a well known fact in biochemistry that the anomeric * hydroxyls in the first carbon C1 are known to be very reactive; in fact they are the first natural link between monosaccharides to form disaccharides and polysaccharides.[9] Hence, the exchange of the protons in the anomeric hydroxyl is likely in a too fast regime for CEST, and will not have a significant contribution to the overall signal.

Furthermore, a closer look at the molecular structure of these sugars reveals 2 hydroxyl groups outside the ring structure (linked to C6 in G and to C1 in F6P and circled in red in figure 4.5.2).

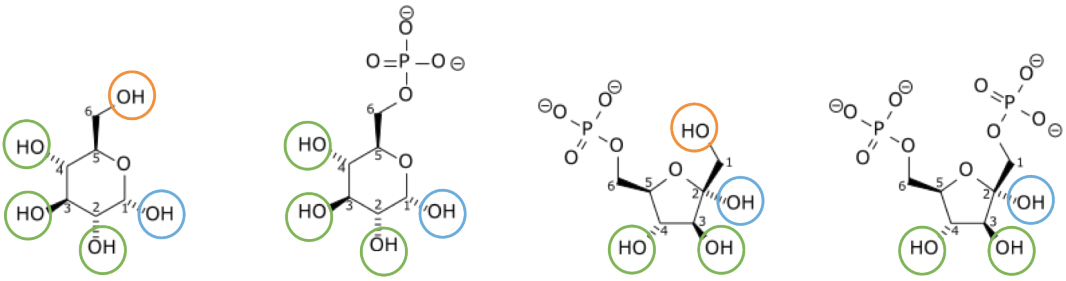

Figure 4.5.2.: *Molecular structure of G, G6P, F6P and F16biP. Hydroxyl groups in the cyclic structure are circled in green and blue, the last one being the anomeric site. Hydroxyls circled in orange are not part of the ring structure of the molecule and have little contribution in the CEST contrast.*

The enzymatic phosphorylation in glycolysis occurs at precisely these hydroxyls, which have a higher degree of mobility due to their position in the molecules. Not surprisingly, the NMR relaxation rate (dipolar relaxation) of hydroxyls groups in C6 has been reported to be more than twice as fast as other hydroxyls in the ring structure (excluding the fast exchange found in the anomeric hydroxyl).[13] This suggests that

*Carbohydrates dissolved in water usually exists in cyclic form. In its formation the linear aldehyde is bended to the side, taking the C5 hydroxyl close to the C1 aldehyde carbon. Once bonded C1 carbon atom becomes a new stereocenter, referred to as the anomeric center, and the α and β isomers are called anomers. The anomeric center is a site of enhanced reactivity in the sugar, in terms of substitution of the carbonyl. The anomeric hydroxyl group and a hydroxyl group of another sugar can join together, releasing a water molecule to form a glycosidic bond.

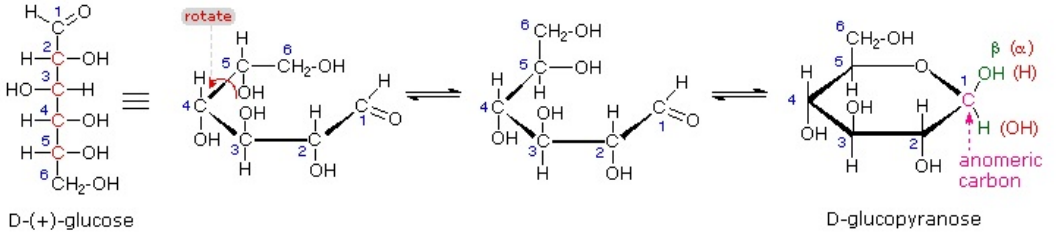

the chemical exchange rate for this particular hydrogen will also be enhanced and as a matter of fact, the second branch in polysaccharide such as starch or glycogen is formed through a link at the C6. See figure 4.5.3.

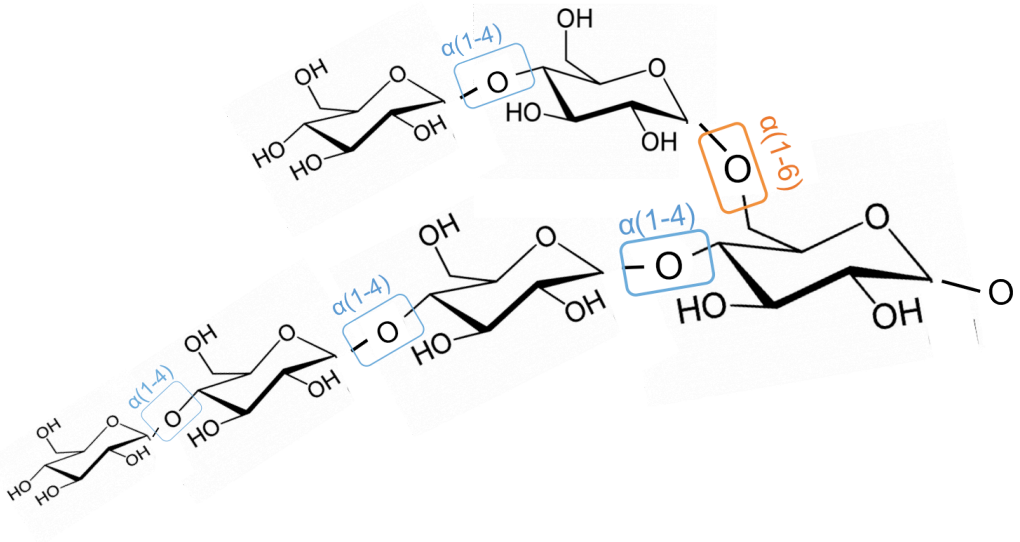

Figure 4.5.3.: *Molecular branched structure of glycogen. Glucose molecules are linked together linearly by $\alpha(1 \rightarrow 4)$ glycosidic bonds (shown in blue). Side branches are linked to the main chains by $\alpha(1 \rightarrow 6)$ glycosidic bonds, formed between hydrogens in C1 and C6 carbons (in orange).*

In this situation, the revised number of protons that would actually produce significant CEST signal would be 3, 3, 2 and 2, for G, G6P, F6P and F16bP respectively. These numbers match reasonably well with the signal ratios observed in the experiments.

These ratios alone cannot explain the subtle signal variations seen between molecules, which probably arise from conformational differences. However, it is reasonable to think, given the similar CEST magnitudes within hexoses and pentoses, that the hydroxyls outside the cyclic structure do not contribute significantly to the production of the CEST contrast.

4.5.2. Concentration

Blood glucose level in healthy humans ranges between 4 and 6 mMolar before meals and rises temporarily up to 8 mMolar shortly after eating. An example of the glycemic response in two healthy volunteers is shown in figure 4.5.3.

Under the right medical supervision these levels can be safely increased up to 15-20 mMolar by a venous infusion of glucose.[14]

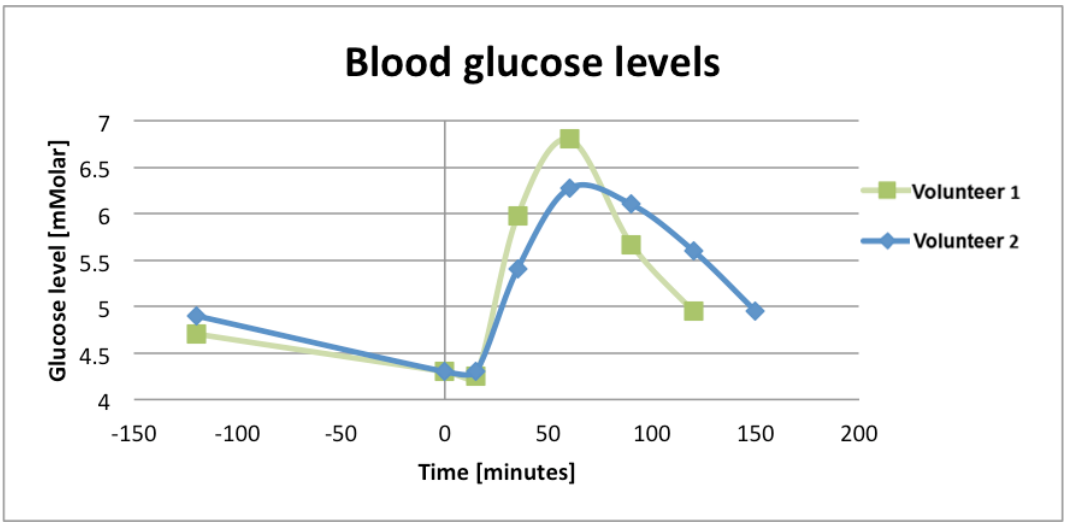

Figure 4.5.4.: *Blood glucose level test of two healthy volunteers. Glycemia rises from a basal level of 4.3 mMolar to a peak of 6.8 mMolar around an hour after food ingestion.*

For the glucoCEST technique to be useful in the clinic one should be able to detect changes in glucose concentration similar to those occurring *in vivo*. In practical words this means that a sample at 10 mMolar glucose concentration should provide significantly higher CEST signal than a 5 mMolar one.

It can be observed from figure 4.5.5 that at 5 mMolar concentration the CEST is significantly lower than at any of the higher concentrations. The increase in signal is biggest for glucose with a 2.1$\pm$0.3 enhancement ratio from 5 to 10 mMolar. In the case of the other 3 sugars the signal increase is not as drastic, however it is still very significant ($p<0.05$). This result arises from liquid solution scanned at pH 7.0 and equivalent B1 power of 1.92 μT.

It should be noted however, that the signal enhancement due to the concentration of glucose (and the rest of the sugars) will be very much dependent on the specific conditions of the environment in which the scan is performed. Different pH values, saturation power, and crucially T_2 relaxation times will yield to completely different enhancement ratios for the same glucose increase. In general fast relaxing media will produce less signal enhancement as the CEST peaks become less defined due to spectral broadening at short T_2 relaxation times. For this reason the investigation of CEST effects at specific conditions for each application is important before predictions of expected signals can be made.

Figure 4.5.6 shows the CEST signal from phantoms in 3% agar. In contrast to the liquid sample, here the signal enhancement is 1.6 $\pm$ 0.2 at best, when moving from from 5 mMolar to 10 mMolar.

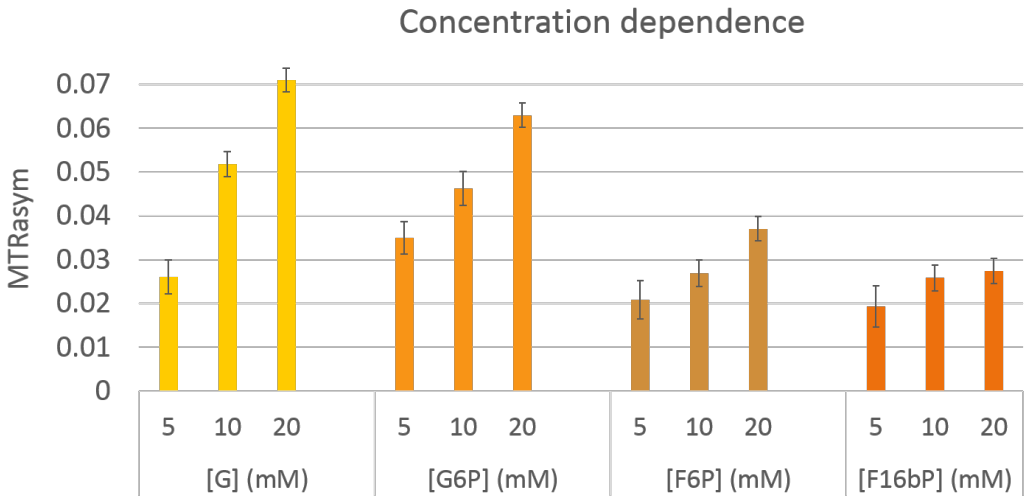

Figure 4.5.5.: *CEST concentration dependence of G, G6P, F6P and F16biP at pH 7.0 and equivalent B1 power of 1.92 μ T. A monotonic increase of the MTR asymmetry with concentration is manifested in all 4 sugars, with significant signal differences between the low and high concentrations.*

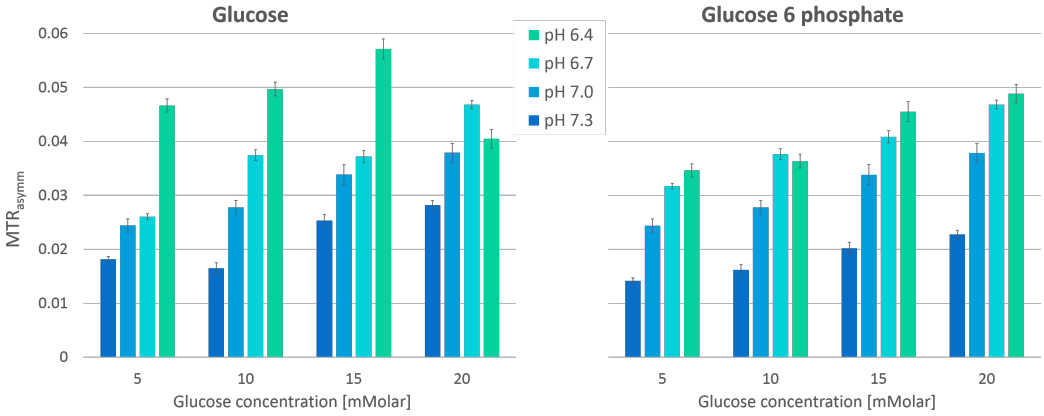

Figure 4.5.6.: *CEST signal of G and G6P solutions in 3% agar at different pH and concentrations. Equivalent B1 saturation power of 1.92 μ T. At these conditions and ranges, the signal enhancement due to pH variation exceeds the contrast due to concentration change.*

Figure 4.5.6 also demonstrates the extent to which pH modulates the CEST outcome, even exceeding the effect due to concentration at these ranges.

[Note: The disproportionately elevated signal of glucose at pH 6.4 is likely a fluke due to inaccurate pH calibration]

4.5.3. pH

As can be seen in figures 4.5.6 and 4.5.7 the pH of the solutions has a profound impact on CEST.
The elevated signal observed at the lowest pH values agrees with the notion of fast exchange rates in the sugars, as when the medium acidifies the exchange rate slows down to a more optimum regime for CEST, therefore producing more contrast. For a discussion on the effect of pH in CEST please refer to 1.4.5.

As in the previous case the observed signal ratios vary from samples in liquid and solid state (agar phantoms). In liquid samples (figure 4.5.7), the pH seems to affect glucose the most while the rest of the sugars appear to have a less acute response to variations in pH. Nonetheless, it can be inferred with no loss in generality that across the physiological range tested, the signal is lowest in basic environments and it increases as the medium acidifies.

4.5.4. Concentration vs pH

Tissues at different pH will have an unequal response to the same amount of glucose delivery. Acidic media, for example the extracellular space of tumours, will display higher glucoCEST enhancement, while a more basic region will have a less pronounced signal increase.

During an in vivo glucoCEST experiment glycemia level may vary between 4 and 20 mMolar (it will depend on the glucose administration route). On the other hand the pH level in healthy and cancerous tissue could vary between 7.3 and 6.7 respectively.[15,16] For this physiologically relevant range, the CEST signal gradient along the concentration and pH axis are both within the same order and it can be argued that glucoCEST alone will not be able to separate what percentage of the measured signal is caused by an increase in glucose concentration and what percentage of it arises from the enhanced effect of being in a more acidic medium.

Considering the agar phantom as the one closer to *in vivo* conditions and the B1 saturation power of 1.6 μ T adequate for clinical use (due to SAR limitations, values around 2 μ T tend to be the maximum allowed saturation power on 3 Tesla clinical scanners), the relation of CEST with concentration and pH is summarised in Figure

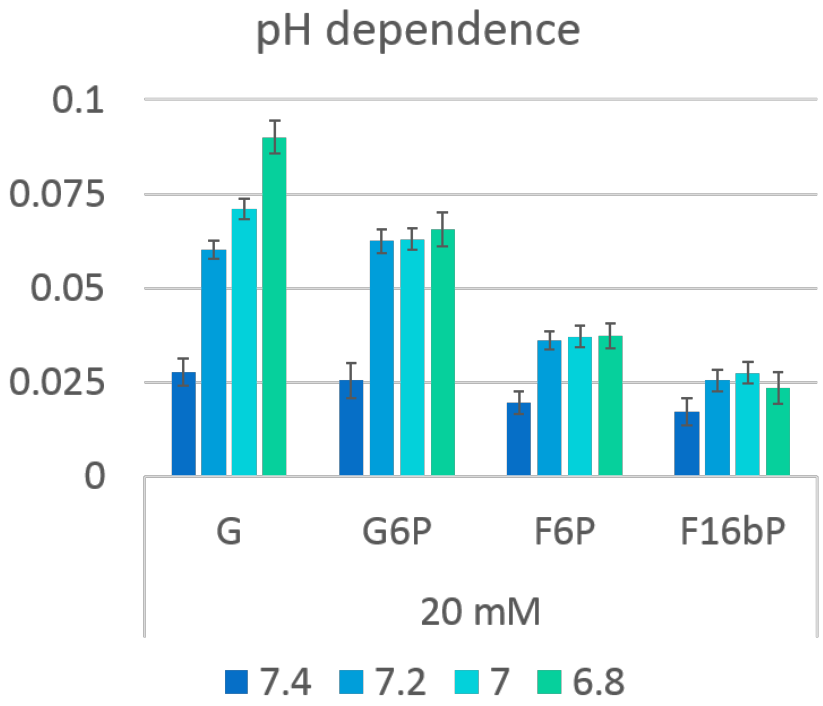

Figure 4.5.7.: *CEST dependence on pH for G, G6P, F6P and F16biP at 20 mmMolar and equivalent B1 power of 1.92 μ T. Acid environment favors the CEST contrast by slowing the exchange rate towards the intermediate exchange regime.*

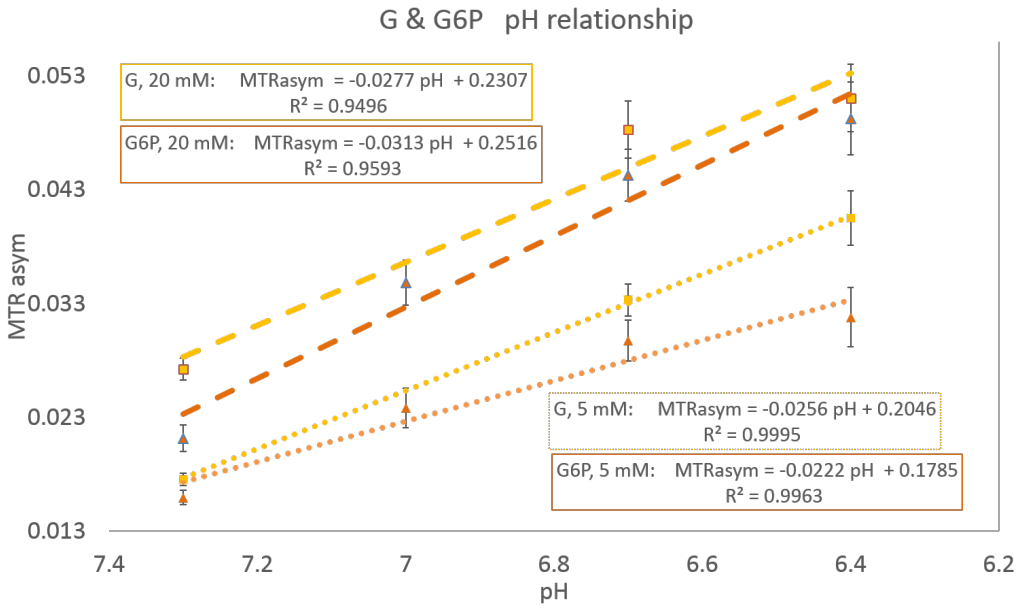

Figure 4.5.8.: *Comparison of the influence of pH and concentration on CEST. The lines show the observed CEST signal in G and G6P at different pH values. The 2 lines on top represent samples at concentration of 20 mMolar, the 2 lines on the bottom at 5 mMolar. Signal intensity from concentrated samples overlap with signal from more diluted but acidic samples.*

4.5.8. Except for the edge cases (in the extreme limits of any physiological relevance), it is not possible to distinguish whether the magnitude of the signal is due to a particular sugar concentration or due to different pH in the sample.

Moving from an environment with pH 7.2 to another with pH 6.7, the observed increase in the mean signal from both sugar together is 0.015 ± 0.003 units of MTR asymmetry. On the other hand the signal increase due to concentration going from 5 to 20 mMolar is 0.010 ± 0.003 units. These results show the variation in pH to be 50 percent more effective in producing the CEST contrast than changes in the concentration.

Although the above ratio will certainly vary depending on the saturation power and tissue parameters, it is fair to conclude that pH variations within the physiological range could alter significantly the results of glucoCEST experiments.

Although only G and G6P are shown here, the same conclusions apply to F6P and F16biP.

4.5.5. Temperature

Contrary to what was reported for glycogen with glycoCEST,[17] CEST signal from the hydroxyl groups in the monosaccharides decreases as temperature increases towards 37°C (see Figure 4.5.9). This effect, although possibly counter-intuitive as the exchange rate speeds up with temperature, demonstrates that each of these sugars at 23°C are already close to the *fast exchange rate* regime, which is not the ideal condition for CEST (see section 1.4.5 in Chapter 1). Any increase in temperature takes the exchange rate further away from the optimum *intermediate exchange rate* best suited for CEST.[17–19] Hence the signal is lower at 37°C than at 23°C.

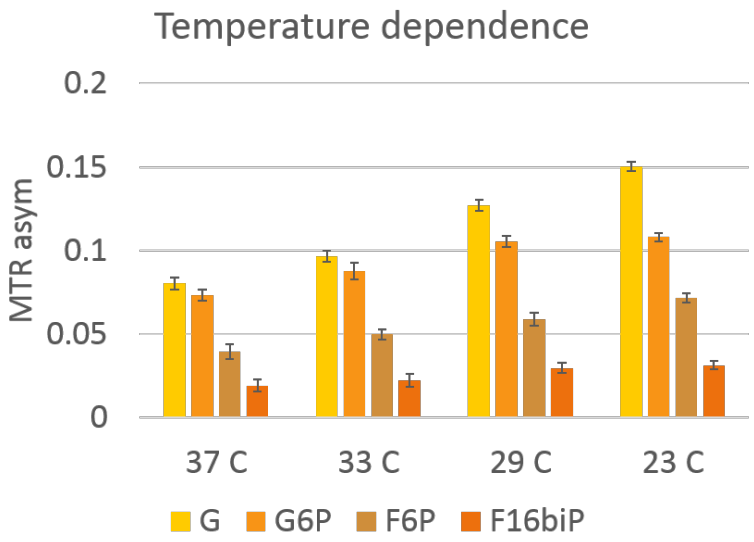

Figure 4.5.9.: *CEST temperature dependence of G, G6P, F6P and F16biP at pH 7.0 and equivalent B1 power of 1.92 μ T. A linear decrease of the MTR asymmetry is observed in all 4 molecules as the temperature raises. The observation fits with the assumption of exchange rates being very rapid in these molecules.*

Generally, exchangeable sites from small molecules, tend to exhibit very fast exchange rates due to their fast tumbling motion (low correlation times). Large macromolecules like glycogen are less mobile and less accessible to the free water, thus their -OH groups have a slower exchange rate. Due to their small size, the signal decrease associated with an increase in temperature is an effect that applies to all the sugar in the study (all monosaccharides). This is a rather unfortunate circumstance for *in vivo* glucoCEST applications which limits the CEST contrast from OH groups in small sized molecules.

As a remark, G6P appears to be less sensitive to variations in temperature as it can be observed from the smaller gradient in Figure 4.5.10. Glucose displays a more

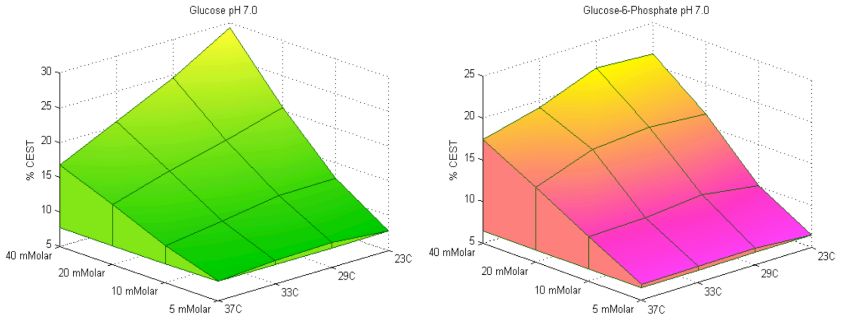

Figure 4.5.10.: *Mean values of CEST signal in G and G6P phantoms at varying temperature and concentration. Left: glucose presents a strong gradient in concentration and temperature. Right: G6P is less sensitive to temperature and offers same signal levels as glucose at 37°C.*

pronounced signal drop, which at 37°C makes the signal of G6P very similar or even higher than glucose.

4.5.6. PBS vs Saline solutions

Controlled preparation of phantoms requires the use of pH buffering salts which allow the titration of the samples to specific pH values. A commonly used concentration (1x PBS) would contain 10 mM PO_4^{3-}, 137 mM NaCl, and 2.7 mM KCl in pure water. The phosphates in the buffered solution act as exchange catalysers by enhancing the dissociation rate of hydroxyl protons (the reader is referred to section 1.4.5 for more information on exchange catalysers). The data in figure 4.5.11 shows a reduced CEST effect in the sample with PBS solution as compared to the one in saline solution. The boost in chemical activity, in this case due to the addition of phosphates, takes the exchange rate above the regime in which the CEST mechanism is efficient, above the intermediate exchange regime. As in the case of high temperatures, sugars dissolved in high amounts of phosphates produce less MTR asymmetry and their potential to produce CEST contrast is reduced.

An exchange rate strongly dependant on phosphates could have profound implications for CEST *in vivo*. As different compartments in the tissues have distinct phosphate contents, it is to be expected that their CEST response will vary from one to another. Incorporating that information in the CEST analysis could help clarify important questions regarding the source of the glucoCEST signal and its variation across different tissue characteristics.

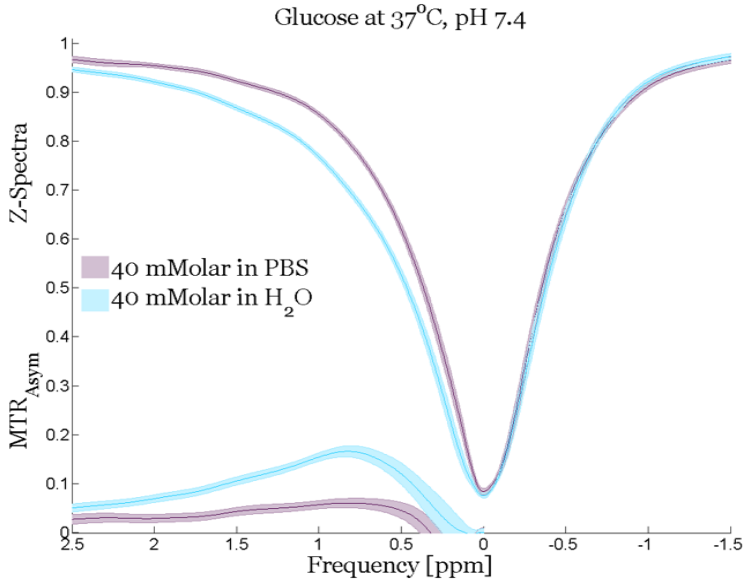

Figure 4.5.11.: *Z-Spectra of 40 mMolar glucose solutions in saline and 1x PBS. Scanned at 37°C and pH 7.4. Exchange catalysis effect of phosphates in PBS reduces the CEST contrast of glucose. This is yet another indication of the fast chemical exchange between glucose hydroxyl protons and water.*

4.5.7. Power

The saturation preparation is essential in CEST experiments as it is during this process that the magnetic labelling takes place before is exchanged with water. As such, the B1 irradiation power is a critical parameter that can enhance or ruin the CEST contrast if used inadequately. In this study a relatively narrow range of power has been explored, which already makes a considerable difference in the intensity of the MTR asymmetry.

Overall, the highest B1 powers used in the study yielded the biggest CEST signal across all phantoms. This is consistent with substances in fast exchange rate for which elevated powers increase the labelling effectiveness.

Nevertheless, using higher powers does not always improve the CEST signal. A good estimate for the optimum power is usually accepted to be $B_1 = \kappa/2\pi$ where κ is the exchange rate of the CEST pool. This relationship, predicted by Woessner *et al.*[20] was introduced for paramagnetic CEST agents which resonate a few tens of ppm away from water. Accordingly, the reduction of available water signal caused by direct saturation and MT is not taken into consideration and the predicted optimum B1 power tends to be too high for diamagnetic CEST agents like sugars. This fact is already acknowledged in a study by Desmond *et al.*[21] where they report lower than

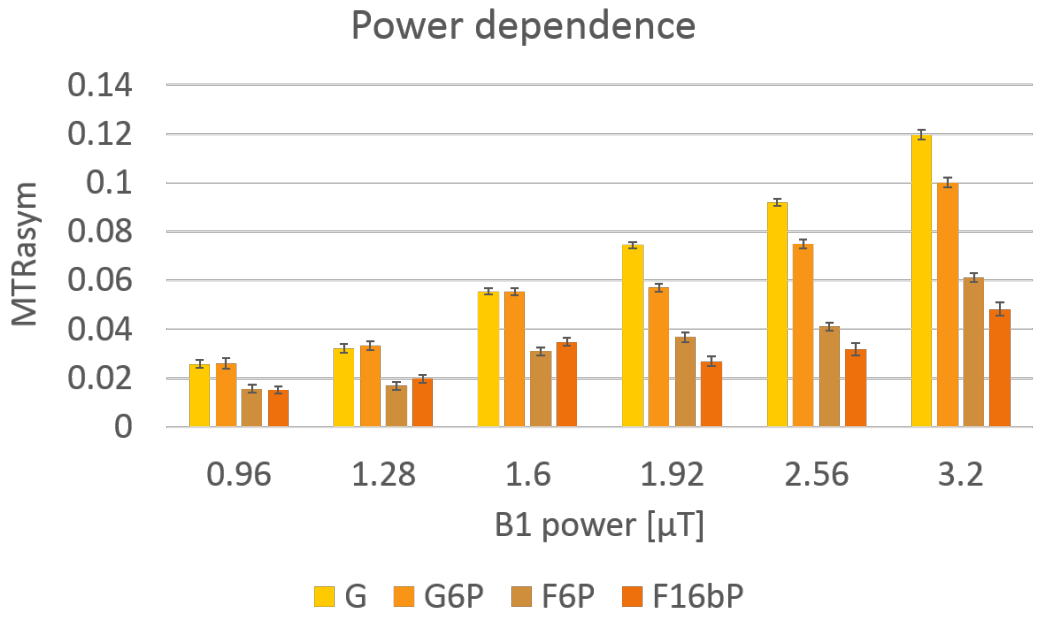

Figure 4.5.12.: *Dependence of B_1 saturation power on observed CEST contrast in G, G6P, F6P and F16biP at 20 mMolar concentration in PBS solution. Generally largest MTR asymmetries are obtained when the molecules are saturated at high powers.*

the predicted values of B1 power to produce the highest CEST contrast.

Besides the SAR considerations, using very elevated powers has the drawback of producing noisier CEST measurements close to water. As the power increases the total magnetization available to produce signal reduces considerably, yielding to noisy data well below the numerically estimated optimum power. This is particularly relevant in non aqueous samples for which saturation profile becomes especially broad due to the short T_2 relaxation rate. In Chapter 3 the relationship between B1 power and resulting CEST signal is discussed for a range of *in vivo* situations.

Owing to the multiple factors involved in the production of CEST contrast, optimum B1 power is approximated using computer simulations (as shown in Chapter 3), and later tested experimentally for each application according to hardware and SAR limitations.

4.5.8. Spatial reproducibility

Two CEST scans were performed for the same phantom where the location of the solutions within the coil was changed. As illustrated in figure 4.5.13 in experiment B the sample was rotated 90 clockwise relative to the position in experiment A.

The results from both experiments show that phantoms at same concentration give

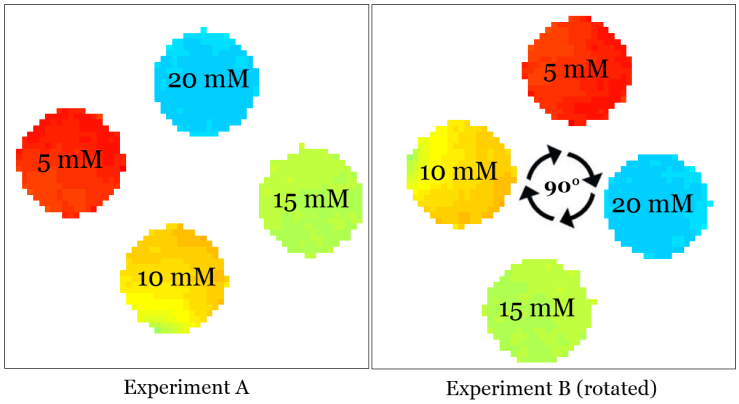

Figure 4.5.13.: *Image of showing the position of each phantom in the first experiment A and in the rotated experiment B.*

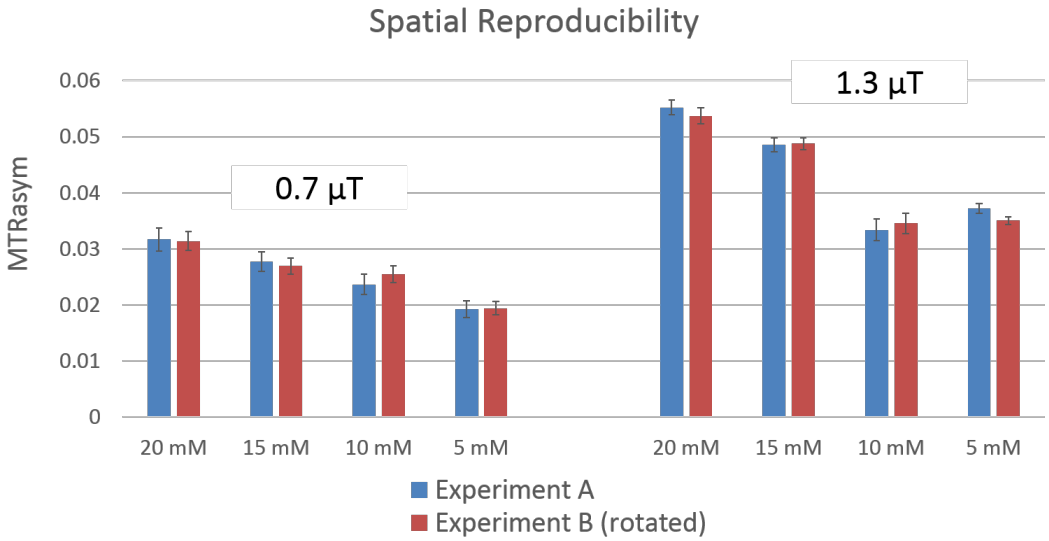

Figure 4.5.14.: *Comparison of the CEST signal obtained for each phantom in experiment A and experimant B. Reproducibility in the measurements demonstrate that CEST contrast is invariant to the position of the coil.*

the same level of CEST regardless of the position in the coil. Comparison between experiments lead to no significant differences between samples in experiment A and B. Only the 5 mMolar solution scanned at 1.3 μ T showed a significant change in signal intensity when rotating the sample ($p<0.05$). Nevertheless, the variation observed in this phantom did not significantly impinge the spatial reproducibility of CEST in this coil. Other factors like small drifts in pH, circulation of water due to a temperature gradient or amount of agar used had generally a bigger impact in the stability of the CEST signal. In this context it is worth noticing that measurements of the phantom at 10 mMolar produced some inconsistent results compared to the pattern observed from the rest of the samples (see Figure 4.5.14). The odd values obtained, which were likely caused by an abrupt field inhomogeneity due the formation of an air bubble in the sample, were reproduced in both the experiment A and B. This test confirmed that the position of the samples within the coil did not have a significant impact in the obtained CEST signal.

Study part 2

4.6. Relaxation in the presence of chemical exchange.

4.6.0.1. Transverse relaxation

Higher sugar concentration phantoms tend to produce wider Z-spectra. The dominating parameter in the widening effect of the Z-spectrum is the transverse relaxation time T_2; shorter relaxation times leading to broader water profiles. One could logically question the cause of the shortening in the measured T_2 value (or increase in relaxation rate R_2) when sugar is diluted in water. In the case of a static solution of sugar and water there are two main reasons that explain the enhancement of relaxation rate R_2.

On one side the sugar content in the sample increases the viscosity of the solution. Viscous solutions contain larger amount of 'bound water' than liquid ones[22] which slows down the molecular rotational correlation time. Long correlation time leads to efficient transverse relaxation (non-efficient 'motional narrowing'), hence the shortening of T_2. At low concentrations of sugar however, the viscosity of the solution does not change significantly,[1] which excludes the viscosity as the cause of enhanced transverse relaxation. This argument can be experimentally verified by

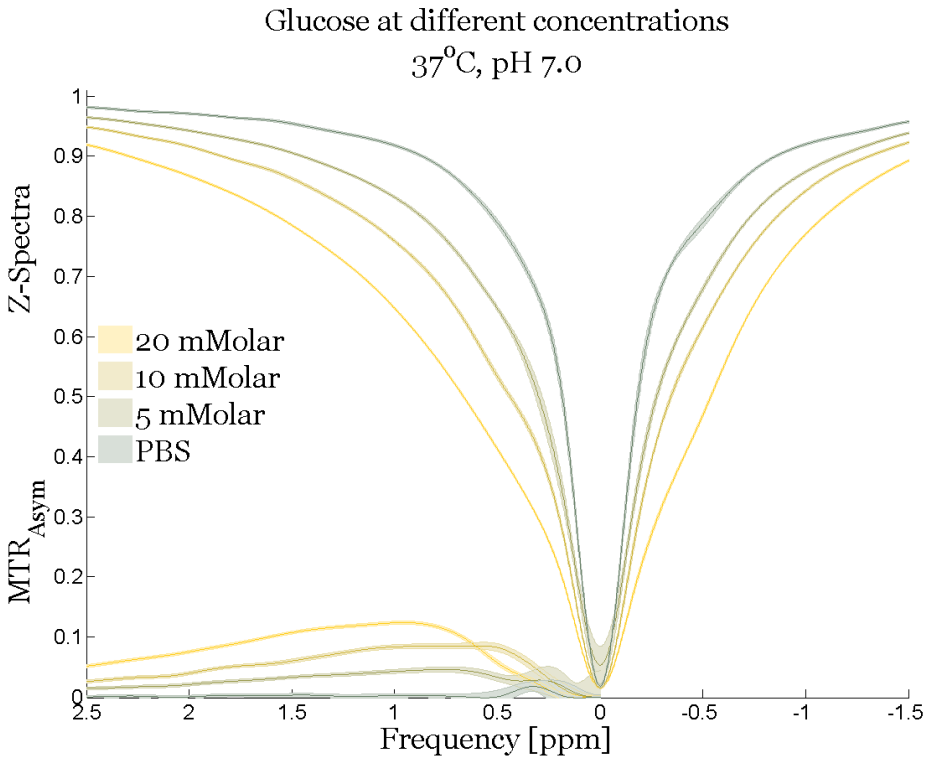

Figure 4.6.1.: *Z-spectra and MTR asymmetry corresponding to PBS and glucose solutions at 3 concentrations. The Z-spectra become wider as the sugar concentration increases.*

measuring T_1 relaxation time (see 4.6.0.2), which is not influenced by the exchange process but does vary with viscosity. The longitudinal relaxation time T_1 is relevant to the final contrast obtained with CEST. However, the influence of the chemical exchange process does not alter T_1 relaxation time itself. Unlike T_2 which can vary significantly, T_1 remains constant for a wide range of exchange rates (see section 4.6.0.2 below).

The second mechanism for enhanced transverse relaxation is the proton exchange process between the hydroxyl group in sugar and free water. The consequence of the increased R_2 relaxation is inherent to the dynamics of the Bloch-McConnell equations, and will be addressed in the following section.

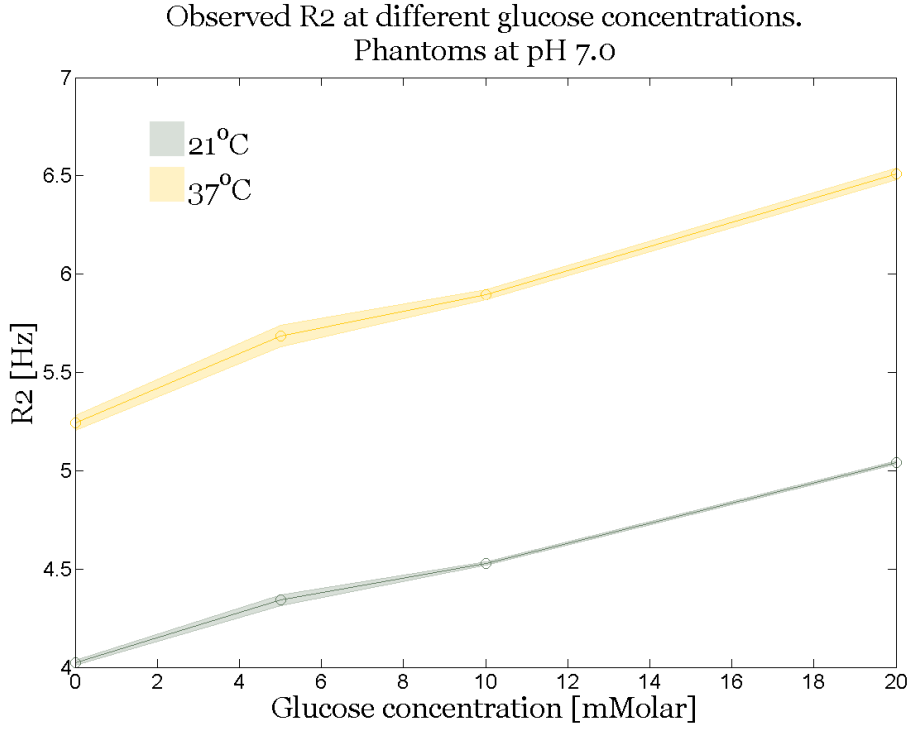

Figure 4.6.2.: *Measured transverse relaxation rate R_2 of glucose solutions as concentration varies. The relaxation rate increases linearly with glucose concentration in both tested temperatures.*

Note: Variations in temperature will also change the transverse relaxation rate. The predictions from the Bloembergen-Purcell-Pound (BPP) theory* is that an in-

*According to the Bloembergen-Purcell-Pound (BPP) theory the relaxation times of pure substances can be expressed in terms of their correlation time τ_c and ω_0 Larmour frequency as:

$$\frac{1}{T_1} = K[\frac{\tau_c}{1+\omega_0^2\tau_c^2} + \frac{4\tau_c}{1+4\omega_0^2\tau_c^2}]$$

crease in temperature should make the T_2 relaxation time longer, as the correlation time τ_c reduces. The experimental observations contradict the theoretical prediction. This discrepancy may have arisen from the way the samples were heated. Temperature gradients inside the phantoms would originate convection currents which could have resulted in a more efficient transverse relaxation rate due to incoherent motion of spins inside the magnetic field.

4.6.0.2. Longitudinal relaxation T_1 in CEST

At concentrations such as the ones used in the phantom study, the effect of the labile pool on the longitudinal relaxation time of water is negligible. The simulated T_1 variation is less than 0.01%, which would be masked by the experimental error.

On the other hand, the T_1 (and T_2) relaxation time will be influenced by the viscosity η of the sample through a change in the correlation time τ_c. The rotational correlation time of a molecule can be estimated by Stoke's law (using a spherical molecule approximation) as:

$$\tau_c = \frac{4\pi\eta r^3}{3kT}$$

Where η is the viscosity of the solvent, r the effective hydrodynamic radius of the molecule, k the Boltzmann constant and T the temperature. According to the BPP theory, a change in viscosity implies a variation in relaxation times, both transverse and longitudinal.

It is fair to conclude from the lack of variation in the observed T_1 (Figure 4.6.3), that at the range of concentration used in the study the viscosity of the glucose solutions remains, for all intends and purposes, constant.

4.6.1. Exchange mediated T_2 relaxation

The chemical exchange process between sugars and water is a complex process in which multiple pools interact with each other.

As in any modelling approach, simplifying the complexity of the problem can help analyse its general behaviour. In this case the minimal working description of

,

$$\frac{1}{T_2} = \frac{K}{2}[3\tau_c + \frac{5\tau_c}{1+\omega_0^2\tau_c^2} + \frac{2\tau_c}{1+4\omega_0^2\tau_c^2}]$$

with $K = \frac{3\mu_0^2}{160\pi^2}\frac{\hbar^2\gamma^4}{r^6}$ being μ_0 the magnetic permeability in empty space, $\hbar$ the reduced Planck constant, γ the gyromagnetic ratio of the nuclei, and r the distance between the nuclei with magnetic dipole moment.[23]

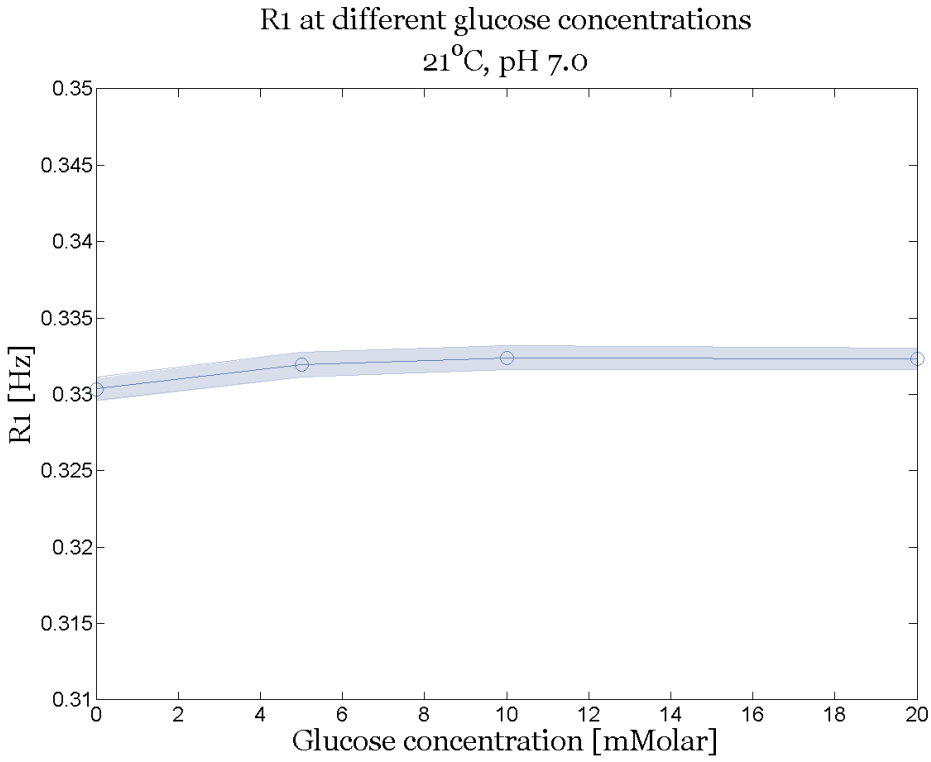

Figure 4.6.3.: *Measured longitudinal relaxation rate R_1 of glucose solutions with concentration. The longitudinal relaxation rate remains constant in the range of glucose concentration tested.*

the chemical exchange process can be described by a two pool exchange model, in which the first exchanging pool represents water and the second one the averaged effect of the hydroxyls protons in glucose molecules. Using this simplified model of chemical exchange, inferences about the system's behaviour can be made.

Based on the Swift-Connick* equation, by substituting the inverse of the lifetime with the chemical exchange rate, the observed transverse relaxation rate R_{2obs} can be described as:

$$R_{2obs} = R_{20} + R_{2ex} \tag{4.6.1}$$

Where R_{20} is the water relaxation rate in the absence of exchange and R_{2ex} is the exchange mediated relaxation rate defined as:

$$\mathrm{R_{2ex}} = \rho\kappa \frac{\mathrm{R_{2b}^2} + \kappa \mathrm{R_{2b}^2} + \delta^2}{(\mathrm{R_{2b}} + \kappa)^2 + \delta^2} \tag{4.6.2}$$

where κ is the exchange rate between pools in Hz, ρ the labile to water proton ratio, R_{2b} the transverse relaxation rate of the CEST pool in Hz and δ the chemical shift difference in $rad.s^{-1}$.

For the case where $\delta \gg R_{2b}$ this equation can be further simplified to:

$$\mathrm{R_{2ex}} = \rho\kappa \frac{\delta^2}{\kappa^2 + \delta^2} \tag{4.6.3}$$

The slope obtained by fitting equation 4.6.1 to the experimental R2 values gives the relationships between the chemical shift δ and the exchange rate *k* of glucose. Assuming that the mean chemical shift for the hydrogen in glucose is the same at all temperatures, it can be deduced that the minimum combined shift δ in glucose lies around 1.09 ppm (see horizontal line in figure 4.6.4).

With a chemical shift of 1.09 ppm, the mean exchange rate *k* for glucose stands at 1400 Hz at $21°C$ and increases to 2800 Hz at $37°C$ (Figure 4.6.4). In the study by Yadav *et al.* values of 1.44 ppm offset and 2200 Hz were reported for glucose at $22°C$. The discrepancies between both results might be due to the different PBS concentration used in the solutions. In this study samples were dissolved in 0.2x PBS as compared to the 1x PBS used by Yadav *et al*. As previously discussed, high concentration of PBS reduces the CEST signal, which can be explained by an increase in the exchange rate. This is in good agreement with the obtained results.

The potential of glucose as a natural transverse relaxation agent has been recently

*Swift and Connick in 1962 developed an equation that relates the bandwidth of the NMR signal to the mole fractions of each pool containing paramagnetic molecules interacting with water.[24]

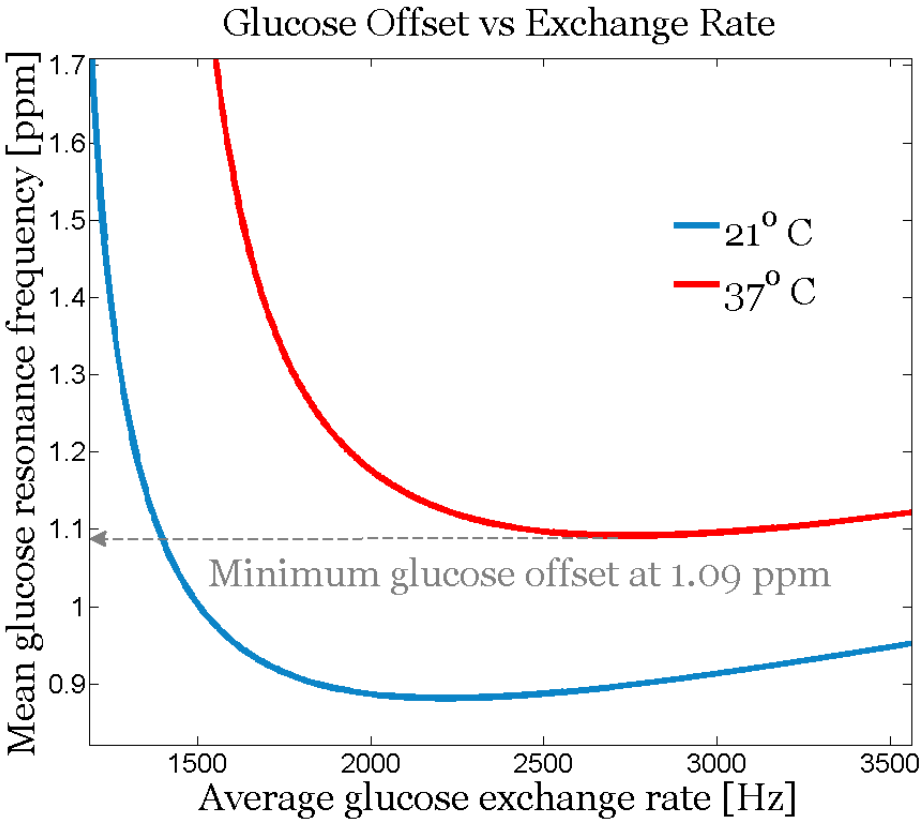

Figure 4.6.4.: *Combined averaged resonant frequency of hydroxyls in glucose in relationship to the mean exchange rate. Data obtained from fitting R_2 and concentration at 23° and 37° C. The predicted minimum resonant frequency of glucose lies around 1.09 ppm from water, granted that the relative resonant frequency δ is independent of the temperature.*

proposed by Yadav *et al.*.[1] This is a very interesting approach for the use of exogenous glucose which has the virtue of being very attractive for clinical use due to its extreme simplicity; just measurements of the transverse relaxation of water while infusing glucose. The acquisition of T_2 maps is fast and based on well established protocols. While the sensitivity of this method is good in liquid samples, it gets compromised as the T_2 of water shortens, as the exchange related relaxation R_{2ex} becomes small compared to R_{20}. This poses a serious practical challenge as it would require precise measurement of T_2 relaxation time with the millisecond accuracy, to be able to detect 20 mMolar concentration in a 3 Tesla scanner.

Numerical simulations demonstrate the small reduction of the transverse relaxation at short T_2 values.

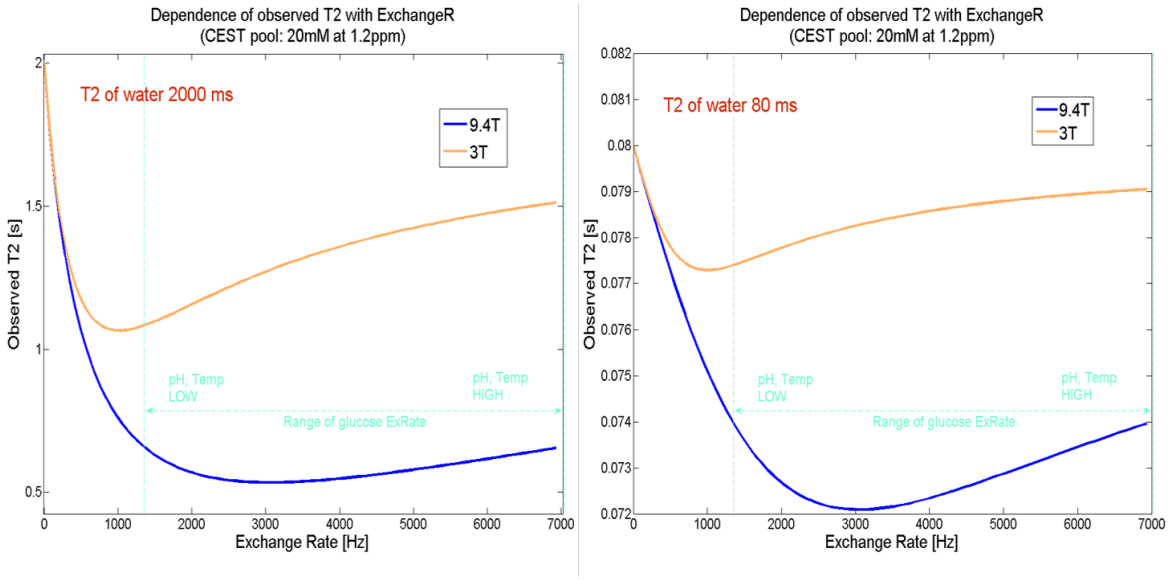

Figure 4.6.5.: *Simulated relation of T_2 relaxation time and concentration of glucose. A two-pool exchange model was used to calculate transverse magnetization in time and then fitted to a mono-exponential recovery, which yielded to the effective values of T_{2obs} at different glucose concentration. Left: simulation run with T_{20} of water set a 2 seconds. Right: simulation run with T_{20} of set at 80 milliseconds. While the shortening of the observed T_2 is notorious at long T_{20} values (on the left), the same concentration of glucose at shorter T_{20} (on the right) results in less than 3 millisecond reduction in optimum exchange rate conditions at 3T.*

In media in which the T_2 relaxation time is mostly conditioned by other factors other than the concentration of sugar, the sensitivity of T_2 measurements to detect variation in sugar content appears to be limited. The example in figure 4.6.6 shows a comparison of T_2 and CEST. It can be observed how while T_2 measurement is insensitive to concentration changes, CEST can still differentiate samples with dif-

ferent content of glucose.

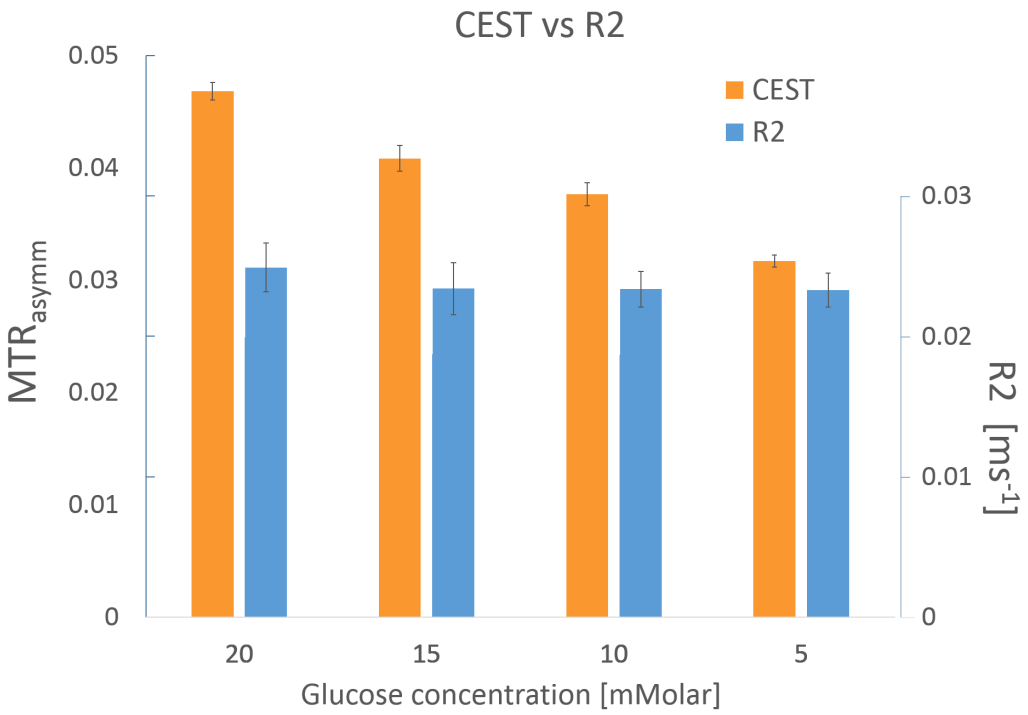

Figure 4.6.6.: *Comparison of T_2 relaxation and CEST at different concentration of glucose in a semi-solid environment. In tissues with short T_2 relaxation times (tens of millisecond), the exchange mediated transverse relaxation R_{2ex} is imperceptible compared to fast self-relaxation rate R_{20}, resulting in a lack of contrast between phantoms. CEST measurements on the other hand still provide enough contrast to separate samples according to their glucose concentration.*

4.6.2. Correlation of T_2 with Z-spectrum width.

As mentioned in the previous section the transverse relaxation influences the width of the Z-spectrum. The relationship between the two parameters can be clearly observed in the scatter plot in figure 4.6.7. At both temperatures (21° C and 37° C) the observed relaxation rate R2 correlates well with the measured width of the Z-spectrum (calculated as the full width at 3^{rd} maximum). Considering the asymmetry due to the exchange is small compared to the water-profile width, the analytical relationship for the $FW3^{rd}M$ can be approximated from the Bloch-McConnell equations as:

$$FW3^{rd}M = 2R_2\sqrt{\frac{\omega_1^2}{2R_1R_2} - 1} \tag{4.6.4}$$

For the range of ω_1 in which saturation can be achieved the expression can be further reduced to:

$$R_2 = 0.5R_1\left(\frac{FW3^{rd}M}{\omega_1}\right)^2 \tag{4.6.5}$$

The expression can be fitted to the experimental data yielding to estimate values of $\omega_1 = 0.96\mu T$ (41 Hz) at both temperatures and effective T_1 of $3.1s; (R_1 = 0.32Hz)$ at $21°C$ and T_1 of 4.3 s ;$(R_1 = 0.23Hz)$ at $37°C$.

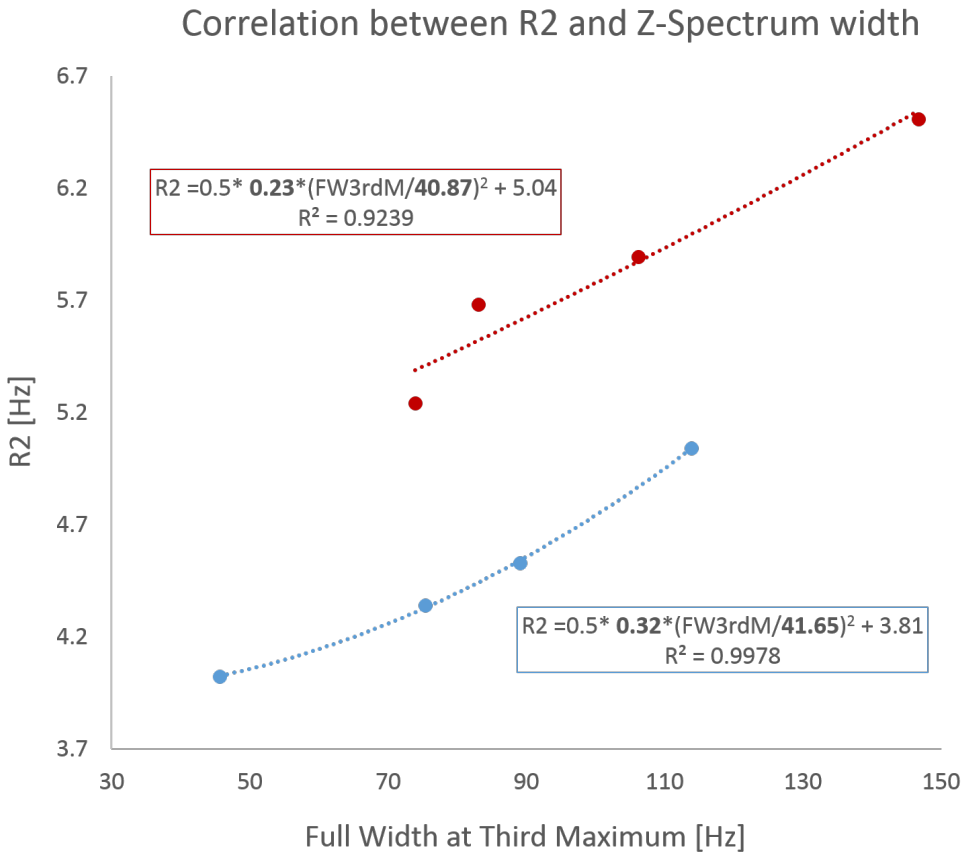

Figure 4.6.7.: *Scatter plot showing measured R_2 versus $FW3^{rd}M$ at varying concentration of glucose. The theoretical derivation predicts a quadratic relationship between the two parameters, which fits very accurately with the data collected at $23°C$ (in blue). Measurements at $37°C$ (in red) appear less consistent, which could be related to distortions from convection currents formed while heating the sample.*

The gap observed in the values of the $FW3^{rd}M$ at different temperatures cannot be explained by this model and requires fitting an additional additive constant. In the same way as in the T_2 measurement (Figure 4.6.2), the motion from convection currents might be the source of the discrepancies between the predicted and the

experimental data. Therefore, results obtained from this approximation should be interpreted with care.

4.7. Conclusion

Results and analysis of the data in this study can be summarised in the following conclusions.

All four molecules scanned in this study are capable of producing CEST contrast. This result supports the hypothesis of the intracellular origin of glucoCEST, particularly considering that the CEST magnitude from G6P is very similar to the observed in glucose. Same levels of signal intensity observed between hexoses and pentoses suggest that the hydroxyl outside the cyclic structure do not contribute significantly to the CEST contrast.

The CEST signal from all four sugars, while different in intensity, are alike in terms of the MTR asymmetry shape and therefore it is not possible to identify a specific molecule from the asymmetry profile. This limits the possibility of tracking the CEST signal through the metabolic process.

The diminished intensity observed at $37^{\circ}C$ confirms the notion of very fast exchange rates involved in the exchange process with monosaccharides. The same conclusion can be deduced from the pH analysis, as well as from the enhanced exchange rates due to the presence of phosphates.

Results in the study indicate that the tissue pH can be a key parameter for the efficient generation of contrast in glucoCEST imaging. The pH of the tissue influences the CEST signal, in most cases to a larger extent than what the expected change in glucose concentration would. The signal intensifies in acid environments and moderates it in more basic media, making quantification of glucose increase particularly difficult in a heterogeneous pH environment.

Along the same lines, the phosphate content of tissues may play an important role too, enhancing or reducing the contrast in certain regions based on the phosphate levels of those tissues.

Having demonstrated the CEST efficiency of these molecules, determination of the signal origin and its relative proportions will depend on parameters such as pH, phosphate concentrations, sugar concentration and volume ratio of each compartment (vascular, interstitial or intracellular). This is an open field of study that can provide useful information for a better understanding of the CEST contrast *in vivo* and its potential applications.

The T_2 relaxivity properties of monosaccharides open up an attractive way of using glucose as perfusion and even metabolic MRI agent, by looking at T_2 variations after administration of glucose. The major advantage of this approach is its simplicity which makes it readily available in any clinical scanner. The question remains on whether the sensitivity of the method is enough to be useful in real clinical applications. In the current study the CEST technique demonstrated an improved sensitivity over T_2 mapping for the detection of small concentration of sugar, particularly in semi-solid tissue where short transverse relaxation time limits the sensitivity to detect variations in T_2.

The CEST technique has a number of drawbacks of its own too. Limitations on B1 power due to SAR and comparatively long scan times are some of the most important for translation to the clinic.

Each of these methods provides an alternative solution for imaging small concentrations of glucose with MRI. The choice of the technique should be decided upon by comparison of both in specific applications, and by considering whether the requirement is the speed and robustness of T_2 mapping or the higher sensitivity of CEST imaging.

Chapter references

[1] Nirbhay N. Yadav, Jiadi Xu, Amnon Bar-Shir, Qin Qin, Kannie W.Y. Chan, Ksenija Grgac, Wenbo Li, Michael T. McMahon, and Peter C.M. van Zijl. "Natural D-glucose as a biodegradable MRI relaxation agent: Glucose as an MRI Relaxation Agent". In: *Magnetic Resonance in Medicine* 72.3 (Sept. 2014), pp. 823–828. ISSN: 07403194. DOI: 10.1002/mrm.25329 (cit. on pp. 121, 143, 150).

[2] Simon Walker-Samuel, Rajiv Ramasawmy, Francisco Torrealdea, Marilena Rega, Vineeth Rajkumar, S. Peter Johnson, Simon Richardson, Miguel Gonçalves, Harold G. Parkes, Erik Arstad, David L. Thomas, R. Barbara Pedley, Mark F. Lythgoe, and Xavier Golay. "In vivo imaging of glucose uptake and metabolism in tumors". In: *Nature Medicine* 19.8 (Aug. 2013). 00044 Cited by 0001, pp. 1067–1072. ISSN: 1078-8956. DOI: 10.1038/nm.3252 (cit. on pp. 121, 130).

[3] Fatima A. Nasrallah, Guilhem Pagès, Philip W. Kuchel, Xavier Golay, and Kai-Hsiang Chuang. "Imaging brain deoxyglucose uptake and metabolism by glucoCEST MRI". In: *Journal of Cerebral Blood Flow & Metabolism* 33.8 (Aug. 2013). 00015 Cited by 0000, pp. 1270–1278. ISSN: 0271-678X. DOI: 10.1038/jcbfm.2013.79 (cit. on p. 121).

[4] Tao Jin, Hunter Mehrens, Kristy S. Hendrich, and Seong-Gi Kim. "Mapping brain glucose uptake with chemical exchange-sensitive spin-lock magnetic resonance imaging". In: *Journal of Cerebral Blood Flow and Metabolism: Official Journal of the International Society of Cerebral Blood Flow and Metabolism* 34.8 (Aug. 2014), pp. 1402–1410. ISSN: 1559-7016. DOI: 10.1038/jcbfm.2014.97. pmid: 24865996 (cit. on p. 121).

[5] Kannie W. Y. Chan, Michael T. McMahon, Yoshinori Kato, Guanshu Liu, Jeff W. M. Bulte, Zaver M. Bhujwalla, Dmitri Artemov, and Peter C. M. van Zijl. "Natural D-glucose as a biodegradable MRI contrast agent for detecting cancer". In: *Magnetic Resonance in Medicine* 68.6 (2012). Cited by 0012, pp. 1764–1773. ISSN: 1522-2594. DOI: 10.1002/mrm.24520 (cit. on p. 121).

[6] Denise R. Ferrier. *Biochemistry*. 6th revised international ed edition. 00519. Philadelphia: Lippincott Williams and Wilkins, June 1, 2013. 560 pp. ISBN: 978-1-4511-8753-3 (cit. on p. 122).

[7] R. Douglas Fields and Geoffrey Burnstock. "Purinergic signalling in neuron–glia interactions". In: *Nature reviews. Neuroscience* 7.6 (June 2006), pp. 423–436. ISSN: 1471-003X. DOI: 10.1038/nrn1928. pmid: 16715052 (cit. on p. 122).

[8] Despo Papachristodoulou, Alison Snape, William H. Elliott, and Daphne C. Elliott. *Biochemistry and Molecular Biology*. Fifth Edition. Oxford University Press, Jan. 30, 2014. 624 pp. ISBN: 978-0-19-960949-9 (cit. on p. 122).

[9] Harvey Lodish, Arnold Berk, Chris A. Kaiser, Monty Krieger, Anthony Bretscher, Hidde Ploegh, Angelika Amon, and Matthew P. Scott. *Molecular Cell Biology: International Edition*. 7th edition edition. W, Aug. 13, 2012. 973 pp. ISBN: 978-1-4641-0981-2 (cit. on pp. 122, 131).

[10] B. Thorens. "Glucose transporters in the regulation of intestinal, renal, and liver glucose fluxes". In: *The American Journal of Physiology* 270.4 Pt 1 (Apr. 1996), G541–553. ISSN: 0002-9513. pmid: 8928783 (cit. on p. 122).

[11] Bernard Thorens and Mike Mueckler. "Glucose transporters in the 21st Century". In: *American Journal of Physiology. Endocrinology and Metabolism* 298.2 (Feb. 2010). 00244, E141–145. ISSN: 1522-1555. DOI: 10.1152/ajpendo.00712.2009. pmid: 20009031 (cit. on p. 122).

[12] Jason W. Locasale and Lewis C. Cantley. "Altered metabolism in cancer". In: *BMC Biology* 8.1 (June 25, 2010), p. 88. ISSN: 1741-7007. DOI: 10.1186/1741-7007-8-88. pmid: 20598111 (cit. on p. 125).

[13] Leszek Poppe and Herman van Halbeek. "NMR spectroscopy of hydroxyl protons in supercooled carbohydrates". In: *Nature Structural & Molecular Biology* 1.4 (Apr. 1994), pp. 215–216. DOI: 10.1038/nsb0494-215 (cit. on p. 131).

[14] Robert G. Hahn, Stefan Ljunggren, Filip Larsen, and Thomas Nyström. "A simple intravenous glucose tolerance test for assessment of insulin sensitivity". In: *Theoretical Biology and Medical Modelling* 8.1 (May 2, 2011), p. 12. ISSN: 1742-4682. DOI: 10.1186/1742-4682-8-12. pmid: 21535887 (cit. on p. 132).

[15] Guanshu Liu, Yuguo Li, Vipul R Sheth, and Mark D Pagel. "Imaging in vivo extracellular pH with a single paramagnetic chemical exchange saturation transfer magnetic resonance imaging contrast agent." In: *Molecular imaging* 11.1 (Feb. 2012). 00042 Cited by 0000, pp. 47–57 (cit. on p. 135).

[16] X. Zhang, Y. Lin, and R. J. Gillies. "Tumor pH and Its Measurement". In: *Journal of Nuclear Medicine* 51.8 (Aug. 1, 2010). 00135, pp. 1167–1170. ISSN: 0161-5505. DOI: 10.2967/jnumed.109.068981 (cit. on p. 135).

[17] P. C. M. van Zijl, C. K. Jones, J. Ren, C. R. Malloy, and A. D. Sherry. "MRI detection of glycogen in vivo by using chemical exchange saturation transfer imaging (glycoCEST)". In: *Proceedings of the National Academy of Sciences* 104.11 (Mar. 13, 2007). 00159, pp. 4359–4364. ISSN: 0027-8424, 1091-6490. DOI: 10.1073/pnas.0700281104 (cit. on p. 138).

[18] Peter C M van Zijl and Nirbhay N Yadav. "Chemical exchange saturation transfer (CEST): what is in a name and what isn't?" In: *Magnetic resonance in medicine* 65.4 (Apr. 2011). Cited by 0073, pp. 927–948. DOI: 10.1002/mrm.22761 (cit. on p. 138).

[19] Guanshu Liu, Xiaolei Song, Kannie W Y Chan, and Michael T McMahon. "Nuts and bolts of chemical exchange saturation transfer MRI". In: *NMR in biomedicine* (Jan. 10, 2013). Cited by 0003. ISSN: 1099-1492. DOI: 10.1002/nbm.2899 (cit. on p. 138).

[20] Donald E. Woessner, Shanrong Zhang, Matthew E. Merritt, and A. Dean Sherry. “Numerical solution of the Bloch equations provides insights into the optimum design of PARACEST agents for MRI”. In: *Magnetic Resonance in Medicine* 53.4 (Apr. 2005), pp. 790–799. ISSN: 0740-3194, 1522-2594. DOI: 10.1002/mrm.20408 (cit. on p. 140).

[21] Kimberly L Desmond and Greg J Stanisz. “Understanding quantitative pulsed CEST in the presence of MT”. In: *Magnetic resonance in medicine: official journal of the Society of Magnetic Resonance in Medicine / Society of Magnetic Resonance in Medicine* 67.4 (Apr. 2012). Cited by 0015, pp. 979–990. ISSN: 1522-2594. DOI: 10.1002/mrm.23074 (cit. on p. 140).

[22] Hirofumi Ono, Hiroyuki Yamada, Shigenobu Matsuda, Kunihiko Okajima, Takeshi Kawamoto, and Hideki Iijima. “1H-NMR Relaxation of Water Molecules in the Aqueous Microcrystalline Cellulose Suspension Systems and Their Viscosity”. In: *Cellulose* 5.4 (Dec. 1, 1998). 00030, pp. 231–247. ISSN: 0969-0239, 1572-882X. DOI: 10.1023/A:1009216015529 (cit. on p. 143).

[23] N. Bloembergen, E. M. Purcell, and R. V. Pound. “Relaxation Effects in Nuclear Magnetic Resonance Absorption”. In: *Physical Review* 73.7 (Apr. 1, 1948). 05431, pp. 679–712. DOI: 10.1103/PhysRev.73.679 (cit. on p. 146).

[24] T. J. Swift and Robert E. Connick. “NMR-Relaxation Mechanisms of O17 in Aqueous Solutions of Paramagnetic Cations and the Lifetime of Water Molecules in the First Coordination Sphere”. In: *The Journal of Chemical Physics* 37.2 (1962), p. 307. ISSN: 00219606. DOI: 10.1063/1.1701321 (cit. on p. 148).

5. Modelling the source of glucoCEST signal

5.1. Contrast in glucoCEST: *The rationale*

Unlike FDG-PET which reports on the uptake and utilisation of glucose, glucoCEST is sensitive to the concentration of sugar in the tissue. However, detection of endogenous sugars is not feasible as their CEST signature is hidden under stronger effects (i.e B1 inhomogeneities, relaxation times, other exchanging molecules) which vary throughout tissues and scans.

Moreover, the steady state concentration of glucose in cancer cells tends to be 3- to 10-fold lower than in normal cells (but not so the glycolytic intermediates which are usually over-expressed[1]). This is likely a consequence of a deficient vasculature in the tumour combined with uncontrolled glycolysis.[2] While in healthy tissues, energy metabolism and blood delivery are tightly coupled through a variety of auto-regulatory mechanisms,[3] cancerous tissues generally display an abnormally high metabolic-rate to blood-perfusion ratio.[4]

In order to generate contrast, 'chemical exchange' based methods like glucoCEST (or exchange dependent T2 variations) rely on the assumption that sugar concentration is heterogeneous in tissues, and more importantly that it varies in time. As such glucoCEST does not measure the amount of sugar in the tissues but rather its variation over a short period of time. (Note the word 'sugar' was specifically chosen, because glucose is not the only substrate that can contribute to the CEST signal. Other substrates in the glycolytic path (G6P, F6P, F16biP, etc) can also add to the net CEST effect, as was shown in Chapter 4. This is a reasonable assumption considering that cancer cells have an aberrant metabolism, with a particularly elevated glycolytic flux.

Provided that the nutrient supply to the tumour cells is scarce to fully meet their metabolic demand and that the auto-regulatory mechanisms are disrupted, a sudden increase in the glucose supply is likely to produce a larger variation of the homoeostatic sugar levels in cancer than in the tightly regulated healthy tissue. The ability

to detect those variations would result in image contrast with intense glucoCEST signal coming from the tumour areas.

Knowledge of whether the observed signal is extracellular, or alternatively it originates from sugars inside the cells, is important in order understand the information provided by the technique. If shown to be intracellular, glucoCEST could offer the possibility of assessing tumour metabolism, which could be useful for the characterization of malignancy. On the contrary if proven to be mostly extracellular, glucoCEST could be informing on blood perfusion in tissues. The study of the possible scenarios in glycolytic dynamics could shed light on the origin of the measured glucoCEST signal. To do so, a mathematical model of glycolysis was built which explores the dynamics and distribution of the different sugars along the glycolytic pathway.

5.2. System Dynamics model of glucose in the tissue.

Most biochemical processes form complex network systems for which intuition alone is not sufficient to fully grasp their dynamical behaviour. In System Dynamics an explicit mathematical description of the network and its interaction allows testing and prediction of the general system's behaviour using computer simulations.

Modulation of the glycolytic rate can lead to different transient state levels of the intermediate sugar. The dynamic study of the transformation of sugar in tissues could help estimate the expected CEST signals, under different physiological conditions. In this context, a compartmental model of glucose delivery in the tissues and its dissociation through glycolysis was built, aimed to obtain a more analytical understanding of the dynamics of glucose and the potential CEST signal associated with it.

The model hereby presented is initially intended to describe the dynamics of glucose entering the brain cells. However, it can also simulate the delivery of glucose to a body cell (not brain) by bypassing the step accounting for the Blood Brain Barrier (BBB).

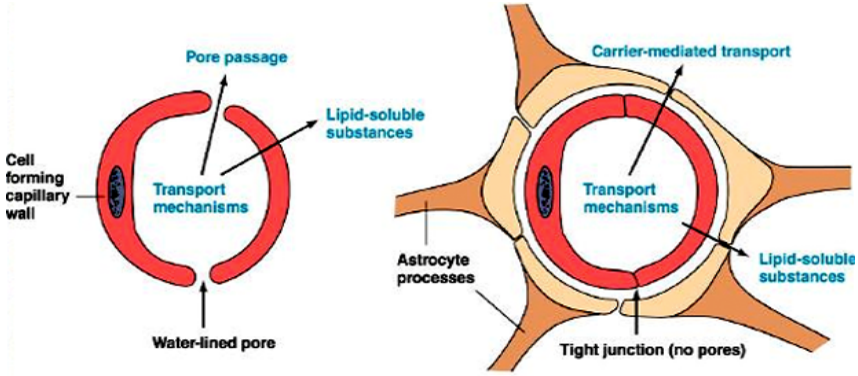

Figure 5.2.1.: *Diagram of the cross-section of capillaries in the body (left) and in the brain (right). The BBB surrounding the brain capillaries exerts a tight control over the passage of metabolites to the cells.*

5.3. A mathematical model of glucose entering the brain

Tumours require large amounts of glucose to support their metabolism. The most important upregulator of glucose entering the brain is the glucose transporter protein GLUT1.[5,6] Dense networks of tangled capillaries, the microvasculature, perfuse all brain regions including tumour tissues. Long endothelial cells joined together by tight junctions form a barrier that prevents glucose from entering the interstitial fluid uncontrolled. Glucose uses GLUT1 to cross both the luminal and abluminal membranes and emerge in the interstitium. GLUT1 is a rate limiting equilibrative glucose transporter, i.e, glucose concentration in the interstitial fluid will tend to equalise with the blood glucose levels in the capillaries, provided a sufficiently large number of transporter molecules is available. Under normal physiological conditions the density of GLUT1 transporters in endothelial cells is low enough to maintain the interstitium glucose concentration well below its corresponding blood concentration. To keep up with the metabolic demands, expression levels of GLUT1 are dynamically increased by reduced availability of glucose and decreased by increased glucose levels.

Glucose from the interstitial fluid, or directly from the capillaries, enters into the cytoplasm by crossing the cell membrane; mediated by the GLUT1 in astrocytes and mediated by the GLUT3 transporter in neurons. The kinetic parameters of these two transporter proteins affect the local distribution of glucose in tissues. In this study

it is assumed the dynamics follow a Michaelis-Menten* type of kinetics.[7,1] Normal GLUT1 density maintains interstitial glucose levels below the blood glucose concentration, and so at glia and neuron levels. GLUT3 has a high affinity for glucose (Km = 1.5 mM) ensuring efficient uptake of glucose by neurons so that neurons can rapidly equilibrate their cytoplasmic glucose concentration with its milieu concentration.[8]

Once inside the cell, free glucose is rapidly converted to glucose-6-phosphate by phosphorylation (mediated via Hexokinase) which reduces glucose concentration in the cytoplasm enabling additional influx of glucose along the concentration gradient. New phosphorylated compounds are produced in subsequent glycolytic reactions (see Chapter 4).

5.4. Outline of the model

Following the above conceptualization a mathematical model was developed that puts together and quantifies some of the regulatory processes controlling glucose dynamics in the brain. Diagrams showing which biochemical processes have been considered in the simulation together with their mutual relationships are displayed in Figures 5.4.1 and 5.4.4. Detailed mathematical equations quantifying these relationships can be consulted in the Matlab code in Appendix G.

The model consists of a set of ordinary differential equations describing the interaction between parameters in different steps of the glycolytic pathway. Equations have been written so that metabolite concentrations equilibrate following a Michaelis-Menten type of kinetics, usually assumed for biochemical models. Parameter values for the transporter kinetics and the enzymatic reactions (Vmax and Km) have been chosen in accordance with the values found in literature, and especially in Simpson et al.[9,8] The model describes a basal glucose income from nutrients that keeps the cell alive and glucose levels stationary under normal metabolic conditions. This represents the normal energy supply by food. In addition, three possible

*Michaelis–Menten kinetics is one of the best-known models of enzyme kinetics. The model takes the form of an equation describing the rate of enzymatic reactions, by relating the reaction rate V to the concentration of a substrate S:

$$V = \frac{d[P]}{dt} = \frac{V_{max}[S]}{K_{\mathrm{M}} + [S]}$$

Where V_{max} represents the maximum rate achieved by the system, at maximum (saturating) substrate concentrations. The Michaelis constant K_{M} is the substrate concentration at which the reaction rate is half of V_{max}. Biochemical reactions involving a single substrate are often assumed to follow Michaelis–Menten kinetics.

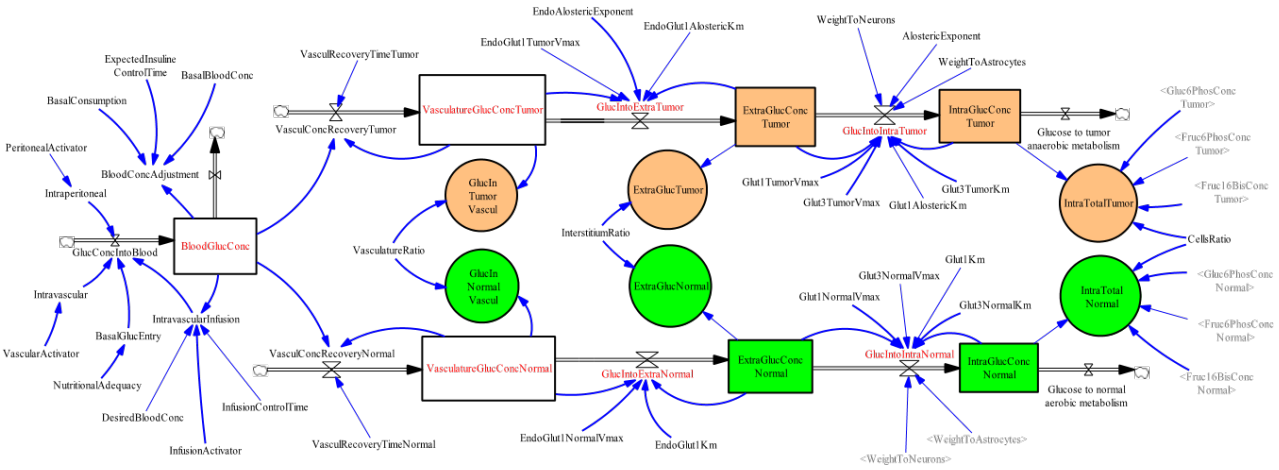

Figure 5.4.1.: *Diagram of the first part of the compartment model illustrating the variables and their relationships in the process of glucose entering the cells. Glucose flux through the four compartments in the model (blood in the main circulatory system, capillaries, interstitial and intracellular space) is modelled by the parameters associated to Glut proteins. From the circulatory blood (where glycaemia is measured), glucose flux evolves differently depending on the characteristics of the tissue: tumour in orange and healthy tissue in green.*

entries of glucose have been implemented in order to analyse the dynamics of the glucose in different scenarios. Extra glucose uptake can be simulated by 1) a single bolus administration via the intravascular route or 2) intraperitoneal route, or 3) by a continuous intravascular infusion of glucose. The continuous intravascular infusion reproduces a glucose clamp experiment in which blood glucose is intended to be kept constant at a specified desired value. In the model the infusion of glucose stops or continues depending on the blood glucose concentration, which is measured every 2 minutes.

Intravascular and intraperitoneal injections have been respectively modelled as a first and third order exponential delay responses to a glucose impulse placed at time=0 minute. Thirty minutes of pre-glucose dosing running of the model permits relevant variables, to reach stationary values so that the glucose administration dynamics is not distorted by transient behaviours. Average delay values for the rise of blood glucose concentration following glucose injections have been adjusted to emulate the glycemic patterns observed in vivo.[12,10,11]

Pancreatic β cells respond to high blood glucose concentration by secreting insulin. Insulin activates the synthesis of glycogen which is stored in the liver and muscle which reduces glucose blood concentration. Insulin continues to be secreted until the blood sugar level has been lowered to normal levels. The expected insulin

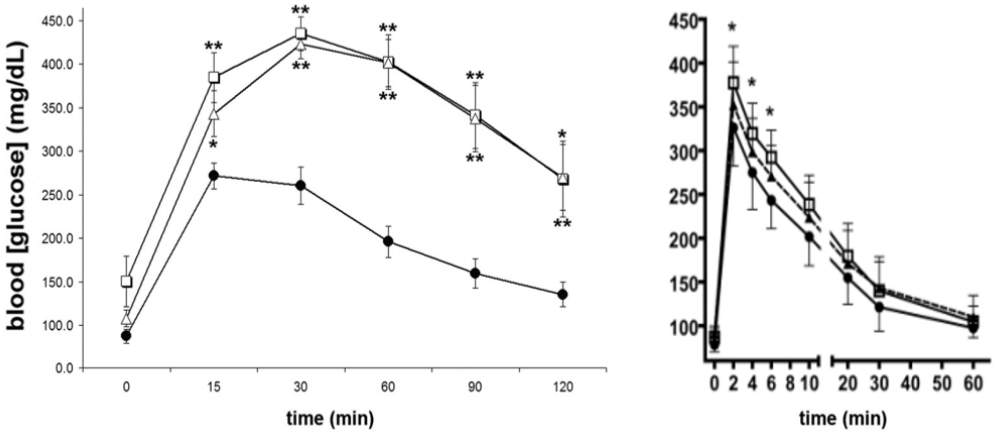

Figure 5.4.2.: *Intra-peritoneal (IP) and intra-venous (IV) glucose tolerance tests performed in fasted mice. Glucose concentration was measured in the tail vein blood after IP and IV injection of filter-sterilized glucose in PBS (2.0 mg glucose/g body weight for IP and bolus dose of 0.5 mg glucose/g of body weight for IV case). Figures reproduces from Tweedie et al. and Lim et al.*[10,11]

control time for the recovery to basal levels seems to be shorter for abrupt increases of glucose (intravascular delivery) than for smoother increases induced by intraperitoneal injections. In the model we have used 50 and 180 minutes for the expected insulin control times for the intravascular and intraperitoneal respectively injections what is roughly compatible with published data in the literature. Figure 5.4.2 illustrates the different time response of blood sugar levels using either the IP or IV route for the administration of glucose. Figure 5.4.3 shows the simulated glycemic response in the model.

Brain is perfused by micro-vessels that facilitate the flow of blood from the global circulation into tissue. Microvasculature glucose concentration is replenished from the global circulation, reaching equilibrium values that may differ from those of the main blood glycaemia. In normal tissue the capillary recovery time is short, allowing fast equilibrium between the microvascular glucose level and the glycaemia in the main circulation. Tumour tissue might have an impaired microvasculature structure hindering its refreshment and perfusion capacity. In this circumstance tumoral microvasculature might reach a glucose concentration equilibrium that is below the main circulatory blood glucose concentration. In the model, normal tissue's refreshment capacity has been modelled assuming that its microvasculature is able to recover up to sixty percent of its glucose concentration discrepancy with main blood circulation in only 1 minute. Larger recovery times can be used to model different degrees of tumour microvasculature impairment if required.

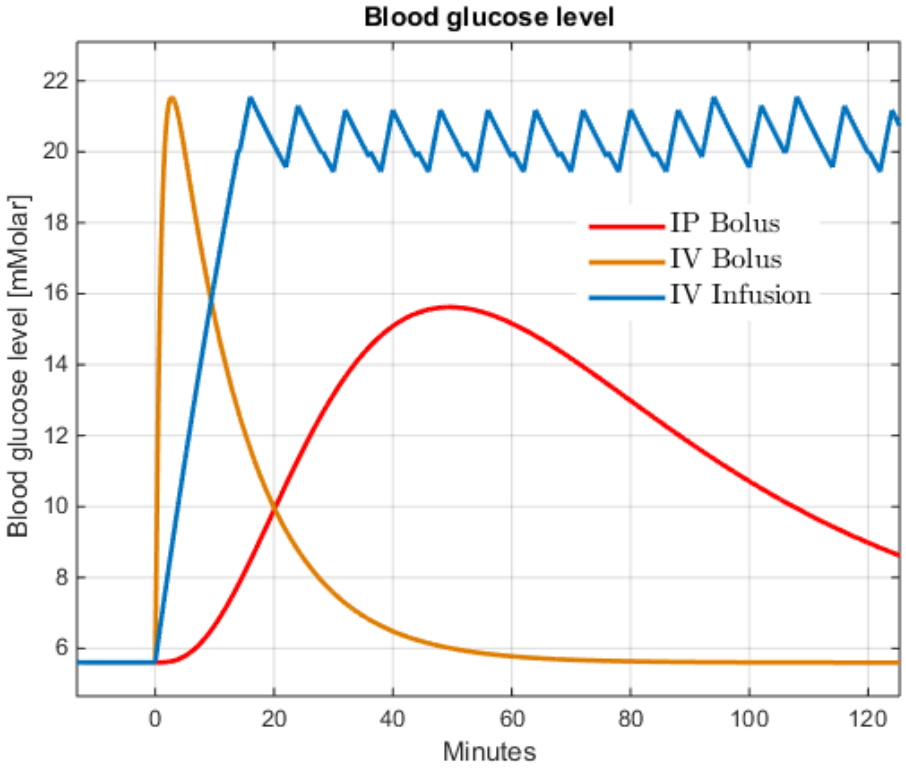

Figure 5.4.3.: *Simulated blood glucose levels following the administration of glucose via an IP bolus, IV bolus and IV infusion. A first and third order impulse functions were used to emulate the IV and IP glucose administration cases respectively, which yield to blood glucose responses similar to the observed in real glucose tolerance tests.*

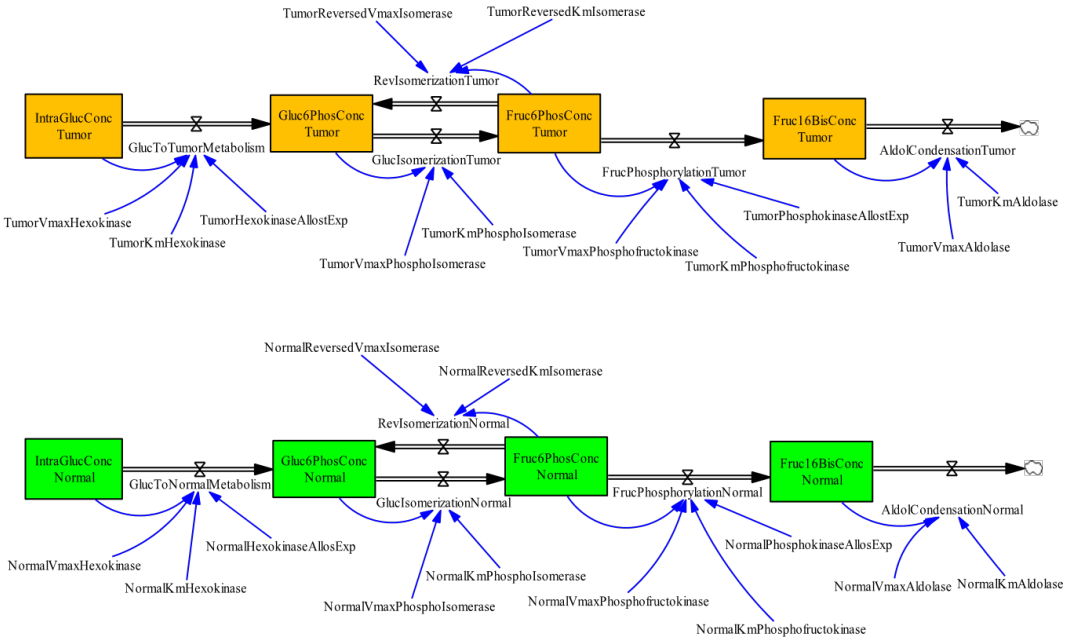

Figure 5.4.4.: *Flow diagram of the model illustrating glycolytic reactions occurring in the cytoplasm of the cells.*

Glucose entering the extracellular milieu across the blood-brain barrier (BBB) has been modelled mediated by GLUT1 transporters. From the extracellular milieu glucose crosses the cell membranes into the cytoplasm mediated by GLUT1 in astrocytes and by GLUT3 in neurons. In the model both entries have been averaged and represented by a single entry, with a one to one neuron to astrocyte ratio. Once in the cell glucose quickly undergoes metabolic transformation through the glycolytic pathway which has been generically represented in the model by a flow of glucose through the metabolism of tumour and normal tissues. This reaction is catalysed by the enzyme hexokinase which quickly reduces the concentration of free glucose inside the cell facilitating its continuous entry mediated by the equilibrative transporters GLUT1 and GLUT3. In successive steps glucose-6-phosphate is isomerized to fructose-6 phosphate which after a new phosphorylation yields fructose-1,6-bisphosphate. Modelling is stopped here with the condensation of this aldol to dihydroxyacetone phosphate.

The above described processes have been represented for both tumoral and healthy tissue with parallel structures although with different appropriate parameter values. Control over glycolytic flux is believed to reside primarily in the transport and phosphorylation steps,[13,14] and therefore to simulate conditions in cancer, expressions of GLUT1 and HK have been significantly increased (by rising the Vmax of these two proteins more than the rest of the enzymes).

Glucose and glycolytic intermediate levels are expressed in millimolar which is not an additive unit. In order to quantify the contribution of each compound to the CEST contrast, their concentrations have been weighted with the volume ratio of each compartment, i.e vasculature, interstitial and intracellular milieu. The volume fractions set to 0.03 for the microvasculature, 0.15 for the interstitium and 0.82 for the cell volume, in agreement with values reported for tumour microstructure.[15,16,17] Finally, the total intracellular signal is calculated by adding the effect of the different glycolytic sugars which are present inside the cell.

5.5. Simulation results and discussion

5.5.1. Increased glycolysis

The overexpression of Glut transporters (notably GLUT1 and GLUT3) and hexokinase (HK) I and II enzymes[14,18,19] leads to basal glycolic rates up to 20 times larger in metastatic cells compared to those in their normals counterparts. In our model tumour basal glycolitic flux is ∼12 times the rate of normal tissue.

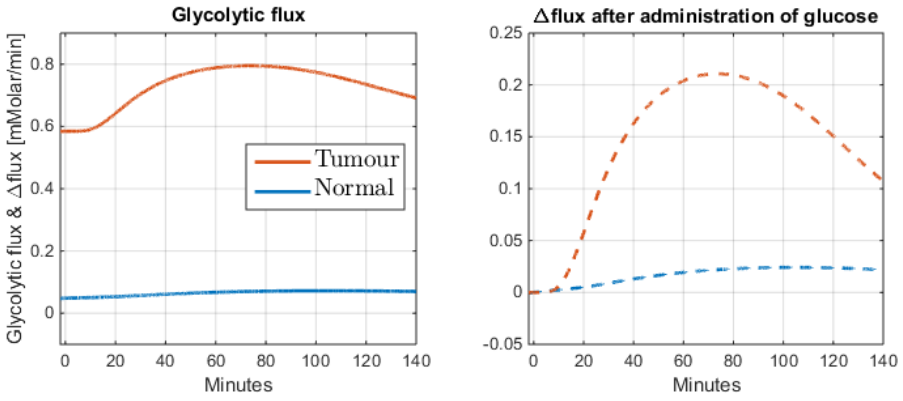

Figure 5.5.1.: *Glycolytic flux and its change caused by an abrupt increase in blood glucose concentration, through healthy and cancerous cells.*

While the activity of other catalytic enzymes are also unregulated, GLUT1 and Hexokinase2 have been reported to exert the main control over the glycolytic flux in tumoral cells, regulating up to 71% of the total glucose uptake rate.[20,21]

Importantly, following a rise in glycaemia the transient glucose uptake in tumours is also enhanced beyond the normal physiological values, resulting in significant variations of the glycolytic rate over time. As shown in figure 5.5.1 the glycolytic flux in cancer cells increases by 0.21mMolar/min (from 0.59 to 0.8 mMolar/min) as the result of an IP bolus of glucose. Meanwhile normal tissue sustains a rate increase

of just 0.024 mMolar/min.

5.5.2. Sugar distribution

Compared to healthy tissues, neoplasms display a different distribution of the glucose intermediate concentrations.
Over-expression of Glut transporters and HK in neoplasic cells induces fast depletion of the interstitial and intracellular glucose in conjunction with an accumulation of glycolytic intermediates inside the cells. This phenomenon, illustrated by the simulations in figure 5.5.2 has also been shown in *in vitro* cell studies,[1,22] where levels of intracellular sugars have been measured to be higher than tissue glucose concentration itself.

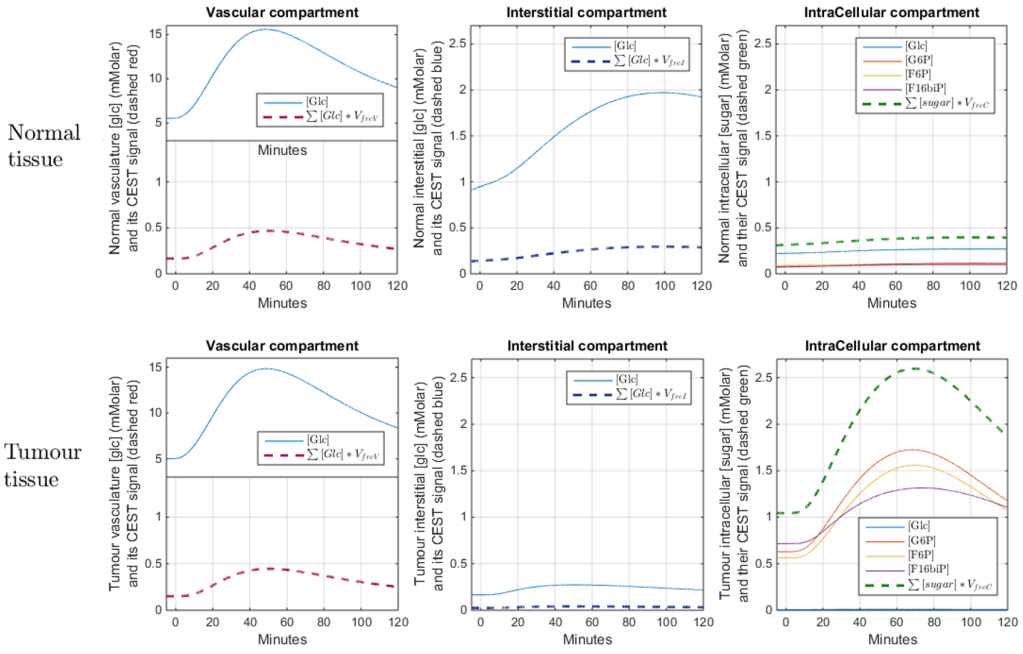

Figure 5.5.2.: *Concentration of glucose and its derivatives in the vascular, interstitial and intracellular spaces following an IP bolus injection of glucose. Dashed lines represent the relative CEST signal intensity in each compartment* $(\sum [sugars] * Volume)$.

The contribution of each compartment to the total glucoCEST signal can be estimated from the relative metabolite concentration and the volume of the compartment. For that purpose the strength of CEST signal has been assumed to be proportional to the volume and sugar concentration but independent of the compartment

itself*.

The graphs in figure 5.5.3 show the relative signal contribution of each compartment (normalised to the maximum GCE). Using the same parameter setting as in figure 5.5.2, the model predicts an overwhelming intracellular contribution in tumours† compared to the mostly vascular component in healthy tissue.

Perhaps the most remarkable lesson to be learnt from these simulations is the importance of timing in the acquisition of CEST images. For instance, in the case of IV bolus the model predicts that 20 minutes after the administration of glucose, more than 80% of the signal in the tumour would be of intracellular origin.

While the model is possibly not accurate enough as to give exact timings, it is possibly robust enough to provide insight about the importance of deciding an appropriate time-frame of the experiment for different glucose inputs.

5.5.3. Estimation of the glucoCEST signal

Based on the phantom study described in Chapter 4 a relation of the expected GCE signal and the sugar concentration increase in the tissue was approximated as 0.2% GCE per mmolar (hexoses were weighted twice as much as the pentoses because of their higher signal).
The millimolar concentrations in each compartment can now be translated into GCE signal and the total expected glucoCEST estimated.

Figure 5.5.4 shows the predicted glucoCEST signal for each of the routes of glucose administration. The fast insulin response in the case of the IV bolus, quickly reduces the amount of glucose in blood and avoids a substantial increase in the transient state concentration of the glycolytic intermediates inside the cell. The result is a lower intensity GCE using the IV bolus route compared to the IP route for the same dose of glucose.

The IV infusion method produces the most intense GCE signal as hyperglycaemia is kept for a prolonged period of time. For these simulations the volume ratio of each compartment was set to be the same for both tumours and healthy tissue. However, the effect of enlarged vascular fraction in tumoral regions can be also simulated.

*The author acknowledges that different physiological conditions in the model compartments (pH, phosphates levels, viscosity) would lead to the modulation of the signal intensity. However these simulations do not account for such effects and treats the compartments indistinctively.

†For this simulation the BBB in the tumour tissue has been assumed to be intact and as such it prevents large glucose leakages to the interstitial space.

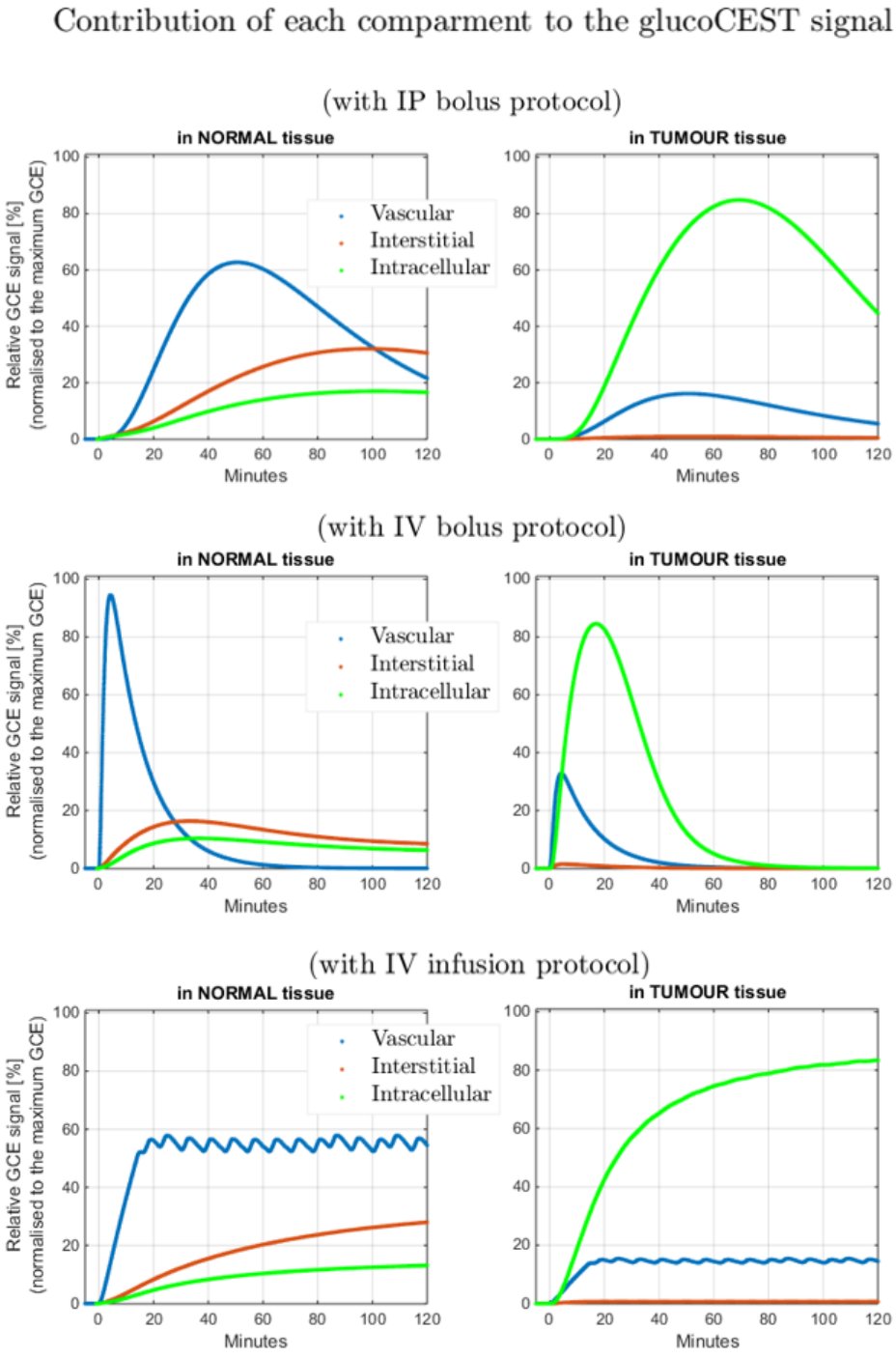

Figure 5.5.3.: *Relative GCE signal in each compartment for healthy and tumour tissues. Each raw represents different routes of glucose administration.*

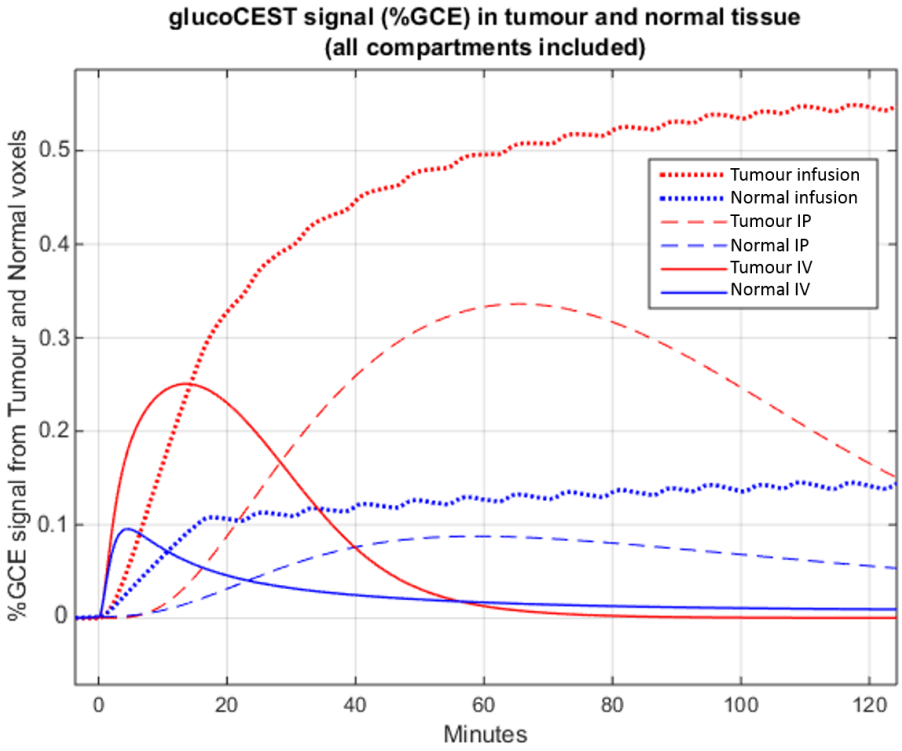

Figure 5.5.4.: *Total estimated glucoCEST signal in tumour and healthy tissue with different methods for glucose administration.*

5.5.4. Comparisons of LS174T and SW1222 tumour cell lines

In our initial glucoCEST study[12] two cancer cell-lines with distinct phenotypes were studied. The LS174T cells are poorly differentiated, whereas the SW1222 display a well-differentiated glandular structure.[23]

To simulate the glucoCEST profile of these distinct tumours, their compartment volume ratios were adjusted in the model to match the experimental values found in a separate study by Panagiotaki et al[24] (see figure 5.5.5).

Comparison of the 18F-FDG measurements in both tumours revealed 1.7 fold higher uptake in SW1222 than in LS174T tumours. The disparity in the metabolic rate between the two cell-lines was simulated by a parameter (*aggressiveness*) which controls the Vmax values of Hexokinase and GLUT1 in the model. The *aggressiveness* value was set to 10 for SW1222 cells and 6 for the LS174T, which gave a glycolytic flux ratio close to the 1.7 (see figure 5.5.6).

Additionally, in order to describe the glucose dynamics outside the brain (where no BBB is present), parameters that controls the *endothelial GLUT1* transport were bypassed.

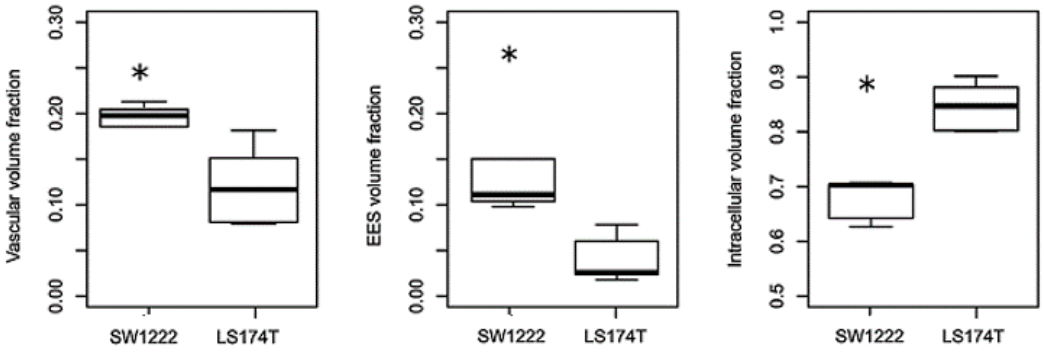

Figure 5.5.5.: *Vascular, interstitial (EEC) and intracellular volume fraction of LS174T and SW1222 tumours measured with VERDICT MRI. Figure modified from.*[24]

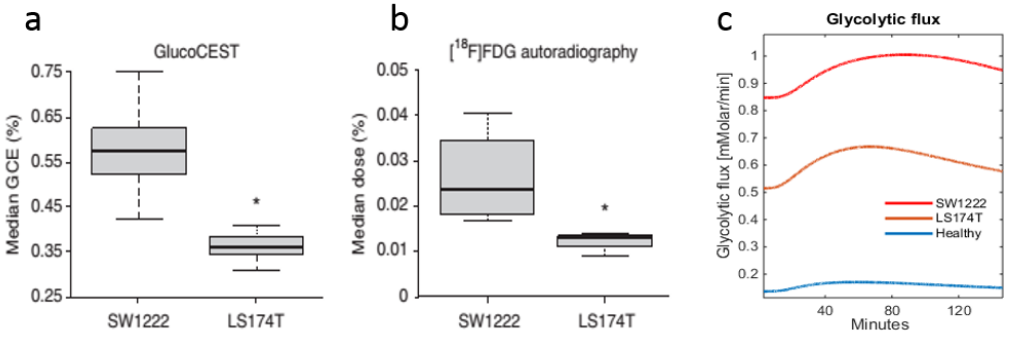

Figure 5.5.6.: *Comparison of LS174T and SW122s metabolic traits. GCE (a), FDG uptake (b) and simulated rate of glycolysis (c).*

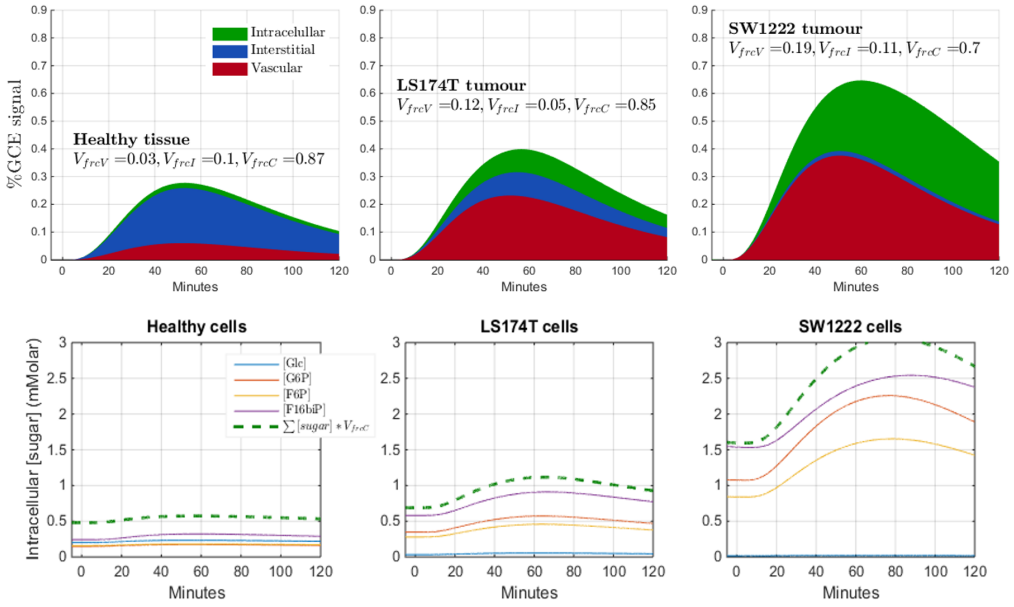

Figure 5.5.7.: *Comparison of the expected GCE signal in healthy, LS174T and SW1222 tumours. Different colours illustrate the contribution of each compartment to the total signal.*

Figure 5.5.7 shows the simulated GCE measurement in normal tissue and both tumours. The most intense GCE signal (0.64% of the $MTR_{asymetry}$) is predicted to arise from the highly glycolytic SW1222 cell line, followed by the signal from LS174T cancer cells (0.4%) and healthy tissue (0.27%). Notably the interstitial contribution is dominant in the normal muscle tissue. This is understandable as in the absence of BBB, the interstitial glucose concentration closely follows the glucose blood level,[25,26] which scaled up by the interstitial volume produced a significant GCE signal.

In the case of *aggressive* tumours however, the interstitial contribution reduces dramatically as over-expressed glucose carriers quickly move glucose into the cell. While glucose is depleted from the extracellular space, fast HK activity generates large amounts of glycolitic intermediates which rise the intracellular concentration. Even a moderate increase brings up the estimated GCE, as most of the tissue volume is comprised of cells.

5.5.5. Source of GCE in LS174T and SW122 tumours

The ratio between the vascular volume fraction of the two cancer cell lines matches remarkably well with the ratio between the observed GCE signal. This would strongly suggest that most of the GCE signal comes from the blood compartment. However,

	Experimental Values				Model Values			
	%GCE	rVascularV	rInterstitialV	rCellularV	Total	Vasc. %GCE	Vas+Inter	Cell. %GCE
SW1222	0.57	0.19	0.11	0.7	0.64	0.36	0.37	0.27
LS174T	0.36	0.12	0.05	0.83	0.4	0.22	0.09	0.09
Muscle	0.17	0.04	0.1	0.85	0.27	0.057	0.30	0.018
SW1222 / LS174T	1.58	1.58	2.2	0.84	1.6	1.64	4.11	3
SW1222 / Healthy	3.35	4.75	1.1	0.82	2.37	6.32	1.24	15
Best fit		1.40	2.33	2.63	**0.98**	2.96	3.29	11.73

Figure 5.5.8.: *Median %GCE and compartment volume fractions measured in SW1222 and LS174T cell line tumours and in muscle tissue (left). Model prediction for the total %GCE and the contribution of each compartment for the same tissues (right). Best fit calculated as the minimum of* $\sqrt{(\frac{SW1222}{LS174T})^2 + (\frac{SW1222}{Heatlhy})^2}$.

looking at the same ratio between SW1222 and healthy tissue it would appear that the contribution from the vascular compartment is overestimated. Furthermore, it is not clear why the interstitial space, which has high concentration of sugar and larger volume than the vascular one, would not contribute to the GCE contrast. Values for these ratios can be found in the table of figure 5.5.8.

For intracellular CEST contribution to be compatible with the measured %GCE ratios, signal from inside the cell is required to be larger in the SW1222 cell line in order to compensate for its smaller intracellular volume ratio. Our simulations prove that this is certainly a possibility and in fact, the inclusion of the CEST contribution from *all three* compartment (predicted by the simulation) seems to give the best fit to the experimental results, rather than just considering the vascular contribution. However, this is quite coincidental as small variations in the model parameters can significantly change the final output. Hence a dominant vascular component remains as a strong possibility to explain the observed glucoCEST in these experiments.

5.6. Consequences of amino-acid production

A notable result from the 13C-NMR (carbon 13 nuclear magnetic resonance) spectroscopy presented in the first glucoCEST study[12] is the high concentration of several amino-acids in the tumour tissue. In the two cancer cell-lines analysed (SW1222 and LS174T) taurine, alanine and glutamine amino-acid peaks were particularly in-

tense, together accompanied by over-expressed lactate from anaerobic glycolysis*.

It is known that pyruvate, the end product of glycolysis, can undergo transamination to alanine mediated by the alanine transaminase (ALT), or serum glutamate-pyruvate transaminase (SGPT).[27] The rate of alanine synthesis is proportional to the intracellular pyruvate concentration, thus an increased glycolysis in tumours could promote alanine production.

On the other hand, glutamine synthesis from glucose has been shown to be a prominent feature of primary gliomas.[28]

Inspection of the CEST capabilities of these amino-acids showed defined peaks around 3ppm in the Z-spectra, demonstrating the potential of these amino-acid in the production of glucoCEST contrast. For details about the preparation of the phantoms shown in figure 5.6.1 please refer to Appendix C.

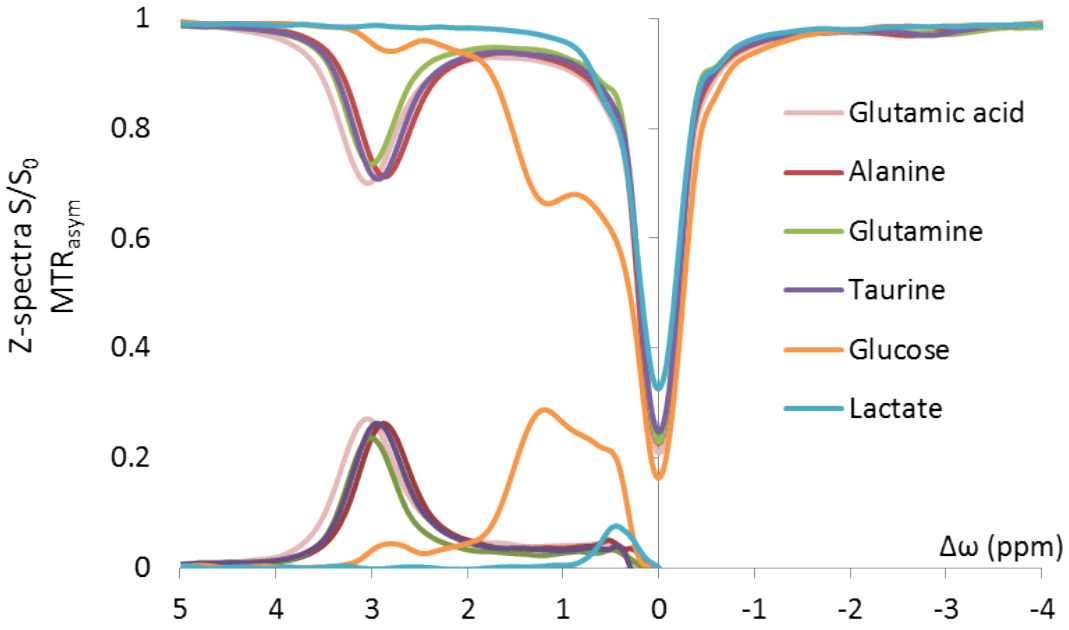

Figure 5.6.1.: *Z- and MTRasym spectra from glucose, lactate, glutamine,glutamate, alanine and taurine. While lactate shows negligible signal, amino acids show distinct CEST peaks centred at 3 ppm from the water frequency.*

Therefore, provided the amino-acids turn-over is enhanced as the result of an elevation in glucose level, amino-acids produced inside the cells could add towards the observed glucoCEST signal.

*Despite being an anaerobic process (no oxygen is consumed), some authors use the misleading term *aerobic glycolysys* to express the the fact that tumour cells undergo anaerobic production of lactate even in abundance of oxygen availability.

5.7. Conclusion

The model presented in this work is an oversimplified description of the full dynamics in glycolysis. More elaborate biochemical systems can certainly help understanding particular pathways or specific key question researchers might want to investigate. An example of this can be seen in figure 5.7.1 which illustrates a model built to account for the influence of the ATP charge (ATP to AMP ratio) in the net glycolytic flux. Another possibility would be to incorporate the anabolic role of glucose e.g. by coupling the glycolysis to the pentose phosphate pathway (ppp), and account for the synthesis of amino acids.

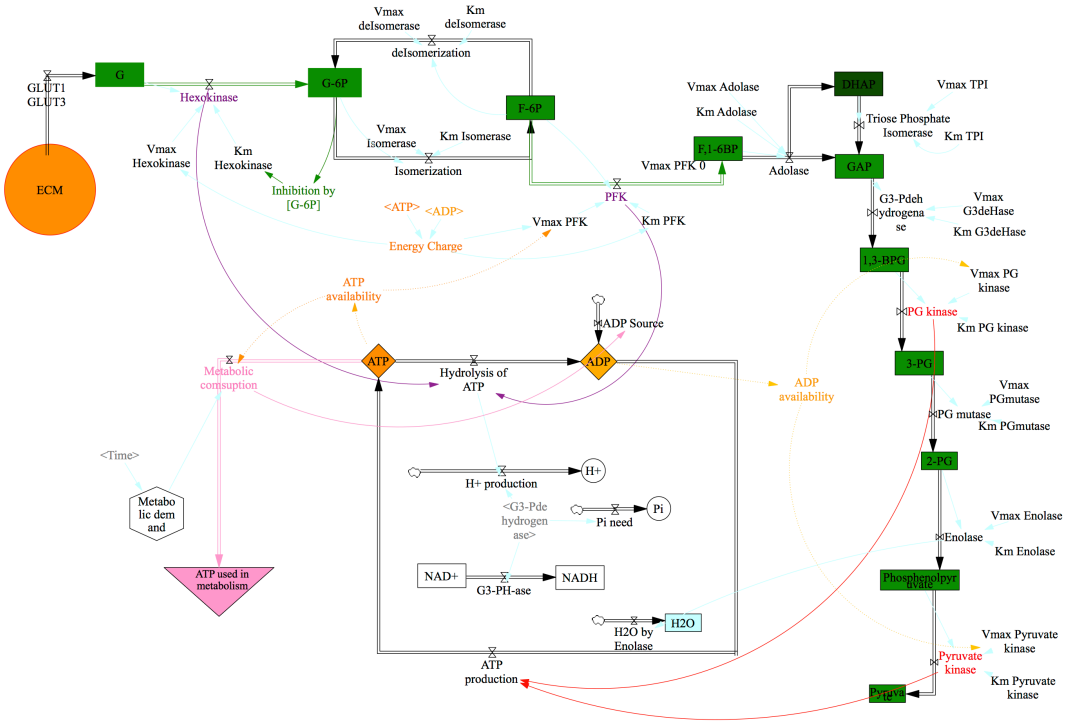

Figure 5.7.1.: *Example of an extended model of glycolysis developed to investigate the influence of the ATP charge [ATP to AMP ratio] in the glycolytic flux of cancer cells.*

However, modelling higher complexity systems inevitably comes with the drawback of increasingly larger number of unknown parameters to deal with. Too many parameters often blur the purpose of the simulation, which should serve to stimulate new insights about the dynamics of the system under study. As such, the purpose of this work was to give a reasonable representation of the processes that might govern the creation of glucoCEST contrast.

Despite its simplicity the model successfully illustrates how variations in the metabolic profile of tumours could dramatically change the observed glucoCEST

signal.

These type of models can also serve as an argument to challenge the notion that glucoCEST cannot give metabolic information because of the dynamics of glycolysis is *too fast* to be captured. The simulations show how fast glycolytic rate is *compatible* with high levels of glycolytic intermediates, and therefore inspection of intracellular metabolism with glucoCEST may be possible.

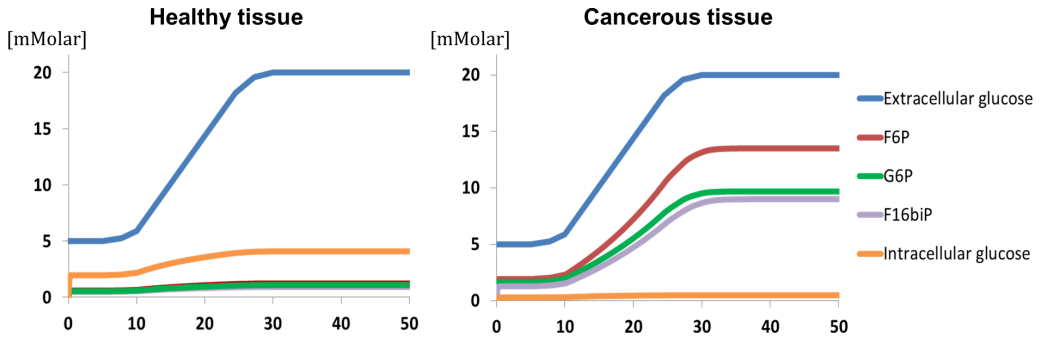

Figure 5.7.2.: *Simulated steady-state values of elevated glycolytic intermediates in a glucose clamp experiment (glycemia 20mMolar) for healthy and cancer tissue. Concentration of intracellular sugars in cancer rise to above 10 mmolar, as documented in Marín-Hernández et al.*[1,22] *Simulation done using the model in Figure 5.7.1.*

It has been shown that values of the glycolytic intermediates in certain cancers cells can reach extremely high values, to concentrations above the normal blood glycaemia, in some cases.[1,22] In tumours with similar characteristics, maintaining a high blood glucose level (with an IV infusion of glucose for instance), could induce build up of intracellular sugars up to values that should be easily detectable with glucoCEST. Simulations in figure 5.7.2 illustrate this effect.

The question still remains whether high intracellular phosphate levels would make detection of CEST signal from cellular sugars impossible.
Examination of the effects of cellular phosphate levels and other physiological buffers on the chemical exchange rate and hence on the CEST signal *in vivo* is an interesting subject for further study.

In a scenario in which detection of intracellular glucoCEST proves to be unrealistic (either because of high phosphate or low glycolytic-sugar levels), glucose in combination with glucoCEST could potentially be used as a natural contrast agent to measure perfusion.

On the other hand, assuming there is a good chance of detecting glucoCEST signal from the intracellular space, discrimination capacity between each compartment could be improved by scanning at the right time or by designing a clever pulse se-

quence aimed to avoid blood contribution, e.g. an *ASL-CEST* protocol. In fact the beauty and power of the model is indeed to give an alternative perspective on the processes governing the glucoCEST contrast and hopefully trigger creative thinking to improve it.

Chapter references

[1] Alvaro Marín-Hernández, Juan Carlos Gallardo-Pérez, Sara Rodríguez-Enríquez, Rusely Encalada, Rafael Moreno-Sánchez, and Emma Saavedra. “Modeling cancer glycolysis”. In: *Biochimica et Biophysica Acta (BBA) - Bioenergetics* 1807.6 (June 2011), pp. 755–767. ISSN: 00052728. DOI: 10.1016/j.bbabio.2010.11.006 (cit. on pp. 159, 162, 168, 177).

[2] Akiyoshi Hirayama, Kenjiro Kami, Masahiro Sugimoto, Maki Sugawara, Naoko Toki, Hiroko Onozuka, Taira Kinoshita, Norio Saito, Atsushi Ochiai, Masaru Tomita, Hiroyasu Esumi, and Tomoyoshi Soga. “Quantitative Metabolome Profiling of Colon and Stomach Cancer Microenvironment by Capillary Electrophoresis Time-of-Flight Mass Spectrometry”. In: *Cancer Research* 69.11 (Jan. 6, 2009). 00310, pp. 4918–4925. ISSN: 0008-5472, 1538-7445. DOI: 10.1158/0008-5472.CAN-08-4806. pmid: 19458066 (cit. on p. 159).

[3] Johnathan D. Tune, Mark W. Gorman, and Eric O. Feigl. “Matching coronary blood flow to myocardial oxygen consumption”. In: *Journal of Applied Physiology (Bethesda, Md.: 1985)* 97.1 (July 2004). 00210, pp. 404–415. ISSN: 8750-7587. DOI: 10.1152/japplphysiol.01345.2003. pmid: 15220323 (cit. on p. 159).

[4] David A. Mankoff, Lisa K. Dunnwald, Savannah C. Partridge, and Jennifer M. Specht. “Blood Flow-Metabolism Mismatch: Good for the Tumor, Bad for the Patient”. In: *Clinical cancer research : an official journal of the American Association for Cancer Research* 15.17 (Sept. 1, 2009). 00020, pp. 5294–5296. ISSN: 1078-0432. DOI: 10.1158/1078-0432.CCR-09-1448. pmid: 19706819 (cit. on p. 159).

[5] Karin Reinicke, Paula Sotomayor, Pedro Cisterna, Carolina Delgado, Francisco Nualart, and Alejandro Godoy. “Cellular distribution of Glut-1 and Glut-5 in benign and malignant human prostate tissue”. In: *Journal of Cellular Biochemistry* 113.2 (Feb. 1, 2012). 00021, pp. 553–562. ISSN: 1097-4644. DOI: 10.1002/jcb.23379 (cit. on p. 161).

[6] Silvia Mangia, Ian A. Simpson, Susan J. Vannucci, and Anthony Carruthers. “The in vivo neuron-to-astrocyte lactate shuttle in human brain”. In: *Journal of neurochemistry* 109 (Suppl 1 May 2009). 00099, pp. 55–62. ISSN: 0022-3042. DOI: 10.1111/j.1471-4159.2009.06003.x. pmid: 19393009 (cit. on p. 161).

[7] James Keener and James Sneyd, eds. *Mathematical Physiology*. Red. by S.S. Antman, J.E. Marsden, and L. Sirovich. Vol. 8/1. Interdisciplinary Applied Mathematics. 02343. New York, NY: Springer New York, 2009. ISBN: 978-0-387-75846-6 978-0-387-75847-3 (cit. on p. 162).

[8] Ian A. Simpson, Donard Dwyer, Daniela Malide, Kelle H. Moley, Alexander Travis, and Susan J. Vannucci. “The facilitative glucose transporter GLUT3: 20 years of distinction”. In: *American Journal of Physiology. Endocrinology and Metabolism* 295.2 (Aug. 2008). 00139, E242–253. ISSN: 0193-1849. DOI: 10.1152/ajpendo.90388.2008. pmid: 18577699 (cit. on p. 162).

[9] Ian A. Simpson, Anthony Carruthers, and Susan J. Vannucci. “Supply and demand in cerebral energy metabolism: the role of nutrient transporters”. In: *Journal of Cerebral Blood Flow & Metabolism* 27.11 (2007), pp. 1766–1791 (cit. on p. 162).

[10] Elizabeth Tweedie, Isabella Artner, Laura Crawford, Greg Poffenberger, Bernard Thorens, Roland Stein, Alvin C. Powers, and Maureen Gannon. “Maintenance of Hepatic Nuclear Factor 6 in Postnatal Islets Impairs Terminal Differentiation and Function of β-Cells”. In: *Diabetes* 55.12 (Jan. 12, 2006). 00018, pp. 3264–3270. ISSN: 0012-1797, 1939-327X. DOI: 10.2337/db06-0090. pmid: 17130469 (cit. on pp. 163, 164).

[11] Soo Lim, Sun Young Ahn, In Chan Song, Myung Hee Chung, Hak Chul Jang, Kyong Soo Park, Ki-Up Lee, Youngmi Kim Pak, and Hong Kyu Lee. “Chronic Exposure to the Herbicide, Atrazine, Causes Mitochondrial Dysfunction and Insulin Resistance”. In: *PLoS ONE* 4.4 (Apr. 13, 2009). 00095. ISSN: 1932-6203. DOI: 10.1371/journal.pone.0005186. pmid: 19365547 (cit. on pp. 163, 164).

[12] Simon Walker-Samuel, Rajiv Ramasawmy, Francisco Torrealdea, Marilena Rega, Vineeth Rajkumar, S. Peter Johnson, Simon Richardson, Miguel Gonçalves, Harold G. Parkes, Erik Arstad, David L. Thomas, R. Barbara Pedley, Mark F. Lythgoe, and Xavier Golay. “In vivo imaging of glucose uptake and metabolism in tumors”. In: *Nature Medicine* 19.8 (Aug. 2013). 00044 Cited by 0001, pp. 1067–1072. ISSN: 1078-8956. DOI: 10.1038/nm.3252 (cit. on pp. 163, 171, 174).

[13] Robert A. Gatenby and Robert J. Gillies. “Why do cancers have high aerobic glycolysis?” In: *Nature Reviews Cancer* 4.11 (Nov. 2004), pp. 891–899. ISSN: 1474-175X, 1474-1768. DOI: 10.1038/nrc1478 (cit. on p. 166).

[14] A. Wolf, S. Agnihotri, J. Micallef, J. Mukherjee, N. Sabha, R. Cairns, C. Hawkins, and A. Guha. “Hexokinase 2 is a key mediator of aerobic glycolysis and promotes tumor growth in human glioblastoma multiforme”. In: *Journal of Experimental Medicine* 208.2 (Feb. 14, 2011). 00171, pp. 313–326. ISSN: 0022-1007, 1540-9538. DOI: 10.1084/jem.20101470 (cit. on pp. 166, 167).

[15] H J Aronen, I E Gazit, D N Louis, B R Buchbinder, F S Pardo, R M Weisskoff, G R Harsh, G R Cosgrove, E F Halpern, and F H Hochberg. “Cerebral blood volume maps of gliomas: comparison with tumor grade and histologic findings.” In: *Radiology* 191.1 (Apr. 1, 1994). 00811, pp. 41–51. ISSN: 0033-8419. DOI: 10.1148/radiology.191.1.8134596 (cit. on p. 167).

[16] Hana Lahrech, Adriana-Teodora Perles-Barbacaru, Soâd Aous, Jean-François Le Bas, Jean-Claude Debouzy, Andrée Gadelle, and Pascal H. Fries. “Cerebral blood volume quantification in a C6 tumor model using gadolinium per (3,6-anhydro) α-cyclodextrin as a new magnetic resonance imaging preclinical contrast agent”. In: *Journal of Cerebral Blood Flow &*

Metabolism 28.5 (Jan. 9, 2008). 00007, pp. 1017–1029. ISSN: 0271-678X. DOI: 10.1038/sj.jcbfm.9600602 (cit. on p. 167).

[17] Seymur Gahramanov, Leslie L. Muldoon, Xin Li, and Edward A. Neuwelt. "Improved Perfusion MR Imaging Assessment of Intracerebral Tumor Blood Volume and Antiangiogenic Therapy Efficacy in a Rat Model with Ferumoxytol". In: *Radiology* 261.3 (Dec. 2011). 00019, pp. 796–804. ISSN: 0033-8419. DOI: 10.1148/radiol.11103503. pmid: 21940504 (cit. on p. 167).

[18] Krushna C. Patra, Qi Wang, Prashanth T. Bhaskar, Luke Miller, Zebin Wang, Will Wheaton, Navdeep Chandel, Markku Laakso, William J. Muller, Eric L. Allen, Abhishek K. Jha, Gromoslaw A. Smolen, Michelle F. Clasquin, R. Brooks Robey, and Nissim Hay. "Hexokinase 2 Is Required for Tumor Initiation and Maintenance and Its Systemic Deletion Is Therapeutic in Mouse Models of Cancer". In: *Cancer Cell* 24.2 (Aug. 2013), pp. 213–228. ISSN: 15356108. DOI: 10.1016/j.ccr.2013.06.014 (cit. on p. 167).

[19] S P Mathupala, Y H Ko, and P L Pedersen. "Hexokinase II: Cancer's double-edged sword acting as both facilitator and gatekeeper of malignancy when bound to mitochondria". In: *Oncogene* 25.34 (Aug. 7, 2006), pp. 4777–4786. ISSN: 0950-9232, 1476-5594. DOI: 10.1038/sj.onc.1209603 (cit. on p. 167).

[20] Sara Rodríguez-Enríquez, Alvaro Marín-Hernández, Juan Carlos Gallardo-Pérez, and Rafael Moreno-Sánchez. "Kinetics of transport and phosphorylation of glucose in cancer cells". In: *Journal of Cellular Physiology* 221.3 (Dec. 2009). 00037, pp. 552–559. ISSN: 00219541. DOI: 10.1002/jcp.21885 (cit. on p. 167).

[21] Anique Herling, Matthias König, Sascha Bulik, and Hermann-Georg Holzhütter. "Enzymatic features of the glucose metabolism in tumor cells". In: *The FEBS journal* 278.14 (July 2011). 00026, pp. 2436–2459. ISSN: 1742-4658. DOI: 10.1111/j.1742-4658.2011.08174.x. pmid: 21564549 (cit. on p. 167).

[22] Alvaro Marín-Hernández, Sara Rodríguez-Enríquez, Paola A. Vital-González, Fanny L. Flores-Rodríguez, Marina Macías-Silva, Marcela Sosa-Garrocho, and Rafael Moreno-Sánchez. "Determining and understanding the control of glycolysis in fast-growth tumor cells. Flux control by an over-expressed but strongly product-inhibited hexokinase". In: *The FEBS journal* 273.9 (May 2006). 00000, pp. 1975–1988. ISSN: 1742-464X. DOI: 10.1111/j.1742-4658.2006.05214.x. pmid: 16640561 (cit. on pp. 168, 177).

[23] Uzma Qureshi Ethaar El Emir. "Predicting response to radioimmunotherapy from the tumor microenvironment of colorectal carcinomas". In: *Cancer research* 67.24 (2008). 00038, pp. 11896–905. ISSN: 1538-7445. DOI: 10.1158/0008-5472.CAN-07-2967 (cit. on p. 171).

[24] E. Panagiotaki, S. Walker-Samuel, B. Siow, S. P. Johnson, V. Rajkumar, R. B. Pedley, M. F. Lythgoe, and D. C. Alexander. "Noninvasive Quantification of Solid Tumor Microstructure Using VERDICT MRI". In: *Cancer Research* 74.7 (Apr. 1, 2014). 00008, pp. 1902–1912. ISSN: 0008-5472, 1538-7445. DOI: 10.1158/0008-5472.CAN-13-2511 (cit. on pp. 171, 172).

[25] B. Aussedat, M. Dupire-Angel, R. Gifford, J. C. Klein, G. S. Wilson, and G. Reach. “Interstitial glucose concentration and glycemia: implications for continuous subcutaneous glucose monitoring”. In: *American Journal of Physiology - Endocrinology and Metabolism* 278.4 (Apr. 1, 2000). 00171, E716–E728. ISSN: 0193-1849, 1522-1555. pmid: 10751207 (cit. on p. 173).

[26] S. N. Thennadil, J. L. Rennert, B. J. Wenzel, K. H. Hazen, T. L. Ruchti, and M. B. Block. “Comparison of glucose concentration in interstitial fluid, and capillary and venous blood during rapid changes in blood glucose levels”. In: *Diabetes Technology & Therapeutics* 3.3 (2001). 00075, pp. 357–365. ISSN: 1520-9156. pmid: 11762514 (cit. on p. 173).

[27] Christopher T. Hensley, Ajla T. Wasti, and Ralph J. DeBerardinis. “Glutamine and cancer: cell biology, physiology, and clinical opportunities”. In: *The Journal of Clinical Investigation* 123.9 (Sept. 2013). 00093, pp. 3678–3684. ISSN: 1558-8238. DOI: 10.1172/JCI69600. pmid: 23999442 (cit. on p. 175).

[28] Elizabeth A. Maher, Isaac Marin-Valencia, Robert M. Bachoo, Tomoyuki Mashimo, Jack Raisanen, Kimmo J. Hatanpaa, Ashish Jindal, F. Mark Jeffrey, Changho Choi, Christopher Madden, Dana Mathews, Juan M. Pascual, Bruce E. Mickey, Craig R. Malloy, and Ralph J. DeBerardinis. “Metabolism of [U-13 C]glucose in human brain tumors in vivo”. In: *NMR in biomedicine* 25.11 (Nov. 2012). 00000, pp. 1234–1244. ISSN: 1099-1492. DOI: 10.1002/nbm.2794. pmid: 22419606 (cit. on p. 175).

6. glucoCEST in glioblastoma

6.1. Introduction

As was demonstrated in the work published by Walker-Samuel[1] glucoCEST is able to detect high signal in cancers and can successfully differentiate between two metabolically distinct human xenograft flank tumours. These results gave a strong motivation to continue research on the application of the technique in other types of cancers.

From a technical perspective, assessing brain tumours with glucoCEST is a natural decision as imaging the brain reduces many of the complications involved in scanning other parts of the body, ie artefacts from fat, large magnetic susceptibility gradients or movement artefacts. More importantly, the gold standard method for the detection of tumours, fludeoxyglucose positron emission tomography (^{18}F-FDG-PET), does not provide sufficient contrast to depict the majority of brain gliomas. The high glucose background in brain makes the technique inefficient in identifying the highly metabolic cancer nodes. As such, amino-acid based radio-labels are becoming increasingly popular in neuro-oncology imaging as opposed to the glucose analogue FDG.[2,3,4,5]

It is logical to think that the same reasons that render ^{18}F-FDG-PET ineffective would make glucoCEST also inadequate for the detection of brain tumours. Nonetheless, due to the fact that FDG and natural glucose do not share the same metabolic path and that glucoCEST could be sensitive to sugars in the glycolytic pathway, it is possible that the two modalities would offer different information. As such glucoCEST could prove to be more valuable than ^{18}F-FDG-PET for the evaluation of brain tumours.

On these premises, in this chapter a feasibility study of using glucoCEST for the assessment of brain tumours is presented.

6.2. Glioblastoma multiforme

Glioblastoma multiforme (GBM) is the most prevalent and most aggressive malignant primary brain tumour in humans. It accounts for more than 50% of all malignant

brain tumours with about 2200 new cases diagnosed each year in England alone.[6] GBM has an extremely poor prognosis with a median survival time of 6 months.

Accurate diagnosis is important to confirm a primary or secondary GBM and to differentiate from other type of brain lesions.

In MRI images, glioblastomas often appear as ring-enhancing lesions, but the structural features are not specific enough and definitive diagnosis of suspected GBM usually requires a biopsy. Due to the tissue heterogeneity across most tumours, even biopsy samples can yield inaccurate tumour grading.

The development of new imaging methods to assist in the precise grading of brain tumours is of great clinical interest. With this goal in mind, in this work various GBM mouse models are investigated using glucoCEST as a potential new method for the assessment of brain cancers.

6.3. Study design

A study was planned with the objective of testing the possibility of using glucoCEST for the assessment of brain tumours.

Three main goals were set. The first one was to investigate the feasibility of detecting signal in the brain as the result of an injection of glucose. Secondly to evaluate whether glucoCEST contrast between tumours and contra-lateral areas could be observed. And lastly to investigate whether different tumour types could be identified from the pattern of their glucoCEST signature over the time of tumour development.

For these purpose mice bearing GBM from different cell lines were scanned in a longitudinal study, allowing screening of the progression of the tumours at different time points.

6.3.1. Cancer cell lines

Five different human primary glioblastoma cell lines were studied. Cancer cells had been extracted from four different patient biopsies and cultured in the laboratory* for research purposes. The xenograft tumours from these cells generally showed a diffuse phenotype, which is commonly observed in humans too. Additionally, well characterised U87 cancer cells were included in the study, which are know to form solid tumours.

*All the cell grafting and histochemistry analysis for this study was performed by the team in the histopathology laboratory led by Prof. Sebastian Brander, at the National Hospital for Neurology and Neurosurgery.

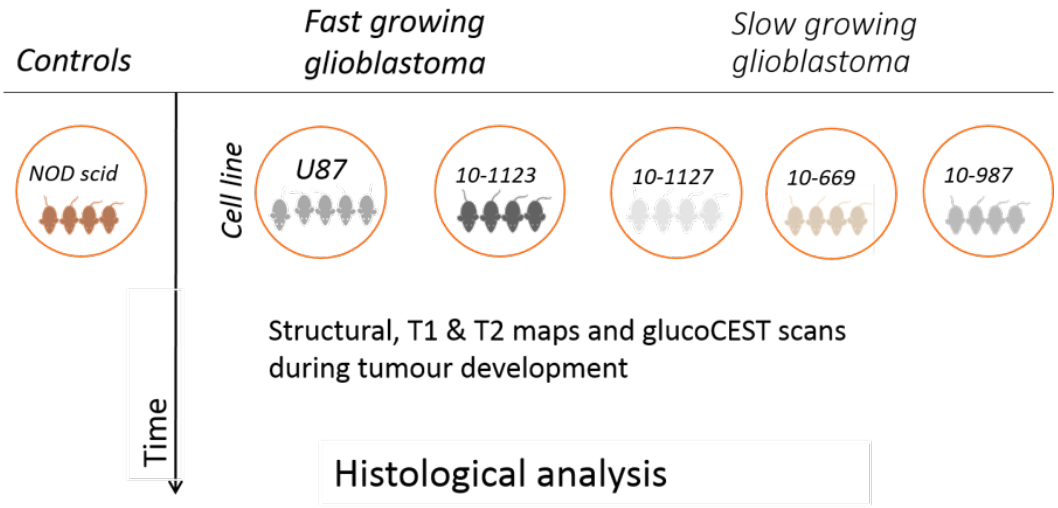

Figure 6.3.1.: *Study plan layout. Mice bearing GBM from five different cell lines were scanned longitudinally with MRI and culled at late stage of cancer for histological analysis. High resolution structural T2 weighted SE images, T1 and T2 maps and glucoCEST were acquired at different stages during the development of GBM tumour.*

Inoculation of cancer cells Human glioblastoma cells were injected intracranially in immune suppressed (NOD-SCID) mice with a slow injection of $5\mu l$ solution containing between 1.8×10^5 and 6×10^5 free cells depending on the cell line.

The time until the formation of tumours varied for individual cell lines, and ranged between 2 weeks, for the most aggressive (U87), to around 12 weeks for the slow growing ones.

6.4. Experimental procedures

6.4.1. Animal preparation

Mice were fasted for 12 hours prior the experiments in order to reduce and stabilize blood glucose levels. Anaesthesia was induced with 3% isoflurane and once animals were asleep the level of anaesthetic was reduced to around 1.3% for the duration of the experiment. A pressure pad placed under the animal's chest was used to monitor the respiration rate. If needed, the level of anaesthetic was adjusted to keep the respiration between 60-90 breaths per minute. Body temperature was monitored with a probe placed on top of the animal and maintained at 37°with a flow of warm air controlled by a SA Instruments Inc. monitoring system (Model 1030). Mice were cannulated via the intra peritoneal (IP) route for the administration of glucose

while in the scanner. A dose of 1g/kg D-glucose was given from a solution of 10% glucose in saline, respectively .

At the late stage of tumour development, animals were culled and brains were extracted for post-mortem histological analysis.

All the procedures were conducted according to protocols approved by the Home Office.

6.4.2. MRI protocols

All scans were performed on a horizontal 9.4T MRI scanner (Agilent Technologies) with a receive-transmit volume coil with an internal diameter of 33mm (Rapid Biomedical).

High resolution structural images ($74\mu m \times 0.5m$) were acquired using a T2 weighted Spin Echo sequence (T2wSE with TR=3s and TE=20ms).

Maps of the longitudinal and transverse relaxation times T1, T2 were also acquired at the beginning and at the end of each experiment. Details for all the sequences used can be found in Appendix B.
Quantification of T1, T2 per pixel was done using Matlab.

CEST sequence Z spectra were acquired using a saturation train of 80 Gaussian pulses prior to a Turbo-FLASH readout. Each Gaussian pulse was 50ms long with flip angle of 540°C and 91% duty cycle, providing an equivalent of 0.9 μT B1 power and 4 second saturation length. Saturation was applied at 57 frequency offsets ranging from -4.5 to 4.5 ppm in a linearly spaced pattern. The total temporal resolution was 4 minutes per block Z spectra. Readout parameters were 2.73ms TR, 1.52ms TE and 20°excitation angle. The K-space was sampled from low to high frequencies for a matrix size of 64 by 64 voxels per slice and a field of view of 20mm by 20mm, with 1.3mm slice thickness. Three parallel slices of the brain were scanned for each saturation train length.

6.4.3. glucoCEST protocol

The animals were first acclimatised to the scanner until a regular respiration pattern was observed. A minimum of three CEST baselines were scanned before the infusion of glucose IP, after which another nine CEST measurement were taken. The glucoCEST signal was calculated as the subtraction of the mean MTR asymmetry between the first and last three CEST images (*post* minus *pre* glucose administration). Z-spectra were fitted to a smoothing spline and corrected for B0 drifts on

a pixel by pixel basis. GlucoCEST enhancement maps (GCE) were obtained by integration of MTR asymmetry between 0.75 and 1.5 ppm.

6.4.4. ROI data analysis

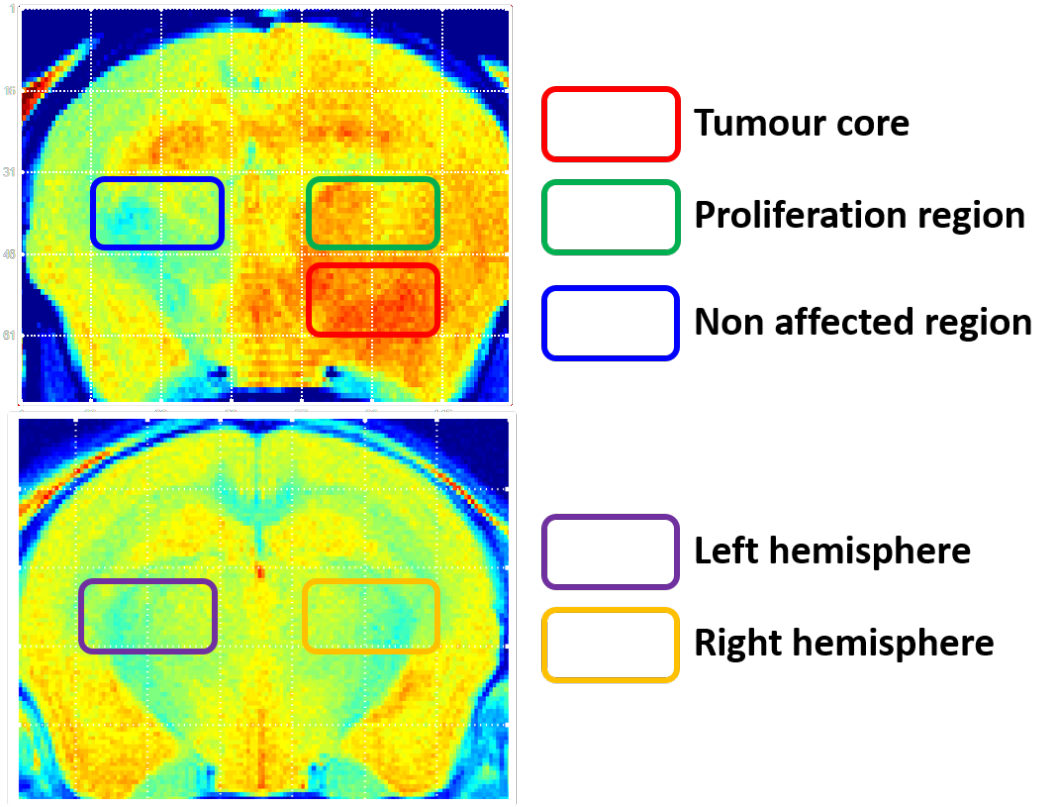

Figure 6.4.1.: *ROIs selection method. In every slice three ROIs presenting different degrees of tumor affection were chosen. The selection was based upon inspection of the structural image at the last scan. In case of no visible tumour, two ROIs were selected, one in each hemisphere.*

From the last scan of every animal, three ROIs were selected from each CEST slice. The ROIs represented the *core* of the tumour, the area adjacent to the tumour (named as proliferating region) and visually unaffected areas (usually contra-lateral region). The selection of these ROI was done upon inspection of T2wSE images at the last scan time. Regions with intense T2 contrast (excluding the ventricles) were assigned the *core* label. If at the last scan-time, an animal had no apparent tumour, two ROIs were selected, one on the right (cell inoculation side) and another one on the left. An example of the ROI selection method can be seen in figure 6.4.1. Once the regions were selected, the same ROIs per mouse where tracked back for all the previous scan, in order to evaluate the progression of the same volume of tissue.

Data from all the acquired scans were translated to a chart and classified into the different categories i.e. ROI number, animal, cell line, scan time, etc. The analysis of these data was done using SPSS software.

6.5. glucoCEST results

Results have been split in to different section. The first section contains the overall statistical analysis of the data in the ROIs selected. The second section is a summary of the most relevant results observed in individual animal cases.

6.5.1. General results

Figure 6.5.1 shows the median GCE signal measured from all the mice in the same cell line group (in rows). *Non-inoculated* and *sham* groups represent mice which had no intracranial injection and intracranial injection of saline (not cancer cells). The rest of the groups are defined by the inoculated cell line. Combined weekly data is displayed in the abscissa, which gives an overview of the growth rate of each cancer cell line. Colour bars represent the different ROIs analysed per group. The initial number of animals per measurement is n=4, except for case of U87 where n=5 mice were scanned. However these numbers reduce at late stages, as some animals had to be culled due to their poor health condition. For every animal results from three CEST slices are counted.

From the presented data, the lack of well defined patterns in the observed GCE signal is probably the first conclusion to make. Variation in the signal appears to be quite random and generalised to all animal groups.

Contrary to what was observed in Amide Proton Transfer (APT) measurements[*] the overall time evolution of the GCE signal does not seem to correlate with the stage of tumour development.

However, some underlying trends can be highlighted for specific cases. Quite consistently an increase of MTR asymmetry is observed in the *core* of solid tumours (U87) and a significant decrease in non-affected areas (contra-lateral and adjacent to the tumour centre).

On the other hand, diffuse tumours show a very variable signal. Among them only the 10-1123 cell line group displays a positive glucoCEST intensity, particularly in

[*] As part of this work the endogenous APT-CEST and relaxation times were analysed for the same animals and ROIs. A summary of these data can be found in Appendix D.

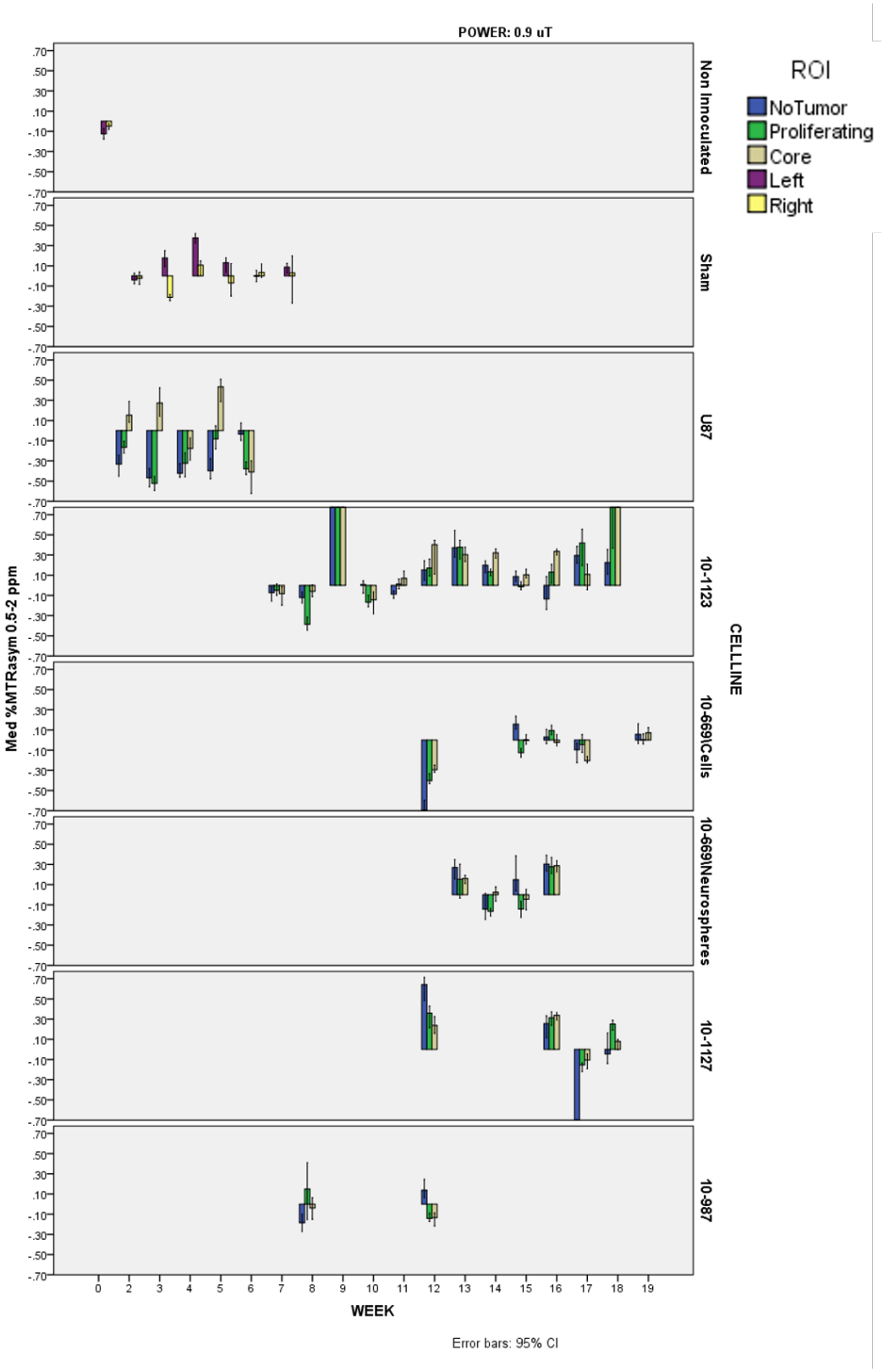

Figure 6.5.1.: *Evolution of the glucoCEST signal for different glioblastoma models. Colour-bars represent the median %GCE value in the specific ROIs. Horizontal axis represents weeks after inoculation of cancer cells.*

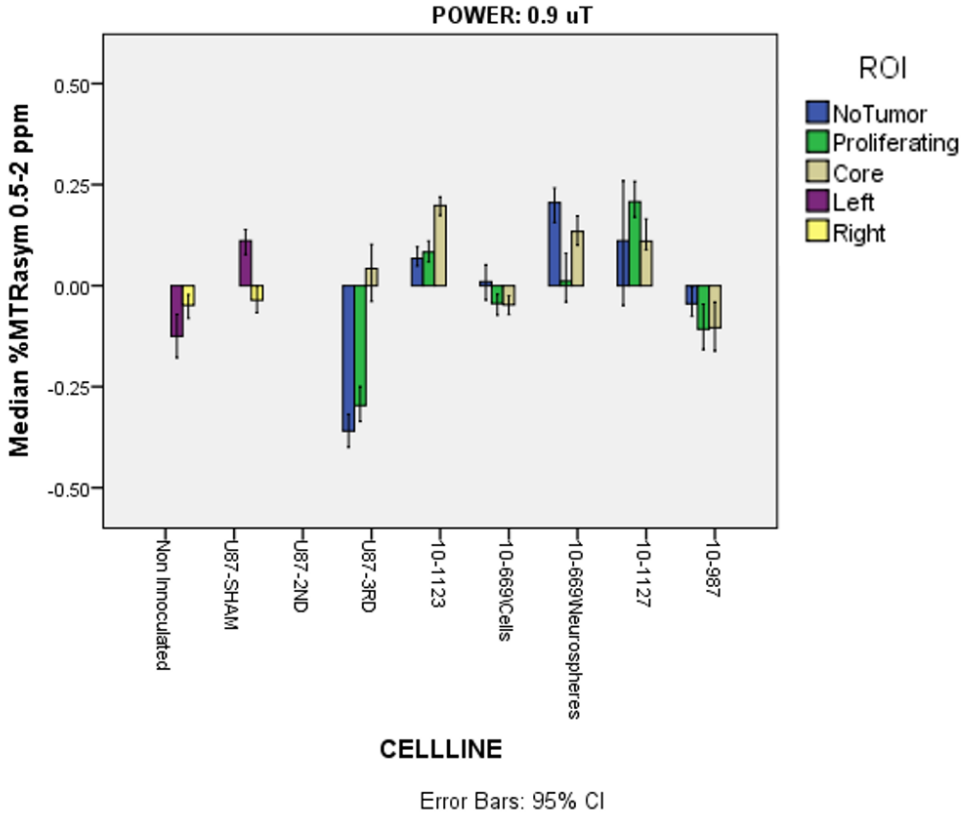

Figure 6.5.2.: *Overall glucoCEST signal for the different GBM cell lines.*

the centre of the tumours, which appears significantly elevated from the rest of the ROIs. This can be better observed in figure 6.5.2.

Overall the data presented does not give enough evidence to conclude whether glucoCEST in brain tumours is significantly enhanced or reduced. While in some cases the results seem to follow a consistent trend, other cases show random variations in the signal.

An issue often encountered during the analysis of individual cases is that the mean GCE signal varied considerably from one scan to the other. On occasion the contrast between two different brain regions would remain very similar, as if the entire signal had been scaled. This type of fluctuations may suggest that the baseline CEST scans (pre-glucose) may have been unstable, resulting in a different normalisation value (please refer to section 3.8 for a discussion on issues with the selection of the normalisation parameter). Other times, the contrast between ROIs would have changed with no apparent pattern, which may be indicative of random signal fluctuations, and a sign of insufficient contrast to noise ratio (CNR).

When dealing with the low signals intensities expected in glucoCEST, the hardware SNR can certainly be a limiting factor for good CNR. However the physiological noise is probably the biggest source of signal instability in this case.

Movement due to irregular respiration (gasping from anaesthesia) can result in severe signal changes. Additionally, the animals' physiology is known to drastically affect the glucoCEST outcome and therefore it is difficult to track the evolution of a small GCE signal through different scans. For instance, a change in the anaesthesia level from 1% to 2% was shown to reduce the observed GCE signal to less than 40% of the baseline value.[7] In this regard, a persistent issue during the glucoCEST scans was to keep the animals under a relatively low anaesthesia so that metabolism of the brain would not be suppressed but still be able to maintain an adequate level of sedation. Often the dose of isoflurane would have to be adjusted during the experiment in order to avoid animals wakening up. This could have changed the glucoCEST signal and compromise the results.

Heterogeneity between tumours, even within the same cell line, can also obscure possible trends in the signal. However, doing the analysis on an individual case basis does not provide any conclusive result either.

Another reason, perhaps an important one, for the inconsistency of the statistical results is the method chosen for the selection of the ROIs used in the analysis. The selected ROIs do not encompass homogeneous regions but rather heterogeneous areas comprised by both tumour and healthy tissues, which results in multi-modal or skewed distributions. This is apparent when looking at the histogram of the same

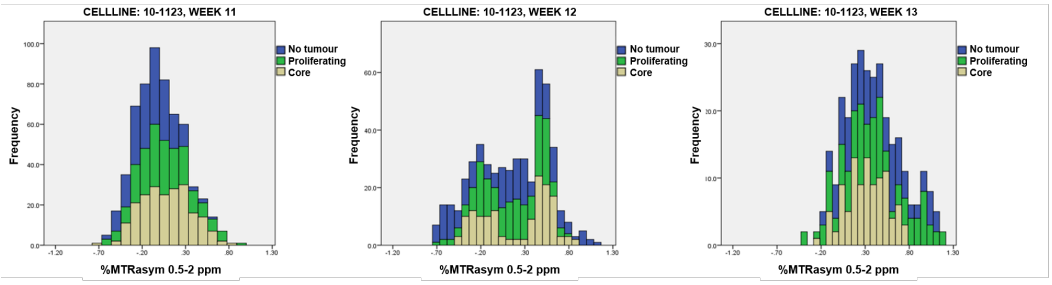

Figure 6.5.3.: *Histograms of the %GCE signal in 10-1123 cell line over three consecutive weeks. As the tumour evolves, the initially normally distributed data splits into a bimodal distribution during the transition towards a higher mean value.*

animal over time (see figure 6.5.3). Perhaps smaller sized and more anatomically shaped ROIs could have produced more robust trends. However, this was not an easy task. Firstly because tumour morphology and consistency changes fast over time, and secondly because smaller ROIs are very difficult to co-register in a longitudinal study. The method used aimed to guarantee that at least a considerable volume of tissue in the ROIs would be the same from one experiment to the other. Nevertheless, the endogenous data from the same ROIs displayed consistent results, suggesting that for broad signal variations the selection of the ROIs is probably adequate (see Appendix D). However, heterogeneous signal variations in regions within the ROIs, run the risk of being averaged out and going unnoticed.

As such, the presented statistical analysis may not capture the full picture. It is worth looking at the particular cases to have a more complete view of what glucoCEST can offer.

6.5.2. Control results

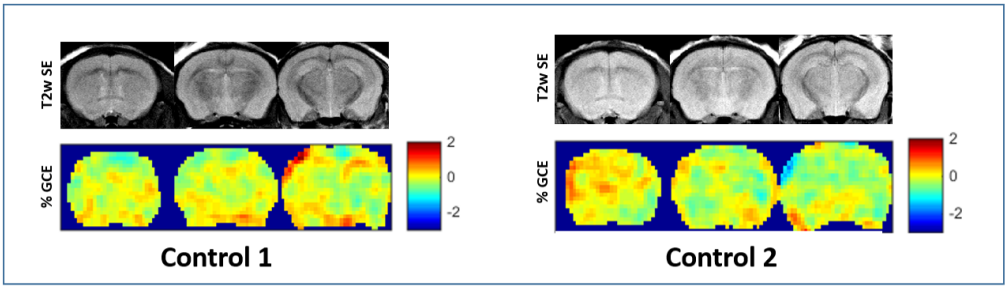

Figure 6.5.4.: *GlucoCEST on control mice. Although some GCE signal is present, control mice tend to display a relatively flat glucoCEST response.*

Control mice tend to exhibit a relatively flat glucoCEST signal response to the administration compared to the tumour cases. Nonetheless, some control animal did show areas of intense glucoCEST contrast, likely as result of the low CNR and high physiological noise. The examples in figure 6.5.4 illustrate the glucoCEST profiles expected from a normal control animal (not the cleanest nor the noisiest examples obtained).

6.5.3. Detection of tumours

Scan of the first animal cohort inoculated with U87 cells only showed significant glucoCEST contrast in one out of four mice. Structural T2wSE images failed to show tumour growth in any of the mice. In the absence of tumour signs, animals were culled for histological analysis and the entire batch was regarded as 'failed inoculation' (A second cohort (n=5) injected with U87 cells was used in the study, from which all animals developed tumours).

Surprisingly inmunohistochemistry results revealed a small nucleus of proliferating cancer cells in the same animal that had an elevated glucoCEST contrast, while the rest three animals were free of cancer cells.

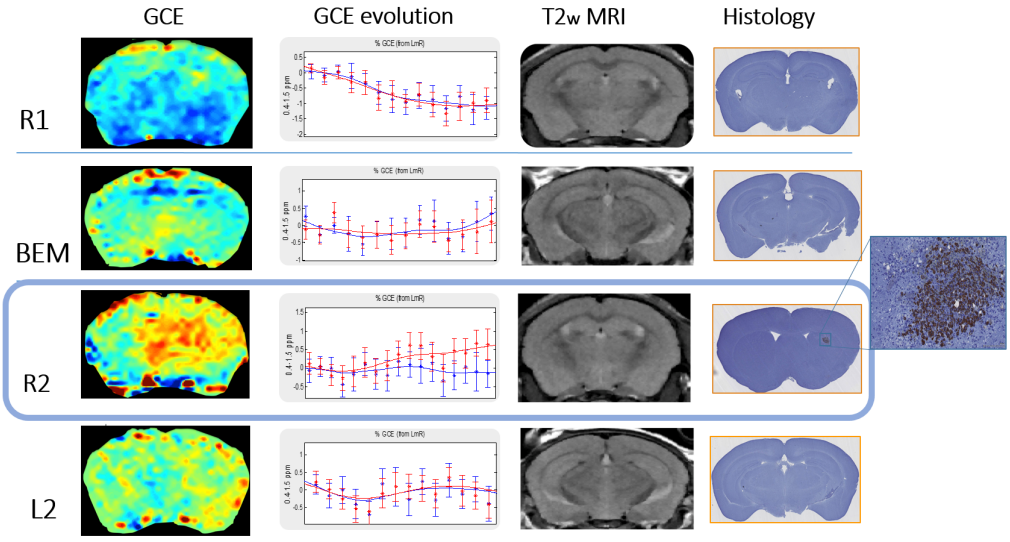

Figure 6.5.5.: *Comparison of the four animals in the 'failed inoculation' cohort. GlucoCEST contrast (1st column) shows contrast enhancement only in the animal with confirmed cancer cell under histological analysis (right column). Second column shows the time-evolution of the mean GCE signal after glucose injection; left hemisphere in blue and right hemisphere in red. In the third column T2wSE images show no sign of tumour.*

6.5.4. Tracking tumour progression

Results in figure 6.5.6 illustrate the case of an animal injected with cell line 10-1127, which displayed a distinct regional GCE signal that evolved over the time of the experiment's length. Histology of the animal (in figure 6.5.7) demonstrated the existence of infiltrated cancer cells, with highest concentrations in the thalamic region where the intracranial inoculation was done.

The density of malignant cells gradually reduces from the original source in the thalamus to the corpus-callosum, from where the cancer cells invade the left hemisphere. Figure 6.5.7 illustrates the pattern described. Arguably the time-course of the tumour growth can be linked to the gradient in cancer cell density. It is remarkable that glucoCEST contrast appears to follows a similar pattern, which suggests the possibility that the method might be sensitive to tumour progression.

Note that in none of the time-points the T2w images gave any indication of tumor presence, which is expected from early stages of diffuse carcinomas.

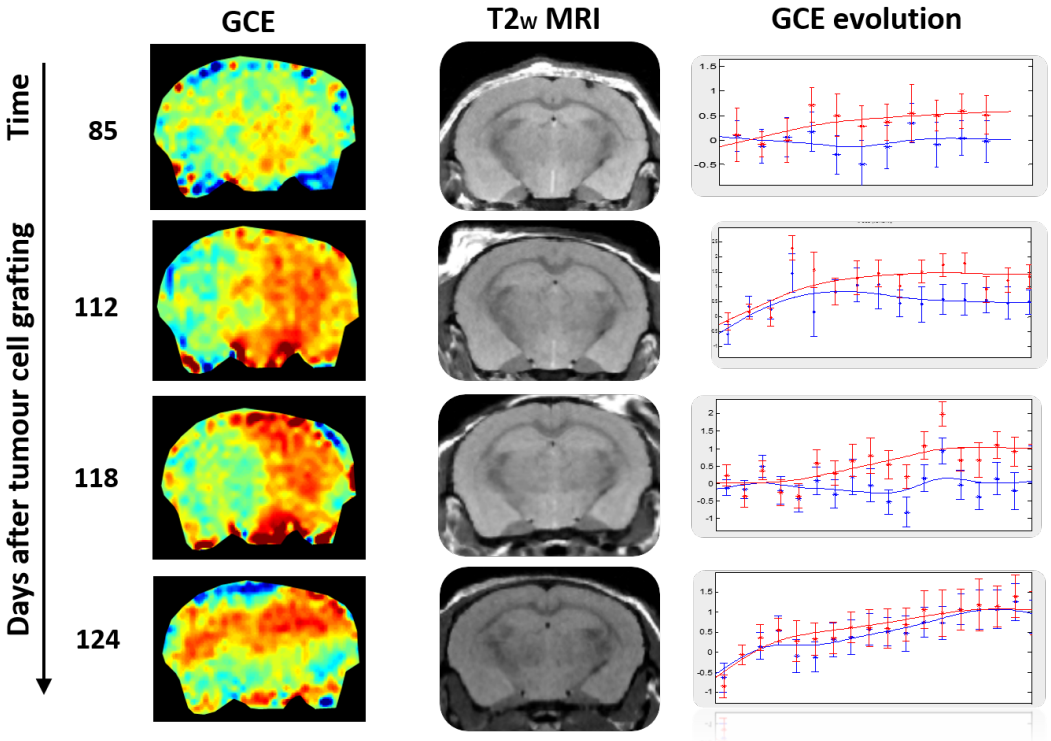

Figure 6.5.6.: *GlucoCEST contrast of the same animal at different scans over the course of the experiment (left). Mean GCE signal after glucose administration from left (blue) and right (red) hemispheres. T2wSe in middle.*

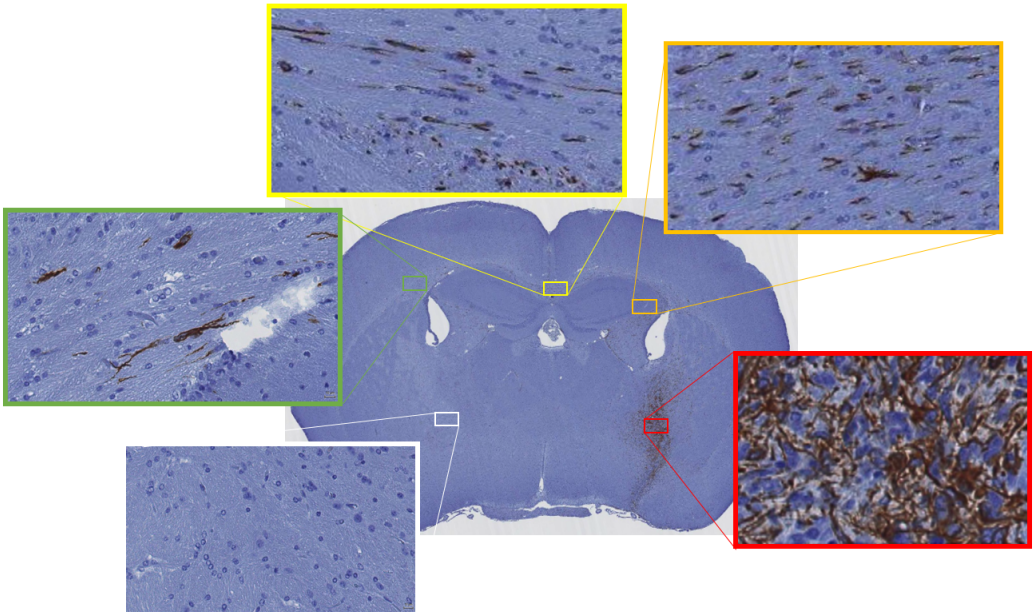

Figure 6.5.7.: *Inmunohistochemistry staining (Vimentin and Haematoxylin counterstain) of the same animal as in figure 6.5.6 showing a regions of different cancer cell density.*

6.5.5. Contrast at early stage of cancer

In all the presented cases, comparison between the GCE maps and the anatomical images seem to suggest that glucoCEST can identify the presence of tumours in an earlier phase than conventional MRI. A paradigmatic example of this is presented in figure (6.5.8), which illustrates the case of an animal injected with 10-1123 cells, scanned at two separate timepoints. GlucoCEST at the first time point displays a larger extension of the tumour than the T2wSE at the same time. However, the structural image acquired 15 day later shows an expanded tumour with similarities with the previously acquired glucoCEST images. In fact the GCE image correlates better with the T2wSE image acquired 2 weeks later (R2=0.13) than with the one at the same time–point (R2=0.027)*.

Cases with similar characteristics can be seen across the different cell lines studied. Example in figure 6.5.9 shows the case of an animal injected with U87 cancer cells that displays a hyperintense signal in the right side of the cortical region from where the tumour grows at a later stage.

*Correlations were calculated based on intensity maps. The author acknowledges a measure of correlation based on mutual information would be preferable to compare data acquired with different imaging techniques.

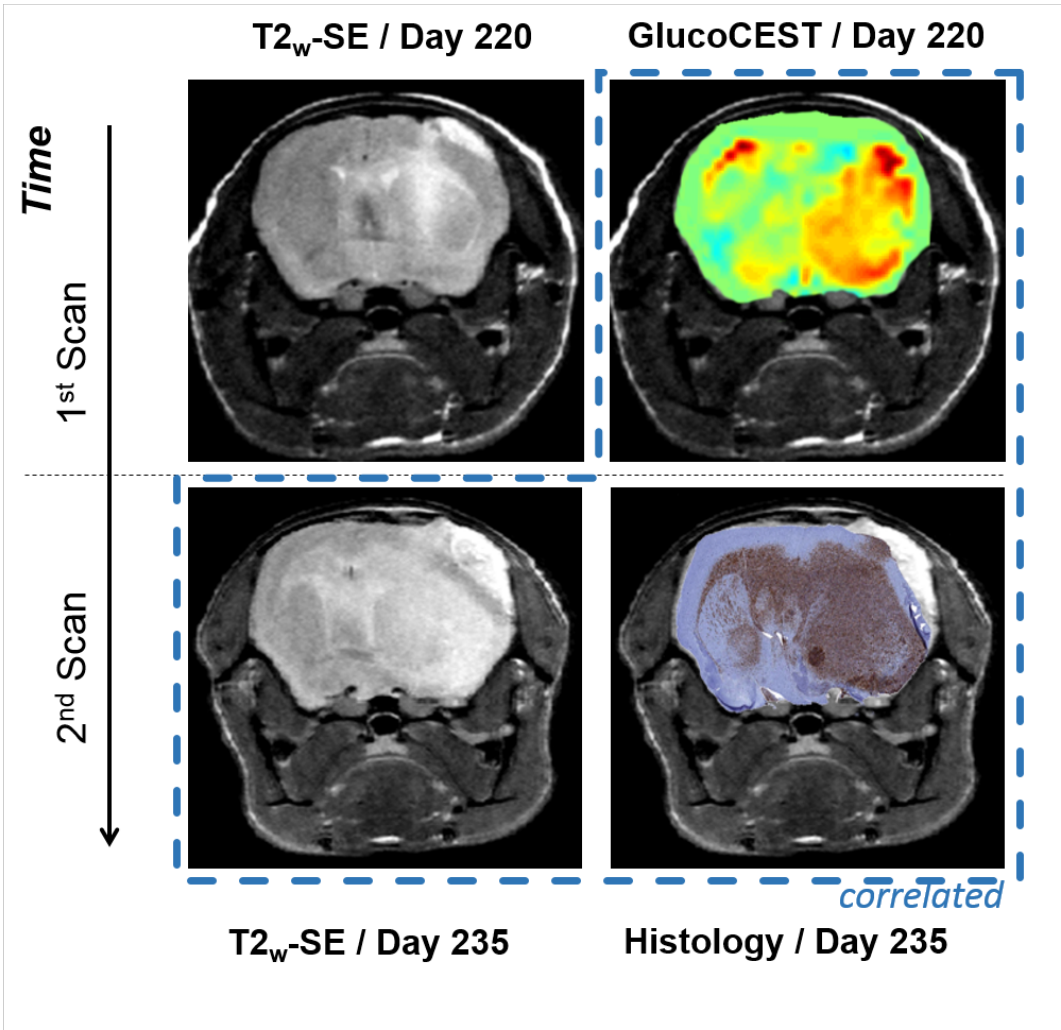

Figure 6.5.8.: *Comparison between glucoCEST, spin echo and histology. At day 220 post tumour inoculation , the SE image does not show the full spread of the tumour, while glucoCEST already displays features that will be detectable 15 days later by T2w SE. The overlay of MR and histology slice shows tumour cells highlighted in brown by a human specific stain (Vimentin), whereas the host brain is shown in blue (Haematoxylin counterstain).*

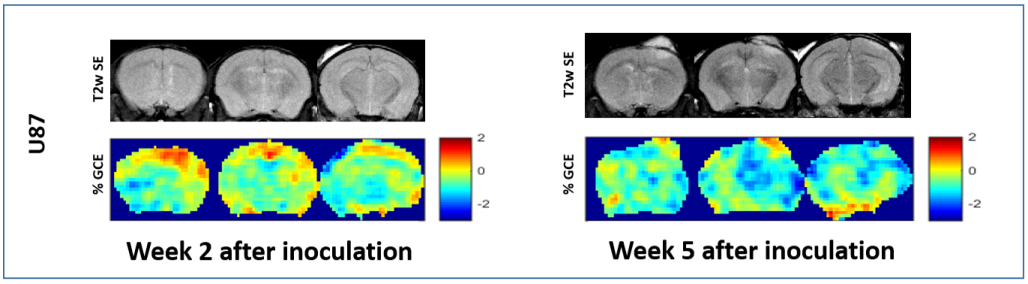

Figure 6.5.9.: *GlucoCEST in U87 cancer cell line showing intense signal in the top of the cortical region from where the tumour grows in a later stage.*

This same effect is manifested, clearer perhaps, in animals with diffuse phenotype tumours. The following examples illustrated two cases of animals bearing diffuse GBM from the 10-987 cell line (see figure 6.5.10). In the set of images scanned at week 8 after inoculation of cancer cells, glucoCEST displays an intense signal in the top right hand side of the brain where the tumour will grow. At this stage T2wSE does not provide signs of any anomaly. At a later stage a normointense signal is observed in areas where cancer has developed but a hyperintense signal around the tumour area, conceivably indicating further expanse of tumour towards the hyperintense regions.

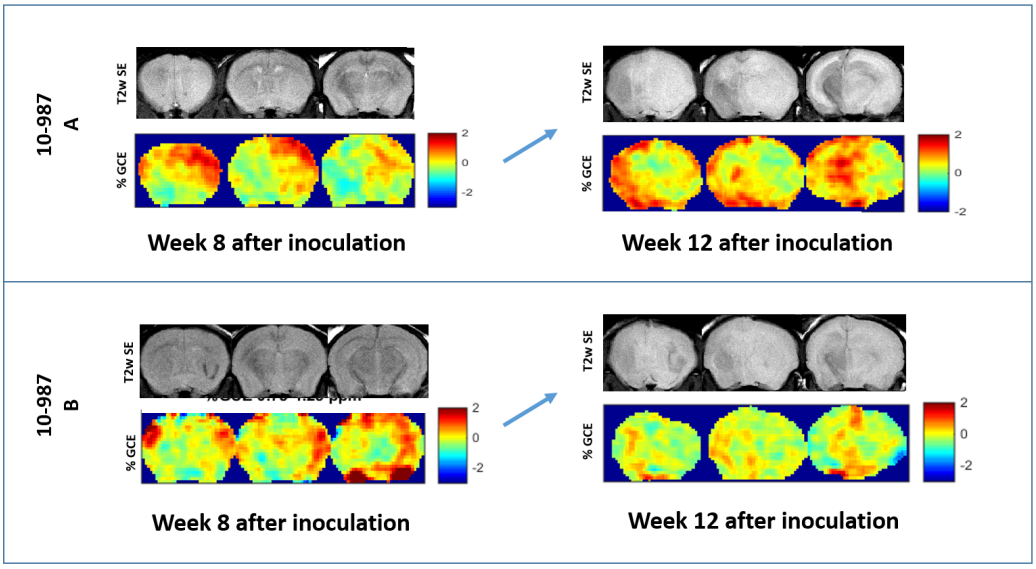

Figure 6.5.10.: *GlucoCEST profile in 10-987 GBM cell line. At week 8, when T2wSE shows no apparent signs of tumour, glucoCEST shows an intense signal in regions of the brain where tumours will start developing. In a later stage a normointense signal is observed in areas where cancer has consolidated and a hyperintense signal around the tumour.*

6.5.5.1. No GCE in areas with consolidated tumour

It is worth emphasising the fact that in most of these cases the GCE images displayed no significant contrast in the regions where the cancer cell had been well consolidated. This was especially true at late stage of tumour development when GCE showed normo-intense signal in the cancer but hyper-intense in areas in which the spread of the cancer was not complete. Figure 6.5.11 shows another example of this effect on a mouse inoculated with 10-1123 cell line and scanned at late stage.

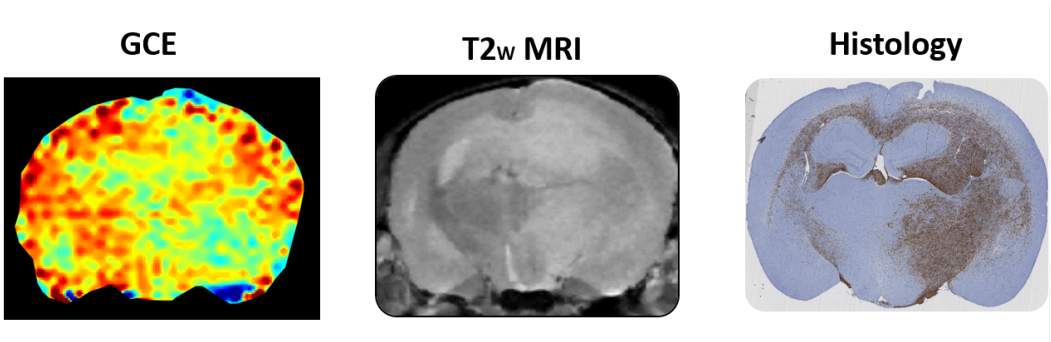

Figure 6.5.11.: *GlucoCEST in advanced stage of GBM, in animal inoculated with cell line 10-1123. Contrast across the brain slice is produced by hyperintense glucoCEST signal in areas with lower density of cancer cells compared to a flat glucoCEST response in highly invaded regions. T2wSe and histology show the extension of the areas most affected by cancer.*

6.6. Changes in relaxation times

As discussed in chapter 4 the transverse relaxation time is susceptible to the concentration of glucose via a chemical exchange mechanism. Using the same ROIs as in the analysis of the glucoCEST data, the median change in the T2 relaxation time were measured in all the experiments performed. The results of theses measurements are summarised in figure 6.6.1, which shows variation of T2 in each animal group per week, and in figure 6.6.2, which presents the combined change of T2 throughout all the scans.

As a general basis T2 relaxation time appears to decrease an average of two milliseconds during the glucoCEST experiment. The effect is overall quite consistent and independent of the cancer cell line studied. The reduction happens across the entire brain (except in the cerebrospinal fluid) and in all phases of the study, which might be indicative of dehydration rather than an effect of the chemical exchange effect from glucose. However, control mice seem to experience a lower reduction

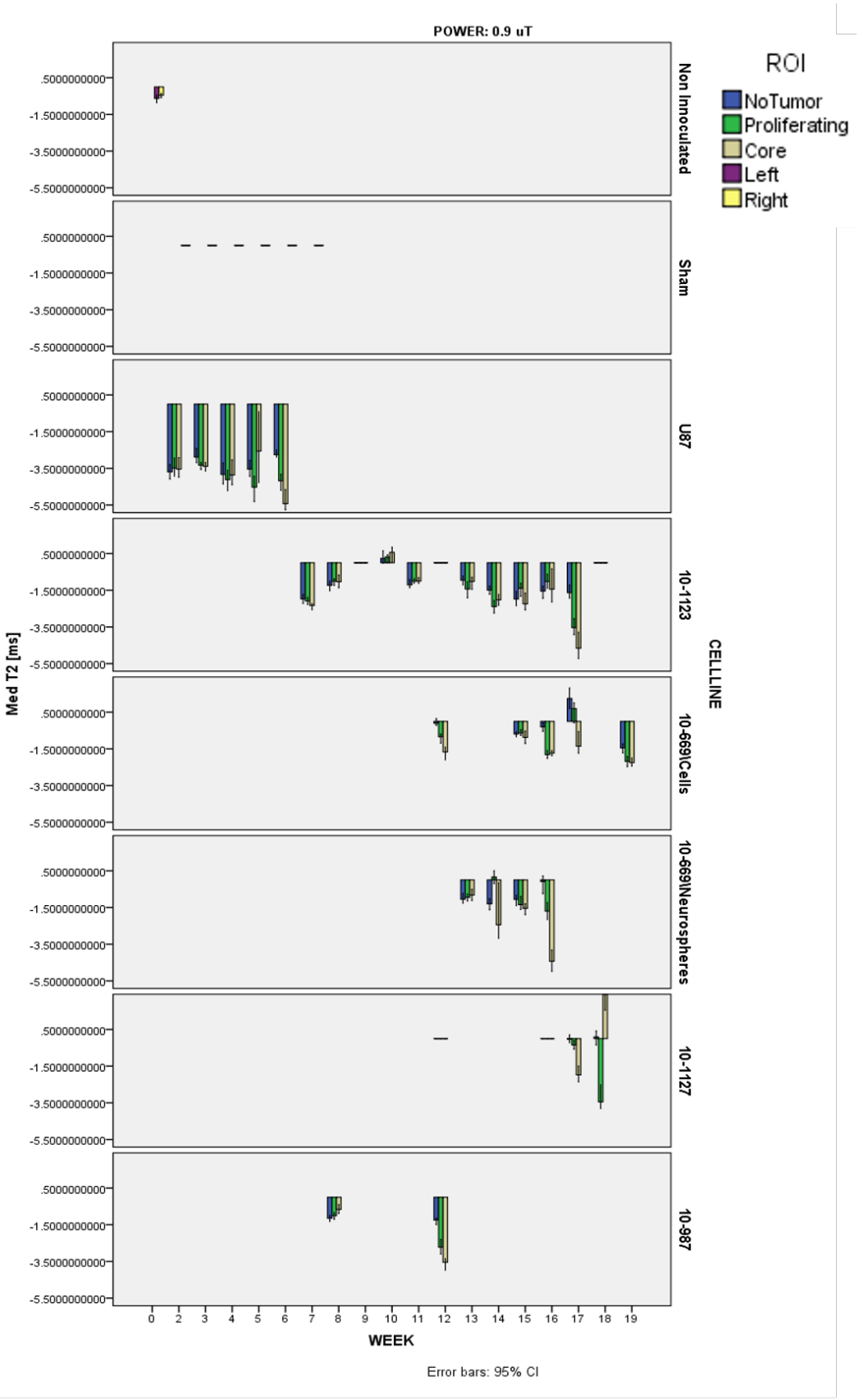

Figure 6.6.1.: *Change in T2 relaxation time after glucose administration for different glioblastoma models. Colour-bars represent the median $\Delta T2$ value in the specific ROIs. Horizontal axis represents weeks after inoculation of cancer cells.*

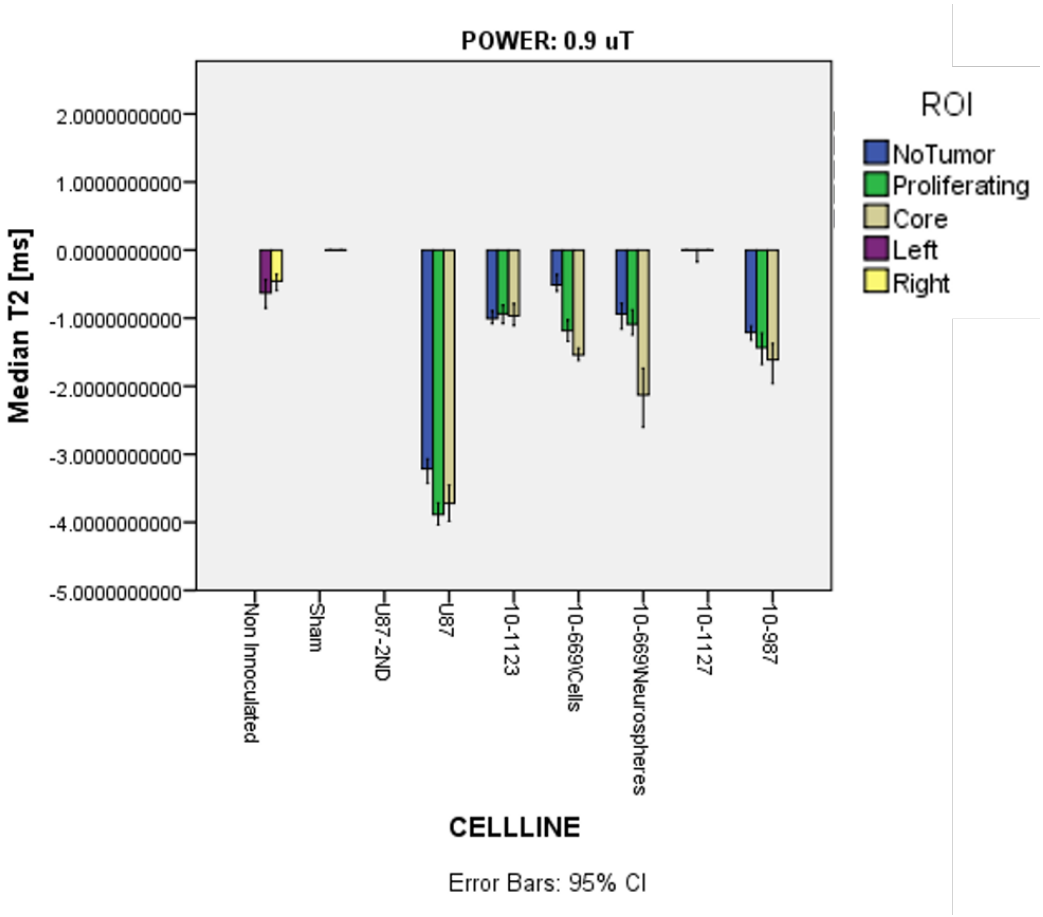

Figure 6.6.2.: *Overall median $\Delta T2$ per cell line group.*

(average of 0.5 ms) compared to the sick animals. Moreover, tumour affected areas appear to display the largest amounts of variation in T2, particularly at late stage of cancer.

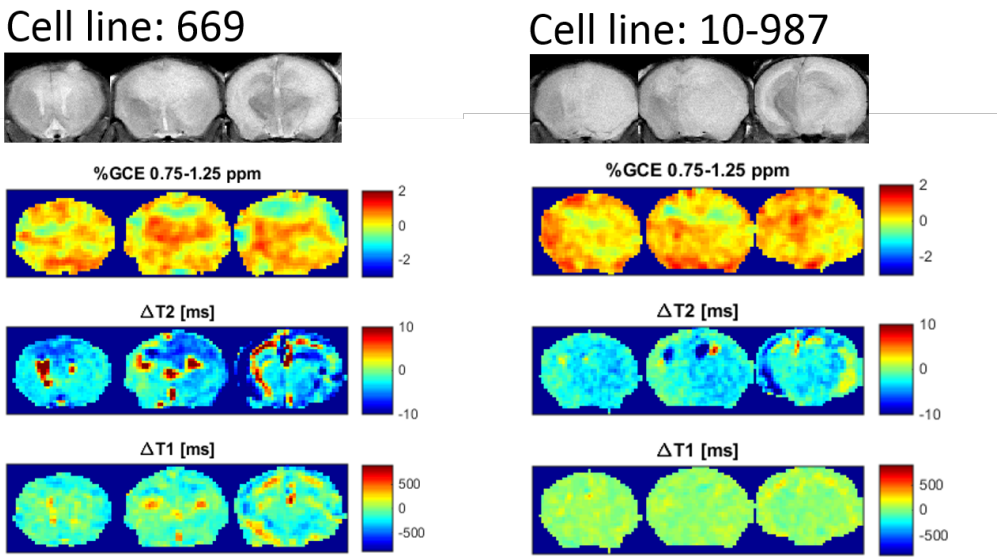

Figure 6.6.3.: *Reduced T2 is observed mostly in region affected by tumour. GlucoCEST at the same time display a less define pattern.*

Figure 6.6.3 illustrates two examples from different cell lines in which T2 of the tumour area is decreased after the injection of glucose. Contrary to what might have been suspected from a theoretical argument, glucoCEST and change in T2 do not seem to correlate. Compared to the glucoCEST signal, the T2 change appears to be more localised in the regions affected by the tumour.

The significance of these results is unclear, as standard T2 weighted images already provide the same information in much higher detail. Nonetheless, in solid phenotype tumours, the observed pattern in the variation of the relaxation time is more interesting. Figure 6.6.4 shows the evolution of a solid tumour (U87 cell line) over a three week time period. In the first scan (at week 3 after inoculation of cancer cells), relaxation times appear relatively even across the three brain slices. Scans of the same animal a week later starts showing regions with largely reduced T2 in the anterior and posterior slices of the brain where tumour onset is visible. The same scan shows another cancer node in the middle of the brain with an increase in T2. The magnitude of these changes reach up to $\pm 20ms$, which account for roughly 15% of the transverse relaxation in those areas. Longitudinal relaxation time T1 shows a similar trend.

In our first analysis these changes were suspected to be a result of the animal moving during the experiment. After cautious inspection of the raw images it was

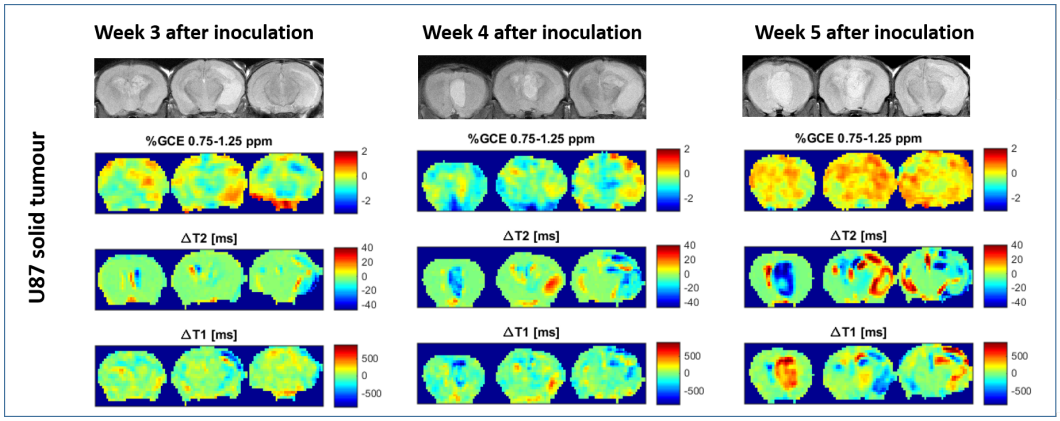

Figure 6.6.4.: *Extreme variations in the relaxation times in U87 solid tumour. At late stage the change in T2 shows an over-intense ringing pattern surrounding the tumour node (on the right hemisphere), while the more centred node displays a hypo-intense signal.*

concluded that the animal remained stable in the same position (less than 1 voxel displacement was measured between pre- and post- glucose administration). Moreover, images from the next scan at week 5 post injection show the same pattern with enhanced contrast.

While the amount of glucose concentration can reduce the observed T2 via chemical exchange mediated relaxation, T1 variations cannot be explained by this mechanism. One way in which such intense changes could be understood, would be by a variation in the water content of the tissue by either a leak from blood vessels or extreme vasoconstriction. The fact that T1 and T2 appear to change in opposite directions (last time point) and witch such a large magnitude, eludes the author's comprehension.

6.7. Conclusion

In this chapter the effects of glucose administration in mice bearing brain gliomas have been studied via glucoCEST and changes in relaxation times (both T1 and T2). Transverse relaxation time T2 was found to reduce in areas affected by diffuse cancer. Solid tumours were found to display marked changes in relaxation times, both longitudinal and transverse.

Unfortunately, the lack of sufficient control data on mice bearing solid tumours (given saline instead of glucose) renders these result inconclusive in order to attribute variation in the relaxation time exclusively to the administration of glucose. The variety of cancer cell lines studied resulted in relatively low numbers per group,

limiting the possibility of solid statistical inference. Arguably this is one of the biggest flaws of this study.

Nevertheless, the extent and cause of the variations in relaxation time of solid tumours, although unclear, appear too evident to be ignored. More research could help understand the physiological reasons behind these observations which might yield information relevant to the study of cancer.

Regarding the results on glucoCEST, the initial hyper intense signal observed in early phases of cancer, followed by a normointense signal in regions with fully developed tumour is a pattern that can be observed in around 40% of the animals studied.

In the presented cases glucoCEST seems to highlight the cancer-affected areas before the appearance of significant changes in the tissue structure, suggesting the possibility that glucoCEST may be sensitive to early phases of cancer. A possible explanation for it is that at early stages of cancer, while brain structures are still undisrupted and the T2 relaxation time is unaffected, tumours cells already proliferate at higher rates demanding more glucose.

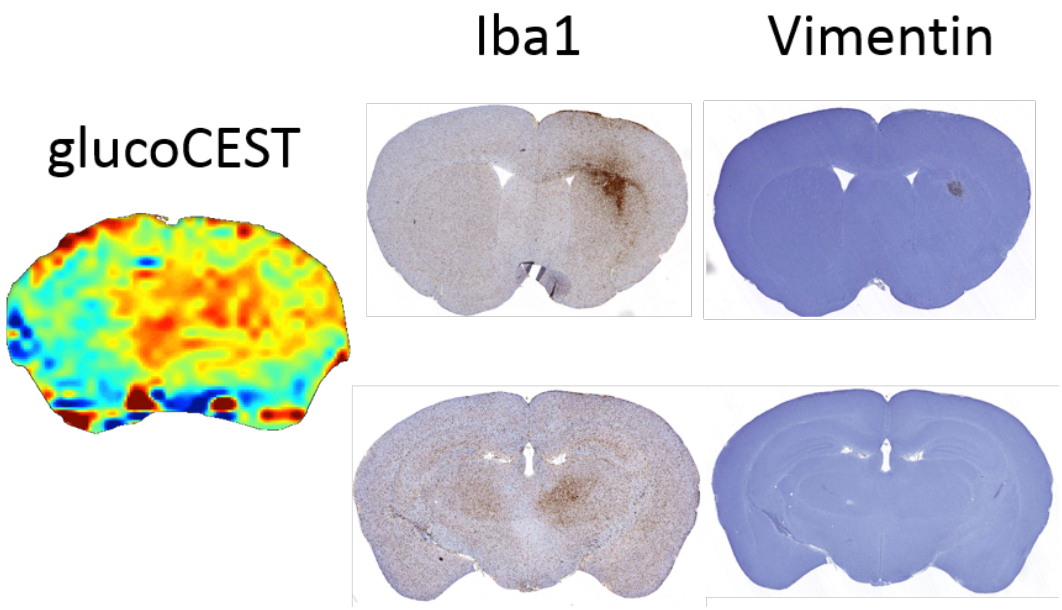

Figure 6.7.1.: *Comparison between glucoCEST, IBA1 and Vimentin immunohistochemistry staining. CEST image corresponds to a volume in between the two histological slices.*

Inflammation signal in areas invaded by malignant cells could also cause elevated metabolic activity and hence an increased glucoCEST signal. As a matter of fact, when animals were culled in early stage of cancer development, the contrast

provided by glucoCEST was found to better match with IBA1* staining than with cancer cell density(see figure 6.7.1).

The cases presented reflect the bright side of the story. The author recognises that given the variability in the observed signal these results could be regarded as mere coincidences. Given the lack of reproducibility and the low contrast to noise in the results, the hypothesis that glucoCEST might be informing on early brain tumour stage is little more than speculation with the current evidence. However, the significance of this hypothesis being true, supported by some very intriguing cases, leaves room for the excitement and encourages more research on the topic.

*IBA1 protein (ionized calcium-binding adapter molecule 1) is present in activated macrophages which are found in tissues with inflammation. IBA1 levels in healthy humans have been found to positively correlate with metabolism and with fasting plasma glucose levels.[8]

Chapter references

[1] Simon Walker-Samuel, Rajiv Ramasawmy, Francisco Torrealdea, Marilena Rega, Vineeth Rajkumar, S. Peter Johnson, Simon Richardson, Miguel Gonçalves, Harold G. Parkes, Erik Arstad, David L. Thomas, R. Barbara Pedley, Mark F. Lythgoe, and Xavier Golay. "In vivo imaging of glucose uptake and metabolism in tumors". In: *Nature Medicine* 19.8 (Aug. 2013). 00044 Cited by 0001, pp. 1067–1072. ISSN: 1078-8956. DOI: 10.1038/nm.3252 (cit. on p. 183).

[2] Anja Smits and Brigitta G. Baumert. "The Clinical Value of PET with Amino Acid Tracers for Gliomas WHO Grade II". In: *International Journal of Molecular Imaging* 2011 (Apr. 28, 2011). 00018, e372509. ISSN: 2090-1712. DOI: 10.1155/2011/372509 (cit. on p. 183).

[3] Karl Herholz, Karl-Josef Langen, Christiaan Schiepers, and James M. Mountz. "Brain Tumors". In: *Seminars in nuclear medicine* 42.6 (Nov. 2012). 00181, pp. 356–370. ISSN: 0001-2998. DOI: 10.1053/j.semnuclmed.2012.06.001. pmid: 23026359 (cit. on p. 183).

[4] Anca-L. Grosu and Wolfgang A. Weber. "PET for radiation treatment planning of brain tumours". In: *Radiotherapy and Oncology*. PET in Radiotherapy Planning 96.3 (Sept. 2010). 00056, pp. 325–327. ISSN: 0167-8140. DOI: 10.1016/j.radonc.2010.08.001 (cit. on p. 183).

[5] Dirk Pauleit, Gabriele Stoffels, Ansgar Bachofner, Frank W. Floeth, Michael Sabel, Hans Herzog, Lutz Tellmann, Paul Jansen, Guido Reifenberger, Kurt Hamacher, Heinz H. Coenen, and Karl-Josef Langen. "Comparison of 18F-FET and 18F-FDG PET in brain tumors". In: *Nuclear Medicine and Biology* 36.7 (Oct. 2009). 00000, pp. 779–787. ISSN: 0969-8051. DOI: 10.1016/j.nucmedbio.2009.05.005 (cit. on p. 183).

[6] Andrew Brodbelt, David Greenberg, Tim Winters, Matt Williams, Sally Vernon, V. Peter Collins, and (UK) National Cancer Information Network Brain Tumour Group. "Glioblastoma in England: 2007-2011". In: *European Journal of Cancer (Oxford, England: 1990)* 51.4 (Mar. 2015). 00000, pp. 533–542. ISSN: 1879-0852. DOI: 10.1016/j.ejca.2014.12.014. pmid: 25661102 (cit. on p. 184).

[7] Fatima A. Nasrallah, Guilhem Pagès, Philip W. Kuchel, Xavier Golay, and Kai-Hsiang Chuang. "Imaging brain deoxyglucose uptake and metabolism by glucoCEST MRI". In: *Journal of Cerebral Blood Flow & Metabolism* 33.8 (Aug. 2013). 00015 Cited by 0000, pp. 1270–1278. ISSN: 0271-678X. DOI: 10.1038/jcbfm.2013.79 (cit. on p. 191).

[8] Michiaki Fukui, Muhei Tanaka, Hitoshi Toda, Mai Asano, Masahiro Yamazaki, Goji Hasegawa, Saeko Imai, Aya Fujinami, Mitsuhiro Ohta, and Naoto Nakamura. “The serum concentration of allograft inflammatory factor–1 is correlated with metabolic parameters in healthy subjects”. In: *Metabolism* 61.7 (July 2012). 00005, pp. 1021–1025. ISSN: 0026-0495. DOI: 10.1016/j.metabol.2011.12.001 (cit. on p. 204).

7. Future work in exogenous CEST

This last chapter outlines the projects that are currently ongoing or planned for the future as continuation of the work done in this thesis. Three projects are described which relate to different application of exogenous CEST methods. The first section contains a brief discussion about the challenges involved in the translation of glucoCEST to the clinic. The second section, describes the application of CEST in combination with the administration of 2DG as a potential method for the control of epileptic seizures and identification of the seizure-onset zones. Lastly, in the third section, a new application of exogenous CEST is explored in which bicarbonate is used as a potential contrast agent to provide alternative information regarding dis-regulation of pH in tumours.

7.1. Translation of glucoCEST to the clinic

GlucoCEST could offer an attractive alternative to ^{18}F-FDG-PET for the diagnosis of cancer and metabolic related disorders. The use of natural glucose as the *contrast agent* in glucoCEST makes the technique safe which allows human studies to be readily approved. The lack of toxicity in glucoCEST allows examination of specific patient populations like children and pregnant women for which nuclear medicine is contraindicated. Additionally glucoCEST would be ideal for longitudinal studies on patients, which could eventually be useful for the assessment of response to therapy and general clinical research.

The translation of glucoCEST to the clinical setting however poses some technical challenges that need to be addressed.

Lower field strengths of human MRI scanners compared to preclinical systems results in smaller chemical shift between water and labile protons, which makes peaks harder to resolve. As a consequence of the reduced chemical shift, spillover (direct saturation) effects are also more pronounced. Thus, the power needed for effective

glucose labelling considerably reduces the net MR signal with the consequent loss of SNR.

Standard MRI imaging sequences seldom make use of RF pulses longer than a few milliseconds. As such clinical scanners have a limited energy capacity in the RF amplifiers which can limit the length of the saturation pulse below the optimum one for CEST. Moreover, due to strict SAR regulations the highest B1 power allowed for scanning patients is lower than the one typically used in preclinical studies, especially for the detection of fast exchanging protons. In these conditions, the detection of the glucoCEST signal becomes extremely challenging. However most of these limitations can be partially overcome by choosing a shorter saturation scheme (without aiming for steady state magnetisation) and an optimum integration range (see suggested guidelines in Figure 2.5.1 and discussion on the selection of appropriate power in section 3.14).

On the bright side, field inhomogeneity is more controlled at low field which reduces the hampering effects of large B0 variations across the image. Transverse relaxation time T2 of tissues increases with reduced field, making the peaks in the Z-spectrum more defined which should compensate for some of the negative consequences of the small chemical shift. From the physiological point of view, glucoCEST performed on humans does not require anaesthesia, hence reducing the risk of low brain metabolic activity found in animal studies using isoflurane.[1]

7.1.1. Suggested approach for clinical glucoCEST

Because of the time constraints in the clinical environment and the low SNR expected from the measurements, it is sensible to target the acquisition on just the offset frequencies most sensitive for the detection of glucose. Sampling a small portion of the offset frequencies instead of the whole Z-spectrum allows more time to repeat acquisitions in order to gain CNR.

For a hypothetical glucoCEST experiment in which glucose concentration in tissues increases by 10 mMolar, it was estimated that around 30 CEST repetitions would be needed in order to detect glucoCEST signal with 95% CI in a clinical setting. These figures were estimated assuming a variability (as the standard deviation) in the CEST measurements to be twice the expected GCE signal. These values were justified based on 1) the mean GCE obtained from phantoms at different glucose concentrations and 2) the variability of the signal measured in healthy volunteers.

A set of the phantom data used for these estimations can be seen in figure 2.5.2 (Chapter 2). These experiments showed an average of 3% GCE for 10 mmolar

glucose increase. Additionally, the standard deviation from the mean CEST signal between scans of the same volunteer was measured to be 3.1% between 2 and 3 ppm, the most sensitive range for glucose detection at 3T.

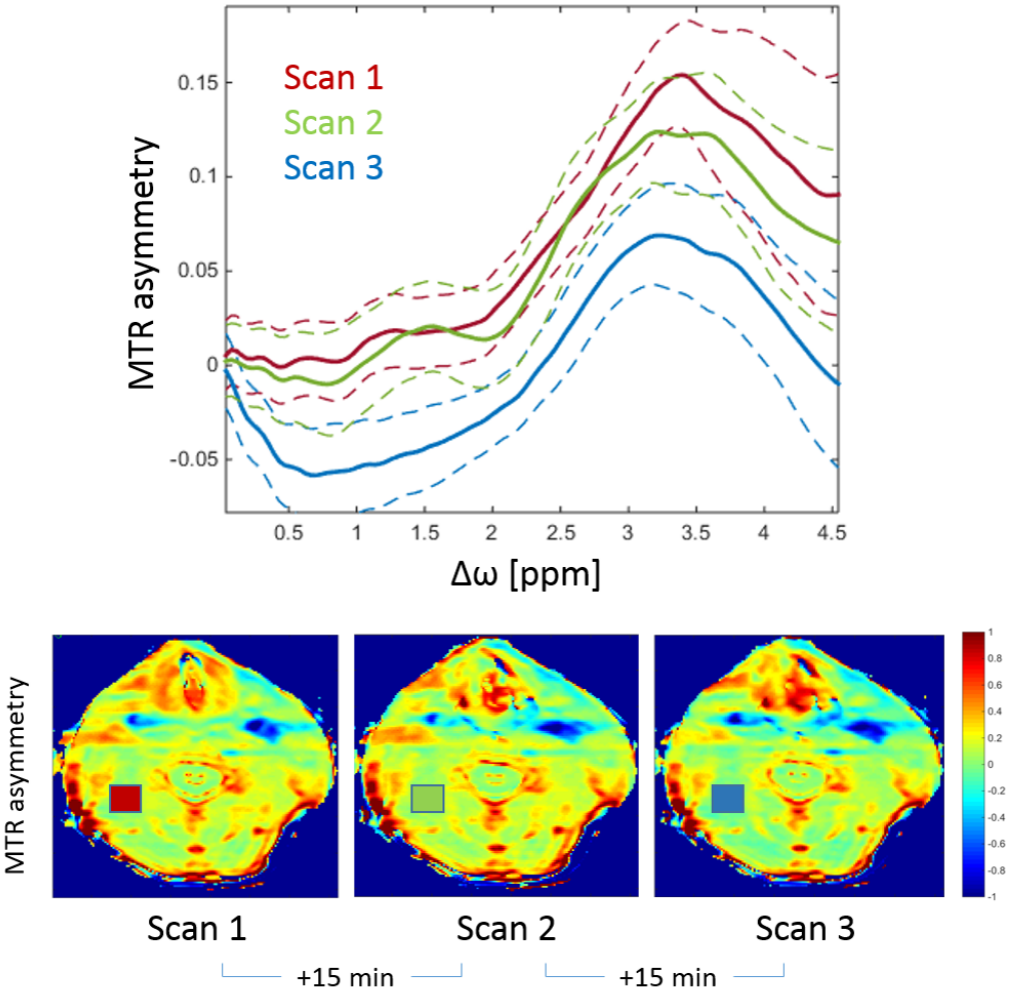

Figure 7.1.1.: *Reproducibility of the MTR asymmetry in the neck of a healthy volunteer scanned every 15 minutes. Mean and STD of the CEST profile over the selected voxel show signal variability (STD) contained below twice the expected GCE signal in the range between 2 and 3 ppm.*

As in fMRI, the low CNR in the glucoCEST data can be dealt by averaging multiple acquisitions. Using this approach an example of a optimised glucoCEST protocol is presented in figure 7.1.2.

The *CEST block* represents CEST measurements at 2.25, 2.5 and 2.75 ppm offsets, which provide maximum MTR asymmetry based on phantom data and simulations at 3T. Saturation power should be set at $\sim 2.6\mu T$ for the duration of around one second, to provide optimum contrast from glucose (see section 3.15). Frequent

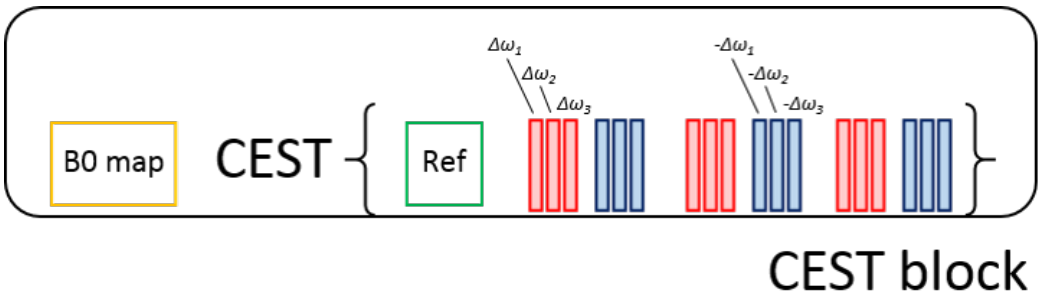

Figure 7.1.2.: *Diagram of the suggested fast acquisition protocol for glucoCEST experiments. Three pairs of offset frequencies (positive and negative) are sampled centred around 2.6 ppm to allow for B0 corrections. Reference and B0 field maps are also acquired regularly to control for potential field drifts.*

B0 maps are also advisable in order to correct for potential field drifts during the glucoCEST experiment.

This protocol has been successfully tested in a Philips Achieva 3T clinical scanner. The time required for the acquisition of a *CEST block* is less that 2 minutes, which provides effectively 15 glucoCEST acquisitions in 10 minutes, including the B0 field maps.

Protocols similar to the one presented offer an acceptable scan time for a the clinical translation of glucoCEST. Currently an ongoing study at University College London Hospital (UCLH) aims to scan 80 cancer patients (20 HN squamous cell carcinoma, 20 Hodgkin's Lymphoma, 20 Glioma low grade and 20 Glioma high grade) with glucoCEST during a continuous IV infusion of glucose.

7.2. 2DG CEST in epilepsy

Epilepsy is the most common serious chronic neurological condition with a prevalence of about 1%. About 30% of all people with epilepsy are inadequately treated by medication; for these people, surgical resection is the best hope of controlling their seizures, but this necessitates the precise localisation of seizure onset. Currently the only practical functional imaging technique available for localisation of seizure onset uses ictal Single Photon Emission Computed Tomography (SPECT) and this has several shortcomings that significantly restrict its use, including a low success rate (±60%), short half-life of the tracer and limited availability. A more readily available method to identify seizure onset zones would therefore be extremely valuable.

The challenge for such an application is to find a tracer that can be injected at the time of a seizure on the ward, and imaged later while reporting on the ictal brain metabolism. As glucose is rapidly used by the brain, glucoCEST signal is likely to quickly fade away, therefore limiting its efficacy for this application. However, alternative molecules such as 2-Deoxy-D-Glucose (2DG)[1] or 3-Oxy-Methyl-Glucose (3OMG) have been shown to stay within the cells for an extended period of time,[2] and could therefore be used as tracers for ictal imaging.

While 2DG has been tried as an adjunct therapy in cancer, some concerns about its safety within the context of epilepsy have arisen, due to its potential cardiac side effects. Alternative, 3OMG is considered to be less toxic than 2DG as it does not serve as a substrate for hexokinase and is therefore entirely excreted by the kidneys.[2]

Furthermore, 2DG (and likely 3OMG) possesses potent anticonvulsant effects[3] that will help localising the seizure onset zone by accumulating within the high metabolic area, and thereby depriving the cells of the energy needed for seizure propagation.

Therefore the aim of this work is to investigate whether such molecules can be used as alternative epileptic tracers with MRI and assess the possibility of eventually replacing ictal SPECT in patients with epilepsy. As such we plan to test both 2DG and 3OMG in rat models of epilepsy, to establish detection thresholds, as well as the potential antiepileptic effects.

This project will go forward from October 2015 onwards thanks to the grand awarder by UCL as part of the Confidence in Concept Scheme.

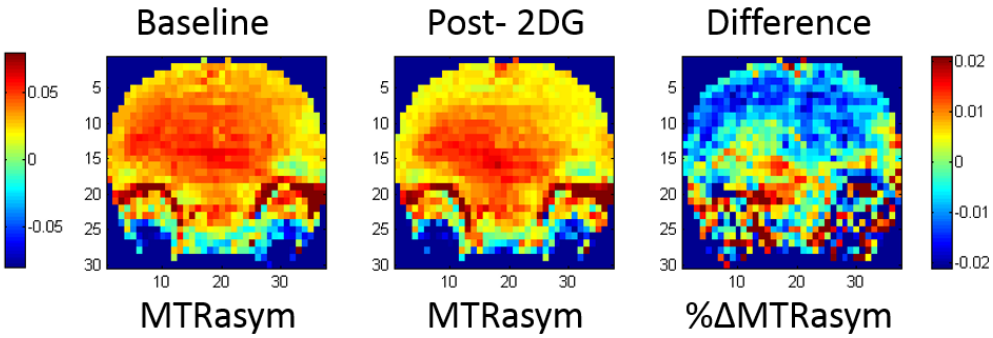

Figure 7.3.1.: *MTR of pre- and post- 2DG injection of a rat undergoing epileptic seizure. Difference images (right) showing a generalised 2DG signal decrease, except for a local increase in the deep grey matter, compatible with increased metabolic activity of the epileptogenic focus.*

7.3. Preliminary data

We have successfully applied our glucoCEST protocol on rats during epileptic seizures and preliminary data demonstrated the possibility to detect a glucoCEST signal from 2DG in the expected epileptogenic foci in n=2 animals.

The results show MTR asymmetry in the 2DG-CEST experiment to decrease significantly ($p<0.05$) in the cortical and hippocampal regions. However a significant signal increase ($p<0.05$) was observed in the deep grey matter region.

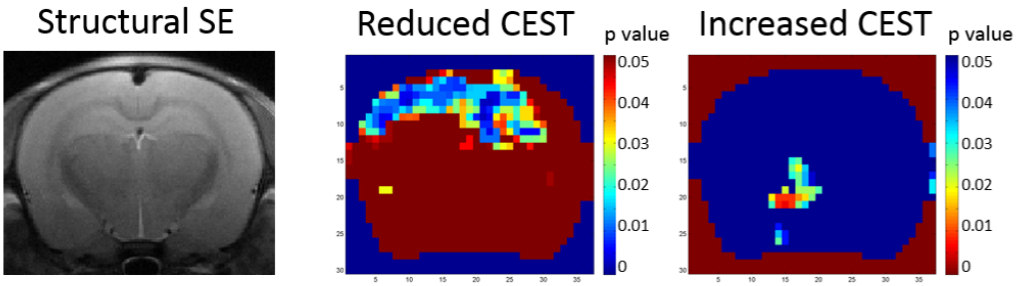

Figure 7.3.2.: *Structural image and p-value maps from t-tests (single tailed) comparing pre and post images (n=5). The first p-value map shows the pixels with significantly reduced CEST asymmetry.The second p-value map shows the pixels with significantly increased CEST asymmetry.*

7.3.1. Methods:

Epileptic seizures were induced by a single dose of kainic acid IP in two rats.
The epilepsy rat model chosen for this project, has been established by Professor Walker's team from the UCL Institute of Neurology which provides a well characterised pattern of epileptic seizure allowing reproducible experiments.

Acquisition of CEST baselines started one hour after an IP injection of Kainic acid (10 mg/Kg) to maximize chances of seizure. After 5 CEST baselines 2DG was injected IP (1g/Kg). During the following hour, 6 post-2DG CEST scans were acquired.

Anaesthesia protocol: Induction with Isoflurane (3%). Once the animals were sedated, injection of a bolus of Medetomidine (0.1 mg/Kg) followed by continuous infusion (0.25 mg/Kg/h). Isoflurane was kept at 0.5% during the experiment.

MRI protocol: High resolution structural image (Fast Spin Echo with 100μm in plane resolution and 0.5mm slice thickness) was acquired before the CEST measurements. CEST images were obtained using the fast gradient echo (Turbo-FLASH) pulse sequence described in Appendix B (400μm in plane resolution with a 2 mm slice thickness) with 57 offsets from -4.5 to 4.5 ppm and 2.5 μT. Integration of the MTR asymmetry was performed in [0.5-1.2] ppm range.

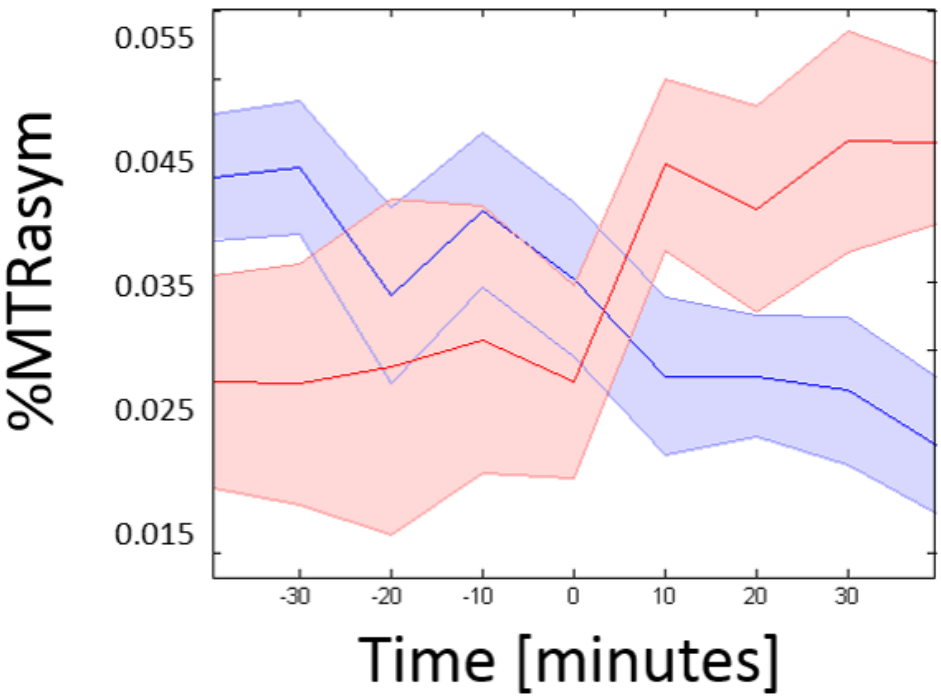

Figure 7.3.3.: *Average 2DG GCE over time. 2DG bolus injected at time=0 minutes. Mean values were calculated for the pixels with significant CEST change ($p<0.05$). Decreased CGE in blue (cortical area in this case). Increased GCE in red (in the thalamus)*

7.4. BicarboCEST

Due to upregulated glycolysis, tumours have an acidic extracellular pH (pHe).[4] It has been reported that the acidic extracellular environment promotes invasion and enhances metastasis, which ultimately offers cancer cells a selective survival advantage.[5] Administration of sodium bicarbonate has been shown to increase the pHe of cancerous (but not in healthy) tissue, leading to reduction of metastasis and tumour invasion.[6] Because of the strong pH dependence of chemical exchange rates, acute variations in tissue pH due to bicarbonate administrations may be detected *in vivo* using CEST MRI.

Under these premises, a small preliminary study was done aimed to explore the use of bicarbonate as bio-marker of tumour progression using CEST.

7.4.1. Methods

Human GBM cells ($3x10^6$) were inoculated intracranially in immune suppressed (NON-SKID) mice (n=12). One cohort received cells from the solid phenotype U87 tumour, a second cohort cells from diffuse human GBM and the last cohort was used as control. Mice were anaesthetized with 1.3% isoflurane and cannulated via the intra-peritoneal route for administration of bicarbonate while in the MRI scanner.

Anatomical scans were acquired with high resolution Turbo Spin Echo (TSE) sequence (TR= 3s, TE= 20ms, ETL= 6, FOV= $20x20mm^2$, slice thickness= 0.5mm, matrix size= 256x256). Three baseline CEST scans were taken prior to the administration of 0.3ml of 8.4% bicarbonate solution. CEST scans were acquired one hour post-bicarbonate infusion. At the severe stage of cancer, animals were culled and brains were fixed for histological analysis.

The CEST signal enhancement due to bicarbonate was calculated as the change in MTR asymmetry pre- and post- bicarbonate administration, integrated between 0.5 and 4 ppm. CEST data were acquired using a fast Gradient Echo readout (TR= 2.73ms, TE= 1.52ms, flip angle= 20°, FOV= 20x20mm2, slice thickness= 1.5mm, matrix size= 64x64) with a saturation train prior the readout of 80 Gaussian pulses at 1.3μT (pulse length= 50ms, flip= 540°, 91% duty cycle). Saturation was applied at 59 equally spaced frequency offsets ranging from -4.5 to 4.5 ppm, giving a temporal resolution of 5 minutes per Z-spectrum block.

According to the spread of tumours, mice were classified in advanced or early stage groups. Mice with visible lesions in the T2w-SE image (>10% of the brain volume)

were considered in advance stage, whereas mice with no appreciable tumour in early stage.

7.4.2. Preliminary results

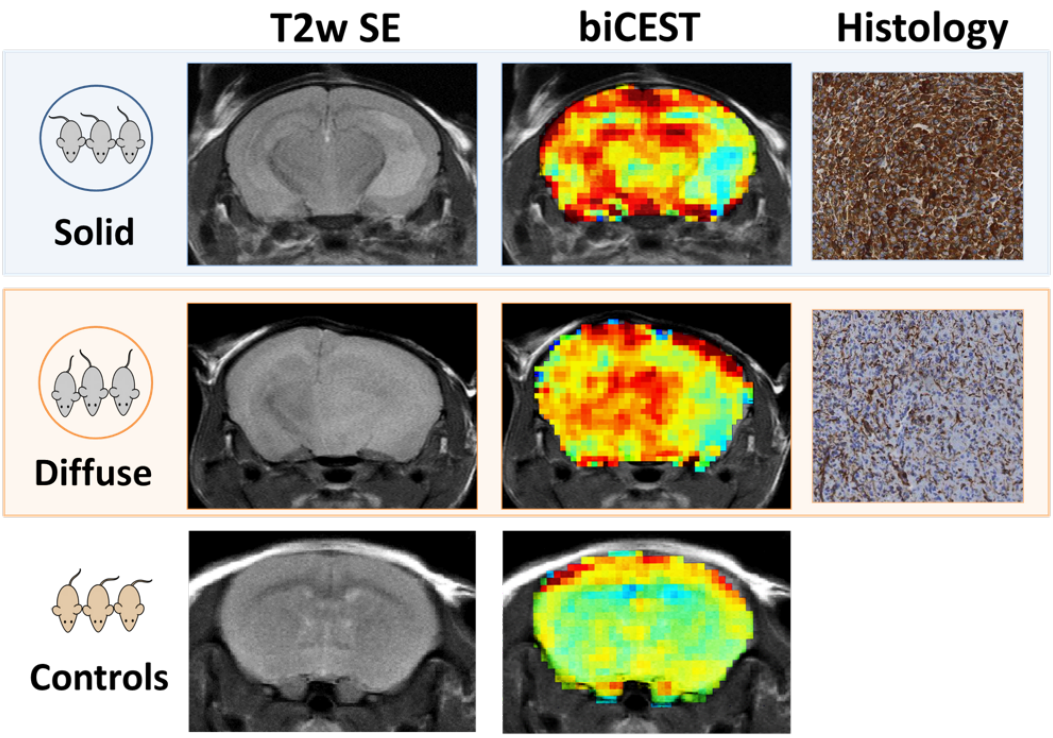

Figure 7.4.1.: *Coronal brain sections showing T2 weighted SE images in 1st column and their corresponding overlaid bicarboCEST images in 2nd column. Human specific immunestaining (vimentin) of each tumour (350x magnification) is shown in 3rd column. The colour code in the bicarboCEST images represent ±3% (red positive, blue negative) of the MTR asymmetry.*

Following bicarbonate administration, glioma-bearing mice display a significant increase ($p<0.05$) of the overall bicarboCEST signal across the brain. In contrast, control animals show a flat response to the bicarbonate. See figures 7.4.1 and 7.4.2. In the solid phenotype group, an elevated bicarboCEST signal is observed outside areas of consolidated glioma, and lower signal in the core of the tumour. This pattern is less clear in the diffuse tumour phenotype group.

An explanation for this behaviour could rely on the morphology of both cancer types. Dense nuclear regions in the core of solid tumours are less perfused, hence less affected by bicarbonate. Diffuse cancers with sparse nuclei allow a more homogeneous perfusion. See 3rd column in figure 7.4.1 for a comparison of tumour cell

density.

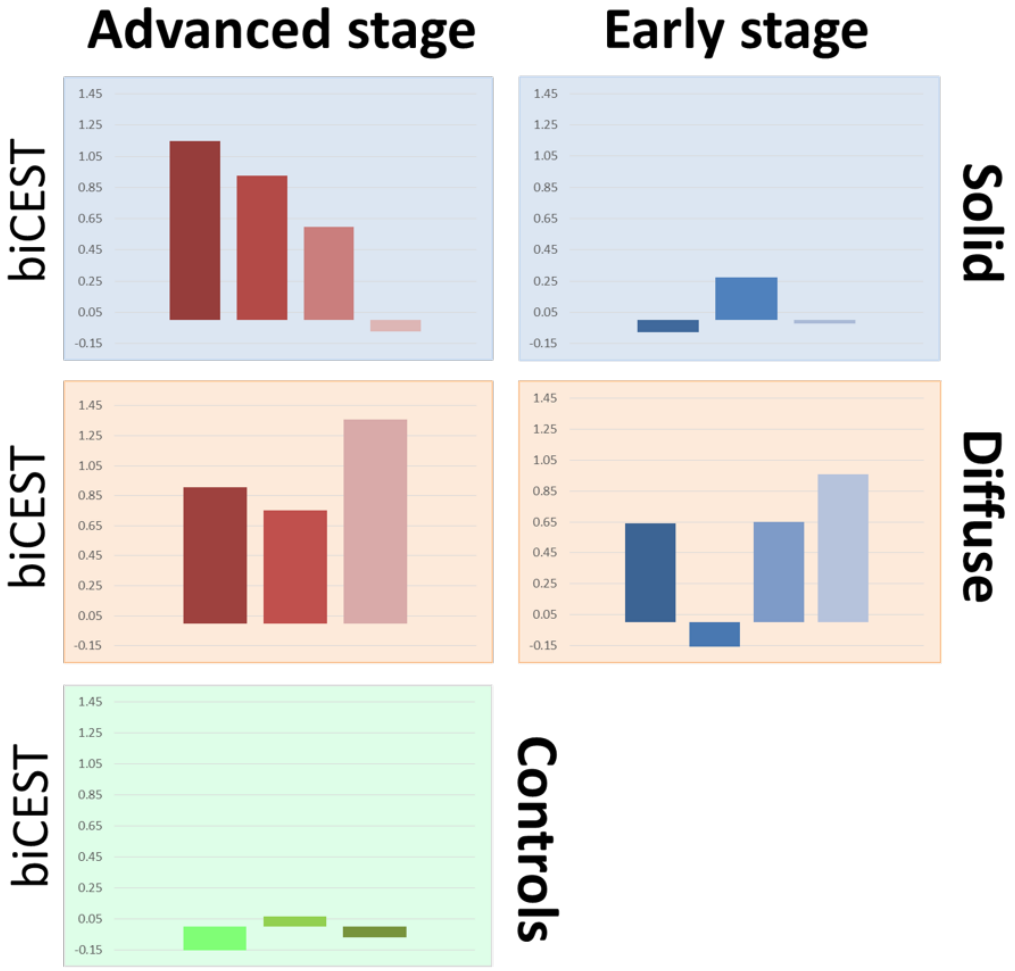

Figure 7.4.2.: *Mean bicarboCEST signal in the brain (measured as the average of all voxels) per animal. Cancer stage groups are separated in columns and tumour type groups in rows. Controls shown in green.*

At the early stage of cancer, while solid tumours still display no significant signal, diffuse gliomas already show increased bicarboCEST levels compared to controls (see figure 7.4.2). At this stage lesions are not appreciable in T2w SE images.

7.4.3. Discussion and conclusion

A proof of concept for a new application of CEST MRI is proposed for early assessment of tumour progression by means of bicarbonate administration. Although very preliminary, the results of the study show encouraging distinction between different tumour types and controls.

Signal in the tumour area appears to be reduced at late stage (similar to what was observed with glucoCEST). Admittedly the trends reported in both glucoCEST and bicarboCEST studies are suspiciously alike.
The fact that in areas of well developed tumour the CEST signal from both methods is hypo-intense, might be a consequence of poor blood perfusion in the region, resulting in a lack of sugar increase or pH change. However, the hyper-intense signal around the tumour-core observed in both techniques is more difficult to interpret. A possible physiological response that would explain these results would be an acute intracellular acidification as a consequence of the bicarbonate administration. In fact numerous studies have reported this effect, producing a ~ 0.2 units of intracellular pH reduction.[7,8,9] In this situation the fast exchanging amines would produce higher CEST signal favoured by the reduced pH environment. On the other hand, signal from amide protons would not experience a significant change provided that the initial pH was already basic (assumption based on the relationships for amide and amine groups described in section 1.4.5 of Chapter 1).

In this context, bicarbonate and glucose have concomitant effects and would likely produce an enhancement of the CEST contrast when used in combination.

Nonetheless, a more thorough study is required to validate this hypothesis and assess the significance of bicarboCEST signal. A collaboration with Prof. Brandner's group from UCL Institute of Neurology, is already established to take this study further and explore the feasibility of bicarboCEST as an early biomarker of diffused glioma.

Aim to explore the use of natural pH buffers such as bicarbonate as bio-marker of tumour progression using CEST.

Chapter references

[1] Fatima A. Nasrallah, Guilhem Pagès, Philip W. Kuchel, Xavier Golay, and Kai-Hsiang Chuang. "Imaging brain deoxyglucose uptake and metabolism by glucoCEST MRI". In: *Journal of Cerebral Blood Flow & Metabolism* 33.8 (Aug. 2013). 00015 Cited by 0000, pp. 1270–1278. ISSN: 0271-678X. DOI: 10.1038/jcbfm.2013.79 (cit. on pp. 208, 211).

[2] Michal Rivlin, Ilan Tsarfaty, and Gil Navon. "Functional molecular imaging of tumors by chemical exchange saturation transfer MRI of 3-O-Methyl-D-glucose". In: *Magnetic Resonance in Medicine* 72.5 (Nov. 1, 2014), pp. 1375–1380. ISSN: 1522-2594. DOI: 10.1002/mrm.25467 (cit. on p. 211).

[3] Mireia Garriga-Canut, Barry Schoenike, Romena Qazi, Karen Bergendahl, Timothy J. Daley, Rebecca M. Pfender, John F. Morrison, Jeffrey Ockuly, Carl Stafstrom, Thomas Sutula, and Avtar Roopra. "2-Deoxy-D-glucose reduces epilepsy progression by NRSF-CtBP-dependent metabolic regulation of chromatin structure". In: *Nature Neuroscience* 9.11 (Nov. 2006). 00250, pp. 1382–1387. ISSN: 1097-6256. DOI: 10.1038/nn1791. pmid: 17041593 (cit. on p. 211).

[4] D. M. Prescott, H. C. Charles, J. M. Poulson, R. L. Page, D. E. Thrall, Z. Vujaskovic, and M. W. Dewhirst. "The relationship between intracellular and extracellular pH in spontaneous canine tumors". In: *Clinical Cancer Research: An Official Journal of the American Association for Cancer Research* 6.6 (June 2000), pp. 2501–2505. ISSN: 1078-0432. pmid: 10873105 (cit. on p. 214).

[5] I. F. Robey, B. K. Baggett, N. D. Kirkpatrick, D. J. Roe, J. Dosescu, B. F. Sloane, A. I. Hashim, D. L. Morse, N. Raghunand, R. A. Gatenby, and R. J. Gillies. "Bicarbonate Increases Tumor pH and Inhibits Spontaneous Metastases". In: *Cancer Research* 69.6 (Mar. 15, 2009), pp. 2260–2268. ISSN: 0008-5472, 1538-7445. DOI: 10.1158/0008-5472.CAN-07-5575 (cit. on p. 214).

[6] Ian F. Robey and Lance A. Nesbit. "Investigating Mechanisms of Alkalinization for Reducing Primary Breast Tumor Invasion". In: *BioMed Research International* 2013 (2013), pp. 1–10. ISSN: 2314-6133, 2314-6141. DOI: 10.1155/2013/485196 (cit. on p. 214).

[7] Kazuya Nakashima, Tetsuo Yamashita, Shiro Kashiwagi, Naoto Nakayama, Tetsuhiro Kitahara, and Haruhide Ito. "The effect of sodium bicarbonate on CBF and intracellular pH in man: Stable Xe-CT and 31P-MRS". In: *Acta Neurologica Scandinavica* 93 (July 1, 1996). 00028, pp. 96–98. ISSN: 1600-0404. DOI: 10.1111/j.1600-0404.1996.tb00561.x (cit. on p. 218).

[8] J. I. Shapiro, M. Whalen, R. Kucera, N. Kindig, G. Filley, and L. Chan. “Brain pH responses to sodium bicarbonate and Carbicarb during systemic acidosis”. In: *American Journal of Physiology - Heart and Circulatory Physiology* 256.5 (May 1, 1989). 00070, H1316–H1321. ISSN: 0363-6135, 1522-1539. pmid: 2541632 (cit. on p. 218).

[9] J. M. Ritter, H. S. Doktor, and N. Benjamin. “Paradoxical effect of bicarbonate on cytoplasmic pH”. In: *The Lancet*. Originally published as Volume 1, Issue 8700 335.8700 (May 26, 1990). 00094, pp. 1243–1246. ISSN: 0140-6736. DOI: 10.1016/0140-6736(90)91305-T (cit. on p. 218).

8. Summary and final remarks

Within this thesis the foundations of glucoCEST technique have been studied through mathematical models, phantom work and *in vivo* experiments. A summary of the work presented is outlined below.

The multi-pool Bloch-McConnell model presented in Chapter 3 has been fundamental for the understanding of the CEST mechanism and the interaction between variables that ultimately govern the image contrast. This model, both in its steady state and dynamic formulations (included in Appendices E and F), help predict the expected outcomes of experiments and serve as powerful tools for the optimisation of the parameters involved in a CEST pulse sequence. Predictions from this model, supported by experimental data, have been used to challenge long established and important concepts such as the required amount of power for optimum glucoCEST results.

The CEST contrast observed in sugars formed along the glycolytic pathway, set the basis for the possibility of intracellular measurements of glucoCEST signal. The results from the phantom study presented in Chapter 4 revealed positive CEST signal in all four molecules studied; particularly intense in the G6P, which is present only inside the cell. Provided that intracellular sugar concentrations are sufficiently elevated in tumours (as has been shown in several documented studies), these findings strongly support the feasibility of exploring cancer metabolism with glucoCEST MRI. The study of the expected glucoCEST signal with a System Dynamics model in Chapter 5 also supports the idea that intracellular signal detection is a likely possibility, despite the extremely fast glycolysis inside the cell.

Results of the animal study in Chapter 6 revealed the complexity in the behaviour of the glucoCEST signal. GlucoCEST produces a hypo-intense signal in well developed tumours compared to the surrounding tissues. Moreover, glucoCEST appears to highlight the cancer-affected areas before the appearance of significant changes in the tissue structure, which suggests the possibility of glucoCEST being particularly sensitive to early phases of cancer. However, the significance of these results is unclear due to the difficulty in the interpretation of the data, the low n numbers and reduced SNR in these experiments. Further studies with rigorous validation of

in vivo measurements are needed, in which glucoCEST can be compared to data from established imaging modalities like ^{18}F-FDG PET.

Clinical translation of CEST will require a big coordinated effort to standardise imaging protocols and measurements before the technique can become a valuable contrast mechanism. With the CEST field rapidly evolving, the future will see new applications and refinements in the data quality. Together with the advancement towards higher field strength MRI systems and fast acquisition protocols, glucoCEST and other CEST modalities could become a complementary addition to imaging protocols for the characterisation of cancer and assessment to treatment response in hospitals across the world.

A. Essential equations in NMR

Equation of motion

The equation of motion that governs the evolution of the magnetisation vector inside a magnetic field is:

$$\frac{d\mathbf{M}(t)}{dt} = \gamma \mathbf{M}(t) \times \mathbf{B}(t) \tag{A.0.1}$$

Where γ is the gyromagnetic ratio of the nuclear spin, $\mathbf{M}(t)$ is the magnetisation vector and $\mathbf{B}(t)$ is the magnetic field.

This equation, which can be taken as a fundamental rule, is at the heart of the the rotation and precession in MRI. Acknowledging that only the perpendicular component of $\mathbf{M}(t)$ will be affected by $\mathbf{B}(t)$, the precession frequency of $\mathbf{M}(t)$, Larmor frequency, can be expressed as $\square_{\mathbf{0}} = \gamma \mathbf{B_0}$ where $\mathbf{B_0}$ represents the static magnetic field.

A useful mathematical device to understand the evolution of the magnetisation vector $\mathbf{M}(t)$, is the use of a **rotating frame of reference**. The equation of motions in a frame of references rotating around the laboratory frame can be written as:

$$\left(\frac{d\mathbf{M}}{dt}\right)_{Rot} = \left(\frac{d\mathbf{M}}{dt}\right)_{Lab} + \square' \times \mathbf{M} \tag{A.0.2}$$

$$\left(\frac{d\mathbf{M}}{dt}\right)_{Rot} = \gamma \mathbf{M} \times \mathbf{B} + \square' \times \mathbf{M} \ = \gamma \mathbf{M} \times \left(\mathbf{B} - \frac{\square'}{\gamma}\right) \tag{A.0.3}$$

where $\square'$ represents the angular frequency vector of the rotating frame with respect to the laboratory frame.

In the laboratory frame, spins precess at the Larmor frequency, however from the point of view of a frame rotating at the Larmor frequency parallel to the static magnetic field, $\square' = \square_0$, the spins will appear stationary:

$$\left(\frac{d\mathbf{M}}{dt}\right)_{Rot} = \gamma \mathbf{M} \times \left(\frac{\square_0}{\gamma} - \frac{\square'}{\gamma}\right) = 0 \tag{A.0.4}$$

Figure A.0.1.: *90° RF pulse seen from different reference frames.*

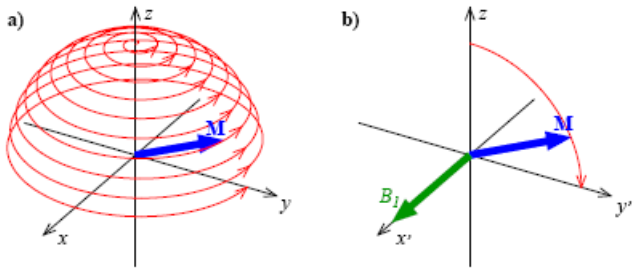

a) laboratory frame. b) frame rotating at Larmor frequency.

The concept of the rotating frame makes it easier to visualize and understand the dynamics of the magnetisation vector. Figure A.0.1 shows an example of a radio-frequency (RF) pulse applied perpendicular to the magnetisation vector **M**, from both the laboratory and rotating frames. While in the laboratory frame the vector **M** precesses around the z axis until it aligns with the y axis, the same event from the rotating frame is described as a single rotation along the x' axis.

Relaxation

The recovery of the magnetisation vector $\mathbf{M}(t)$ towards its thermal equilibrium value is called relaxation. This process is mediated by two different physical phenomena, spin-lattice and spin-spin interactions.

The longitudinal (or spin-lattice) relaxation, associated with the **T1** characteristic time, derives from the redistribution of the spin states in order to reach the thermal equilibrium. As a consequence, the z component of the nuclear spin magnetisation, Mz, evolves towards the thermal equilibrium value, M_0. This relationship can be expressed as:

$$M_z(t) = M_0 - [M_0 - M_z(0)]e^{-t/T_1} \tag{A.0.5}$$

The transverse (or spin-spin) relaxation corresponds to the loss of coherence of the transverse magnetisation $M_\perp$, perpendicular to the static magnetic field B_0. **T2** is the decay constant for the spin-spin relaxation process. From an initial state $M_\perp(0)$ at time zero, the transverse magnetisation decays as follows:

$$M_\perp(t) = M_\perp(0)e^{-t/T_2} \tag{A.0.6}$$

Bloch equations

The combination of the two relaxation processes with the equation of motion results in what is called the Bloch equations:

$$\frac{d\mathbf{M}(t)}{dt} = \gamma \mathbf{M}(t) \times \mathbf{B}(t) - \frac{\mathbf{M}_{\parallel} - \mathbf{M_0}}{T_1} - \frac{\mathbf{M}_{\perp}}{T_2} \tag{A.0.7}$$

where $\mathbf{M}_{\parallel}$ and $\mathbf{M}_{\perp}$ are respectively the parallel and perpendicular projections of the magnetisation vector $\mathbf{M}$ along the static magnetic field $\mathbf{B_0}$.

Choosing the static magnetic field to be along the z axis and breaking down the vectorial identity into its Cartesian components yields to:

$$\begin{aligned}
\frac{dM_x(t)}{dt} &= \gamma \left[M_x(t) B_z(t) - M_z(t) B_y(t) \right] - \frac{M_x(t)}{T_2} \\
\frac{dM_y(t)}{dt} &= \gamma \left[M_z(t) B_x(t) - M_x(t) B_z(t) \right] - \frac{M_y(t)}{T_2} \\
\frac{dM_z(t)}{dt} &= \gamma \left[M_x(t) B_y(t) - M_y(t) B_x(t) \right] - \frac{M_z(t) - M_0}{T_1}
\end{aligned} \tag{A.0.8}$$

Given an isolated set of spins in a magnetic field $\mathbf{M}(t)$, the behaviour of the magnetisation vector $\mathbf{M}(t)$ is fully described by the Bloch equations.

B. Pulse sequences and relaxometry analysis

B.1. T1 map sequence

Quantification of the longitudinal relaxation time T1 was performed using a modified Inversion Recovery Gradient Echo sequence. A global adiabatic inversion pulse was applied on resonance with water followed by an inversion time TI and a GE readout with echo time set at the minimum possible value (TE= 1.09ms). Phase encoding lines were acquired from low to high frequency (inverse centric k-space sampling), providing fast images but heavily weighted on the centre of k-space. TE was set to 1.09ms (minimum possible) and TR_{RO} (which refers to TR between readouts) to 2.03ms. Each acquisition was followed by a 20 seconds delay and spoiler gradients (duration = 1.3s and amplitude = 2G/cm) to obtain full signal recovery before the next inversion pulse. The sequence was repeated 20 times with different TI values, exponentially spaced from 70ms to 20s. Figure B.1.1 shows the diagram of the pulse sequence.

B.2. T2 map sequence

Quantification of the transverse relaxation time T2 was done using a Carr Purcell Meiboom Gill (CPMG) sequence. It consisted of a 90 degree excitation pulse in the x axis (sinc shaped and 1ms long) followed by 40 refocusing pulses in the y axis (flip angle 180°, sinc shaped and 1ms long).

B.3. CEST sequence

The CEST sequence consisted of two parts, pre-saturation at a frequency offset (fsat) followed by turbo-flash GE readout (same as for T1 maps). Saturation was achieved with a train of 80 Gaussian shaped pulses, each at 50ms duration and with an inter-

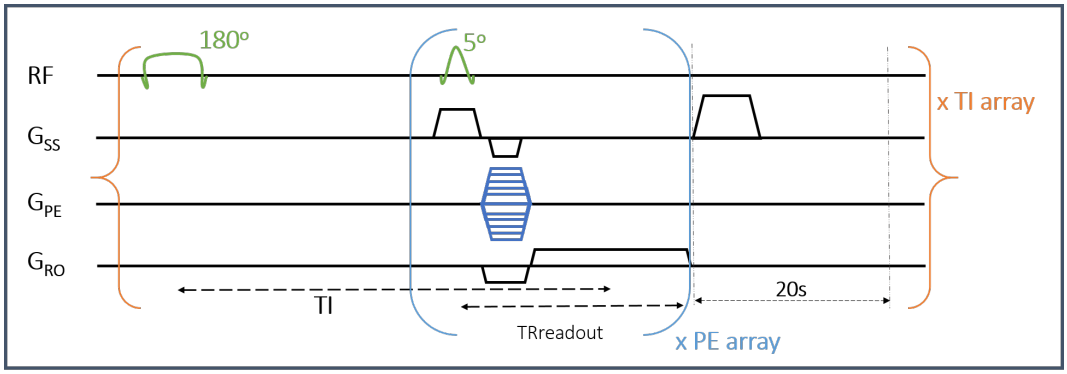

Figure B.1.1.: *Illustration of the T1 map sequence. RF pulses are shown in green, slice select and frequency encoding gradients in black and phase encoding gradients in blue. The orange brackets indicate the array of 18 TI values.G_{SS}, G_{PE}, G_{RO} correspond to the slice selection, phase encoding and readout gradients respectively. TI represents to the wait time between the application of the inversion recovery and the readout pulses*

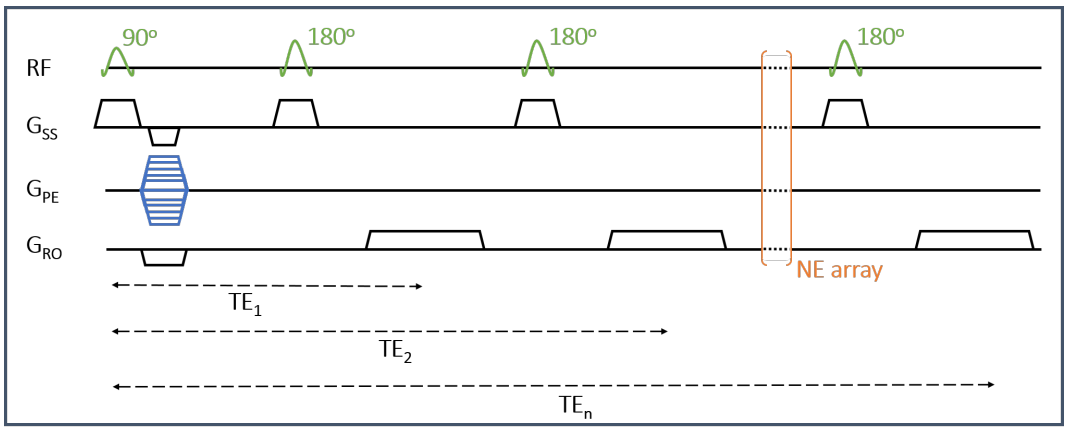

Figure B.2.1.: *Illustration of the CPMG sequence used for the quantification of T2 maps. The RF pulses are shown in green, the gradients in black and the phase encode table in blue. Orange colour represents the array of echo times (NE=40), where each echo corresponds to a different T2 weighted image. Slice refocusing crushers were applied for 2ms at amplitude 10G/cm.*

pulse delay of 1ms. The flip angle of the saturation pulses ($\propto$B1 power) was adjusted to obtain CEST profiles at different saturation power.

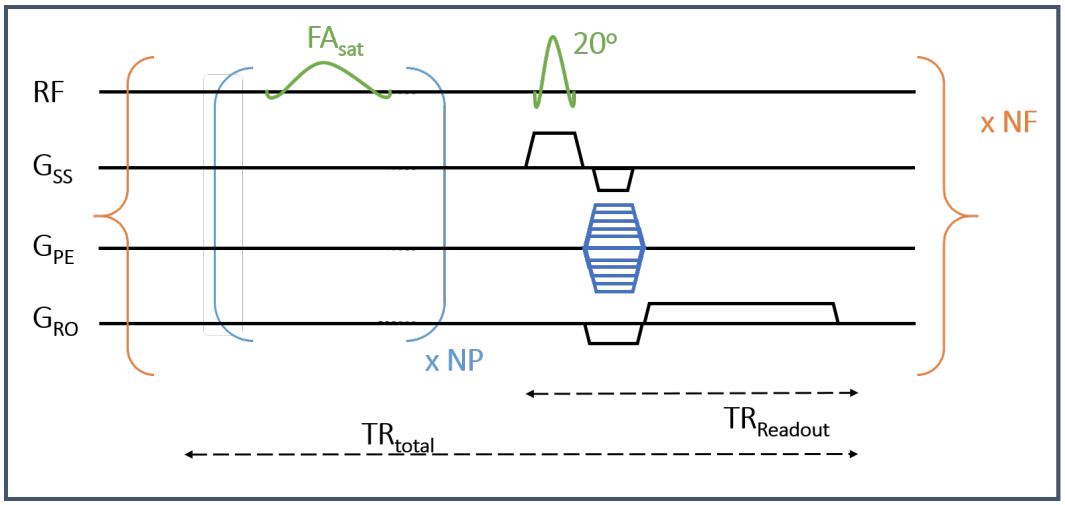

Figure B.3.1.: *Illustration of the CEST sequence used. All RF pulses are displayed in green. Slice select and frequency encoding gradients in black and phase encoding gradients in dark blue. The light blue bracket indicates the number of saturation pulses applied (NP). The saturation RF pulse prior to the excitation pulse is applied with no inter-pulse delay (total number of saturation pulses 80). FA_{sat} indicates the flip angle of each saturation pulse. TR_{RO} refers to the readout time alone, while TR_{total} to the total aquisition time between frequency offsets in the Z-spectrum. The loop corresponding to the Z-offset frequncies (NF) is displayed in orange*

B.4. Relaxometry

Quantification of T1 values was done assuming a mono-exponential longitudinal relaxation to fit the data to equation B.4.1:

$$M_z(TI) = M_{eq}.|1-2e^{-TI/T1}| \tag{B.4.1}$$

where M_{eq} is the signal at full recovery, T1 the longitudinal relaxation time and TI the inversion time.

Quantification of T2 values was done assuming a mono-exponential traverse relaxation and fitting the data to equation B.4.2:

$$M_z(TE) = M_0.e^{-TE/T2} \tag{B.4.2}$$

where M_0 is the constant representing the intensity at zero echo time, T2 the traverse relaxation time and TE the echo time. In order to avoid errors from inhomogeneous RF pulses, only the even echoes were used in the fitting.

All the data analysis was done in a pixel by pixel basis using in-house made Matlab codes.

C. CEST in amino acids

As mentioned in section 5.6, ^{13}C NMR spectroscopy of SW1222 and LS174T tumours revealed that glucose is transformed into lactate and a number of different amino acids, as part of the metabolic activity of these cancer cells. Amino acids contain -NH and -OH groups that are susceptible to be detected by CEST and hence may contribute to the measured glucoCEST signal. In order to investigate this, a new experiment was carried out in which a set of phantoms with molecules found in the tumours were scanned to evaluated their CEST response.

Amino acids phantom study:

Method Phantoms with solutions (1% PBS) of the following substances were prepared: lactate, glutamate, glutamine, taurine and alanine, which accounted for the most abundant amino acids found in ^{13}C NMR.[1] The samples were arranged in 10 and 50 mMolar concentrations and scanned with two different RF powers, $1\mu T$ and $2\mu T$. Temperature was set to 37°C and pH calibrated at 7.4. The pulse sequence and scan parameter used were the same as in the previous study.

Figure C.0.1.: *Exchangeable sites in amino acids*

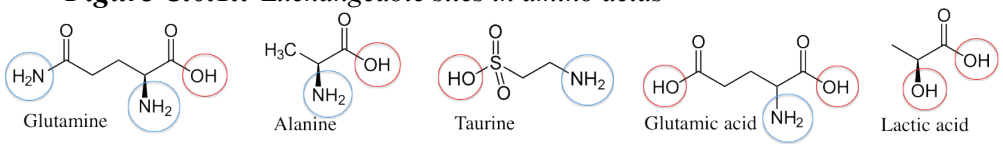

Results In contrast to the broad glucose peak observed at 1 ppm, results from the amino acids showed distinct CEST peaks centred around 2.9 ppm. The reason for the different resonant frequencies is attributable to the type of exchangeable site involved, -NH in the case of amino acids while -OH in glucose. It is worth noting that contained within the structure of these amino acids, there are also hydroxyl groups

which do not display any CEST peak. The extreme mobility of small molecules confers a very fast exchange rate, which becomes too fast for sites like the hydroxyl groups that resonate close to water, at around 1 ppm. Hence, the signal derives essentially from -NH groups with a minor contributions from -OH, as can be seen in lactate, which contains no -NH sites.

Figure C.0.2.: *CEST effect from amino acids*

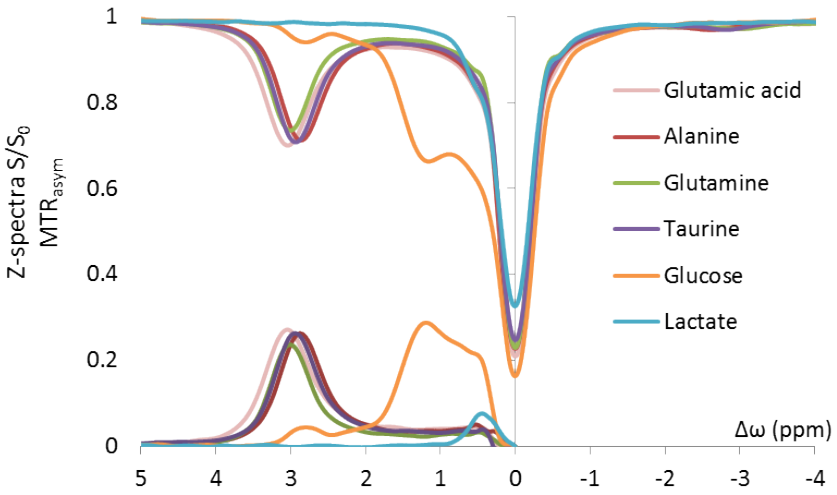

Z- and MTRasym spectra from glucose, lactate, glutamine, glutamate, alanine and taurine. While lactate shows negligible signal, amino acids show distinct CEST peaks centred at around 2.9 ppm.

In *in vivo* experiments, CEST peaks appear much less defined than *in vitro*, which is why it is customary to calculate an overall CEST signal over a range of frequencies. The average CEST signal (integrated between 0 and 4 ppm) from glutamine, glutamate, taurine and alanine was 77% of that found in glucose. On the other hand, lactate showed a smaller CEST effect, accounting for 10% of the signal from glucose. These ratios get even more stretched when the MTR_{asym} is integrated from 0.75 to 4 ppm (as done for our initial study[1]), leading to ratios of 83% for the amino acids and a negligible 4% in the case of lactate.

Under the assumption that increased glucose uptake in tumours would also bring an up-regulation of amino acid production, the results suggest that glucoCEST signal could be consequence of an increase in both glucose and amino acids concentration.

References

[1] Simon Walker-Samuel, Rajiv Ramasawmy, Francisco Torrealdea, Marilena Rega, Vineeth Rajkumar, S. Peter Johnson, Simon Richardson, Miguel Gonçalves, Harold G. Parkes, Erik Arstad, David L. Thomas, R. Barbara Pedley, Mark F. Lythgoe, and Xavier Golay. "In vivo imaging of glucose uptake and metabolism in tumors". In: *Nature Medicine* 19.8 (Aug. 2013). 00044 Cited by 0001, pp. 1067–1072. ISSN: 1078-8956. DOI: 10.1038/nm.3252 (cit. on pp. 231, 232).

D. Endogenous CEST in xenograft glioblastoma models

As seen in Chapter 1, endogenous APT contrast has been shown to be a useful technique for the investigation of cancer, as it can inform on various important aspects of tumour physiology such as pH or protein concentration levels and it has been proposed as a powerful method to differentiate necrosis and recursive tumour tissue.

While the main focus of this work was the study of the glucoCEST method, the data acquired for the study presented in Chapter 6 is also useful to explore the native CEST contrast in glioblastomas. A brief summary of the findings in the endogenous CEST profile of these tumours is accounted in this appendix. As part of the same study, the methodology and animal models used are the same as the ones described in Chapter 6. In this section, APT-CEST is compared to relaxation times T1 and T2 over the progression of different glioblastoma models inoculated in mice.

T1 and T2 maps show a clear increase in the tumour affected areas both in solid and diffused phenotype cell-lines. Figures D.0.1 and D.0.2 show increased values for the *core* of the tumour followed by elevation in the *proliferating* region at a later stage. The regions labelled as *no tumour* (not affected by inspection of T2wSE), do not show any significant increase in the relaxation times; only at the late state of the diffused cases. APT on the other hand, displays a distinct pattern with an initial increase of the mean MTR asymmetry followed by a sudden decrease at certain a phase in the development of the cancer. The abrupt change the APT response manifests at different times in individual cell-lines, as it would be expected from different growth rates. It is worth noting that when the APT signal starts changing the contrast between core, proliferation and non tumour regions increases too. Remarkably regions with no apparent tumour display a fast signal decrease, which could be associated to either a reduction of the endogenous amide concentration or to an increase in the aliphatic NOEs. These phenomena might be linked to changes in protein concentrations or pH as the result of cancer. What is more relevant of

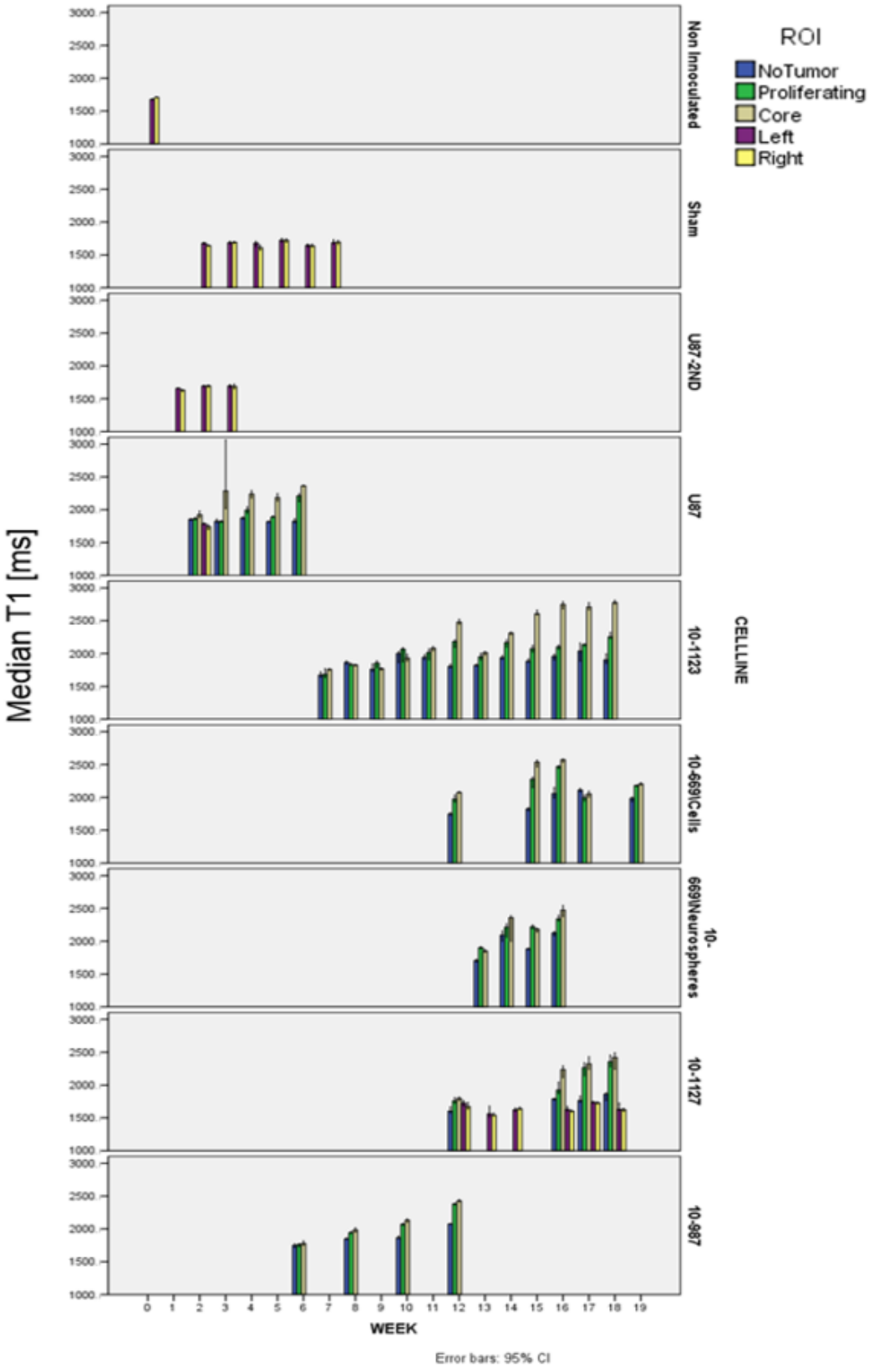

Figure D.0.1.: *Evolution of the T1 relaxation time for different glioblastoma models. Colour-bars represent the median T1 value in the specific ROIs. Horizontal axis represents weeks after inoculation of cancer cells.*

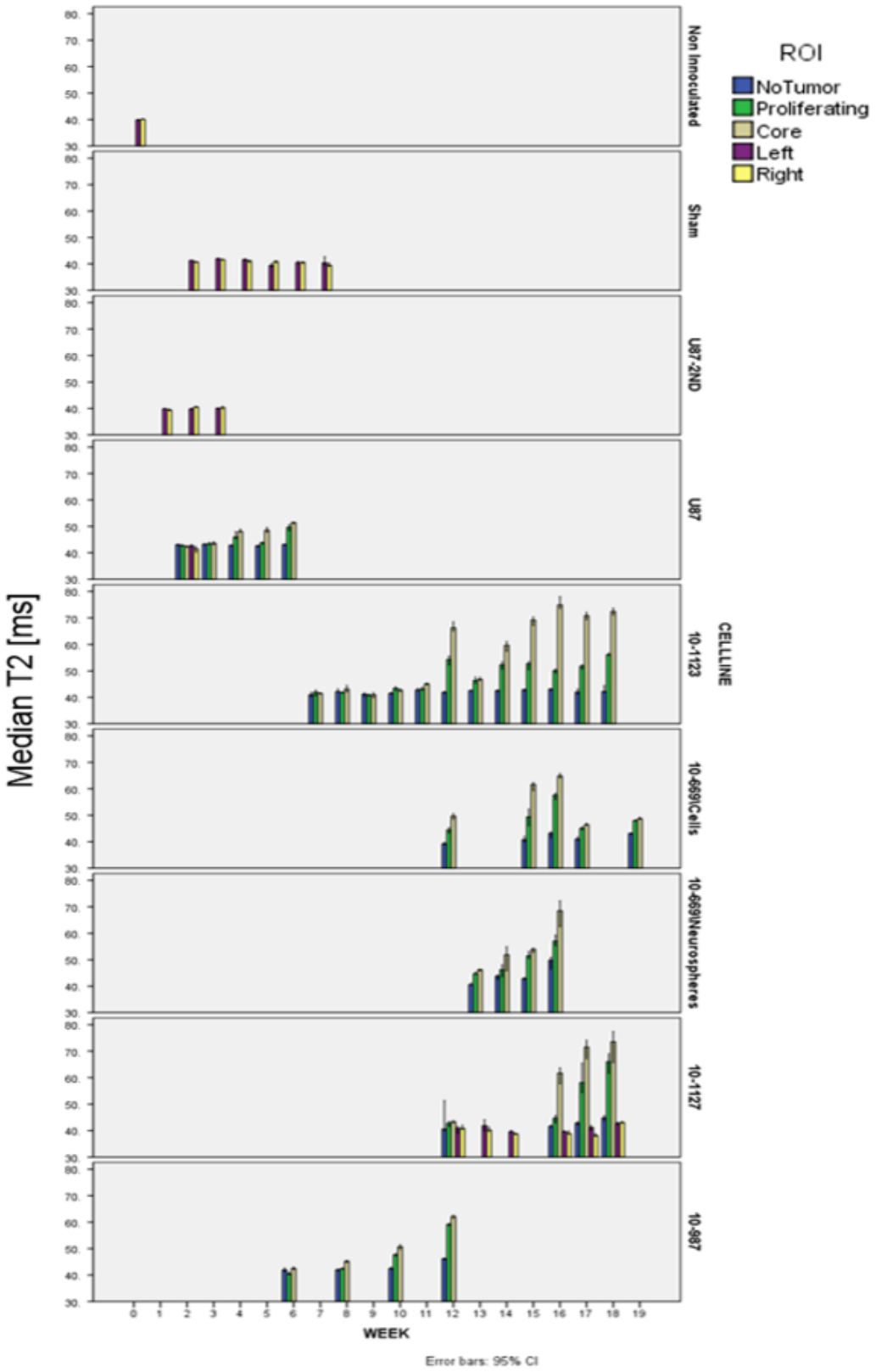

Figure D.0.2.: *Evolution of the T2 relaxation time for different glioblastoma models. Colour-bars represent the median T2 value in the specific ROIs. Horizontal axis represents weeks after inoculation of cancer cells.*

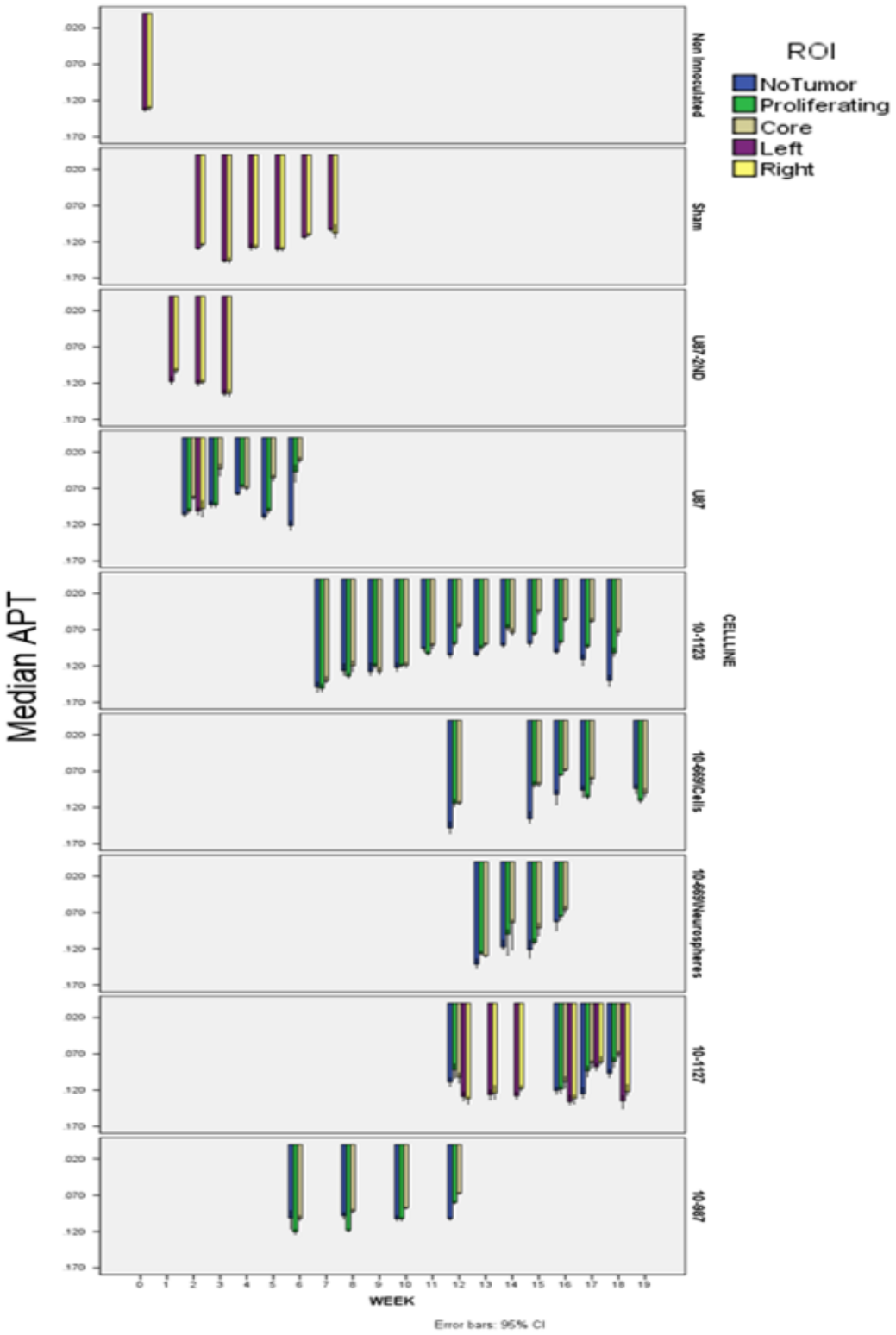

Figure D.0.3.: *Evolution of the APT (MTR asymmetry at 3.5 ppm) signal different glioblastoma models.*

this behaviour is that it occurs before changes in the T1 or T2 maps are apparent. Inspection of pH in these tissues could shed more light and clarify this hypothesis. As a last remark, is also interesting to point out that APT appears to distinguish the effects the injury caused by the intracraneal injection better than T1 or T2 maps (see the first week 2 after inoculations).

E. 9-Pool exchange model based on Bloch-McConnell equations. Time dependent simulation.

E.1. Definition of the model

```
frame
%% 9 Pool Bloch–McConell Model

function dM=Cool9Pool_Model(t,M,RFppm)
global  glucoseMolarity num_gauss interpuseDelay duration B0  FlipA gamma ppm ppmb ppmc ppmd ppme ppmf ppmg
      ppmh ppmi  M0a M0b M0c M0d M0e M0f M0g M0h M0i T2a T1a T2b T1b T2c T1c T2d T1d T2e T1e T2f T1f T2g T1g
      T2h T1h T2i T1i kb kc kd ke kf kg kh ki B1eq
format long
dM=zeros(25,1);

%% Constants
w0=gamma*B0;

D=w0*10^–6/(2*pi)*RFppm;
dc=w0*10^–6/(2*pi)*ppmc;
dd=w0*10^–6/(2*pi)*ppmd;
de=w0*10^–6/(2*pi)*ppme;
df=w0*10^–6/(2*pi)*ppmf;
dg=w0*10^–6/(2*pi)*ppmg;
dh=w0*10^–6/(2*pi)*ppmh;
di=w0*10^–6/(2*pi)*ppmi;
db=w0*10^–6/(2*pi)*ppmb;

t0=0;
tmax=(t0+duration/2);
s=duration/5.86;
% figure,plot(tt,Agilent_gaussian,tt,exp(–((tt–tmax)/s).^2/2),'r')

% timeperstep=duration/shape_points;
% nstepstoadd=round(interpuseDelay/timeperstep);
% gaussianBlock=cat(1,Agilent_gaussian,zeros(nstepstoadd,1));
% gaussTrain=repmat(gaussianBlock,[20,1]);
% trainLenght=num_gauss*(duration+interpuseDelay);
% time=linspace(0,trainLenght,numel(gaussTrain));
% figure,plot(time,gaussTrain)
% FA = gamma *  Amp*s*sqrt(2*pi)

FA=FlipA*pi/180;%[rad]
Amp=FA/(s*sqrt(2*pi)*gamma);

% yy=0; %for the begining of the loop
% for n=1:num_gauss
% yy=yy+exp(–((tt–(tmax+(n–1)*(duration+interpuseDelay)))/s).^2/2);
% end
```

```
% GaussTrain=Amp*yy;
% figure,plot(tt,GaussTrain)

yy=0; %for the begining of the loop
for n=1:num_gauss
yy=yy+exp(-((t-(tmax+(n-1)*(duration+interpuseDelay)))/s).^2/2);
end
B1=Amp*yy;

                                        %% Overwrte Pulses and use constant equivalent B1
                                        B1=B1eq;
%% %%%%%%%%%%%%%%%%%%%%%%%%%%%%%%%%%%%%%%%%%%%%
% %Square pulse a
% ti=0.3;
% tf=5;
% Ba=0;
% if (ti <= t) && (tf > t)
%     Ba=B1;
% end
%%%%%%%%%%%%%%%%%%%%%%%%%%%%%%%%%%%%%%%%%%%%%%%%

%% %%%%%%%%%%%%%%%%%%%%%%%%%%%%%%%%%%%%%%%%%%%%
% %Square pulse b
% delay=0.00372;
% ti2=tf+delay;
% tf2=0.55+delay;
% Bb=0;
% if  (ti2 <= t) && (tf2 > t)
%     Bb=0*1*B1;
% end
% % %%%%%%%%%%%%%%%%%%%%%%%%%%%%%%%%%%%%%%%%%%%%
%  B1=Ba+Bb;

%%%%%%%%%%%%%%%%%%%%%%%%%%%%%%%%%%%%%%%%%%%%%%%%%%%%%%%%%%%%%%%%
%Pulse Sequence
% mtcrusher=3*10^-3; %time duration at the end of sat pulse train.
% Bef_Read=0.008; %time delay before the readout pulse.
% Aft_Read=4.5*10^-3;  %time delay after the readout pulse.
%
% %%% Saturation pulses train
% SatFlip=7000; %in degree.
% SatPulse=50*10^-3; %time duration of the sat pulse.
% SatDelay=4*10^-6; %time duration between sat pulses.
%
% SatFlipRad=SatFlip*pi/180;
% %B1c_Sat=SatFlipRad/(gamma*(SatPulse+SatDelay)); i thinks its worng
% sigmaSat=SatPulse/7;
% A_Sat=SatFlipRad/(sqrt(2*pi)*gamma*sigmaSat);
%
% b0=4*10^-6;
% t0=3.5*sigmaSat;
% b=0;
% B1=0; %just to start with
%
% for p=1:10
%     spike=A_Sat*(exp(-(t-t0-b-Aft_Read).^2/(2*sigmaSat^2)));
%     b=b+b0+SatPulse+SatDelay;
%     B1=B1+spike;
% end

%%%%%%%%%%%%%%%%%%%%%%%%%%%%%%%%%%%%%%%%%%%%%%
% % Readout pulse
% ReadFlip=90;  %in degree too.
% ReadPulse=20*10^-3; %time duration of the readout pulse.
% Bef_Read=12*10^-6;
% mtcrusher=12*10^-6;
% sigmaRead=ReadPulse/7;
% ReadFlipRad=ReadFlip*pi/180;
% %B1c_Read=ReadFlipRad/(gamma*(ReadPulse)); % [T] For 20 degrees, 2ms pulse
% A_Read=ReadFlipRad/(sqrt(2*pi)*gamma*sigmaRead);
% Readout=A_Read*(exp(-(t-(mtcrusher+Bef_Read+ReadPulse/2)-b).^2/(2*sigmaRead^2)));

Readout=0;
B1=B1+Readout;
% B1=10^-6
%%%%%%%%%%%%%%%%%%%%%%%%%%%%%%%%%%%%%%%%%%%%%%%%%%%%%%%%%%%%%%%%
```

```
%%%%%%%%%%%%%%%%%%%%%%%%%%%%%%%%%%%%%%%%%%%%%%%
%B1=0 %% To apply no pulses at all  &&&

% TR=b0+p*(SatPulse*SatDelay)+mtcrusher+Bef_Read+Aft_Read+ReadPulse;
%%%%%%%%%%%%%%%%%%%%%%%%%%%%%%%%%%%%%%%%%%%%%%%%%%%%%%%%%%%%%%%%%%%%%%%%%
%Triangular  pulse
% tia=0.0;
% tfb=0.05;
% tfa=(tfb-tia)/2;
% tib=tfa;
% B1=0;
% if (tia <= t) && (tfa >= t)
%     B1=200*5*20*0.1175*10^-6*t;
% end
% if  (tib < t) && (tfb > t)
%      B1=200*5*20*0.1175*10^-6*(2*tfa-t);
% end
%%%%%%%%%%%%%%%%%%%%%%%%%%%%%%%%%%%%%%%%%%%%%%%%%%%%%%%%%%%%%%
 w1=gamma*B1;
%%%%%%%%%%%%%%%%%%%%%%%%%%%%%%%%%%%%%%%%%%%%%%%%%%%%%%%
% if (w1==0)
%     D=0;
%     dc=0;
% end

if t> num_gauss*(duration+interpuseDelay) %%sets the offset of the readout pulse to the water freq
D=0;
end
%%%%%%%%%%%%%%%%%%%%%%%%%%%%%%%%%%%%%%%%%%%%%%%%%%%%%%

%% Superlorentzian function
q=10000;
% p=1000;
o = linspace(0, pi/2, q);
%D=1000*logspace(log10(0.01),log10(213),p);
%o_m=repmat(o',1,p);
%D_m=repmat(D,q,1);

value=sin(o).*(2/pi).^0.5*T2b./abs(3*cos(o).^2-1).*exp(-2*((D-db).*T2b./(abs(3*cos(o).^2-1))).^2); % -dcb
      added to shift the mt pool
da=pi/(2*(q-1)).*value;
Amt=sum(da); %superlorentzian function for every D
Rrfb=Amt*w1^2*pi; %Rrfb(1,p)=1*Amt*w1^2; not sure if we have to multiply by w1^2

%% EQUATIONS
dM(1) =(-1/T2a-kc*M0c-kd*M0d-ke*M0e-kf*M0f-kg*M0g-kh*M0h-ki*M0i)*M(1) +(-2*pi*D)*M(2)+ M0a*(kc*M(4)+kd*M(7)+ke
      *M(10)+kf*M(13)+kg*M(16)+kh*M(19)+ki*M(22));

dM(2)=2*pi*D*M(1)+(-1/T2a-kc*M0c-kd*M0d-ke*M0e-kf*M0f-kg*M0g-kh*M0h-ki*M0i)*M(2) -w1*M(3)+M0a*(M(5)*kc+M(8)*kd
      +M(11)*ke+M(14)*kf+M(17)*kg+M(20)*kh+M(23)*ki);

dM(3)=w1*M(2)+(-1/T1a-kc*M0c-kd*M0d-ke*M0e-kf*M0f-kg*M0g-kh*M0h-ki*M0i)*M(3)+ M0a*(M(6)*kc+M(9)*kd+M(12)*ke+M
      (15)*kf+M(18)*kg+M(21)*kh+M(24)*ki) +M0a/T1a;


dM(4)=kc*M0c*M(1)+(-1/T2c-kc*M0a)*M(4)-2*pi*(D-dc)*M(5);

dM(5)=kc*M0c*M(2)+2*pi*(D-dc)*M(4)+(-1/T2c-kc*M0a)*M(5)-w1*M(6);

dM(6)=kc*M0c*M(3)+w1*M(5)+(-1/T1c-kc*M0a)*M(6)+M0c/T1c;


dM(7)=kd*M0d*M(1)+(-1/T2d-kd*M0a)*M(7)-2*pi*(D-dd)*M(8);

dM(8)=kd*M0d*M(2)+2*pi*(D-dd)*M(7)+(-1/T2d-kd*M0a)*M(8)-w1*M(9);

dM(9)=kd*M0d*M(3)+w1*M(8)+(-1/T1d-kd*M0a)*M(9)+M0d/T1d;


dM(10)=ke*M0e*M(1)+(-1/T2e-ke*M0a)*M(10)-2*pi*(D-de)*M(11);

dM(11)=ke*M0e*M(2)+2*pi*(D-de)*M(10)+(-1/T2e-ke*M0a)*M(11)-w1*M(12);

dM(12)=ke*M0e*M(3)+w1*M(11)+(-1/T1e-ke*M0a)*M(12)+M0e/T1e;
```

```
dM(13)=kf*M0f*M(1)+(-1/T2f-kf*M0a)*M(13)-2*pi*(D-df)*M(14);

dM(14)=kf*M0f*M(2)+2*pi*(D-df)*M(13)+(-1/T2f-kf*M0a)*M(14)-w1*M(15);

dM(15)=kf*M0f*M(3)+w1*M(14)+(-1/T1f-kf*M0a)*M(15)+M0f/T1f;


dM(16)=kg*M0g*M(1)+(-1/T2g-kg*M0a)*M(16)-2*pi*(D-dg)*M(17);

dM(17)=kg*M0g*M(2)+2*pi*(D-dg)*M(16)+(-1/T2g-kg*M0a)*M(17)-w1*M(18);

dM(18)=kg*M0g*M(3)+w1*M(17)+(-1/T1g-kg*M0a)*M(18)+M0g/T1g;


dM(19)=kh*M0h*M(1)+(-1/T2h-kh*M0a)*M(19)-2*pi*(D-dh)*M(20);

dM(20)=kh*M0h*M(2)+2*pi*(D-dh)*M(19)+(-1/T2h-kh*M0a)*M(20)-w1*M(21);

dM(21)=kh*M0h*M(3)+w1*M(20)+(-1/T1h-kh*M0a)*M(21)+M0h/T1h;


dM(22)=ki*M0i*M(1)+(-1/T2i-ki*M0a)*M(22)-2*pi*(D-di)*M(23);

dM(23)=ki*M0i*M(2)+2*pi*(D-di)*M(22)+(-1/T2i-ki*M0a)*M(23)-w1*M(24);

dM(24)=ki*M0i*M(3)+w1*M(23)+(-1/T1i-ki*M0a)*M(24)+M0i/T1i;


dM(25)=kb*M0b*M(3)+(-Rrfb*M0b-1/T1b-kb*M0a)*M(25)+M0b/T1b;
```

E.2. Execution of the model

```
frame
%% Executes 9 Pool Bloch-McConnell Model
clear all
format long
tic
global  glucoseMolarity num_gauss interpuseDelay duration B0  FlipA gamma ppm ppmb ppmc ppmd ppme ppmf ppmg
     ppmh ppmi M0a M0b M0c M0d M0e M0f M0g M0h M0i   T2a T1a T2b T1b T2c T1c T2d T1d T2e T1e T2f T1f T2g T1g
     T2h T1h T2i T1ikb kc kd ke kf kg kh ki B1eq

gamma=42.576*10^6*2*pi; %[ s-1 T-1]
B0=9.384;
FlipA=540;%1666%1200%793;%793;
num_gauss=118;
interpuseDelay=1*10^-3; % [in s].........
duration=50*10^-3;%.1*10^-3;
ppm=0*1.2; %Rf pulse off resonance frequency from water pool

%% B1eq calculation
nsigma=5.84; %number of sigmas the pulse shape uses. Calculated from shape lib.
% gamma=267.513*10^6; %Gyromagnetic ratio (/s/T)
% FA=input('What is the saturation flip angle (per Gaussian) [degrees]?  ');
FA=FlipA*pi/180; %to radians
Duration=duration
IntDelay=interpuseDelay
sigma=duration/nsigma;

intePercentage=erf(nsigma/sqrt(2));
B1eq=sqrt(FA^2*sqrt(pi)/(2*pi*sigma*gamma^2*(Duration+IntDelay)*intePercentage))

%% Ofset frequency of each pool
ppmc=1.1; %CEST pool off resonance frequency from water pool
ppmd=2;
ppme=2.9;
ppmf=2.1;
ppmg=3.5;
ppmh=-2;
ppmi=-3.15;
ppmb=0;
```

```
%% Initial Pool Concentrations
% 10%glucose=10g/100ml=555mMolar of glucose in h2o
glucoseMolarity=125;%[mMolar]
M0a=1;

M0c=1*glucoseMolarity/(1000*55*1); %Glucose pools
M0d=1*glucoseMolarity/(1000*55*1); %Glucose pools
M0e=1*glucoseMolarity/(1000*55*1); %Glucose pools

M0f=0.003272;%1/611;%AMINE
M0g=0.001472;%1/786;%AMIDE
M0h=0/100;
M0i=M0a/31;%NOE
M0b=M0a/11;%MT %i had it 75

%% exchange rates
pH=7.6;
% AminesEx=10.^(pH-5.2);
AminesEx=10.^(pH-4.5); %At 2ppm
% AmidesEx=5.57*10.^(pH-7.2);
AmidesEx=5.57*10.^(pH-6.4); % At 3.5 ppm
incrfac=0.0025*10.^(pH-4.3)+0.5; %At 2ppm

 kc=700*incrfac;
 kd=2500*incrfac;
 ke=1700*incrfac;

kf=AminesEx;
kg=AmidesEx;
kh=10;
ki=5;%NOE
kb=50;%MT

%% Relaxation times
% T2a=0.04; T1a=1.85;
        T2a=0.06; T1a=2.5;  %% in tumour

T2c=0.006; T1c=1.2;
T2d=0.017; T1d=1.2;
T2e=0.017; T1e=1.2;
        T2c=0.1; T1c=1.2;
        T2d=0.1; T1d=1.2;
        T2e=0.07; T1e=1.2;

T2f=0.0006; T1f=1.1;%Amines
T2g=0.0018; T1g=1.1;%Amides
T2h=0.005; T1h=1;
T2i=0.00042; T1i=1;%NOE
T2b=0.00001; T1b=1;%MT

if B0==3
T2a=0.069; T1a=1.085;
T2c=0.006*1.4; T1c=0.9;
T2d=0.017*1.4; T1d=0.9;
T2e=0.017*1.4; T1e=0.9;
T2f=0.0010*1.4; T1f=0.8;%Amines
T2g=0.0015*1.4; T1g=0.8;%Amides
T2h=0.005*1.4; T1h=0.8;
T2i=0.00042*1.4; T1i=0.8;%NOE
T2b=0.00001*1.4; T1b=0.8;%MT
end

tspan = linspace(0,6,6001);
% M=zeros(64*5000,9);
% T=zeros(64*5000,1);
M0=[0,0,M0a,0,0,M0c,0,0,M0d,0,0,M0e,0,0,M0f,0,0,M0g,0,0,M0h,0,0,M0i,M0b];
ppmrange=4

offsetpoints=51;%77
% options=odeset('MaxStep',0.0001);

t=zeros(numel(tspan),offsetpoints);
M=zeros(numel(tspan),numel(M0),offsetpoints);
 RFppm_array=-ppmrange+(1:offsetpoints-1)*2*ppmrange/(offsetpoints-1); %Rf frequency from water pool
for ii=1:offsetpoints;%81;
    % RFppm_array(ii)=-ppmrange+(ii-1)*2*ppmrange/(offsetpoints-1); %Rf frequency from water pool
```

```
     RFppm=RFppm_array(ii);
%  [t, M] = ode45(@Cool9Pool_Model, tspan, M0,options);
% [t, M] = ode15s(@Cool9Pool_Model, tspan, M0);
 %[t, M ] = ode45(@Cool9Pool_Model, tspan, M0);
 [t(:,ii), M(:,:,ii) ] = ode45(@(t,M) Cool9Pool_Model_28Aug2015(t,M,RFppm), tspan, M0);
ii
end
All_M=M;
t=t(:,1);
offset=1:offsetpoints;
%   ppm=-ppmrange+(offset-1)*2*ppmrange/(offsetpoints-1); %Rf frequency from water pool
dirname='C:\Users\ftorrealda\Dropbox\PhD\'
% filename=(['cool9pool_results_incrfactX2_3T_WM', sprintf('%.2g%',10^6*B1eq),'uT_', sprintf('%.0f%',
     glucoseMolarity), 'Mmglucose']);
filename='DinamicModelResults_2'
fullname=([dirname,filename])
save(fullname,'All_M','t','RFppm_array');
toc
%% Plots
figure,plot(t,squeeze(All_M{offset}(:,3))),title('Mz of Water')
transverseM=squeeze(sqrt(All_M{offset}(:,1).^2+All_M{offset}(:,2).^2));
figure,plot(t,-squeeze(All_M{offset}(:,1))),
hold on, plot(t,-squeeze(All_M{offset}(:,2)),'g')
hold on, plot(t,transverseM,'k')
title('Mx of Water in blue,  My in green, total transverse in black')

t2fit=0

if t2fit==1
%% FIT
%% Fit: 'Observed T2 fit'.
[xData, yData] = prepareCurveData( t, transverseM );

% Set up fittype and options.
ft = fittype( 'exp1' );
ex = excludedata( xData, yData, 'box', [0.001 5 0 1] );
opts = fitoptions( 'Method', 'NonlinearLeastSquares' );
opts.Display = 'Off';
opts.StartPoint = [1.00019005897766 -1.75734781332529];
opts.Exclude = ex;

% Fit model to data.
[fitresult, gof] = fit( xData, yData, ft, opts );

% Plot fit with data.
figure( 'Name', 'Observed T2 fit' );
h = plot( fitresult, xData, yData, ex );
legend( h, 'Transverse M vs. time', 'Excluded points', 'Fitted T2 curve', 'Location', 'NorthEast' );
% Label axes
xlabel( 'Time' );
ylabel( 'Transverse M' );
grid on
hold on
%% ENDOF FIT
end %end of t2fit

clear Mzall Mza
TE=0.002 % TE (in seconds)
for ii=1:offsetpoints
Mzall(ii,:)=(All_M{ii}(:,3)*exp(-TE./T2a)+All_M{ii}(:,6)*exp(-TE./T2c)+All_M{ii}(:,9)*exp(-TE./T2d) + All_M{ii
     }(:,12)*exp(-TE./T2e)+All_M{ii}(:,3)*exp(-TE./T2f) + All_M{ii}(:,15)*exp(-TE./T2g) + All_M{ii}(:,18)*exp
     (-TE./T2h)+All_M{ii}(:,21)*exp(-TE./T2i) + All_M{ii}(:,24)*exp(-TE./T2b) + All_M{ii}(:,25)*exp(-TE./T2a))
      ./(M0a +M0b+ M0c+ M0d+ M0e+ M0f+ M0g+ M0h+ M0i);
Mza(ii,:)=All_M{ii}(:,3);
end
%%%%%%%%%%%%%%%%%%%%%%%%%%%%%%%%%%

normRange=[4 4.5];
normR= [round(normRange(1)*(offsetpoints/2/ppmrange)+offsetpoints/2) : round(normRange(2)*(offsetpoints/2/
     ppmrange)+offsetpoints/2)];
normRi= [offsetpoints-round(normRange(2)*(offsetpoints/2/ppmrange)+offsetpoints/2) : offsetpoints-round(
     normRange(1)*(offsetpoints/2/ppmrange)+offsetpoints/2)];
norm=(mean(Mzall(normR,:))+mean(Mzall(normRi,:)))/2;
Mzall_norm=Mzall./repmat(norm,[offsetpoints,1]);

% ZAsym=flip(ZSpectra(1:round(np/2),:),1)-ZSpectra(round(np/2):np,:);
```

```
%%%%%%%%%%%%%%%%%%%%%%%%%%%%%%%
ppms=linspace(-ppmrange,ppmrange,offsetpoints);
ppms_half=linspace(0,ppmrange,round(offsetpoints/2));

Asym=flip(Mzall_norm(1:round(offsetpoints/2),:),1)-Mzall_norm(round(offsetpoints/2):end,:);
figure,plot(ppms_half,Asym(:,1:1000:end))
A725=Asym;
diff=(A7220-A725);
figure,plot(ppms_half,100*diff(:,300:300:end))

[X,Y]=meshgrid(ppms_half(1:round(offsetpoints/2)),squeeze(tspan(1,1:200:end)));
figure,surfc(X,Y,100*Asym(:,1:200:end)')
 figure,surfc(X,Y,100*(A7220(:,1:200:end)'-A725(:,1:200:end)'))
% figure,surfc(X,Y,100*A6820(:,1:102:end)')
% figure,surfc(X,Y,100*A685(:,1:102:end)')
% [X,Y]=meshgrid(ppms,squeeze(tspan(1,1:102:end)));
% figure,surfc(X,Y,Mzall_norm(:,1:102:end)')
% zlim([-15 20])
% xlim([0 startppm])
% hold on
%  ss=surf(X,Y,100*Asym(:,1:102:end)')
ss=findobj(gca,'Type','surface')
ss.FaceColor = 'interp'
% ss.FaceAlpha = 0.4
ss.LineWidth = 0.1
 ss.LineStyle = '-'
ss.EdgeColor = [0.1 0.1 0.1]%'interp'%[0.2 0.2 0.2]%'none'
hh=gca;
hh.Projection='perspective'
title([{'%MTR_{asym} in time'},{'[glc]=5 mMolar'}])
title('Time evolution of GCE ')
title({'GCE \Delta[glc] = 15 mMolar'})

xlabel('\Delta\omega (ppm)')
ylabel('Time (s)')
zlabel('% MTR_{asymmetry}')
%     zlabel([{'\Delta %MTR_{asymmetry}'},{'(\Delta[glc] = 15 mMolar)'}])
 set(gca,'FontSize',13);%,'fontWeight','bold')
   set(findall(gcf,'type','text'),'FontSize',14,'FontName','Georgia')
% hh.XColor='full'
%  set(gca)
%  shading interp
%%
 figure
[~,h] = contourf(X,Y,100*diff(:,1:200:end)');       %# get handle to contourgroup object
% [~,h] = contourf(X,Y,100*Asym(:,1:200:end)');       %# get handle to contourgroup object
% [~,h] = contourf(X,Y,100*A7220(:,1:200:end)');       %# get handle to contourgroup object

%# change the ZData property of the inner patches
hh = get(h,'Children');    %# get handles to patch objects
% set(hh, {'ZData'}, cellfun(@(X) -10*ones(size(X)), get(hh,{'XData'}), 'UniformOutput',false))
h.ShowText = 'off';
 h.LevelStep = 0.0333;
 h.LineWidth = 0.1

xlabel('\Delta\omega (ppm)')
ylabel('Time (s)')
zlabel('% MTR_{asymmetry}')
% zlim([-10 5])
% xlim([0 ppmrange])
title('%MTR_{asym} in time 20')
set(gca,'FontSize',15);%,'fontWeight','bold')
%              set(findall(gcf,'type','text'),'FontSize',27)
set(findall(gcf,'type','text'),'FontSize',15,'FontName','Georgia')
%%
figure,
for read=1:nreads

    readtime=tspan(1)+read/nreads*timespan; %time at which you want to inspect the magnetizatio
    h=plot(ppms,squeeze(Mzall(:,read)),ppms_half,10*Asym(:,read));
    axis([-ppmrange ppmrange -1 2])
    text(.1,.5,['\fontsize{16} \color[rgb]{0 .5 .5}Saturation lenght ', sprintf('%.1f%', readtime)])
F(read)=getframe;
end

%% DISPLAY ANIMATION
```

```
figure
axis([−6 6 0 1])
movie(F,1)

%% SHOW MTRasym in time
figure
plot (t,M(:,3)/1,'b')%,T,M(:,9)/(0.0054),'m')%,T,M(:,2))
% plot (t,m(:,3)/1,'r',t,m(:,9)/(0.0054),'b')
title('5 sat pulses/readout')
xlabel('t [s]')
ylabel('Mz/M0 water')
```

F. Steady-State 8-Pool Bloch-McConnell model

```
frame
%% Bloch–McConnell Equations.  STEADY STATE solution of an 8 Pool Model
clear all
format long
tic
    inWaterGlucoseSolution=0
    inwhitematter=0 %Otherwise values for white matter are taken.
    ingreymatter=0
    intumour=1
interaction_CD=0; %to add a connection between pools C and D

%% Constants
gamma=42.576*10^6*2*pi; %[Radians s–1 T–1]
B0= 9.384; %T
w0=gamma*B0;
np=301;%77;%;1001;

One_ppm=w0/2/pi*10^–6;
maxmynumMT=2%4; %   MT array
maxmynumNOE=2%; %   NOE array
maxmynumAmine=2%; %   Amines array
maxmynumAmide=2%; %   Amides array

maxmynumpH=4; %   pH array
maxmynumT1=2; %   T1a array
maxmynumT2=2; %   T2a array
maxmynumB1=10; %  B1 array
maxmynumG=3;%    Glucose concentration array
superMM=zeros(22,np,maxmynumG,maxmynumB1,maxmynumT2,maxmynumT1,maxmynumpH,maxmynumAmide,maxmynumAmine,
      maxmynumNOE,maxmynumMT);

for mynumMT=2:maxmynumMT
    mynumMT
for mynumNOE=2:maxmynumNOE
    mynumNOE
for mynumAmine=2:maxmynumAmine
for mynumAmide=2:maxmynumAmide

for mynumpH=4:maxmynumpH
for mynumT1=2:maxmynumT1
for mynumT2=2:maxmynumT2
for mynumB1=1:maxmynumB1
for mynumG=1:maxmynumG
    % B1equivalent for Agilent Gaussian
nsigma=5.84; %number of sigmas the pulse shape uses. Calculated from shape lib.
FAarray=[540,793,1100,1605,2000,3000,4500,6000,9000,12000];
FAarray=[360,540,793,1100,1605,2000,3000,4500,6000,9000];

FA=FAarray(mynumB1);
FA=FA*pi/180; %to radians
% Duration=input('What is duration of the pulse [ms]?  ');
Duration=50;
Duration=Duration/1000; %to secs
% IntDelay=input('Do you have an interpulse delay? How many milli seconds?  ');
IntDelay=1;
IntDelay=IntDelay/1000; %to secs
sigma=Duration/nsigma;
```

```
intePercentage=erf(nsigma/sqrt(2));

B1eq=sqrt(FA^2*sqrt(pi)/(2*pi*sigma*gamma^2*(Duration+IntDelay)*intePercentage));
B1=B1eq;
% B1eqA=10^-6*[1 2 5 9 15];
% B1=B1eqA(mynumB1);
B1array(mynumB1)=B1;
% B1=((mynumB1-1)*1+0.5)*10^-6
%%
w1=gamma*B1;%  %w1 goes in rad/s   whereas delta ,ppmc and exRates in Hz    in the equations delta is
      multiplied by 2pi

%% Pool parameters
%% Relative concentration
M0a=1; %water
proteinConc=90*1;%in mMolar
 glucoseMolarity=5+120*(mynumG-1);%in mMolar
 glucoseMol_array(mynumG)=glucoseMolarity;
%pool sizes
M0b=1*M0a/11; %MT pool
M0b=M0b/2*mynumMT;
    if inwhitematter==1
        M0b=0.14*M0a; %White Matter MT pool
    elseif ingreymatter==1
        M0b=0.06*M0a; %Grey MatterMT pool
%       M0b=0.14*M0a; %Grey MatterMT pool
    end
M0c=2*proteinConc/(1000*55); %Amine
M0c=M0c/2*mynumAmine;

M0d=0.90*proteinConc/(1000*55);%Amide
M0d=M0d/2*mynumAmide;

M0f=1*M0a/31; % NOE
M0f=M0f/2*mynumNOE;
% % % % % % M0e=3*glucoseMolarity/(1000*55)/2; %%Glucose pools
% % % % % % M0g=1*glucoseMolarity/(1000*55)/2; %
% % % % % % M0h=0.2*glucoseMolarity/(1000*55)/2; %
M0e=1*glucoseMolarity/(1000*55)/1; %%Glucose pools
M0g=1*glucoseMolarity/(1000*55)/1; %
M0h=1*glucoseMolarity/(1000*55)/1; %

M0e_array(mynumG)=M0e;
M0g_array(mynumG)=M0g;
M0h_array(mynumG)=M0h;

%% pH
pH=6.5+0.25*(mynumpH-1);
% pH=6.6+(mynumpH-1)*(0.2)
   pH=7.6
pHarray(mynumpH)=pH;
% pHRange(mynumpH,:)=char(['pH ',sprintf( '%.1f%',pH)]);

%%%%%%%%%%%%%%%%%%%%%%%%%%%%%%%%%%%%%%%%%%%%%%%%%%%%%%%%%%%%
%% Relaxation Times of each spin species
% T1s
T1a=1.65+0.2*(mynumT1-1);
T1b=1;%for MT
T1c=1.1;
T1d=1.1;
T1f=1; %for fat or NOE
T1e=1.2; %glucose1
T1g=1.2;%glucose2
T1h=1.2;%glucose3

% T2a=3.2*exp(-M0b*140);%T2a=0.04;
T2a=0.02+0.02*(mynumT2-1);
T2b=0.00001;%for MT*1.8
T2c=0.0006;
T2d=0.0018;
T2f=0.00042;% NOE
T2e=0.1;
T2g=0.1;%
T2h=0.07;%

if intumour==1
```

```
    T1a=2.5;
    T2a=60*10^-3;
end
%%%%%%%%%%%%%%%%%%%%%%%%%%%%%%%%%%%%%%%%%%%%%%%%
%% AT 3T  Relaxation Times
if B0==3
    % T1s
    B0factorT1=0.81;

    T1a=T1a*B0factorT1;%
    T1b=T1b*B0factorT1;%for MT
    T1c=T1c*B0factorT1;
    T1d=T1d*B0factorT1;
    T1f=T1f*B0factorT1; %for fat or NOE
    T1e=T1e*B0factorT1;
    T1g=T1g*B0factorT1;
    T1h=T1h*B0factorT1;
        if inwhitematter==1
            T1a=1.084;
        elseif ingreymatter==1
            T1a=1.820;
        elseif intumour==1
            T1a=2.5;
        end
    % T2s
    B0factorT2=1.9;

    T2a=T2a*B0factorT2;
    T2b=T2b*B0factorT2;%for MT*1.8
    T2c=T2c*B0factorT2;
    T2d=T2d*B0factorT2;
    T2f=T2f*B0factorT2;% NOE
    T2e=T2e*B0factorT2;
    T2g=T2g*B0factorT2;%
    T2h=T2h*B0factorT2;%
     if inwhitematter==1
            T2a=69*10^-3;
     elseif ingreymatter==1
            T2a=99*10^-3;
     elseif intumour==1
            T2a=140*10^-3;
     end
end
%%%%%%%%%%%%%%%%%%%%%%
T2array(mynumT2)=T2a;
T1array(mynumT1)=T1a;

%% Resonant frequencies from water
ppmb=0*-3.5;
ppmc=+2.1; %AMINE
ppmd=3.5; % AMIDE
ppmf=-3.15;%-3.2; NOE

ppme=1.1;
ppmg=2;
ppmh=2.9;
%% Tranfer rates
% K0=0;Ka=25;Kb=1.2*10^10;pKw=14; % values that allow lower exchange rates for acidic environments
% K0=1000;Ka=25;Kb=0.7*10^10;pKw=14; % values that match Chan, van Zijl MRM2012
% KexG=K0+Ka*10.^(-pH)+Kb*10.^(pH-pKw);
% Rb=50;   %fot MT
% Rc=KexG*0.55;  %s^(-1)
% Rd=KexG*0.75;

%from pH mapping based on the ratiometric amide and amine relationship from
%endogenous CEST  Kim Desmond1, Greg Stanisz 1,2
% pH=[6.4 6.7 7 7.3]
AminesEx=10.^(pH-5.2);
AminesEx=0.5*10.^(pH-4.5); %At 2ppm
    AminesEx=10.^(pH-4.5); %At 2ppm  FROM THE COOL9POOL model

AmidesEx=5.57*10.^(pH-7.2);
AmidesEx=5.57*10.^(pH-6.4); % At 3.5 ppm

Rc=1*AminesEx;
Rd=1*AmidesEx;
```

```
Rf=5; %for fat or NOE
Rb=50; %MT

% incrfac=2;
incrfac=0.0025*10.^(pH-4.3)+0.5; %At 2ppm
%  Re=935*incrfac;
%  Rg=1700*incrfac;
%  Rh=1250*incrfac;
%
 Re=700*incrfac;%700
 Rg=2500*incrfac; %4000
 Rh=1700*incrfac; %1700

%Pool sizes taking the saturation efficency into account.
PUT_SAT_EFFIENCIENCY=0;

 if PUT_SAT_EFFIENCIENCY==1
% alphab=w1^2/(w1^2+Rb^2);
alphac=w1^2/(w1^2+Rc^2);
alphad=w1^2/(w1^2+Rd^2);
alphae=w1^2/(w1^2+Re^2);
alphaf=w1^2/(w1^2+Rf^2);
alphag=w1^2/(w1^2+Rg^2);
alphah=w1^2/(w1^2+Rh^2);

%%New Saturation efficiecy to account for relaxation in XY plane
% alphab=w1^2/(w1^2+Rb^2*T2b);%%%%%%%%%%%%%%%%%%%%%%% You might want to use the previous one
alphac=w1^2/(w1^2+Rc^2*T2c);%%%%%%%%%%%%%%%%%%%%%%% You might want to use the previous one
alphad=w1^2/(w1^2+Rd^2*T2d);%%%%%%%%%%%%%%%%%%%%%%% You might want to use the previous one
alphae=w1^2/(w1^2+Re^2*T2e);%%%%%%%%%%%%%%%%%%%%%%% You might want to use the previous one
alphaf=w1^2/(w1^2+Rf^2*T2f);%%%%%%%%%%%%%%%%%%%%%%% You might want to use the previous one
alphag=w1^2/(w1^2+Rg^2*T2g);%%%%%%%%%%%%%%%%%%%%%%% You might want to use the previous one
alphah=w1^2/(w1^2+Rh^2*T2h);%%%%%%%%%%%%%%%%%%%%%%% You might want to use the previous one
%%Endof New Saturation efficiecy to account for relaxation in XY plane

% M0b=M0b*alphab;
M0c=M0c*alphac;
M0d=M0d*alphad;
M0e=M0e*alphae;
M0f=M0f*alphaf;
M0g=M0g*alphag;
M0h=M0h*alphah;
 end

%  Rcd=abs(AmidesEx-AminesEx)./(AmidesEx+AminesEx)/4/(1-abs(1-M0d/M0c));
%  Rinteract=20*M0a./(M0d+M0c).*Rcd;
  Rinteract=5000 ;%pH independent. For NH2 to NH exchange rate [H+] not important inside the protein structure
       .  can it be??

%% %%%%%%%%%%%%%%%%%%%%%%%%%%
%% IF PHANTOM
if inWaterGlucoseSolution==1 && B0>9 && B0<10

ppme=1.2;
ppmg=2.1;
ppmh=2.88;

M0b=0;
M0c=0;
M0d=0;
M0f=0;

    T1a=5;
    T2a=0.08;

    T1e=1.2;
    T1g=1.2;
    T1h=1.2;

    T2e=0.1;
    T2g=0.1;%
    T2h=0.1;%
    factor=1
 Re=700*factor;%700
 Rg=2500*factor; %4000
 Rh=1700*factor; %1700
```

```
end
%%
dcb=w0*10^-6/(2*pi)*ppmb;
dcc=w0*10^-6/(2*pi)*ppmc;
dcd=w0*10^-6/(2*pi)*ppmd;
dce=w0*10^-6/(2*pi)*ppme;
dcf=w0*10^-6/(2*pi)*ppmf;
dcg=w0*10^-6/(2*pi)*ppmg;
dch=w0*10^-6/(2*pi)*ppmh;

%for the cone picture
% wrf=w0*(1+ppm*10^-6);
% B0eff=(w0-wrf)/gamma; %in Z direction
%Beff=[B1,0,B0eff];
%%%%%%%%%%%%%%%%%%%%%%%%%%%%%%%%%%%%%%%%%%%%%%%%%%%%%%%%%%%%%%%%%%%%%%%%%%%%%%%%
MM=zeros(22,np);
Rrfb=zeros(1,np);
 D=zeros(1,np);
 ppm=zeros(1,np);
 maxoffsetppm=6;
 ppms=linspace(-maxoffsetppm,maxoffsetppm,np);
%   ppms=logspace(0,5,np);
for p=1:np
% ppm=2*maxoffsetppm/(np-1)*(p-1)-maxoffsetppm;
ppm=ppms(p);
D=w0*10^-6/(2*pi)*ppm;
% ppm(p)=ppm;
%% Superlorentzian function
q=10000;
o = linspace(0, pi/2, q);
% value=sin(o).*(2/pi).^0.5*T2b./abs(3*cos(o).^2-1).*exp(-2*(2*pi*(D-dcb).*T2b./(abs(3*cos(o).^2-1))).^2); % -
      dcb added to shift the mt pool
  value=sin(o).*(2/pi).^0.5*T2b./abs(3*cos(o).^2-1).*exp(-2*((D-dcb).*T2b./(abs(3*cos(o).^2-1))).^2); % -dcb
        added to shift the mt pool
da=pi/(2*(q-1)).*value;
Amt=sum(da); %superlorentzian function for every D
Rrfb=Amt*w1^2*pi; %Rrfb(1,p)=1*Amt*w1^2; not sure if we have to multiply by w1^2

Rrfb_all(p)=Rrfb;

 %% 8 pool system

%% Tranfer rates
Rbp=Rb;%Rb; %fot MT
Rcp=Rc;%s^(-1)
Rdp=Rd;
Rep=Re;
Rfp=Rf;
Rgp=Rg;
Rhp=Rh;

dm1=[(-1/T2a-Rc*M0c-Rd*M0d-Re*M0e-Rf*M0f-Rg*M0g-Rh*M0h),-2*pi*D,0,0,Rc*M0a,0,0,Rd*M0a,0,0,Re*M0a,0,0,Rf*M0a
      ,0,0,Rg*M0a,0,0,Rh*M0a,0,0];
dm2=[2*pi*D,(-1/T2a-Rc*M0c-Rd*M0d-Re*M0e-Rf*M0f-Rg*M0g-Rh*M0h),-w1,0,0,Rc*M0a,0,0,Rd*M0a,0,0,Re*M0a,0,0,Rf*M0a
      ,0,0,Rg*M0a,0,0,Rh*M0a,0];
dm3=[0,w1,(-1/T1a-Rbp*M0b-Rcp*M0c-Rdp*M0d-Rep*M0e-Rf*M0f-Rg*M0g-Rh*M0h),Rbp*M0a,0,0,Rcp*M0a,0,0,Rdp*M0a,0,0,
      Rep*M0a,0,0,Rfp*M0a,0,0,Rgp*M0a,0,0,Rhp*M0a];

dm6=[0,0,Rbp*M0b,(-1/T1b-Rrfb*M0b-Rbp*M0a),0,0,0,0,0,0,0,0,0,0,0,0,0,0,0,0,0];

if interaction_CD==1   %   Interaction between Pool C and Pool D

dm7=[Rc*M0c,0,0,0,(-1/T2c-Rc*M0a-Rinteract*M0d),-2*pi*(D-dcc),0,Rinteract*M0c,0,0,0,0,0,0,0,0,0,0,0,0,0];
dm8=[0,Rc*M0c,0,0,2*pi*(D-dcc),(-1/T2c-Rc*M0a-Rinteract*M0d),-w1,0,Rinteract*M0c,0,0,0,0,0,0,0,0,0,0,0,0];
dm9=[0,0,Rcp*M0c,0,0,w1,(-1/T1c-Rcp*M0a-Rinteract*M0d),0,0,Rinteract*M0c,0,0,0,0,0,0,0,0,0,0,0,0];


dm10=[Rd*M0d,0,0,0,Rinteract*M0d,0,0,(-1/T2d-Rd*M0a-Rinteract*M0c),-2*pi*(D-dcd),0,0,0,0,0,0,0,0,0,0,0,0];
dm11=[0,Rd*M0d,0,0,0,Rinteract*M0d,0,2*pi*(D-dcd),(-1/T2d-Rd*M0a-Rinteract*M0c),-w1,0,0,0,0,0,0,0,0,0,0,0,0];
dm12=[0,0,Rdp*M0d,0,0,0,Rinteract*M0d,0,w1,(-1/T1d-Rdp*M0a-Rinteract*M0c),0,0,0,0,0,0,0,0,0,0,0,0];
else

dm7=[Rc*M0c,0,0,0,(-1/T2c-Rc*M0a),-2*pi*(D-dcc),0,0,0,0,0,0,0,0,0,0,0,0,0,0,0];
dm8=[0,Rc*M0c,0,0,2*pi*(D-dcc),(-1/T2c-Rc*M0a),-w1,0,0,0,0,0,0,0,0,0,0,0,0,0,0];
dm9=[0,0,Rcp*M0c,0,0,w1,(-1/T1c-Rcp*M0a),0,0,0,0,0,0,0,0,0,0,0,0,0,0];
```

```
dm10=[Rd*M0d,0,0,0,0,0,0,(−1/T2d−Rd*M0a),−2*pi*(D−dcd),0,0,0,0,0,0,0,0,0,0,0,0,0];
dm11=[0,Rd*M0d,0,0,0,0,0,2*pi*(D−dcd),(−1/T2d−Rd*M0a),−w1,0,0,0,0,0,0,0,0,0,0,0,0];
dm12=[0,0,Rdp*M0d,0,0,0,0,0,w1,(−1/T1d−Rdp*M0a),0,0,0,0,0,0,0,0,0,0,0,0];
end
                %   ENDOF Interaction between Pool C and Pool D

dm13=[Re*M0e,0,0,0,0,0,0,0,0,0,(−1/T2e−Re*M0a),−2*pi*(D−dce),0,0,0,0,0,0,0,0,0,0];
dm14=[0,Re*M0e,0,0,0,0,0,0,0,0,2*pi*(D−dce),(−1/T2e−Re*M0a),−w1,0,0,0,0,0,0,0,0,0];
dm15=[0,0,Rep*M0e,0,0,0,0,0,0,0,0,w1,(−1/T1e−Rep*M0a),0,0,0,0,0,0,0,0,0];


dm16=[Rf*M0f,0,0,0,0,0,0,0,0,0,0,0,0,(−1/T2f−Rf*M0a),−2*pi*(D−dcf),0,0,0,0,0,0,0];
dm17=[0,Rf*M0f,0,0,0,0,0,0,0,0,0,0,0,2*pi*(D−dcf),(−1/T2f−Rf*M0a),−w1,0,0,0,0,0,0];
dm18=[0,0,Rfp*M0f,0,0,0,0,0,0,0,0,0,0,0,w1,(−1/T1f−Rfp*M0a),0,0,0,0,0,0];


dm19=[Rg*M0g,0,0,0,0,0,0,0,0,0,0,0,0,0,0,0,(−1/T2g−Rg*M0a),−2*pi*(D−dcg),0,0,0,0];
dm20=[0,Rg*M0g,0,0,0,0,0,0,0,0,0,0,0,0,0,0,2*pi*(D−dcg),(−1/T2g−Rg*M0a),−w1,0,0,0];
dm21=[0,0,Rgp*M0g,0,0,0,0,0,0,0,0,0,0,0,0,0,0,w1,(−1/T1g−Rgp*M0a),0,0,0];


dm22=[Rh*M0h,0,0,0,0,0,0,0,0,0,0,0,0,0,0,0,0,0,0,(−1/T2h−Rh*M0a),−2*pi*(D−dch),0];
dm23=[0,Rh*M0h,0,0,0,0,0,0,0,0,0,0,0,0,0,0,0,0,0,2*pi*(D−dch),(−1/T2h−Rh*M0a),−w1];
dm24=[0,0,Rhp*M0h,0,0,0,0,0,0,0,0,0,0,0,0,0,0,0,0,0,w1,(−1/T1h−Rhp*M0a)];
%%%%%%%%%%%%%%%%%%%%%%%%%%%%%%%%%%%%%%%%%%%%%%%%%%%%%%%%%%%%%%%%%%%%%%%%%%%%%%%%%%%%%

%% Put into a matrix
A=[dm1;dm2;dm3;dm6;dm7;dm8;dm9;dm10;dm11;dm12;dm13;dm14;dm15;dm16;dm17;dm18;dm19;dm20;dm21;dm22;dm23;dm24];
B=[0;0;M0a/T1a;M0b/T1b;0;0;M0c/T1c;0;0;M0d/T1d;0;0;M0e/T1e;0;0;M0f/T1f;0;0;M0g/T1g;0;0;M0h/T1h];

M=A\(−B);  %look "matrix division"
MM(:,p)=M;

end

superMM(:,:,mynumG,mynumB1,mynumT2,mynumT1,mynumpH,mynumAmide,mynumAmine,mynumNOE,mynumMT)=MM;
end
end
end
end
end

end
end
end
end

%% Signal attenuation with T2
T2=[T2a,T2b,T2c,T2d,T2e,T2f,T2g,T2h];
% AllMz=cat(3,squeeze(superMM(3,:,:,1,1)),squeeze(superMM(4,:,:,1,1)),squeeze(superMM(7,:,:,1,1)),squeeze(
      superMM(10,:,:,1,1)),squeeze(superMM(13,:,:,1,1)),squeeze(superMM(16,:,:,1,1)),squeeze(superMM
      (19,:,:,1,1)));
clear AllMz
AllMz=cat(ndims(superMM),squeeze(superMM(3,:,:,:,:,:,:,:,:,:,:,:)),squeeze(superMM
      (4,:,:,:,:,:,:,:,:,:,:,:)),squeeze(superMM(7,:,:,:,:,:,:,:,:,:,:,:)),squeeze(superMM
      (10,:,:,:,:,:,:,:,:,:,:,:)),squeeze(superMM(13,:,:,:,:,:,:,:,:,:,:,:)),squeeze(superMM
      (16,:,:,:,:,:,:,:,:,:,:,:)),squeeze(superMM(19,:,:,:,:,:,:,:,:,:,:,:)),squeeze(superMM
      (22,:,:,:,:,:,:,:,:,:,:,:)));

TE=0.002;
if B0==3
    TE=0.007;
end

T2DECAY=exp(−TE./T2)';
tosize=size(AllMz);
tosize=tosize(1:end−1);
T2DECAY=repmat(T2DECAY,[1 tosize]);
T2DECAY = shiftdim(T2DECAY,1);
T2DECAY=reshape(T2DECAY,size(AllMz));

M0=[M0a,M0b,M0c,M0d,M0e,M0f,M0g,M0h];
M0_mat=repmat(M0', [1,3]);
M0_mat(5,:)=M0e_array; M0_mat(7,:)=M0g_array; M0_mat(8,:)=M0h_array;
M0_mat = sum(M0_mat,1);
```

```
thesize=size(AllMz);
Norm_M0 = repmat(M0_mat', [1, thesize(1),thesize(3:end-1)]);
Norm_M0=permute(Norm_M0, [2,1,3,4,5,6,7,8,9,10,11,12]);

ZSpectraR_pure=nansum(AllMz.*T2DECAY,ndims(superMM));%./Norm_M0;
ZSpectraR_pure=reshape(ZSpectraR_pure,[thesize(1:end-1)]);
% clear AllMz T2DECAY Norm_M0 superMM Norm_M0
%  ZSpectraR=sum(AllMz,3)/sum(M0);
%  ZSpectraR=squeeze(superMM(3,:,:,1,1));

%% ADD NOISE
rawNoiseAmp=0.00/100*mean(M0_mat); %Amplidtude of the raw noise
rawNoise=rawNoiseAmp*randn(size(ZSpectraR_pure));%typically in our scans 300/12000

phyN=zeros(1,np);
phyamp=0*1/100*mean(M0_mat); %Amplidtude of the physiological noise
phyfrequency=70/100;
rnN=rand(size(ZSpectraR_pure));
rnN(rnN>phyfrequency)=0;
phyNoise=phyamp*rnN.*(randn(size(ZSpectraR_pure))-1);

ZSpectraR=abs(rawNoise+ZSpectraR_pure.*(1+phyNoise));
clear phyNoise phyN rnN rawNoise T2DECAY
%% NORMALISE
NormalisedAtM0=1
if NormalisedAtM0==1%dont change this
    Size_1freq=size(ZSpectraR);
    Size_1freq=[1,Size_1freq(2:end)];
    norm=mean(M0_mat)*ones(Size_1freq);
    ZSpectra=ZSpectraR./repmat(norm,[np,1]);

else
    normRange=[4.3 4.5];
    normRange=[2 3];

    normR=[round(normRange(1)*(np/2/maxoffsetppm)+np/2):round(normRange(2)*(np/2/maxoffsetppm)+np/2)];
    % normRi=[np-round(normRange(2)*(np/2/maxoffsetppm)+np/2):np-round(normRange(1)*(np/2/maxoffsetppm)+np/2)
        ];
    norm=(mean(ZSpectraR_pure(normR,:,:,:,:,:,:,:,:,:)));%+mean(ZSpectraR_pure(normRi,:,:,:,:,:,:,:,:,:)))
        /2;

    ZSpectra=ZSpectraR./repmat(norm,[np,1]);
end
%% Select what power, pH... to plot
whatpower = 6;   whatpH    = 4;
whatT2    = 2;   whatT1    = 2;
whatAmide = 2;   whatAmine = 2;
whatNOE   = 2;   whatMT    = 2;

ZSpectra_plot=ZSpectra(:,:,whatpower,whatT2,whatT1,whatpH,whatAmide,whatAmine,whatNOE,whatMT);
ZAsym=flip(ZSpectra_plot(1:round(np/2),:,:,:,:,:,:,:,:,:),1)-ZSpectra_plot(round(np/2):np
    ,:,:,:,:,:,:,:,:,:);
% sprintf('%.1f%',B1eq*10^6)
figure
subplot(3,1,1),titl=[{'Glucose increase \it{in vivo} \rm\bfconditions'},{['B1=',sprintf('%.1f%',B1array(
    whatpower)*10^6),'\muT']}];
title(titl), hold on
plot(ppms,squeeze(ZSpectra_plot),'LineWidth',1),legend('5 mM','15 mM','25 mM','Location','southwest'),legend('
    boxoff')
ylabel('Z-Spectra')
    set(gca, 'xdir','reverse')
%       axis([-1.5 4 0.6 1.01])
xlim([-1.5 4])
subplot(3,1,2)
plot(ppms(round(np/2):end),100*squeeze(ZAsym),'LineWidth',1),hold on,
ylabel('%MTR_A_s_y_m')
    set(gca, 'xdir','reverse')
      axis([0 4 -8 5])
legend('5 mM','15 mM','25 mM','Location','northwest'),legend('boxoff')
subplot(3,1,3)
plot(ppms(round(np/2):end),100*(ZAsym(:,3)-ZAsym(:,1)),'g'),hold on,
plot(ppms(round(np/2):end),100*(ZAsym(:,2)-ZAsym(:,1)),'Color',[0.1,0.4,0.6],'LineWidth',1)
    set(gca, 'xdir','reverse')
     axis([0 4 0 7])
hold on,
ylabel([{'%MTR_A_s_y_m'},{'difference'}])
```

```
xlabel('Frequency (ppm)')
legend('\Delta [glc] 20 mM','\Delta [glc] 10 mM','Location','northwest'),legend('boxon')
set(gca, 'LooseInset', get(gca,'TightInset'))
legend('boxoff')
             set(gca,'FontSize',13);%,'fontWeight','bold')
%              set(findall(gcf,'type','text'),'FontSize',27)
               set(findall(gcf,'type','text'),'FontSize',15,'FontName','Georgia')
figurename=(['C:\Users\ftorrealda\Dropbox\1_FiguresPhD\simulations\','NOISYglucosechange_',sprintf('%.2g%'
      ,10^6*B1array(whatpower)),'uT']);
figurename = strrep(figurename, '.', '');
%                 saveas(gcf,figurename,'fig')
%                 saveas(gcf,figurename,'png')
%                  close
%%%%%%
%%  MTRex
plotMTRex=0;
if plotMTRex==1

MTrex=-1./flip(ZSpectra_plot(1:round(np/2),:,:,:,:),1)+1./ZSpectra_plot(round(np/2):np,:,:,:,:);
% sprintf('%.1f%',B1eq*10^6)
figure
subplot(3,1,1),titl=[{'Glucose increase \it{in vivo} \rm\bfconditions'},{['B1=',sprintf('%.1f%',B1array(
      whatpower)*10^6),'\muT']}];
title(titl), hold on
plot(ppms,squeeze(ZSpectra_plot),'LineWidth',1),legend('5 mM','15 mM','25 mM','Location','southwest'),legend('
      boxoff')
ylabel('Z-Spectra')
     set(gca, 'xdir','reverse')
%        axis([-1.5 4 0.6 1.01])
xlim([-1.5 4]);
subplot(3,1,2)
plot(ppms(round(np/2):end),100*squeeze(MTrex),'LineWidth',1),hold on,
ylabel('%MT_{Rex}')
     set(gca, 'xdir','reverse')
       axis([0 4 -8 5])
legend('5 mM','15 mM','25 mM','Location','northwest'),legend('boxoff')

subplot(3,1,3)
plot(ppms(round(np/2):end),100*(MTrex(:,3)-MTrex(:,1)),'g'),hold on,
plot(ppms(round(np/2):end),100*(MTrex(:,2)-MTrex(:,1)),'Color',[0.1,0.4,0.6],'LineWidth',1)
     set(gca, 'xdir','reverse')
      axis([0 4 0 7])
hold on,
ylabel([{'%MT_{Rex}'},{'difference'}])
xlabel('Frequency (ppm)')
legend('\Delta [glc] 20 mM','\Delta [glc] 10 mM','Location','northwest'),legend('boxon')
set(gca, 'LooseInset', get(gca,'TightInset'))
legend('boxoff')
             set(gca,'FontSize',13);%,'fontWeight','bold')
%              set(findall(gcf,'type','text'),'FontSize',27)
               set(findall(gcf,'type','text'),'FontSize',15,'FontName','Georgia')
figurename=(['C:\Users\ftorrealda\Dropbox\1_FiguresPhD\simulations\','MTRex_NOISYglucosechange_',sprintf('%.2g
      %',10^6*B1array(whatpower)),'uT']);
figurename = strrep(figurename, '.', '');
%                 saveas(gcf,figurename,'fig')
%                 saveas(gcf,figurename,'png')
%                  close
end
%% BiggerErroratHighPower
runErroratHighPower=1;

if runErroratHighPower==1
    NumRepetitions=5 % Calculates the standard error based on how many cest measurements you have.
Nleves=[1 1/2.5 1/10 1/100];
% Nleves=[0.1 0.5 2.5 10];
figure
mycolor={'-r','-y','-g','-b','k'}
clear actualNoiseamp
for ii=1:4
ZSpectra_pure_n=ZSpectraR_pure./repmat(norm,[np,1]);
%   ZSpectra_pure_n=-1./ZSpectra_pure_n; %To Show MTRex instead of MTRasym (in the GCE vs Power and Noise
      graph)
ZS= squeeze(ZSpectra_pure_n(:,2,:,whatT2,whatT1,whatpH,whatAmide,whatAmine,whatNOE,whatMT) - ZSpectra_pure_n
      (:,1,:,whatT2,whatT1,whatpH,whatAmide,whatAmine,whatNOE,whatMT));
ZAsym= flip(ZS(1:round(np/2),:,:,:,:),1)-ZS(round(np/2):np,:,:,:,:);
```

```
intRange=[2 3];
intRangeR=[round(intRange(1)*(np/2/maxoffsetppm)+np/2):round(intRange(2)*(np/2/maxoffsetppm)+np/2)];
intRangeRh=[round(intRange(1)*(np/2/maxoffsetppm)+np/2):round(intRange(2)*(np/2/maxoffsetppm)+np/2)] -round(np
    /2)+1;

IntMean=mean(ZAsym(intRangeRh,:),1);
actualNoiseamp(ii)=rawNoiseAmp*Nleves(ii);

Err_sigma=(actualNoiseamp(ii)./squeeze(norm(1,1,:,whatT2,whatT1,whatpH,whatAmide,whatAmine,whatNOE,whatMT)));
Err_sigma=sqrt(2)*sqrt(2)*Err_sigma; %sqrt(2)*sqrt(2)* to account for substraction of Left and Right sides +
    the same for 2 glucose concentrations
SEM=Err_sigma/sqrt(NumRepetitions*numel(intRangeRh));
SEM_post_processed=Err_sigma/sqrt(9*3*NumRepetitions*numel(intRangeRh));

hold on,shadedErrorBar_new(B1array*10^6,100*IntMean,100*SEM,mycolor{ii})
end

bestPoint=IntMean'./SEM;
bestPoint=0.1*bestPoint/max(bestPoint);
hold on,plot(B1array*10^6,bestPoint,mycolor{5})

ylabel([{'\Delta %MTR_A_s_y_m'},{'from 5 to 15 mM glucose'}])
xlabel('Saturation Power (\muT)')
% legend('\Delta 10 mM','\Delta 20 mM','Location','northwest'),legend('boxoff')
 title([{'Sensitivity of GCE vs B1 power \itin vivo\rm\bf conditions'},{['Integration range from ',sprintf('
     %.1f%',intRange(1)), ' to ',sprintf('%.1f%',intRange(2)),' ppm']}])
legend(['SNR=',sprintf('%.0f%',1/actualNoiseamp(1))], ['SNR=',sprintf('%.0f%',1/actualNoiseamp(2))] ,['SNR=',
    sprintf('%.0f%',1/actualNoiseamp(3))], ['SNR=',sprintf('%.0f%',1/actualNoiseamp(4))] ,['GCE/SE'], '
    Location','best','FontName','Georgia')
   set(gca,'FontSize',13);%,'fontWeight','bold')
   set(findall(gcf,'type','text'),'FontSize',14,'FontName','Georgia')
figurename=(['C:\Users\ftorrealda\Dropbox\1_FiguresPhD\simulations\','GCEvsB1power',sprintf('%.1f%',intRange
    (1)), 'to',sprintf('%.1f%',intRange(2))]);
if B0==3
    figurename=(['C:\Users\ftorrealda\Dropbox\1_FiguresPhD\simulations\','At3T_GCEvsB1power',sprintf('%.1f%',
        intRange(1)), 'to',sprintf('%.1f%',intRange(2))]);
end
figurename = strrep(figurename, '.', '')
axis([10^6*B1array(1),10^6*B1array(end),-0.1,1.6])
 set(gca,'TickDir','out','TickLabelInterpreter','latex')
%     saveas(gcf,figurename,'fig')
%     saveas(gcf,figurename,'png')
end

%% Calculation of best B1 power
ZS_all=squeeze(ZSpectra_pure_n(:,2,:,:,:,:,:,:,:,:)-ZSpectra_pure_n(:,1,:,:,:,:,:,:,:,:));
ZAsym_all=flip(ZS_all(1:round(np/2),:,:,:,:,:,:,:,:),1)-ZS_all(round(np/2):np,:,:,:,:,:,:,:,:);
ppms_h=ppms(round(np/2):end);

actualNoiseamp=rawNoiseAmp;
Err_all=2*(actualNoiseamp./squeeze(norm(1,1,:,:,:,:,:,:,:,:)));
SEM_all=Err_all/sqrt(NumRepetitions);
SEM_mat(1,:,:,:,:,:,:,:,:,:,:)=SEM_all;
ZAsym_all1=ZAsym_all./repmat(SEM_mat, size(ZAsym_all,1),1,1,1,1,1,1,1,1,1,1,1);

% % % Plot GCE/SEM vs B1 vs ppm    at diferent T2s
% for ii=1:numel(T2array)
%     whatT2=ii;
% GCE_SEM=squeeze(ZAsym_all1(:,:,whatT2,whatT1,whatpH,whatAmide,whatAmine,whatNOE,whatMT));
%    figure,contourf(B1array*10^6,ppms_h,GCE_SEM)
%    ylabel('\Delta\Omega [ppm]'); zlabel('GCE/SEM'); xlabel('B1  [\muT]')
% title(['T2=',sprintf('%.0f%','T2array(whatT2)'), 'ms'])
% % % end

 %endof Plot GCE/SEM vs B1 vs ppm
%% Contour Plots
 do_contour=0
 if do_contour==1

[~,best_B1]=max(ZAsym_all1,[],2);
best_B1=squeeze(best_B1);
best_B1array=B1array(best_B1);

   ppm_t2_b1=best_B1array(:,:,whatT1,whatpH,whatAmide,whatAmine,whatNOE,whatMT); %[Freqs and T2s,:,:,:]
   figure,contour(T2array*10^3 ,ppms_h,ppm_t2_b1*10^6,'levellist',B1array(1:2:end)*10^6,'showtext','off'),
        colormap('jet')
```

```
   ylabel('\Delta\Omega [ppm]'); xlabel('T2 [ms]'); zlabel('B1  [\muT]')
    title('Surface of maximal GCE/SEM')

% intRange=[3 3];
intRangeR=[round(intRange(1)*(np/2/maxoffsetppm)+np/2):round(intRange(2)*(np/2/maxoffsetppm)+np/2)];
intRangeRh=[round(intRange(1)*(np/2/maxoffsetppm)+np/2):round(intRange(2)*(np/2/maxoffsetppm)+np/2)] -round(np
     /2)+1;

IntMean_all=squeeze(mean(ZAsym_all1(intRangeRh,:,:,:,:,:,:,:),1));
% actualNoiseamp=rawNoiseAmp;
% Err_all=2*(actualNoiseamp./squeeze(norm(1,1,:,:,:,:,:,:,:,:)));
% SEM_all=Err_all/sqrt(NumRepetitions*numel(intRangeRh));

% bestPoint=IntMean_all./SEM_all;
% bestPoint=0.1*bestPoint./repmat(max(bestPoint,[],1), maxmynumB1, 1,1,1,1,1,1,1);
% [~, pbp]=max(bestPoint, [], 1);
% pbp=squeeze(pbp);
% BpT2=pbp(:,whatT1,whatpH,whatAmide,whatAmine,whatNOE,whatMT);
% for bb=1:numel(BpT2)
%     B1T2(bb)=B1array(BpT2(bb));
% end
% figure, plot(T2array*10^3, B1T2*10^6)
% xlabel('T2 [ms]'); ylabel('B1 [uT]')

%% Calculation of the min CNR for GCE detection
SNRarray=[900,1000,1200,1600,2000,2500,3000,4000,5000];
SNRarray=[70 80 95 120 150 200 250 400 700 1000];
Noisearray=1./SNRarray;
SensMap=zeros(size(ZAsym_all,1),size(ZAsym_all,3));
GCEideal=zeros(size(ZAsym_all,1),size(ZAsym_all,3));
Err_min=zeros(size(ZAsym_all,1),size(ZAsym_all,3));
SensMapA=zeros(size(ZAsym_all,1),size(ZAsym_all,3),numel(SNRarray));
for ii=1:numel(SNRarray)
   Noise=Noisearray(ii);
Err_all=2*(Noise./squeeze(norm(1,1,:,:,:,:,:,:,:,:)));

Err_rep=Err_all(:,:,whatT1,whatpH,whatAmide,whatAmine,whatNOE,whatMT);
ZAsym_rep=ZAsym_all(:,:,:,whatT1,whatpH,whatAmide,whatAmine,whatNOE,whatMT);
 NumRepetitions=1;
SEM_rep=Err_rep/sqrt(NumRepetitions);
for ippm=1:numel(ppms_h)
    for jT2=1:numel(T2array)
       [~,B1pos]=find(B1array == ppm_t2_b1(ippm,jT2));
        GCEideal(ippm,jT2)=ZAsym_rep(ippm,B1pos,jT2);
        Err_min(ippm,jT2)=SEM_rep(B1pos,jT2);
    end
end
MinDiff=GCEideal-Err_min;
ppp=MinDiff>0;

% SensMap=SensMap+ppp*SNRarray(ii);
% SensMap(SensMap~=SNRarray(ii))=0;
% SensMapA(:,:,ii)=SensMap;
SensMapA(:,:,ii)=ppp
% figure, surf(T2array*10^3,ppms_h,MinDiff),caxis([-0.00001,0.00001])
end
SensMapS=sum(SensMapA,3);

for ii=1:numel(SNRarray)
SensMapS(SensMapS==ii)=SNRarray(numel(SNRarray)+1-ii);
end
% figure,surf(SensMapS)
figure,contourf(T2array*10^3,ppms_h,SensMapS,'levellist',SNRarray,'showtext','on')
ylabel('\Delta\Omega [ppm]'); xlabel('T2 [ms]'); zlabel('GCE-\sigma')
title('Signal detection threshold (CI=95%) for 10 mMolar glucose increase.    SNR ')

end
%%   APT peak Calculations
APTpeakCalculations=0;

if APTpeakCalculations==1
measureAtppm=3.5
dd=measureAtppm-ppmS
dfrac=dd/ppmGap

SPoint=round(np*(maxoffsetppm+ppmS)/(2*maxoffsetppm))
```

```
EPoint=round(np*(maxoffsetppm+ppmE)/(2*maxoffsetppm))
measuredPoint=round(np*(maxoffsetppm+measureAtppm)/(2*maxoffsetppm))

ValueLine=ZSpectra(SPoint,:)+dfrac*(ZSpectra(EPoint,:)-ZSpectra(SPoint,:))
Valuemeasured=ZSpectra(measuredPoint,:)

APTp=ValueLine-Valuemeasured
figure,plot(APTp,pHarray)
end
%% PLOT MTR asym
ZSpectra_plot2=squeeze(ZSpectra(:,:,:,whatT2,whatT1,whatpH,whatAmide,whatAmine,whatNOE,whatMT));
%   ZSpectra_pure_n=-1./ZSpectra_pure_n; %To Show MTRex instead of MTRasym (in the GCE vs Power and Noise
      graph)
ZAsym=flip(ZSpectra_plot2(1:round(np/2),:,:,:,:,:,:,:,:,1)-ZSpectra_plot2(round(np/2):np,:,:,:,:,:,:,:,:)
      ;

Dg1=glucoseMol_array(2)-glucoseMol_array(1);
Dg2=glucoseMol_array(3)-glucoseMol_array(1);
% % figure
% % axis([-1.5 4 0.6 1.01])
% % area(ppms(round(np/2):end),100*squeeze(ZAsym(:,:)),'LineWidth',1),hold on,
% % ylabel('%MTR_A_s_y_m')
% % xlabel('\Delta\omega  [ppm]')
% % set(gca, 'xdir','reverse')
% % legendCell = cellstr(num2str(B1array'*10^6, ['B1=%.1f','\mu T']))
% % legend(legendCell)
% % title(['GCE with ',sprintf('%.0f%',Dg1),' mM glucose increase  VS Power'])
% % legendCell2=cellstr([legendCell(1);'';'';legendCell(2);'';'';legendCell(3);'';'';legendCell(4);'';'';
      legendCell(5);'';'';legendCell(6);'';'';legendCell(7);'';'';legendCell(8);'';'';legendCell(9);'';'';
      legendCell(10);'';''])
%%%%%%
colors=jet(maxmynumB1);
figure,hold on,
for ii=1:size(ZSpectra_plot2,3)
plot(ppms,squeeze(ZSpectra_plot2(:,1,ii)),'Color',[colors(ii,:)],'LineWidth',1)
end

for ii=1:size(ZSpectra_plot2,3)
%  plot(ppms,squeeze(ZSpectra_plot2(:,2,ii)),'Color',[colors(ii,:)],'LineWidth',2,'',:),
   plot(ppms,squeeze(ZSpectra_plot2(:,2,ii)),'Color',[colors(ii,:)],'LineWidth',2,'LineStyle',':'),
%plot(ppms(round(np/2):end),1*squeeze(ZAsym(:,1,ii)),'Color',[colors(ii,:)],'LineWidth',1)
%plot(ppms(round(np/2):end),1*squeeze(ZAsym(:,2,ii)),'Color',[colors(ii,:)],'LineWidth',1)
plot(ppms(round(np/2):end),1*squeeze(ZAsym(:,2,ii,:,:,:,:,:,:,:)-ZAsym(:,1,ii,:,:,:,:,:,:,:)),'Color',[
      colors(ii,:)],'LineWidth',2)
plot(ppms,zeros(size(ppms)),'k', 'LineWidth',0.2,'color',[0.3 0.3 0.3])

end
ylim([-0.1 1.1])
ylabel('Z-Spectra')
set(gca, 'xdir','reverse')
legendCell = cellstr(num2str(B1array'*10^6, ['B1=%.1f','\mu T']))
legend(legendCell)

%%%%%%
figure,hold on
for ii=2:2%1:size(ZSpectra_plot2,3)
plot(ppms,squeeze((ZSpectra_plot2(:,1,ii)+0.07752*0)/(max(ZSpectra_plot2(:,1,ii))+0.07752*0)),'Color',[colors(
      ii,:)],'LineWidth',1)
%legend([sprintf('%.0f%',glucoseMol_array(1)),' mM'],[sprintf('%.0f%',glucoseMol_array(2)) ,' mM'],'Location
      ','southwest'),legend('boxoff')
end
legend(legendCell)

hold on,
for ii=2:2%1:size(ZSpectra_plot2,3)
plot(ppms,squeeze((ZSpectra_plot2(:,2,ii)+0.07752*0)/(max(ZSpectra_plot2(:,1,ii))+0.07752*0)),'Color',[colors(
      ii,:)],'LineWidth',1,'LineStyle','-.')
plot(ppms(round(np/2):end),1*squeeze(ZAsym(:,1,ii)),'Color',[colors(ii,:)],'LineWidth',1)
plot(ppms(round(np/2):end),1*squeeze(ZAsym(:,2,ii)),'Color',[colors(ii,:)],'LineWidth',1,'LineStyle','-.')
% plot(ppms(round(np/2):end),1*squeeze(ZAsym(:,2,ii)-ZAsym(:,1,ii)),'Color',[colors(ii,:)],'LineWidth',1)
plot(ppms,zeros(size(ppms)),':')
end
ylabel('MTRasymmetry & Z-Spectra')
xlabel('Saturation Power (\muT)')
set(gca, 'xdir','reverse')
%%%%%%%
```

```
%% plot the asymmetry only
figure,hold on,
for ii=4:4%size(ZSpectra,3)
plot(ppms(round(np/2):end),1*squeeze(ZAsym(:,2,ii)-ZAsym(:,1,ii)),'Color',[colors(ii,:)],'LineWidth',1)
end
ylabel('MTRasymmetry & Z-Spectra')
xlabel('Saturation Power (\muT)')
legend(legendCell)
set(gca, 'xdir','reverse')

figure,hold on
for ii=2:2%1:size(ZSpectra_plot2,3)
plot(ppms,squeeze((ZSpectra_plot2(:,1,ii)+0.07752*0)/(max(ZSpectra_plot2(:,1,ii))+0.07752*0)),'k','LineWidth'
      ,1.5)
%legend([sprintf('%.0f%',glucoseMol_array(1)),' mM'],[sprintf('%.0f%',glucoseMol_array(2)) ,' mM'],'Location
      ','southwest'),legend('boxoff')
end
legend(legendCell)

hold on,
for ii=2:2%1:size(ZSpectra_plot2,3)
plot(ppms,squeeze((ZSpectra_plot2(:,2,ii)+0.07752*0)/(max(ZSpectra_plot2(:,1,ii))+0.07752*0)),'k','LineWidth'
      ,1.5)
plot(ppms(round(np/2):end),1*squeeze(ZAsym(:,1,ii)),'k','LineWidth',1.5)
plot(ppms(round(np/2):end),1*squeeze(ZAsym(:,2,ii)),'k','LineWidth',1.5)
% plot(ppms(round(np/2):end),1*squeeze(ZAsym(:,2,ii)-ZAsym(:,1,ii)),'Color',[colors(ii,:)],'LineWidth',1)
plot(ppms,zeros(size(ppms)),'k', 'LineWidth',0.5)
end
ylabel('MTRasymmetry & Z-Spectra')
xlabel('Saturation Power (\muT)')
ylim([-0.01 1.01])
set(gca, 'xdir','reverse')
%%%%%%%%%%%%%%%%%%%%%%%%%%%%%%%%%%%%%%%%%%%%%%%%%%%%%%%%%%%%%%%%%%%%%%%%%%%%%%%
```

G. Compartmental model of glycolysis and glucose distribution

G.1. Definition of the model

```
frame
%% Definition of the glycolysis and glucose distribution model

function [Derivatives_Fluxes]=GlucoseVasculature(t,x,Itype)
global InfusionActivator DesiredBloodConc InfusionControlTime MaximumInfusionFlow InfusionInitialTime
      VasculatureRatio_tumour InterstitiumRatio_tumour CellsRatio_tumour VasculatureRatio_normal
      InterstitiumRatio_normal CellsRatio_normal pumpStatus PeritonealActivator VascularActivator InjectionDose
       InjectionTime

isbraincell=10; % 1 for yes. 100 for no.
aggressiveness=10;%*10 for SW1222, *6 for LS174T

%% Parameters definition
AlostericExponent = 1;
BasalBloodConc = 5.6;
BasalConsumption = 0.1;

EndoAlostericTumor = 1;
EndoAlostericNormal = 1;
EndoGlut1Km = 1;
EndoGlut1KmTumor = EndoGlut1Km;
EndoGlut1NormalVmax = 0.11*isbraincell;
EndoGlut1TumorVmax = EndoGlut1NormalVmax*1;

Glut1Km = 6.9/2;
Glut1NormalVmax = 0.3;
Glut1TumorVmax = Glut1NormalVmax*aggressiveness;%%%
Glut3NormalKm = 0.3;
Glut3TumorKm = Glut3NormalKm;
Glut3NormalVmax = 0.1;
Glut3TumorVmax = Glut3NormalVmax*aggressiveness;%%

NormalHexokinaseAllosExp = 1.5;
NormalKmAldolase = 1;
NormalKmHexokinase = 0.1;
NormalKmPhosphofructokinase = 0.4;
NormalKmPhosphoIsomerase = 0.7;
NormalPhosphokinaseAllosExp = 2;
NormalReversedKmIsomerase = 0.7;
NormalReversedVmaxIsomerase = 4;
NormalVmaxAldolase = 0.7;
NormalVmaxHexokinase = 0.085;
NormalVmaxPhosphofructokinase = 1;
NormalVmaxPhosphoIsomerase = 5;

TumorVmaxHexokinase = NormalVmaxHexokinase*aggressiveness*5; %
TumorHexokinaseAllostExp = NormalHexokinaseAllosExp/2;%%%%%%
TumorKmAldolase = NormalKmAldolase;
TumorKmHexokinase = NormalKmHexokinase;
```

```
TumorKmPhosphofructokinase = NormalKmPhosphofructokinase;
TumorKmPhosphoIsomerase = NormalKmPhosphoIsomerase;
TumorPhosphokinaseAllostExp = NormalPhosphokinaseAllosExp/2;%%%%
TumorReversedKmIsomerase = NormalReversedKmIsomerase;
TumorReversedVmaxIsomerase = NormalReversedVmaxIsomerase;
TumorVmaxAldolase = NormalVmaxAldolase*2;%%%%%%%%
TumorVmaxPhosphofructokinase = NormalVmaxPhosphofructokinase*1.25;
TumorVmaxPhosphoIsomerase = NormalVmaxPhosphoIsomerase*1;

NutritionalAdequacy = 1;

VascularDelay = 1;
PeritonealDelay = 35;
% VasculatureRatio = 0.03; % Attention !!!(Make it a global parameter or  Modify this parameter also in
     IntegrateGlucoseVasculature2)
VasculRecoveryTimeNormal = 1;
VasculRecoveryTimeTumor = 1;
WeightToAstrocytes = 0.5;
WeightToNeurons = 0.5;

%% State variables definition
BloodGlucConc=x(1);
ExtraGlucConcTumor=x(2);
IntraGlucConcTumor=x(3);
Gluc6PhosConcTumor=x(4);
Fruc6PhosConcTumor=x(5);
Fruc16BisConcTumor=x(6);
ExtraGlucConcNormal=x(7);
IntraGlucConcNormal=x(8);
Gluc6PhosConcNormal=x(9);
Fruc6PhosConcNormal=x(10);
Fruc16BisConcNormal=x(11);
Nperitoneal1=x(12);
Nperitoneal2=x(13);
Nperitoneal3=x(14);
Nvascular1=x(15);
VasculatureGlucConcNormal=x(16);
VasculatureGlucConcTumor=x(17);

% Type of injection configurations
InjectionDuration=0.1;

if t<InjectionTime
    Injection=0;
elseif t>InjectionTime+InjectionDuration
    Injection=0;
else
    Injection=InjectionDose/InjectionDuration;
end

Fperitoneal1 = Injection;
Fperitoneal2 = 3 * Nperitoneal1 / PeritonealDelay;
Fperitoneal3 = 3 * Nperitoneal2 / PeritonealDelay;
FperitonealOutput = 3 * Nperitoneal3 / PeritonealDelay;
Fvascular1 = Injection;
FvascularOutput = Nvascular1 / VascularDelay;

% Injections
Intraperitoneal=PeritonealActivator*FperitonealOutput;
Intravascular=VascularActivator*FvascularOutput;

% Infusion configuration
pumpStatus(1)=0;
if t<InfusionInitialTime
    IntravascularInfusion=0;
else
    %IntravascularInfusion=InfusionActivator*min(MaximumInfusionFlow, max(0,4*(DesiredBloodConc-x(1))/
        InfusionControlTime));
    if t/2-floor(t/2)<0.1  %% Infusion pump is turned on/off depeding on the Glc level, every 2 minutes
        check_pump=(DesiredBloodConc-x(1))>0;
        pumpStatus=cat(2,pumpStatus,check_pump);
    end
    IntravascularInfusion=InfusionActivator*MaximumInfusionFlow*pumpStatus(end);
end

% Insuline control time definition
```

```
if VascularActivator==1
    ExpectedInsulinControlTime=50;
else
    ExpectedInsulinControlTime=180;
end

%% Equations
AldolCondensationNormal = NormalVmaxAldolase * Fruc16BisConcNormal / ( NormalKmAldolase + Fruc16BisConcNormal
      );

AldolCondensationTumor = TumorVmaxAldolase * Fruc16BisConcTumor / ( TumorKmAldolase + Fruc16BisConcTumor );

BasalGlucEntry = NutritionalAdequacy*BasalConsumption;

BloodConcAdjustment=4*(BloodGlucConc-BasalBloodConc)/ExpectedInsulinControlTime+BasalConsumption;

% ExtraGlucNormal = InterstitiumRatio_normal * ExtraGlucConcNormal;

% ExtraGlucTumor = ExtraGlucConcTumor * InterstitiumRatio_tumour;

FrucPhosphorylationNormal = NormalVmaxPhosphofructokinase * Fruc6PhosConcNormal ^ NormalPhosphokinaseAllosExp
      / ( NormalKmPhosphofructokinase ^NormalPhosphokinaseAllosExp + Fruc6PhosConcNormal ^
      NormalPhosphokinaseAllosExp);

FrucPhosphorylationTumor = TumorVmaxPhosphofructokinase * Fruc6PhosConcTumor ^ TumorPhosphokinaseAllostExp / (
       TumorKmPhosphofructokinase ^ TumorPhosphokinaseAllostExp + Fruc6PhosConcTumor ^
      TumorPhosphokinaseAllostExp );

GlucConcIntoBlood = BasalGlucEntry + Intraperitoneal + Intravascular + IntravascularInfusion;

GlucIntoExtraNormal = EndoGlut1NormalVmax * ( VasculatureGlucConcNormal - ExtraGlucConcNormal ) ^
      EndoAlostericNormal / ( EndoGlut1Km ^ EndoAlostericNormal  + ( VasculatureGlucConcNormal -
      ExtraGlucConcNormal )^ EndoAlostericNormal);

GlucIntoExtraTumor = EndoGlut1TumorVmax * ( VasculatureGlucConcTumor - ExtraGlucConcTumor) ^
      EndoAlostericTumor / ( EndoGlut1KmTumor ^ EndoAlostericTumor+ ( VasculatureGlucConcTumor -
      ExtraGlucConcTumor ) ^ EndoAlostericTumor);

GlucIntoIntraNormal = WeightToAstrocytes * Glut1NormalVmax * ( ExtraGlucConcNormal - IntraGlucConcNormal ) / (
       Glut1Km + ( ExtraGlucConcNormal - IntraGlucConcNormal ) ) + WeightToNeurons * Glut3NormalVmax * (
      ExtraGlucConcNormal - IntraGlucConcNormal ) / ( Glut3NormalKm + ( ExtraGlucConcNormal -
      IntraGlucConcNormal ) );

GlucIntoIntraTumor = WeightToAstrocytes * Glut1TumorVmax * ( ExtraGlucConcTumor - IntraGlucConcTumor ) ^
      AlostericExponent / ( Glut1Km ^ AlostericExponent + ( ExtraGlucConcTumor - IntraGlucConcTumor ) ^
      AlostericExponent ) + WeightToNeurons * Glut3TumorVmax * ( ExtraGlucConcTumor - IntraGlucConcTumor ) / (
      Glut3TumorKm + ( ExtraGlucConcTumor - IntraGlucConcTumor ) );

% GlucInNormalVascul = VasculatureRatio_normal*VasculatureGlucConcNormal;

% GlucInTumorVascul = VasculatureRatio_tumour*VasculatureGlucConcTumor;

GlucIsomerizationNormal = NormalVmaxPhosphoIsomerase * Gluc6PhosConcNormal / ( NormalKmPhosphoIsomerase +
      Gluc6PhosConcNormal );

GlucIsomerizationTumor = TumorVmaxPhosphoIsomerase * Gluc6PhosConcTumor / ( TumorKmPhosphoIsomerase +
      Gluc6PhosConcTumor );

GlucToNormalMetabolism = NormalVmaxHexokinase * IntraGlucConcNormal ^ NormalHexokinaseAllosExp / (
      NormalKmHexokinase ^ NormalHexokinaseAllosExp + NormalVmaxHexokinase  ^ NormalHexokinaseAllosExp );

GlucToTumorMetabolism = TumorVmaxHexokinase * IntraGlucConcTumor ^ TumorHexokinaseAllostExp / (
      TumorKmHexokinase ^ TumorHexokinaseAllostExp + IntraGlucConcTumor ^ TumorHexokinaseAllostExp );

%IntraTotalNormal = CellsRatio_normal * ( IntraGlucConcNormal + Gluc6PhosConcNormal   + Fruc6PhosConcNormal +
      Fruc16BisConcNormal );

% IntraTotalTumor = CellsRatio_tumour * ( IntraGlucConcTumor + Gluc6PhosConcTumor + Fruc6PhosConcTumor +
      Fruc16BisConcTumor );

RevIsomerizationNormal = NormalReversedVmaxIsomerase * Fruc6PhosConcNormal / ( NormalReversedKmIsomerase +
      Fruc6PhosConcNormal );

RevIsomerizationTumor = TumorReversedVmaxIsomerase * Fruc6PhosConcTumor / ( TumorReversedKmIsomerase +
      Fruc6PhosConcTumor );
```

```
% TotalGlucInNormal = ExtraGlucNormal+GlucInNormalVascul+IntraTotalNormal;

% TotalGlucInTumor = ExtraGlucTumor+GlucInTumorVascul+IntraTotalTumor;

VasculConcRecoveryNormal=(BloodGlucConc-VasculatureGlucConcNormal)/VasculRecoveryTimeNormal;

VasculConcRecoveryTumor=(BloodGlucConc-VasculatureGlucConcTumor)/VasculRecoveryTimeTumor;

%% Derivatives definition
Derivatives_Fluxes=[GlucConcIntoBlood - BloodConcAdjustment                                % BloodGlucConc
      Derivative
    GlucIntoExtraTumor - GlucIntoIntraTumor                                          % ExtraGlucConcTumor
          Derivative
    GlucIntoIntraTumor - GlucToTumorMetabolism                                       % IntraGlucConcTumor
          Derivative
    GlucToTumorMetabolism + RevIsomerizationTumor - GlucIsomerizationTumor           % Gluc6PhosConcTumor
          Derivative
    GlucIsomerizationTumor - FrucPhosphorylationTumor - RevIsomerizationTumor        % Fruc6PhosConcTumor
          Derivative
    FrucPhosphorylationTumor - AldolCondensationTumor                                % Fruc16BisConcTumor
          Derivative
    GlucIntoExtraNormal - GlucIntoIntraNormal                                        % ExtraGlucConcNormal
          Derivative
    GlucIntoIntraNormal - GlucToNormalMetabolism                                     % IntraGlucConcNormal
          Derivative
    GlucToNormalMetabolism + RevIsomerizationNormal - GlucIsomerizationNormal        % Gluc6PhosConcNormal
          Derivative
    GlucIsomerizationNormal - FrucPhosphorylationNormal - RevIsomerizationNormal     % Fruc6PhosConcNormal
          Derivative
    FrucPhosphorylationNormal - AldolCondensationNormal                              % Fruc16BisConcNormal
          Derivative
    Fperitoneal1 - Fperitoneal2                                                      % Nperitoneal1
          Derivative
    Fperitoneal2 - Fperitoneal3                                                      % Nperitoneal2
          Derivative
    Fperitoneal3 - FperitonealOutput                                                 % Nperitoneal3
          Derivative
    Fvascular1 - FvascularOutput                                                     % Nvascular1
          Derivative
    VasculConcRecoveryNormal - GlucIntoExtraNormal                                   %
          VasculatureGlucConcNormal Derivative
    VasculConcRecoveryTumor - GlucIntoExtraTumor                                  %
          VasculatureGlucConcTumor Derivative
    AldolCondensationNormal
    AldolCondensationTumor];

%% Fluxes
%Fluxes=[AldolCondensationNormal,AldolCondensationTumor];
```

G.2. Execution of the model

```
frame
%% Integration of the glycolysis and glucose distribution model

global InfusionActivator DesiredBloodConc InfusionControlTime MaximumInfusionFlow InfusionInitialTime
      VasculatureRatio_tumour InterstitiumRatio_tumour CellsRatio_tumour VasculatureRatio_normal
      InterstitiumRatio_normal CellsRatio_normal PeritonealActivator VascularActivator InjectionDose
      InjectionTime

%% Time span of the simulation
timespan=[-300,150];
TimeSpan = linspace(timespan(1),timespan(2),(timespan(2)-timespan(1))*60);

%% Initial values of the state variables
BloodGlucConcIni=5.61
ExtraGlucConcTumorIni=5.5043
IntraGlucConcTumorIni=0.02
Gluc6PhosConcTumorIni=0.05
Fruc6PhosConcTumorIni=0.05
Fruc16BisConcTumorIni=0.05
ExtraGlucConcNormalIni=1.7
```

```
IntraGlucConcNormalIni=0.0501
Gluc6PhosConcNormalIni=0.0219
Fruc6PhosConcNormalIni=0.05
Fruc16BisConcNormalIni=0.04
Nperitoneal1Ini=0
Nperitoneal2Ini=0
Nperitoneal3Ini=0
Nvascular1Ini=0
VasculatureGlucConcNormalIni=5.6
VasculatureGlucConcTumorIni=5.5
fluxNomalIni=0.3
fluxTumorIni=3

Initials=[BloodGlucConcIni, ExtraGlucConcTumorIni, IntraGlucConcTumorIni, Gluc6PhosConcTumorIni,
      Fruc6PhosConcTumorIni, Fruc16BisConcTumorIni, ExtraGlucConcNormalIni, IntraGlucConcNormalIni,
      Gluc6PhosConcNormalIni, Fruc6PhosConcNormalIni, Fruc16BisConcNormalIni, Nperitoneal1Ini, Nperitoneal2Ini,
       Nperitoneal3Ini, Nvascular1Ini, VasculatureGlucConcNormalIni, VasculatureGlucConcTumorIni, fluxNomalIni,
       fluxTumorIni];

%%  volume ratios
GBM=[3,15,82]/100;
SW122=[19,11,70]/100;
LS174T=[12,5,85]/100;

VasculatureRatio_tumour = SW122(1);
InterstitiumRatio_tumour =  SW122(2);
CellsRatio_tumour =  SW122(3);

VasculatureRatio_normal = 0.04;
InterstitiumRatio_normal = 0.15;
CellsRatio_normal = 0.81;

%% Infusion parameters
InfusionActivator=0;

MaximumInfusionFlow=1.2;
DesiredBloodConc=20;
InfusionControlTime=10;
InfusionInitialTime=0;

%% Boulus injection
PeritonealActivator=1;
VascularActivator=0;

InjectionDose=20;
InjectionTime=—0;

%% Maximum time step
Options=[odeset('InitialStep',0.001)];

%% Runge—Kutta Integrator
[t,x]=ode23(@GlucoseVasculature4b,TimeSpan,Initials,Options);%GlucoseVasculature4

%% Susceptible variables for plotting
BloodGlucConc=x(:,1);
ExtraGlucConcTumor=x(:,2);
IntraGlucConcTumor=x(:,3);
Gluc6PhosConcTumor=x(:,4);
Fruc6PhosConcTumor=x(:,5);
Fruc16BisConcTumor=x(:,6);
ExtraGlucConcNormal=x(:,7);
IntraGlucConcNormal=x(:,8);
Gluc6PhosConcNormal=x(:,9);
Fruc6PhosConcNormal=x(:,10);
Fruc16BisConcNormal=x(:,11);
VasculatureGlucConcNormal=x(:,16);
VasculatureGlucConcTumor=x(:,17);
FluxNormal=x(:,18);
FluxTumor=x(:,19);

IntraTotalNormal = CellsRatio_normal * ( IntraGlucConcNormal + Gluc6PhosConcNormal + Fruc6PhosConcNormal/2 +
      Fruc16BisConcNormal/2 );

IntraTotalTumor = CellsRatio_tumour * ( IntraGlucConcTumor + Gluc6PhosConcTumor + Fruc6PhosConcTumor/2 +
      Fruc16BisConcTumor/2 );
```

```
IntravascularInfusion=InfusionActivator*min(MaximumInfusionFlow, max(0,4*(DesiredBloodConc-BloodGlucConc)/
      InfusionControlTime));

ExtraGlucNormal = InterstitiumRatio_normal * ExtraGlucConcNormal;

ExtraGlucTumor =  InterstitiumRatio_tumour * ExtraGlucConcTumor;

GlucInNormalVascul = VasculatureRatio_normal*VasculatureGlucConcNormal;

GlucInTumorVascul = VasculatureRatio_tumour*VasculatureGlucConcTumor;

TotalGlucInNormal = ExtraGlucNormal+GlucInNormalVascul+IntraTotalNormal;

TotalGlucInTumor = ExtraGlucTumor+GlucInTumorVascul+IntraTotalTumor;


%%%%%%%%%%%%%%%%%%%%%%%%%%%%%%%%%%%%%%%%%%%%%%%%%%%%%%%%%%%%%%%%%%%%%%%%%%%%%%%%%%%%%%%%%%%%%%%
%%%%%%%%%%%%%%%%%%%%%%%%%%%%%%%%%%%%%%%%%%%%%%%%%%%%%%%%%%%%%%%%%%%%%%%%%%%%%%%%%%%%%%%%%%%%%%%
%% PLOTS
xmax=120;
ymax=2.7;
pp=1;%multiplicative factor just to scale the figures
%  Tumour Concetrations and Signal contribution
figure(1)
close
figure(1),
annotation('textbox', [0.0032309057637272 0.476697659563142 0.0850159404888416 0.0798969072164947], 'String','
      Tumour tissue', 'LineStyle','none','Interpreter','latex' 'FontSize',18, 'FitBoxToText','off');
subplot(1,3,1)
plot(t,VasculatureGlucConcTumor)
hold on, plot(t,pp*GlucInTumorVascul,'--','LineWidth',2, 'Color',[0.635294 0.07843 0.18431])
title('Vascular compartment')
xlabel('Minutes')
ylabel({['Tumour vasculature [glc] (mMolar)'],['and its CEST signal (dashed red)']})
grid
ylim([0 ymax])
xlim([-5 xmax])
legend({'[Glc]','$ \sum{[Glc]*V_{frcV}}$'},'Interpreter','latex');

subplot(1,3,2)
plot(t,ExtraGlucConcTumor)
hold on, plot(t,pp*ExtraGlucTumor,'--','LineWidth',2,'Color',[0.0784 0.168622 0.5490197])
title('Interstitial compartment')
xlabel('Minutes')
ylabel({['Tumour interstitial [glc] (mMolar)'],['and its CEST signal (dashed blue)']})
grid
ylim([0 ymax])
xlim([-5 xmax])
legend({'[Glc]','$ \sum{[Glc]*V_{frcI}}$'},'Interpreter','latex');

subplot(1,3,3)
plot(t,IntraGlucConcTumor,t,Gluc6PhosConcTumor,t,Fruc6PhosConcTumor,t,Fruc16BisConcTumor)
hold on, plot(t,pp*IntraTotalTumor,'--','Color',[0 0.498 0],'LineWidth',2)
title('IntraCellular compartment');
xlabel('Minutes')
ylabel({['Tumour intracellular [sugar] (mMolar)'],['and their CEST signal (dashed green)']})
grid
ylim([0 ymax])
xlim([-5 xmax])

legend1 = legend({'[Glc]','[G6P]','[F6P]','[F16biP]','$ \sum{[sugar]*V_{frcC}}$'},'Interpreter','latex');
set(legend1, 'Position',[0.858951707891635 0.522491349480969 0.065959952885748 0.193771626297578]);

%%  Normal tissue Concetrations and Signal contribution
figure(2),
close
figure(2)
annotation('textbox', [0.0032309057637272 0.476697659563142 0.0850159404888416 0.0798969072164947], 'String','
      Normal tissue', 'LineStyle','none', 'Interpreter','latex', 'FontSize',18, 'FitBoxToText','off');

subplot(1,3,1)
plot(t,VasculatureGlucConcNormal)
hold on,plot(t,pp*GlucInNormalVascul,'--','LineWidth',2, 'Color',[0.635294 0.07843 0.18431])
title('Vascular compartment')
xlabel('Minutes')
ylabel({['Normal vasculature [glc] (mMolar)'],['and its CEST signal (dashed red)']})
```

```
grid
ylim([0 ymax])
xlim([-5 xmax])
legend_v = legend({'[Glc]','$ \sum{[Glc]*V_{frcV}}$'},'Interpreter','latex');

subplot(1,3,2)
plot(t,ExtraGlucConcNormal)
hold on,plot(t,pp*ExtraGlucNormal,'--','LineWidth',2,'Color',[0.0784 0.168622 0.5490197])
title('Interstitial compartment')
xlabel('Minutes')
ylabel({['Normal interstitial [glc] (mMolar)'],['and its CEST signal (dashed blue)']})
grid
ylim([0 ymax])
xlim([-5 xmax])
legend_e = legend({'[Glc]','$ \sum{[Glc]*V_{frcI}}$'},'Interpreter','latex');

subplot(1,3,3)
plot(t,IntraGlucConcNormal,t,Gluc6PhosConcNormal,t,Fruc6PhosConcNormal,t,Fruc16BisConcNormal)
hold on,plot(t,pp*IntraTotalNormal,'--','Color',[0 0.498 0],'LineWidth',2)
title('IntraCellular compartment');
xlabel('Minutes')
ylabel({['Normal intracellular [sugar] (mMolar)'],['and their CEST signal (dashed green)']})
grid
ylim([0 ymax])
xlim([-5 xmax])
legend1 = legend({'[Glc]','[G6P]','[F6P]','[F16biP]','$ \sum{[sugar]*V_{frcC}}$'},'Interpreter','latex');

%% GCE definitions
baseline=-timespan(1)*60-10;
TumourSignal=TotalGlucInTumor-TotalGlucInTumor(baseline);
NormalSignal=TotalGlucInNormal-TotalGlucInNormal(baseline);

%% Total Signal in tumour and normal tissue
GCE_mMolar_ratio=0.2;
figure(3)
plot(t,GCE_mMolar_ratio*TumourSignal,':','Color',[0.85 0.32 0.098],'Linewidth',2)
hold on, plot(t,GCE_mMolar_ratio*NormalSignal,':','Color',[0 0.447 0.741],'Linewidth',2)
xlabel('Minutes')
ylabel('%GCE signal from Tumour and Normal voxels')
grid
title({'glucoCEST signal (%GCE) in tumour and normal tissue','(all compartments included)'})
%legend2 = legend('Tumour','Normal tissue');
%set(legend2,'Position',[0.758951707891635 0.522491349480969 0.055959952885748 0.193771626297578],'FontSize
      ',18,'Interpreter','latex');
ylim([-0.2*GCE_mMolar_ratio 4*GCE_mMolar_ratio])
xlim([-5 xmax])

%% Blood glucose level
figure(4)
plot(t,BloodGlucConc,'r')%,t,TumourSignal*8,'.r',t,NormalSignal*8,'.c')
xlabel('Minutes')
ylabel('Blood glucose level [mMolar]')
grid
title({'Blood glucose level'})

%% Glycolytic fluxes
FluxN=(FluxNormal(2:end)-FluxNormal(1:end-1))/(t(2)-t(1));
FluxT=(FluxTumor(2:end)-FluxTumor(1:end-1))/(t(2)-t(1));
t1=t(2:end);
%%%%%%%%

figure(5)
subplot(1,2,1)
plotrange=(baseline-120):length(FluxN);
plot(t1(plotrange),FluxT(plotrange),'LineWidth',2, 'Color',[0.851 0.3250 0.098]);
hold on,plot(t1(plotrange),FluxN(plotrange),'LineWidth',2, 'Color',[0 0.447 0.741]);
xlim([-2,140])
ylim([-0.0 1.0])
xlabel('Minutes')
ylabel('Glycolytic flux & \Deltaflux [mMolar/min]')
grid
title({'Glycolytic flux'})
legend2 = legend('Tumour','Normal');
set(legend2,
   'FontSize',14,'Interpreter','latex');
```

```
subplot(1,2,2)
plot(t1(plotrange),FluxN(plotrange)-FluxN(baseline),'--','LineWidth',2,'Color',[0 0.447 0.741]);
hold on, plot(t1(plotrange),FluxT(plotrange)-FluxT(baseline),'--','LineWidth',2,'Color',[0.851 0.3250 0.098]);
xlim([-2,140])
xlabel('Minutes')
title('\Deltaflux after administration of glucose')
grid

%% Contribution of each compartmet to the GCE signal
sss=1;
total_GCE_tumour=0+GlucInTumorVascul-sss*GlucInTumorVascul(baseline)+ExtraGlucTumor-sss*ExtraGlucTumor(
    baseline)+IntraTotalTumor-sss*IntraTotalTumor(baseline);
vascular_GCE_tumour=100*(GlucInTumorVascul-GlucInTumorVascul(baseline))./total_GCE_tumour;
extra_GCE_tumour=100*(ExtraGlucTumor-ExtraGlucTumor(baseline))./total_GCE_tumour;
intra_GCE_tumour=100*(IntraTotalTumor-IntraTotalTumor(baseline))./total_GCE_tumour;

total_GCE_normal=0+GlucInNormalVascul-sss*GlucInNormalVascul(baseline)+ExtraGlucNormal-sss*ExtraGlucNormal(
    baseline)+IntraTotalNormal-sss*IntraTotalNormal(baseline);
vascular_GCE_normal=100*(GlucInNormalVascul-GlucInNormalVascul(baseline))./total_GCE_normal;
extra_GCE_normal=100*(ExtraGlucNormal-ExtraGlucNormal(baseline))./total_GCE_normal;
intra_GCE_normal=100*(IntraTotalNormal-IntraTotalNormal(baseline))./total_GCE_normal;

%% in tumour
figure(6)
subplot(1,2,2)
% plot(t,vascular_GCE_tumour,t,extra_GCE_tumour,t,intra_GCE_tumour)
plot(t,TumourSignal./max(TumourSignal).*vascular_GCE_tumour,'.',t,TumourSignal./max(TumourSignal).*
    extra_GCE_tumour,'.',t,TumourSignal./max(TumourSignal).*intra_GCE_tumour,'g.')%,
 axis([-5 120 -0.1 101])
xlabel('Minutes')
% ylabel({'Relative GCE signal', '(normalised to the maximum GCE) [%]'})
grid
title({'in TUMOUR tissue'})

%% in normal
subplot(1,2,1)
% plot(t,vascular_GCE_normal,'--',t,extra_GCE_normal,'--',t,intra_GCE_normal,'--')
plot(t,NormalSignal./max(NormalSignal).*vascular_GCE_normal,'.',t,NormalSignal./max(NormalSignal).*
    extra_GCE_normal,'.',t,NormalSignal./max(NormalSignal).*intra_GCE_normal,'g.')
axis([-5 120 -0.1 101])
xlabel('Minutes')
ylabel({'Relative GCE signal [%]', '(normalised to the maximum GCE)'})
grid
title({'in NORMAL tissue'})
legend1 = legend('Vascular','Interstitial','Intracellular');
set(legend1, 'Position',[0.346 0.4413399891284 0.188 0.130], 'Interpreter','latex','FontSize',14,'EdgeColor'
    ,[0.93 0.93 0.933]);

  annotation(figure(6),'textbox',[0.217 0.596 0.545 0.068],'String',{['Contribution of each comparment to the
      glucoCEST signal'];['$V_{frcV}=0.2,V_{frcI}=0.2,V_{frcC}=0.6$','  and IP bolus protocol)']},'LineStyle'
      ,'none','Interpreter','latex','FontSize',18,'FontName','Helvetica','FitBoxToText','off');

%% Total CEST splited in compartment Contribution
vascular_GCE_tum=(GlucInTumorVascul-GlucInTumorVascul(baseline))*GCE_mMolar_ratio;
extra_GCE_tum=(ExtraGlucTumor-ExtraGlucTumor(baseline))*GCE_mMolar_ratio;
intra_GCE_tum=(IntraTotalTumor-IntraTotalTumor(baseline))*GCE_mMolar_ratio;

vascular_GCE_nor=(GlucInNormalVascul-GlucInNormalVascul(baseline))*GCE_mMolar_ratio;
extra_GCE_nor=(ExtraGlucNormal-ExtraGlucNormal(baseline))*GCE_mMolar_ratio;
intra_GCE_nor=(IntraTotalNormal-IntraTotalNormal(baseline))*GCE_mMolar_ratio;

figure,
subplot(1,2,1),hold on,
area(t,intra_GCE_nor+extra_GCE_nor+vascular_GCE_nor,'facecolor',[0 0.6 0],'edgecolor','none')
area(t,extra_GCE_nor+vascular_GCE_nor,'facecolor',[0.09 0.3 0.7],'edgecolor','none')
area(t,vascular_GCE_nor,'facecolor',[0.7 0.0 0.1],'edgecolor','none')
 axis([-5 120 -0.0 0.9])
xlabel('Minutes')
 ylabel({'\%GCE signal'},'fontsize',16,'interpreter','latex')
title({'\bf{Healthy tissue}';['$V_{frcV}=$',sprintf('%.2g%',VasculatureRatio_normal),'$, V_{frcI}=$',sprintf('
    %.2g%',InterstitiumRatio_normal),'$, V_{frcC}=$',sprintf('%.2g%',CellsRatio_normal)]},'FontWeight','bold'
    ,'FontSize',14,'Interpreter','latex');
grid
subplot(1,2,2),hold on,
area(t,intra_GCE_tum+extra_GCE_tum+vascular_GCE_tum,'facecolor',[0 0.6 0],'edgecolor','none')
area(t,extra_GCE_tum+vascular_GCE_tum,'facecolor',[0.09 0.3 0.7],'edgecolor','none')
```

```
area(t,vascular_GCE_tum,'facecolor',[0.7 0.0 0.1],'edgecolor','none')
 axis([-5 120 -0.0 0.9])
xlabel('Minutes')
% ylabel({'Relative GCE signal', '(normalised to the maximum GCE) [%]'})
% title({['\bf{Tumour tissue}'];['$V_{frcV}=%',0.2,V_{frcI}=$',sprintf('%.2g%',InterstitiumRatio_normal),'$V_{
      frcC}=0.6$']},title({'\bf{Tumour tissue}';['$V_{frcV}=$',sprintf('%.2g%',VasculatureRatio_tumour),'$, V_{
      frcI}=$',sprintf('%.2g%',InterstitiumRatio_tumour),'$, V_{frcC}=$',sprintf('%.2g%',CellsRatio_tumour)]},'
      FontWeight','bold','FontSize',14,'Interpreter','latex');
legend({'Intracelullar','Interstitial','Vascular'},'interpreter','latex','edgecolor','none','fontsize',12)
grid

% %% Plot inplane contrast (tumour-normal)
% TminusN=(intra_GCE_tum+extra_GCE_tum+vascular_GCE_tum)-(intra_GCE_nor+extra_GCE_nor+vascular_GCE_nor);
% TplusN=(intra_GCE_tum+extra_GCE_tum+vascular_GCE_tum)+(intra_GCE_nor+extra_GCE_nor+vascular_GCE_nor);
% figure,
% hold on,
% area(t,TminusN,'facecolor',[0.3 0.7 0.7],'edgecolor','none')
%  axis([-0 120 -0.05 0.4])
% xlabel('Minutes')
%  ylabel({'$\% \Delta GCE $'},'fontsize',16,'interpreter','latex')
% %  title({'Contrast resolution= $\frac{GCE_{Tumor}-GCE_{Healthy}}{GCE_{Tumor}+GCE_{Healthy}}$'}
%  title({'Contrast resolution. [$\Delta(GCE_{Tumor}-GCE_{Healthy})$]'},'FontWeight','bold','FontSize',14,'
      Interpreter','latex');
% grid
```

Contributions from this work

Grant applications

- Horizon 2020. 'GLucoCEST Imaging of Neoplastic Tumours (GLINT)'.
- Confidence in Concept (CiC) scheme. 'GlucoCEST as an ictal MRI method in epilepsy'.

Peer reviewed publications

- 'Validation of Amide Proton Transfer MRI as a measure of pH by 31-P NMR in a piglet model of Hypoxic Ichemic Encephalopathy', M. Rega, F. Torrealdea, A. Bainbridge, C. Uria, D. L. Thomas, N. Robertson, X. Golay. *JCBFM 2015 (under review)*.
- 'In vivo Imaging of Tau pathology using Multi-Parametric Quantitative MRI', J. A. Wells, J. M. O'Callaghan, H. E. Holmes, N. M. Powel, R. A. Johnson, S. Siow, F. Torrealdea, O. Ismail, S. Walker-Samuel, X. Golay, M. Rega, S. Richardson, N. Fox, A. J. Schwarz, Z. Ahmed, T. K. Murray, M. J. O'Neill, E. C. Collins, N. Colgan, M. F. Lythgoe. *Neuroimage 2015*.
- 'Imaging glucose in tumours'. S. Walker-Samuel, R. Ramasawmy, F. Torrealdea, M. Rega, S. P. Johnson, V. Rajkumar, M. Goncalves, E. Arstad, D. Thomas, R. B. Pedley, M. F. Lythgoe, X. Golay. *Nature Medicine 2013*.

Communications

1. 'Optimisation of glucoCEST signal for application in tumours'. F. Torrealdea, M. Rega, X. Golay (ESMRMB, Edinburgh 2015 & International workshop on CEST, Philadelphia 2015).

2. 'Bicarbonate as a theragnostic CEST agent for glioma models'. F. Torrealdea, M. Rega, S. Brandner, D. Thomas, S. Walker-Samuel, X. Golay (ISMRM, Milan 2014 & 4th International workshop on CEST, Turin 2014).

3. 'GlucoCEST for the detection of human xenograft glioblastoma at early stage'. F. Torrealdea, M. Rega, A. Richard-Loendt, S. Brandner, D. L. Thomas, S. Walker-Samuel, X. Golay (ISMRM, Salt lake city USA, 2013).

4. 'Imaging pH changes in the piglet brain after acute hypoxia-ischemia using amide proton transfer MRI'. M. Rega, F. Torrealdea, A. Bainbridge, D. Price, K. Broad, I. Fiernes, M. Ezzati, A. Oliver-Taylor, R. Burnett, C. Uria, N. Robertson, S. Walker-Samuel, D. L. Thomas, X. Golay (ESMRMB, Toulouse 2013 & ESPR, Porto 2013).

5. 'Detection of protein accumulation by amide proton transfer in the spinal cord of SOD1 mice using exchange-modulated Laser sequence (EX-L)'. M. Rega, F. Torrealdea, A. Gray, J. Dick, P. Smethurst, L. Greensmith, K. Sidle, S. Walker-Samuel, D. L. Thomas, X. Golay (ISMRM, Salt lake city USA, 2013).

6. 'GlucoCEST of tumour xenografts provides equivalent information to [18F]FDG autoradiography'. F. Torrealdea , S. Walker-Samuel, R. Ramasawmy, M. Rega, S. P. Johnson, V. Rajkumar, M. Goncalves, D. Thomas, R. B. Pedley, M. F. Lythgoe, X. Golay (4th International workshop on CEST, Annapolis 2012).

7. 'Investigation of CEST effects in hexoses and pentoses of the glycolytic pathway'. F. Torrealdea, M. Rega, M. Lythgoe, D. L. Thomas, S. Walker-Samuel, X. Golay (ISMRM, Melbourne, 2012).

8. 'Comparison of glucoCEST enhancement with 18-F FDG autoradiography'. S. Walker-Samuel, R. Ramasawmy, F. Torrealdea, M. Rega, S. P. Johnson, V. Rajkumar, M. Goncalves, D. L. Thomas, R. B. Pedley, M. F. Lythgoe, X. Golay (ISMRM, Melbourne, 2012).

9. 'Dynamic glucose- enhanced (DCE) MRI: A proof of principle study'. S. Walker-Samuel, R. Ramasawmy, F. Torrealdea, M. Rega, S. P. Johnson, V. Rajkumar, D. L. Thomas, R. B. Pedley, M. F. Lythgoe, X. Golay (ISMRM, Melbourne, 2012).

10. 'Assessment of tumour glucose uptake using glucoCEST'. S. Walker-Samuel, S. P. Johnson, F. Torrealdea, M. Rega, S. Richardson, R. Ramasawmy, D. L. Thomas, R. B. Pedley, M. F. Lythgoe, X. Golay (ISMRM, Montreal, 2011).